Preparation and Characterisation of Magnetic Nanostructured Samples for Inelastic Neutron Scattering Experiments

Dissertation
zur Erlangung des Doktorgrades
des Fachbereichs Physik
der Universität Hamburg

vorgelegt von

Wolfgang Kreuzpaintner

aus Dingolfing

Hamburg
2010

Gutachter der Dissertation:
    Prof. Dr. A. Schreyer
    Prof. Dr. H. P. Oepen

Gutachter der Disputation:
    Prof. Dr. A. Schreyer
    Prof. Dr. M. Müller

Datum der Disputation:
    22. Juni 2010

Vorsitzender des Prüfungsausschusses:
    Dr. A. Chudnovskiy

Vorsitzender des Promotionsausschusses:
    Prof. Dr. J. Bartels

Leiterin des Departments Physik:
    Prof. Dr. D. Pfannkuche

Dekan der MIN-Fakultät:
    Prof. Dr. H. Graener

Kurzfassung

Die Weiterentwicklung der Strukturierungsmethoden dünner Filme hat zu einem erheblichen Interesse an der Dynamik magnetischer Nanostrukturen und an dem möglichen Einsatz inelastischer Neutronenstreuung (INS) zu ihrer Untersuchung geführt.

Diese Arbeit beschreibt den Aufbau und die Implementierung von Apparaturen am GKSS Forschungszentrum für die Herstellung großflächiger lateral submikrometer- und nanometer-strukturierter Proben für künftige INS Experimente.

Nach einem kurzen Resümee zu Spinwellen in Nanostrukturen wird die Entwicklungsarbeit an neuen, anwendungsspezifischen Geräten wie einer Hoch-Vakuum (HV) Ionenstrahlätzanlage und einer Ultra-Hoch-Vakuum (UHV) Elektronenstrahlverdampferanlage beschrieben.

Proben mit Ni-Nanopunkten sowie Ni- und neuartigen Gd-Nanodrähten wurden mittels komplementärem Einsatz von Ionenzerstäuben, Laserinterferenzlithographie, Elektronenstrahlverdampfen und Selbstorganisation hergestellt.

Im Rahmen der Probenherstellung wurden auch Studien zum epitaktischen Wachstum von Ni auf Si(100) Substraten durchgeführt. Diese führten zur Entwicklung eines neuartigen Beschichtungsprozesses, der durch gezieltes Nachregeln der Temperatur das direkte epitaktische Wachstum von Ni auf Si mit bisher unerreichter kristalliner Qualität ermöglicht.

Die Ergebnisse der verschiedensten Charakterisierungsexperimente an den hergestellten lateral nanostrukturierten Proben sind anschließend, nebst verschiedener Analyseverfahren wie Distorted-Wave Born Approximation (DWBA), dargestellt. Diese umfassen Rasterelektronenmikroskopie (SEM), Elektronenmikrosondenanalyse, Raster- und Magnetkraftmikroskopie (AFM/MFM), Vibrating-Sample-Magnetometer-Messungen (VSM), Röntgen-Diffraktion (XRD) und Reflektivitätsmessungen (XRR), unpolarisierte und polarisierte Neutronenstreuung sowie off-spekuläre Röntgen- und Neutronenstreuexperimente mittels "rocking scans" und Flugzeit-Neutronen-Kleinwinkelstreuung unter streifendem Einfall (TOF-GISANS).

Die Analyse einer Probe mit Gd-Nanodrähten mittels TOF-GISANS führte darüber hinaus zu einer neuartigen Auswertetechnik, die die Nutzung eines "weißen" Neutronenstrahls erlaubt und im Vergleich zu monochromatisch arbeitenden Geräten das Abscannen von Bereichen im reziproken Raum ohne Änderung des Neutronen-Einfallswinkels ermöglicht. Die Technik ist im Rahmen der Probencharakterisierung dargestellt und wurde auch zur Analyse von Ni-Nanodrähten herangezogen.

Abstract

Recent advances in thin-film structuring techniques have generated significant interest in the dynamics of spin waves in magnetic nanostructures and the possible use of inelastic neutron scattering (INS) for their investigation.

This thesis describes the design and implementation, at GKSS Research Centre, of equipment for preparation of large and laterally submicron and nanometre structured magnetic samples for such future INS experiments.

After a brief résumé on spin waves in nanostructures, the development work on new purpose-designed equipment, including high vacuum (HV) argon ion beam milling and ultra high vacuum (UHV) e-beam evaporation setups, is described.

Ni nanodot as well as Ni and novel Gd nanowire samples were prepared using combinations of sputter deposition, laser interference lithography, argon ion beam milling, e-beam evaporation and self organisation techniques.

With reference to sample preparation, epitaxial growth studies for Ni on Si(100) substrate were performed, resulting in the development of a new deposition process, which by thermal tuning allows for the direct epitaxial growth of Ni on Si with unprecedented crystalline quality.

The results of various characterisation experiments on the prepared nanostructured samples, including Scanning Electron Microscopy (SEM), microprobe analysis, Atomic and Magnetic Force Microscopy (AFM/MFM), Vibrating Sample Magnetometry (VSM), X-ray Diffraction (XRD) and Reflectivity (XRR), unpolarised and Polarised Neutron Scattering (PNR) and off-specular scattering by x-rays and neutrons using rocking scans and Time-Of-Flight Grazing Incidence Small Angle Neutron Scattering (TOF-GISANS), together with various analysis procedures such as Distorted-Wave Born Approximation (DWBA), are reported.

The analysis of a Gd nanowire sample by TOF-GISANS led to a novel evaluation technique which in comparison with single wavelength methods allows portions of reciprocal space to be scanned without changing the angle of incidence by use of a white neutron beam. The technique is demonstrated in the context of sample characterisation, where it is also applied to the analysis of Ni nanowires.

Contents

Chapter 1

Introduction

Recent advances in thin-film preparation and structuring techniques and the industrial demand for increasingly higher magnetic storage densities have created a significant interest in the magnetic properties of sub-micrometre and nanoscale laterally structured magnetic thin films and multilayers [1–3]. In this context, the spinwave dynamics is a critical parameter for writing speed and storage stability [4–8], and great advances have been made on both theoretical and experimental observations of standing and propagating spinwaves in various lateral structures ranging from two dimensional systems [4, 9, 10] to nanoparticle crystals [11, 12]. The outstanding property of such nanostructures is generally the quantisation of spin wave frequencies, which is due to the (usually at least two-dimensional) confinement in nanostructures. Experimental research in this field is mainly carried out using Brillouin Light Scattering (BLS) techniques [13, 14], or Ferromagnetic Resonance (FMR) measurements [4]. These techniques have in common the advantage that they do not require a large assembly of nanostructures, but can be applied even when there are very few magnetic structures present in the specimen. This fits well with the usual sample preparation method of electron beam lithography, which is unrivaled in precision by other methods for writing structures on a nanoscale but at the cost of slow speed.

Although technologically challenging preparation methods such as nanoimprint and x-ray lithography have already been developed because of the prospective use of large nanopatterned media in magnetic storage devices [15, 16], more recent and more cost efficient techniques for producing larger sample areas or even three dimensional volumes include self-organisation processes of magnetic particles (e.g. embedded in polymer chains) which can form nanostructured layers or supercrystals [11, 17] with layer-by-layer growth. Due to the less demanding preparation steps, self-organisation is also widely used for research on a laboratory level. However, self-organisation is also less perfect on a large scale and hence only smaller areas are usually investigated where sufficient order exists.

As spin-$\frac{1}{2}$ particles, neutrons have a magnetic moment and when used as a probe with wavelengths in the magnitude of Å have energies that are comparable to the excitation energies of magnons. Inelastic Neutron Scattering (INS) is thus the most direct and consequently best established method for probing spinwave distributions in bulk materials [18]. It is also a candidate for studying the magnetic dynamics of

nanostructures, especially as this method can access regions of the Brillouin zone which cannot be probed by other means. Apart from delivering complementary data, INS is the only technique that (as well as probing standing spin waves in noninteracting confined particles as do BLS and FMR) could also investigate propagating spinwaves in two or three dimensional assemblies of interacting nanoparticles and is therefore essential for obtaining consistent spinwave dispersion spectra in such systems [19].

From an experimental viewpoint, INS relies on the presence of significant amounts of material. This is due to the inelastic cross section of neutrons being several orders of magnitude smaller than the structural and magnetic elastic cross sections, resulting in a very low intensity of the signal. The outstanding capabilities of INS on a Dy/Y superlattice structure have already been demonstrated [20]; however, compared to several hundreds of pairs of magnetic layers, nanostructures offer a much smaller amount of material and thus a smaller scattering volume. The use of rare earth elements, such as Dy or Gd, is favourable because their large magnetic moments also reduce the required amount of material for INS. However, due to the strong reactivity of rare earth elements, only laterally nanostructured samples based on rare earth compounds, such as oxides, silicides or carbides, have so far been investigated [21, 22]. It is this lack of samples having a large magnetic moment and which are precisely structured on a sufficiently large area or volume that explains why INS has so far not been used to probe the spinwave dynamics of ordered lateral magnetic nanostructures.

In this broader context, the aim of the present work was to extend the application of INS into the range of laterally nanostructured magnetic samples by finding ways to increase the scattered neutron signal intensity by several orders of magnitude. This can be done on both the instrumental and the specimen side. This project focuses mainly on the sample preparation by creating experimental capabilities at GKSS Research Centre for preparing large sub-micrometre structured samples for proposed future INS experiments. The publications which directly resulted from this work are given in the List Of Publications (LOP) on page 129.

In the following, spinwaves in nanostructures and their theoretical description are first introduced in chapter 2, where also a novel theoretical approach to describing spin wave dynamics in two and three dimensional nanostructured samples is considered and effects for two and three dimensional assemblies of nanodots are described [LOP-1]. The situation for nanowires and the experimental relevance of theoretical predictions for this work are also briefly commented upon.

The thin film deposition and structuring methods used for sample preparation are then briefly reviewed in chapter 3, and the development work carried out on new sample preparation and vacuum equipment over the duration of this project is described in chapter 4. The applied sample analysis methods are discussed in chapter 5, followed by the description of the development of a new deposition method for direct epitaxial growth of Ni on Si with unprecedented crystalline quality (chapter 6) [LOP-2], which will allow the preparation of nanostructures with a well defined crystalline relationship to be carried out[1].

---

[1]Proof of concept is given in appendix A.2

The application of the described deposition and structuring methods for the preparation of samples is given in chapter 7, together with the parameters of sample preparation for Ni nanostructures and the first reported Gd nanowires.

The characterisation results of the prepared samples by several applied techniques (including a Distorted-Wave Born Approximation based analysis of off-specular x-ray data) are then given in chapter 8, where also the novel use of the new combined GKSS Reflectometer and Small Angle Neutron Scattering instrument REFSANS at the FRM II neutron source in Garching for the analysis of nanostructured samples by TOF-GISANS [LOP-3] is described.

The conclusions drawn from this project and an outline of possible further research, including a road map towards INS on REFSANS, are given in chapter 9.

Chapter 2

Spin Waves in Nanostructures

This chapter discusses spin waves in nanodot and nanowire assemblies, including a theoretical approach developed during this project for interacting 2D and 3D super-lattices of nanosized ferromagnetic spheres. The current experimental relevance of this theory is also described.

2.1 Nanodot Assemblies

2.1.1 2 Dimensional Assembly of Nanodots

Generally "2-dimensional nanodot arrays" refers to lithographically fabricated, and hence plain, structures of round or rectangular nanodots. The most commonly treated problem of spin waves in such systems is on noninteracting nanodots of a particular shape, which corresponds in practice to an investigation of the energies and the profiles of standing spin wave modes.

However, an analytical solution for non-ellipsoidal particles is currently not possible. Hence, in order to obtain an approximate but solvable theoretical approach that can describe experimental results, two physical properties are considered:

One is the flat shape of such nanostructures, with a thickness which is typically much lower than the lateral dimensions[1]. This allows for theoretical solutions to be independent on the out-of-plain z coordinate perpendicular to the plane in which the nanostructures are arranged and the common approximative theory for such systems is based on the results that are obtained for continuous magnetic films [23].

The second physical property is the smooth character of the demagnetisation field in the majority of experimental situations, which allows approximate solutions for appropriate symmetries, determined by the particle shape, to be written. The most complete description of such approaches can be found in [4] for the case of plain round dots (accounting for the explanation of FMR experiments) and in [14] for rectangular nanostructures (explaining BLS results). In general, the approximative

---

[1] From an experimental viewpoint, this is due to the well-controllable thickness of thin layers, but less advanced lateral structuring techniques.

equation for frequencies and energies ($\hbar\omega$), respectively, of spin wave Eigenmodes for all shapes of flat particles is found as

$$\omega_{mn}^2 = (\omega_H^{mn} + \alpha\omega_M k_{mn}^2)(\omega_H^{mn} + \alpha\omega_M k_{mn}^2 + \omega_M F_{mn}(k_{mn}L)) \tag{2.1}$$

where m, n are the quantum numbers which originate from the confinement in the x, y plain, α is the exchange stiffness constant, ω_H^{mn} (often in the form of $\omega_H^{mn} = g(H \pm 4\pi M_0)$) accounts for the energy input from the external and demagnetizing fields, and $F_{mn}(k_{mn}L)$ is the quantised matrix element of the dipole–dipole interaction with wave vector k_{mn} and particle thickness L. Although $F_{mn}(k_{mn}L)$ is also shape dependent, in some experimental cases it is nevertheless possible to set $F_{mn}(k_{mn}L)$ equal to the corresponding term of a continuous, laterally unstructured, thin film. In more precise calculations, however, the difference for nanostructured and continuous thin films [23] can be taken into account by perturbation theory. The values of the excitation wave vectors $|k_{mn}|$ are obtained from the boundary conditions of the corresponding nanoparticle. However, finding these boundary conditions is usually not trivial as electrodynamic boundary conditions leave the amplitude of the dynamic magnetisation at the confining edges of the magnetic nanostructures undefined. Common assumptions in the calculations are therefore that the boundary conditions at the edges of the nanostructure are either unpinned ($\frac{\partial \vec{m}}{\partial n} = 0$ on the surface of the nanostructure with n being the normal to the surface) or pinned ($\vec{m} = 0$). Both assumptions give the quantisation condition for the spin wave vector components for rectangular particles in the form of

$$k_m = \frac{m\pi}{w}, \quad k_n = \frac{n\pi}{l}, \quad k_{mn} = \sqrt{k_m^2 + k_n^2} \tag{2.2}$$

where w and l are the width and the length of the nanoparticle with $w \gg L$, $l \gg L$. In these cases the Eigenfunctions are either cosinusoidal or sinusoidal. For round nanoparticles even the approximate analytical approach is more complicated, as with the particle shape also the Eigenfunctions change their form into Bessel functions. Moreover, no separate components k_m, k_n exist due to the cylindrical symmetry and radial wave vectors $\vec{k}_{mn}$ must be introduced. $\vec{k}_{mn}(R)$ (with R being the radius of a single nanodot) then corresponds to the expression

$$J_n(k_{mn}r)|_{r=R} = 0 \tag{2.3}$$

for the pinned case and

$$\left.\frac{d}{dr}J_n(k_{mn}r)\right|_{r=R} = 0 \tag{2.4}$$

for unpinned boundary conditions. The indices correspond to the number of the mode or antimode m and give the order n of the radial Bessel function and consequently determine the shape of the Eigenmode. However, this naive point of view does not, in basically all cases, explain the experimental results. Hence, so-called "dipolar" boundary conditions are necessary and have been derived for magnetically soft nanostripes and nanoparticles [14, 24]. For magnetically hard nanoparticles the boundary conditions should be a composition of the anisotropy and the dipolar

conditions on the surfaces. Additionally, it should be noted that these theoretical calculations of boundary conditions are usually not sufficient to describe the results of real experiments as the occurence of roughness, defects and strains on the surface of nanoparticles cause significant experimental deviations from the theoretically calculated anisotropy.

For spin wave dispersions in interacting ensembles, the task becomes even more complicated. There are results for propagating spin waves in ensembles of interacting round dots [25] and new results have been obtained in this project for 3D ensembles of spherical nanoparticles [LOP-1].

2.1.2   Three Dimensional Nanocrystals

Progress in the chemical preparation of superparamagnetic nanospheres of very narrow size distribution which are embedded in polymer chains and have a tendency to self-organise has shown that the third dimension must be taken into account in describing interacting nanoparticles. Such nanosphere particles have been used to grow ordered 3D nanocrystals [11, 12] using layer by layer growth.

Given the small size of the magnetic nanoparticles in such ensembles, storage stability (related to the enhancement of the energy barrier between the two possible ground states of uniaxial nanoparticles) becomes an important consideration. Apart from enhancing the nanoparticle anisotropy, which usually decreases with decreasing particle size, interparticle interactions of dipolar origin influence the storage stability via the energy barrier. Therefore, much attention has already been paid to this question [5, 26] and it is known that the effect of the dipolar interaction strongly depends on the order in the nanoparticle superlattices [27].

There exist several theoretical approaches for studying very small [28] (quantum) and comparably large [29, 30] (classical) interacting nanostructures. However, the first theoretical investigation of the spin wave dispersion in 3D nanoparticle systems was presented as a result of the efforts in this work in collaboration with GKSS colleague H. Tartakovskaya in [LOP-1] and compared to the behaviour of the corresponding 2D systems. By applying a linear combination of atomic orbitals (LCAO) method (compare also with [31]) to the analysis of propagating spin waves in 2D and 3D superlattices consisting of spherical ferromagnetic nanoparticles, a considerably different effect of the dipolar interaction on 2D and 3D superlattices was found and the specific parameters of the 3D hexagonal close-packed (hcp) system were calculated.

Due to the competition between the crystalline anisotropy within each particle and the dipolar interaction between the particles, the calculated spin wave dispersion indicates a phase transition between a ferromagnetic and a presumably[2] helicoidal order. It was also shown in [LOP-1] that in the case of a 3D hexagonal close packed arrangement of magnetic nanoparticles, the dipolar interaction decreases the relaxation time for ferromagnetically ordered arrays of nanoparticles (figure 2.1).

---

[2]The spin wave theory presented in [LOP-1] suggests that the magnetic order should be helicoidal rather than ferromagnetic or anti-ferromagnetic. The question is however not answered conclusively and requires further investigation [19].
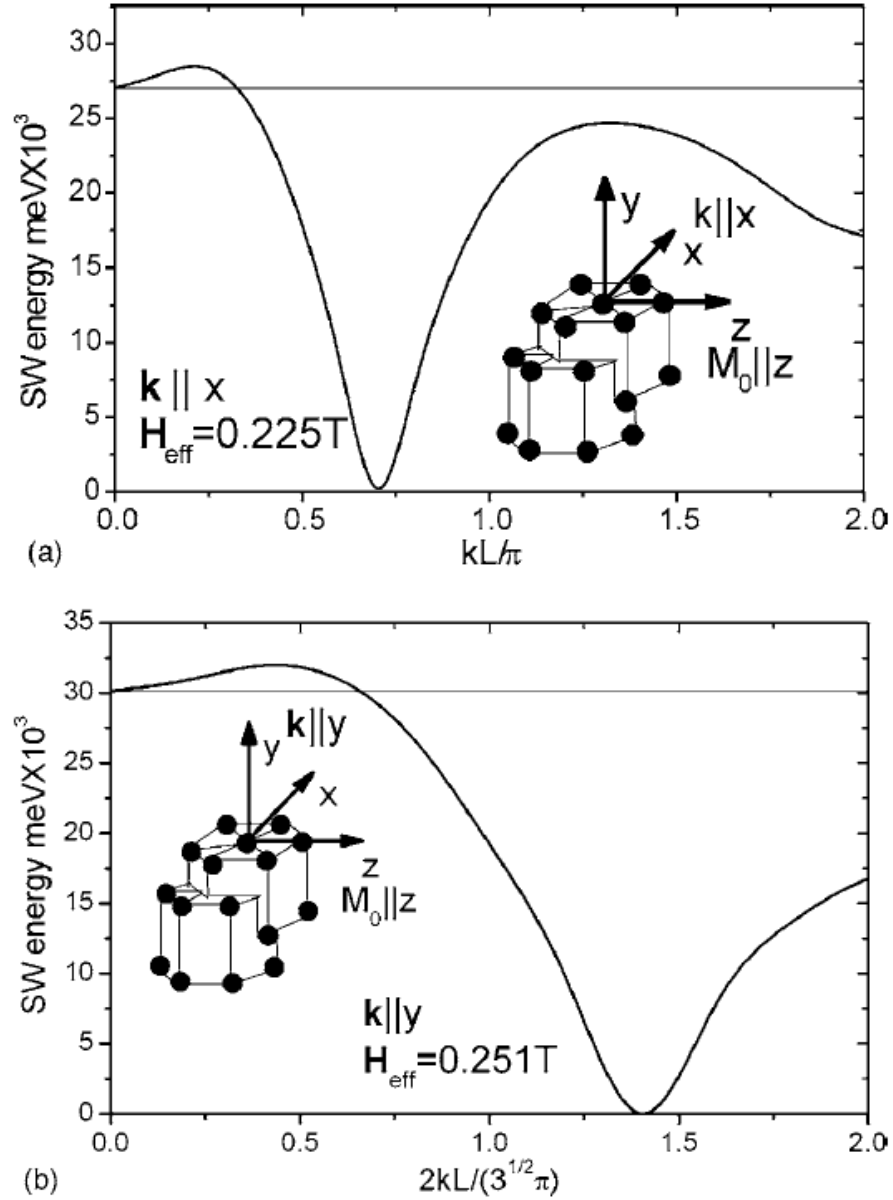
Figure 2.1: *Uniform mode energy dispersion in an hcp superlattice of ferromagnetic spheres for $\vec{M}_0 \parallel z$, with (a) $k \parallel x$ and (b) $k \parallel y$. The horizontal lines indicate the energy of the uniform mode as obtained for the same case of $H_{eff} = 0$, but without dipolar intersphere interaction. The ratio between the radius R of the nanospheres and their centre-to-centre distances L is $\frac{R}{L} = \frac{5}{12}$ (taken from [LOP-1]).*

2.2   Nanowires

Nanowires are usually of "infinite" length and hence the problem of describing their spin wave dynamics is reduced by one dimension due to the missing confinement in that direction. For nanowires of finite length the nanodot approach presented in 2.1.1 can be used.

2.2.1   One and Two Dimensional Nanowires

Together with some approaches to approximately describe the spin wave dynamics in nanowires, which are based on the theory of spinwave propagation in a thin infinite film, some new approaches have been developed in recent years. The intention for such investigations is usually to get a more specific description for mainly infinite nanowires with a real two dimensional confinement. However, progress could only be made by introducing certain constraints. In [29] a theory for spin wave modes in ferromagnetic nanowires of different cross sections was developed applying the extinction theorem and the so-called "conformal mapping" formalism (CMF) on round, elliptical and rectangular structures. The major advantage of CMF is that it is applicable to nanowires of any given cross section and that it does not use a set of Eigenfunctions as basis. However, it is of limited use because it is restricted to magnetostatic modes with no exchange coupling, it is not applicable to nanostructures with rectangular cross section but those with large widths and small heights and it is also restricted to cases in which the magnetisation lies along the axis of the nanowire (Damon-Eshbach geometry). Its major failing is that it cannot be applied to cases with the magnetisation perpendicular to the wires (BackWards Volume MagnetoStatic (BWVMS) spin wave geometry) [32].

The various shortcomings of CMF are the reason why it is currently not used to explain Brillouin light scattering results (for example for spin wave modes in ferromagnetic permalloy stripes [10]). Instead, the well established method of "diagonal approximation" (DA) is used in most experimental papers (described for dots in 2.1.1 with the mathematical background given in [23]) since it is also more applicable to the common experimental situations of nanowires with a small aspect ratio and allows the exchange interaction to be taken into account. A simplification of DA can be obtained by assuming that high-order spin wave modes do not interact with the lowest modes. This is usually the case if there is a significant exchange interaction compared to the magnitude of the dipolar interaction. Although the non-diagonal elements of the dipolar–dipolar interaction tensor (equation 2.1) can be neglected, in order to calculate the spin wave dispersion, integro-differential equations which are obtained on the basis of Green functions must nevertheless be solved numerically. The results presented in figure 3 (Damon-Eshbach geometry) and figure 4 (BWVMS geometry) of [10] demonstrate the complexity of such families of spin wave modes.

Due to the confinement of the structures, spin waves in nanowires have a continuous energy spectrum along the wire and discrete wave vectors perpendicular to this direction. For longitudinally magnetised wires the group velocity of the guided modes is negative and the spin waves are of the volume character. For nanowires

magnetised perpendicularly along their width the modes have a positive group velocity and are of both kinds i. e. volume and localised modes.

2.3   Relevance to This Work

Certain theoretical approaches to the spin wave dispersion in magnetic nanostructures exist or have been motivated by this project.

While interacting 2D and 3D nanostructures have already been considered theoretically, INS is currently the only prospective technique for measuring such interacting spin wave modes experimentally; however, it requires a significant amount of scattering volume. It is currently not practical to produce the required large samples of interacting nanoparticles by readily available laboratory methods other than by self-organisation which has the limitation of an insufficient long-range order.

All other standard laboratory sample preparation methods are currently limited in the area or volume that can be prepared, or they do allow for larger areas or volumes to be structured but are limited in their periodicity and structure size.

Thus, this project focuses on the initial step of preparing highly regularly long-range ordered non-interacting 2D magnetic nanostructured systems (nanodots and nanowires) of sufficiently large areas that offer enough material for probing non-interacting spin wave modes by INS. Based on the obtained experimental results, the next step is then to prepare interacting systems and to eventually evaluate the results on the basis of the theoretical models outlined in this chapter.

Chapter 3

Sample Preparation Techniques

In order to prepare samples of sufficient quantity for inelastic neutron scattering experiments, specialised thin film deposition and structuring techniques are necessary. Depending on the reactivity of the thin film material, magnetic films are usually deposited under high vacuum (HV) or even ultrahigh vacuum (UHV) conditions. This chapter briefly reviews the thin film deposition and structuring methods used in this project on a more general level and describes the sample preparation equipment available at the start of the project. Additional development work carried out to extend these capabilities is then described in detail in chapter 4.

3.1 Sputter Deposition

3.1.1 Sputter Deposition Technique

Sputtering is probably the most commonly used thin film deposition method with the sputter target consisting of the intended thin film material. In the most simple implementation, a negative potential of a few $100\,V$ to $1000\,V$ is applied to a water cooled sputter target (cathode) whilst the thin film substrate is left at chamber potential (anode). When an inert gas (usually argon) is admitted into the vacuum chamber as the so-called "working gas", a cascade ionisation of argon takes place, causing a shower of positively charged argon ions to hit the sputter target. These ions transfer their energy and cause the ejection of atoms or molecules from the sputter target with considerable amounts of kinetic energy (10-$100\,eV$). The atoms or molecules then condense on the substrate. Due to collisions with argon gas on the way to the substrate the sputtered atoms/molecules lose energy and usually have no more than about $10\,eV$ of kinetic energy upon reaching the substrate (figure 3.1). Further, depending on the working pressure and target-to-substrate distance, each of the collisions with the working gas atoms causes the atoms or molecules to be deflected and hence to reach the surface of the substrate from partially randomised directions. One advantage of this effect is that it leads to reasonably uniform film thicknesses even across textured or structured substrate surfaces. However, the fact that deposition also occurs on parts of the substrate that lie out of sight of the actual sputter source can be a disadvantage if one requires a directed deposition method.
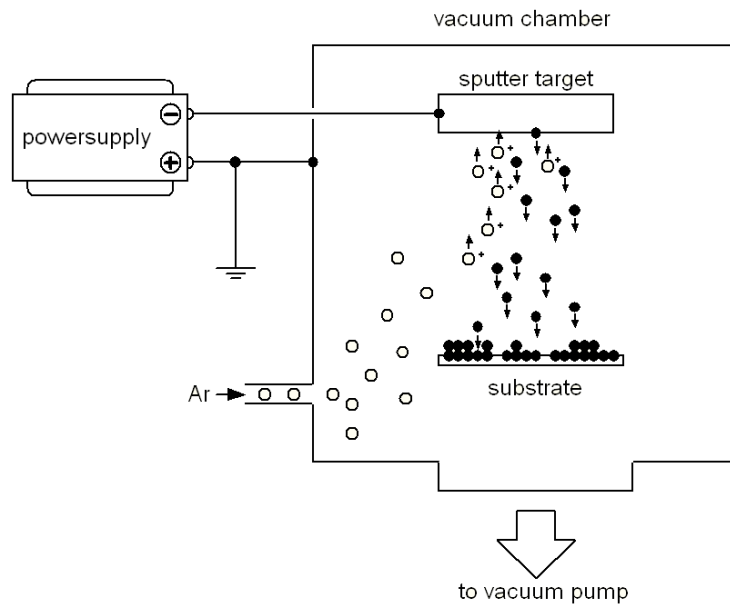
Figure 3.1: *Schematic diagram of the sputter deposition technique with the target located above the substrate. Working gas ions sputter atoms or molecules off the target which then are deposited onto the substrate.*

The above technique, known as glow discharge diode sputtering, typically works in pressure ranges of 1 mbar to 100 mbar. More advanced sputtering techniques are also used, such as magnetron sputtering, which implements a magnetic field at the sputter target. This magnetic field causes the electrons in the plasma discharge to spiral toward the anode, increasing the ionisation probability for the working gas before recombination. The magnetic field also acts as a trap for the ionised working gas atoms, directing them more efficiently toward the target surface. These two effects allow the working gas pressure inside the deposition chamber to be decreased to approximately 10^{-3} mbar, allowing for a cleaner deposition process.

For the deposition of non-conductive materials a radio frequency (RF) modulated current is applied. This avoids charging of the sputter target whilst the highly mobile radio frequency modulated electrons ionise the working gas. Due to the different mobility of argon ions and electrons a self bias effect directs the argon ions toward the sputter target.

Today sputtering is a very advanced deposition technique and amorphous, poly-crystalline and epitaxial films have been grown using this technique.

3.1.2 Implementation at GKSS

GKSS has a magnetron sputter deposition chamber under operation with a base pressure P_{base} in the range of 10^{-8} mbar and a working pressure P_{working} of typically above 10^{-4} mbar. It is especially good at handling large and long substrates as it was originally designed for the deposition of x-ray mirrors. However, the capabilities
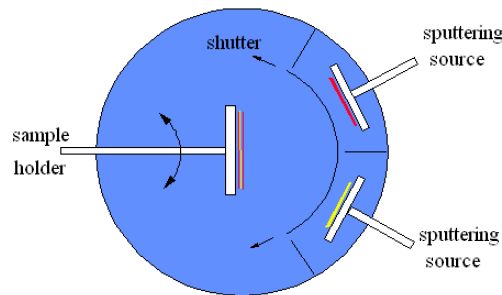
Figure 3.2: *Schematic of the GKSS sputter deposition chamber with relative positions of the sputter sources, the rotateable substrate holder and the shutter.*

of handling very large substrate sizes could not be fully used in this work as only substrates of up to 2.5 cm in diameter could be managed in the structuring process that follows the film growth (7.1).

The high-vacuum sputter chamber is equipped with two circular 7.6 cm DC magnetron sputter sources and, depending on the requirements it is either equipped with a water cooled or a bakeable substrate holder. In either of these two configurations the substrate is rotateable around its normal to ensure more uniform film thicknesses. A liquid nitrogen cooled cryotrap is implemented for improving the vacuum quality and can also be used to indirectly cool a substrate by absorbing its black body radiation. Substrate temperature can be monitored by a Pt/PtRh thermocouple and regulated within $\pm 3\,^\circ$C. Samples can be loaded through an airlock system via a magnetically coupled transfer rod without the need to break the vacuum. The distances between sputter targets and substrate are usually approximately 25 cm at an angle of 22.5° to the normal of the substrate. The amount of deposited material can be controlled by a shutter system. Figure 3.2 shows a schematic diagram of the deposition apparatus and figure 3.3 shows a photograph. It should be noted that no in-situ thickness control is available for the sputter chamber. Instead, ex-situ x-ray reflectometry measurements (5.5) are used to determine the exact thickness of the deposited film, which in turn provides calibration information on the opening time of the shutter.

This sputter deposition setup was used in the preparation of nanostructured samples for scattering analysis as described in 7.1.1.

3.2   Electron Beam Evaporation

Another widely used deposition method is thermal evaporation, often operated in the form of electron beam evaporation. In this process the kinetic energy of a focused high current electron beam heats up a source material which is located inside a water cooled hearth (figure 3.4).

Electron beam evaporation allows the use of a wide range of materials, since the temperature that can be reached is only dependent on the thermal conduction
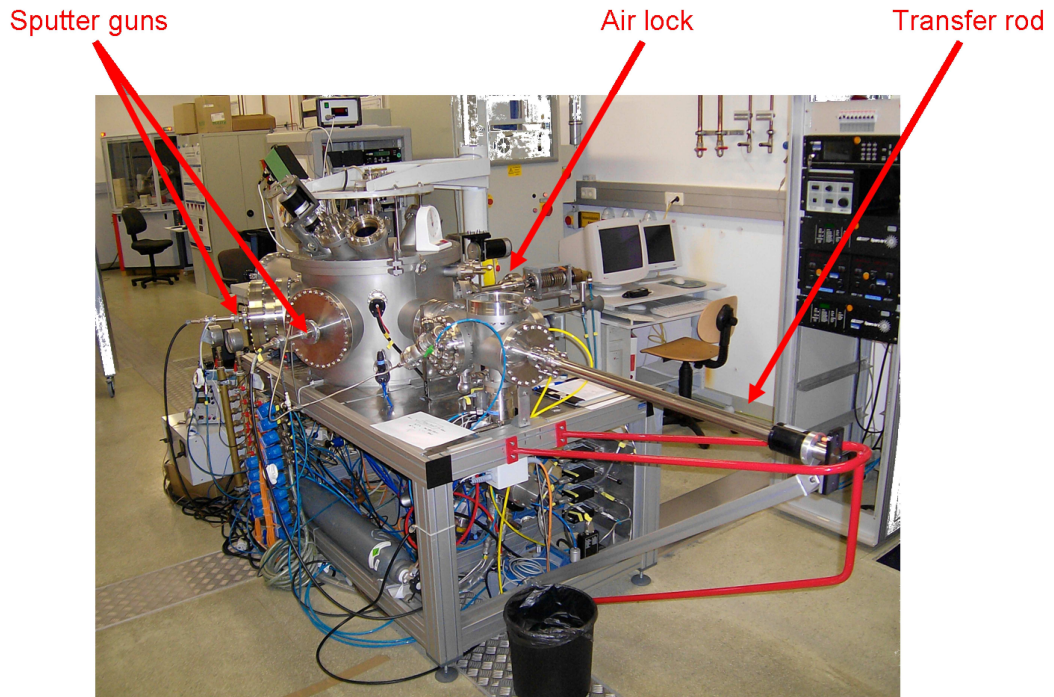
Figure 3.3: *Labelled photograph of the GKSS sputter deposition chamber.*

between the material source and the hearth. The evaporated atoms usually have kinetic energies of around $0.1\,$eV which leads to high quality films of low roughness on the substrate. Electron beam evaporation operates at working pressures below $10^{-5}\,$mbar and in the implementation chosen for this work has typical evaporant working pressures of $10^{-8}\,$mbar (7.2.2). This results in an undisturbed evaporant beam, as the evaporant does not interact with any working or rest gas molecules. Also, the kinetic energy of the adatoms or admolecules is lower than in sputter deposition which leads to less intrinsic surface mobility of the adsorbates when reaching the substrate. This results in a better control on the growth parameters by controlling the substrate temperature. The directed behaviour of the evaporant beam is especially required for the deposition of nanosized wires by self shading of a prestructured substrate as described in 7.2. An e-beam evaporation vacuum chamber was built for this work and is described in detail in 4.3.

3.3   Laser Interference Lithography

In order to laterally structure thin magnetic films, a method for preparation of a nanostructured mask on the entire sample surface by a single step process was required. Laser-interference lithography is a suitable method for this as it can easily be used to uniformly structure large areas in a reasonable amount of time.

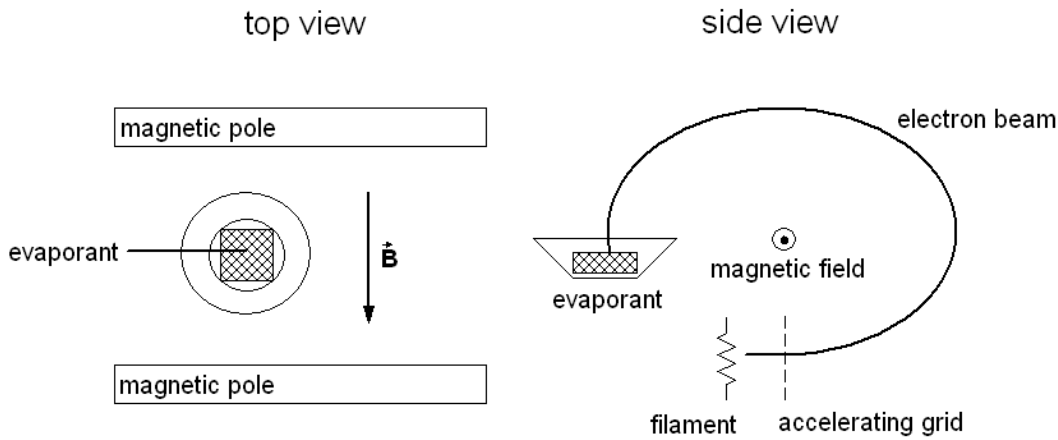top view   side view

Figure 3.4: *Operating principle of an e-beam evaporation unit: the field of a pair of permanent magnets directs an electron beam onto an evaporant material situated on a water-cooled hearth. The kinetic energy of the electrons evaporates the target material whose vapor can be deposited onto a substrate located above the evaporant source (after [33]).*

3.3.1   Laser Interference Lithography Technique

In this method, a substrate is first spin-coated with positive or negative photoresist and then exposed by an interfering ultra-violet laser beam before it is chemically developed. A schematic diagram of the lithography apparatus is given in figure 3.5: an ultra-violet laser beam is conditioned and widened so that it can illuminate the full sample surface. By directing the beam through a beam splitter and by deflecting the two separate beams with mirrors such that they are brought to interference on the sample surface, a line pattern on the sample surface is exposed into the previously spin-coated photoresist layer. By rotating the sample 90° around its normal and by performing another exposure step, not only a line pattern, but also a dot pattern can be prepared. Wet chemical development removes the exposed photoresist and a photoresist mask remains on the sample, which can be transferred into the underlying sample layer by chemical or physical etching.

3.3.2   Implementation at University of Hamburg

The setup used for this work is located in the class 10 cleanroom at University of Hamburg. A photograph of the laser interference lithography setup is shown in figure 3.6. The applied ultra-violet laser of this apparatus has a wavelength of $\lambda = 364\,\text{nm}$. The structure size of an interference grating can be adjusted through
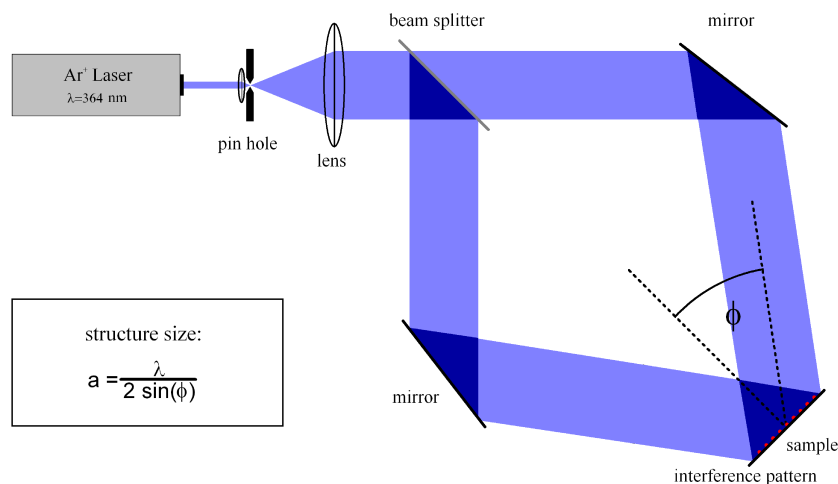
Figure 3.5: *Schematic of the laser interference lithography setup as used for structuring photoresist on a continuous magnetic thin layer*

the interference angle ϕ of the laser beam as shown in figure 3.5 and the minimum structure size a is limited by the wavelength λ of the applied laser via the relation

$$a = \frac{\lambda}{2 \sin \phi}.$$

Thus, the structure sizes that can be prepared with this arrangement are all larger than approximately 200 nm.

3.4 Argon Ion Beam Milling

Transfer of the laser interference lithography mask into the underlying thin film is performed by argon ion beam milling.

Although this method is not always suitable for semiconductor treatment due to its high contamination potential, physical etching is often performed by bombarding a workpiece with ionised inert (usually argon) or reactive gas atoms (e. g. oxygen) and is referred to as "ion beam milling" or "ion beam etching". On reaching the target the kinetic impact energy of the ions strikes out atoms or molecules from the target. In principle, this is similar to the sputter deposition process described in 3.1 except that the ionisation process does not take place directly in front of the target but in a separate part of the vacuum chamber from where the ions are directed onto a workpiece with the intention of removing material. The workpiece is often rotated under an angle to the direction of the ionbeam. A schematic of a typical setup can be found in [34].

Figure 3.6: *Labelled photograph of the laser interference lithography setup. The yellow tint is due to the light in the clean room. Visible are the Argon ion laser, the beam conditioning and exposure control setup and the deflection mirrors with the sample position (Photograph by Carsten Graf von Westarp). The beam splitter is located behind a black screen in the centre of the photo.*

As endpoint detection, the gas-molecules inside the vacuum chamber are typically analysed for atoms of the work piece by secondary ion mass spectroscopy. A transition from one detected element to another indicates the transition from one sample layer to another.

For this sample preparation step a new vacuum chamber was designed, as described in 4.2. In the chosen implementation a gridded Kaufman type ion gun (figure 3.7) is used and whose working principle is therefore briefly outlined: at working pressures at or below 5×10^{-4} mbar, a gas discharge in the region of a hot cathode ionises argon working gas. The ions are accelerated toward the workpiece through a pair of plane extraction grids and the resulting ion current depends on the exact operating parameters of the ion gun but is typically in the mA range. The extracted ion beam is neutralised with electrons by an additional neutraliser filament to avoid beam spreading caused by the repulsive electrostatic forces of the ions. The typically large diameter of this type of ion gun allows a uniform removal of material from the workpiece over a wide area.
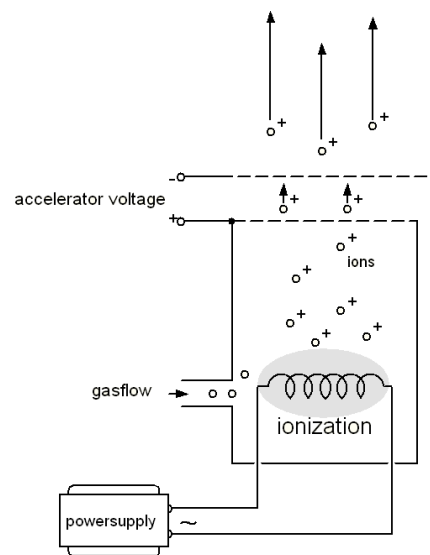
Figure 3.7: *Basic principle of operation of a Kaufman ion gun: A plasma is sustained in a discharge region by a hot filament cathode. An electric field then accelerates the ions near the extraction grids towards the substrate.*

Chapter 4

Development of Sample Preparation Equipment

At the beginning of this project available equipment for the preparation of large and sub-micrometre to nanometre laterally structured samples was inadequate to perform all required sample preparation steps and had to be extended. The development work performed, is given in this chapter. Specifically, for the top-down structuring process described in more detail in 7.1 a high-vacuum (HV) argon ion beam milling (3.4) process chamber was constructed from available vacuum equipment. In the bottom-up structuring process described in 7.2 also highly reactive material (Gd) was used besides the mainly applied Ni. Consequently, the deposition method and the choice of material demanded the construction of an ultra-high-vacuum (UHV) electron beam evaporation chamber. This chapter describes the design of the argon ion beam milling vacuum chamber and the electron beam evaporation chamber and the construction work performed, including electronic circuits and LabVIEW™ programs following the philosophy of highest possible cost efficiency. Figure 4.1 gives an impression of the setup, including peripheral equipment, and shows both vacuum chambers connected to each other such that the argon ion beam milling HV part can be operated as an airlock for the UHV e-beam chamber. The HV chamber also holds a sputter deposition source that can be used for adding a capping layer after deposition by e-beam evaporation. In the future a sophisticated sample holder will allow the full interoperability of both chamber parts as one unit and is described in 4.4. LabVIEW™ control-software was also developed for a newly purchased commercial high temperature furnace, which is used for the substrate structuring process described in 7.2.1.

4.1 High Temperature Furnace

For the newly purchased commercial high temperature furnace of type CARBOLITE™ HTF 1700, a computer program was required which could precisely control and record the temperature sequence to ensure the reproducibility of the self organisation process used to pre-structure sapphire substrates (7.2.2). As the temperature controller Eurotherm™ 3216 implemented in the furnace was a new product and not

Figure 4.1: *Overview of the sample preparation equipment constructed mainly from available vacuum components. Shown are the UHV electron beam evaporation chamber (at left), the HV argon ion beam milling chamber (at right; this also acts as an airlock system) and peripheral equipment. The computer screens on the table show the LabVIEW™ computer control programs developed for the system.*
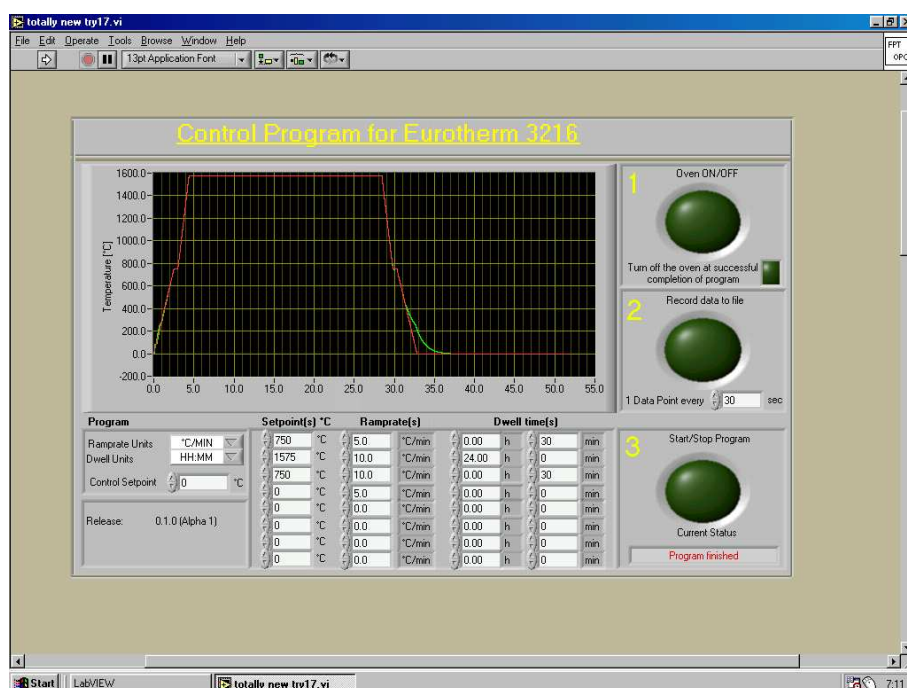
Figure 4.2: *LabVIEW*™ *control program for operation of the CARBOLITE*™ *HTF 1700 furnace. This allows a temperature sequence to be programmed and recorded to a file.*

yet supported by the commercially available control program, a LabVIEW™ program which provides the required functionality had to be written.

4.1.1 LabVIEW™ Control Program

Figure 4.2 shows the user interface of the program. The input block below the display section allows the programming of a temperature sequence with up to 8 set-points, ramp rates and dwell times. The display plots this programmed profile[1]. To start the program, the operator simply has to follow the numbering of the green buttons on the right of the display section. Step 1 turns on the furnace and decides if it should be turned off at the end of the programmed temperature routine. Step 2 selects whether the temperature curves are to be recorded into a tabulator separated text file and sets the corresponding interval of data collection. Step 3 transfers all programmed parameters from the computer to the Eurotherm™ controller and starts the execution of the programmed temperature sequence, but can also be used to manually interrupt the program.

A photograph of the setup[2] is given in figure 4.3 and the corresponding source-code of this program is described in appendix B.1.

---

[1]After initiating a programmed sequence, the display is reset and shows the momentary setpoint temperature in red and the actual temperature of the furnace in green

[2]As data collection does not require significant processing power, this program is installed on a 133 MHz Pentium™ class PC with 32 MB of RAM, running LabVIEW™ 6.1 under MS Windows 98™

Figure 4.3: *Photograph of the CARBOLITE™ HTF 1700 furnace which was used to perform the annealing of sapphire substrates.*

4.2   Ar Ion Beam Milling Vacuum Chamber

The quality of a vacuum chamber is usually defined by its base pressure, which is in turn a result of the leak rate and the pumping speed. At a given pumping speed, mainly the outgassing of components and the quality of the seals define the base pressure. As the vacuum chamber used for the argon ion beam milling also has to fulfill the role of an airlock for the UHV e-beam evaporation vacuum system, the chamber and pumping system are now discussed in more detail.

4.2.1   Chamber and Seals

As can be seen in figure 4.4, the ion beam milling part of the newly built vacuum apparatus mainly consists of a DN 100 CF six-way cross with flanged-on ion gun, quick access door, sputter gun, pump, gate valve to the main chamber and an edge welded bellow as x-shifter, which carries a preliminary substrate holder (4.4.3) and can be used to transfer samples into the UHV e-beam chamber. Most of the parts are sealed with copper gaskets, reducing the leak rate and allowing an easy upgrade of the vacuum quality at a later time. Currently, the quick access door and the entire pumping system are viton sealed, mainly due to the non-availability of a conflat flanged pump. The gate valve to the main chamber is currently also equipped with a viton sealed gate, which however will be replaced with a full metal gate valve when the final substrate holder (4.4) is installed. The attached sputter deposition gun for deposition of a capping layer is currently also partially viton sealed and attached using a CF suitable viton ring as it also acts as an access port to the chamber.
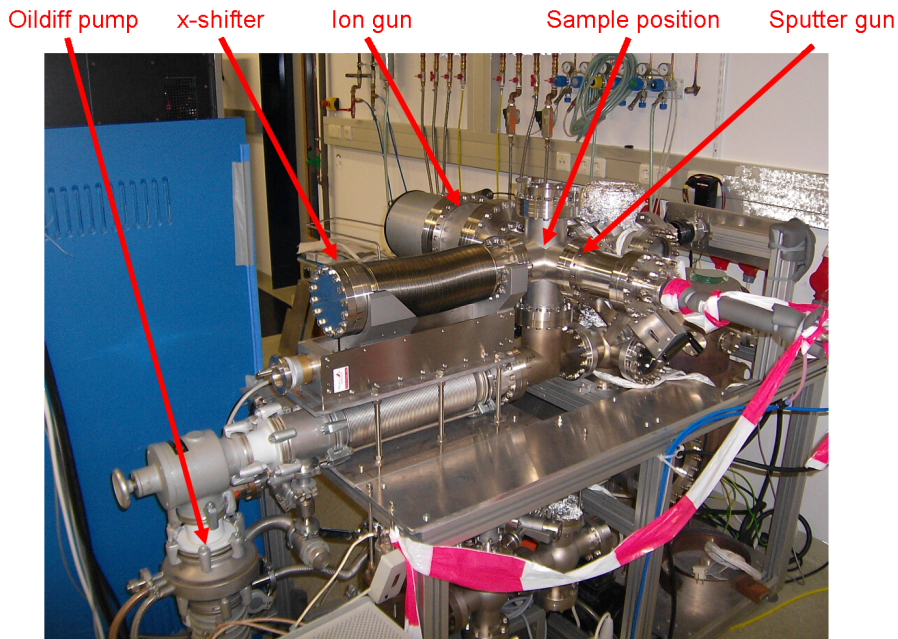
Figure 4.4: *Photograph of the constructed vacuum system. The essential components are labelled.*

4.2.2   Pumping System

The pumping system of the airlock and argon ion beam milling chamber consists of an ISO flanged standard oil diffusion pump with a pumping speed of $160\,l/s$ with a rotary backing pump and an additional water cooled oil trap on the recipient side. As oil diffusion pumps can not be operated against air, an angle valve on the recipient side of the oil diffusion pump and a three-way valve in the backing line bypass the HV pump and allow pumping down of the vacuum chamber to 10^{-2} mbar before opening the valves to the oil diffusion pump. All the seals from the oil diffusion pump to the 6 way cross of the airlock are made of viton. Although the base pressure inside the vacuum system can be below 1×10^{-7} mbar in this configuration, as a future upgrade it is planned to replace the oil diffusion pump with an oil-free working pump to avoid potential contamination of the vacuum with pump oil which could interact with the argon ion beam milling process.

4.2.3   Gauges

A Bayard Alpert hot cathode ionisation type gauge is used as the main pressure gauge. Since this type of gauge only works at pressures below approximately 10^{-3} mbar, a convectron gauge monitors the vacuum pressure above this point in the vacuum chamber and the pressure in the backing line of the oil diffusion pump is measured by a separate convectron gauge. Both are operated by manual gauge controllers. The hot cathode ionisation gauge is controlled by a digital Leybold Heraeus© IM-210D, which also has an analog output port with a voltage proportional to the pressure read from the ionisation gauge. This voltage can be read into a computer and processed further (4.3.3).
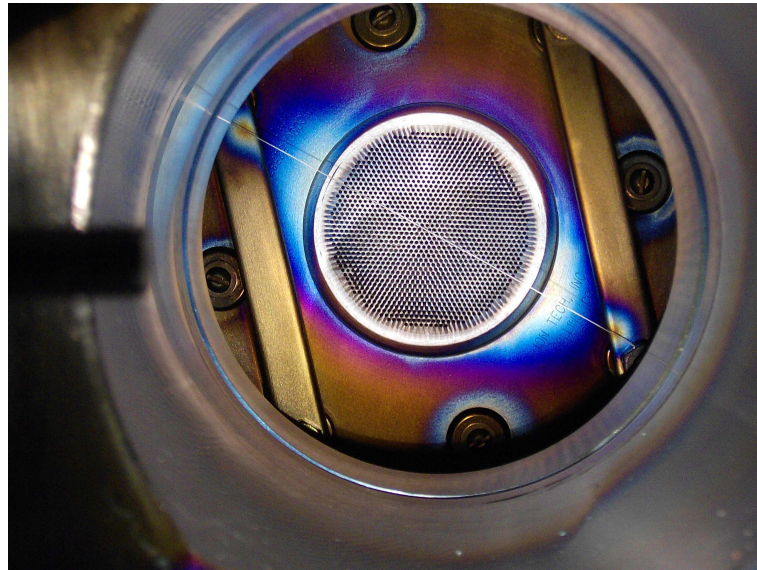
Figure 4.5: *View from the sample position onto the Kaufmann type ion gun used for argon ion beam milling. Visible is the plane pair of extraction grids with a diameter of 2 inches, that extracts the ions from the discharge region behind them and directs the ions toward the workpiece. The neutraliser filament running diagonally injects electrons into the argon ion beam such that the resulting ion beam is neutralised and hence counteracts potential beam spreading caused by the repulsive electrostatic forces of the argon ions.*

4.2.4   Ion Gun

The implemented ion gun is a $5.1\,\mathrm{cm}$ (2 inch) diameter gridded Kaufman ion gun of type ION TECH$^{\textcircled{c}}$ 5-1500-150, in which a gas discharge in the region of a hot cathode ionises the working gas. The working gas flow is adjustable by a commercial MKS$^{\textcircled{c}}$ PR 4000 gas flow controller with a corresponding electric valve. With this arrangement, gas flow rates of approximately $0.275\,\mathrm{sccm}$ give typical working pressures of $3 \times 10^{-4}\,\mathrm{mbar}$.
The power supply of type ION TECH$^{\textcircled{c}}$ MPS 3000 FC includes all necessary components in one chassis and all essential parameters can be operated automatically. The user interface of the LabVIEW$^{™}$ computer program written to accurately control the duration of the etching process is shown in figure 4.6. The circuit built to connect the computer with the power supply unit and the source code of the computer program are explained in appendix B.2.

The LabVIEW$^{™}$ program switches the state of the RTS line of a serial PC port and hence allows a time control over the etching process. This control mechanism must currently be used as only a preliminary sample holder (4.4.3) is available. The final sample holder (4.4) will include an in-situ resistance measurement option which will allow electrical detection of the endpoint of the etching process and corresponding routines will be included into this program.
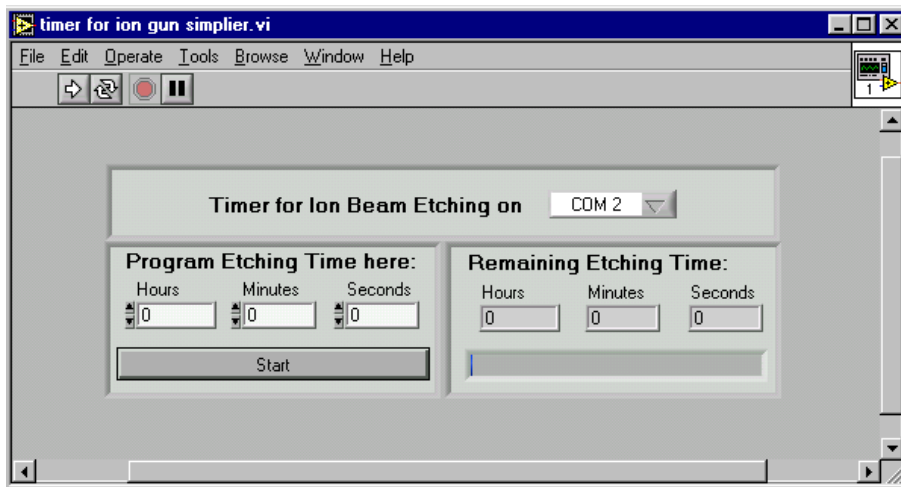
Figure 4.6: *User interface of the LabVIEW™ program for controlling the argon ion beam milling process. In its current state, this is a simple timer program that switches the RTS Line of the serial port.*

4.3 Electron Beam Evaporation Chamber

The second vacuum chamber system, again designed mainly from available standard vacuum components with just minor additional expenditure for an e-beam evaporator, is a UHV chamber for the deposition of thin films and nano structures by means of e-beam evaporation. It is shown in figure 4.7.

4.3.1 Vacuum Chamber Design and Pumping System

For the deposition of thin films and especially for the deposition of rare earth materials a very good vacuum in the ultra high vacuum regime is required. Hence, the deposition part of the vacuum setup is fully metal sealed. This includes all the flanges and also the sealing faces of all the valves.

The UHV chamber mainly consists of two six-way DN 100 CF crosses mounted on each other. In the upper-most of these crosses are located the sample position and components to control the deposition process. These include a shutter system (made of a rotary feed-through and parts of an aluminium can) and the quartz balance used as a rate and deposition monitor. Additionally, a mirror is implemented to view the evaporation hearth of the e-beam evaporator through a window located 90° to the evaporation source. Locating the window outside the line of sight of the evaporation material avoids deposition onto the window. A photograph of the sample position inside the vacuum chamber is given in figure 4.8. The second six-way cross holds the other parts in place and extends the distance from the source to the substrate to approximately 50 cm. Underneath it, a commercial six pocket e-beam evaporator of type TELEMARK™ 568-05 is implemented in a custom chamber part with a DN 100 CF flange above the active pocket. Its linear design allows one of six hearths to be moved into the electron beam for evaporation without breaking the vacuum for changing the material. Co-evaporation, however, is not possible
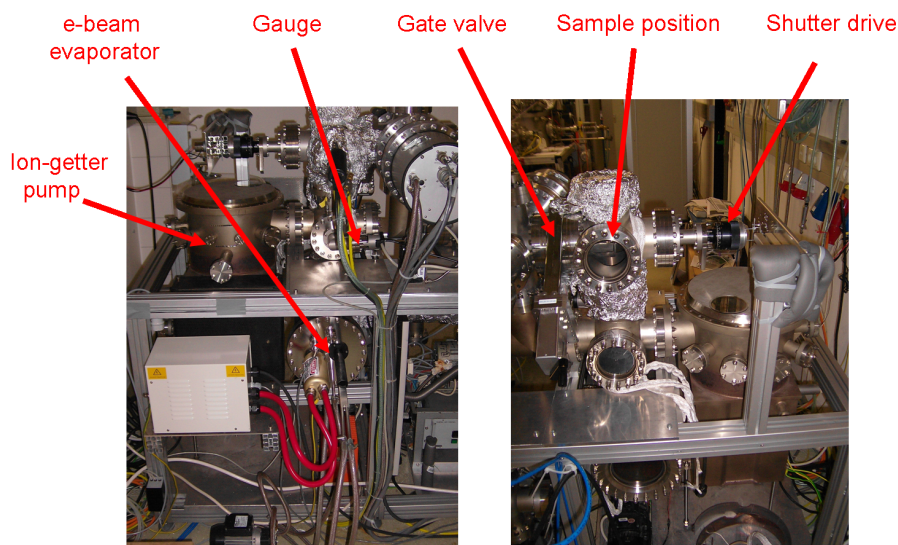
Figure 4.7: *Photographs of electron beam evaporation part of the vacuum chamber system as seen from opposite sides. Visible are the relative locations of electron beam evaporator, sample position, gauge, pump and the shutter driving mechanism.*

with this design. The TELEMARK™ TT-6 power supply for the e-beam evaporator can be controlled by an INFICON™ IC/4 deposition controller which reads out a standard water cooled 6 MHz gold quartz balance for in situ monitoring of the film thickness and the deposition rate and which in turn is connected to a computer for deposition control via an RS-232 serial port.

An additional DN 100 CF flange is available on this chamber part to attach a turbo molecular pump of type Pfeiffer TPU-200; this can be sealed-off from the main chamber through a fully metal sealed DN 100 CF angle valve as shown in figure 4.9.

The backing line of the oil diffusion pump of the HV chamber is also used for the turbo pump of the UHV e-beam chamber. On the side opposite the turbo molecular pump is attached an ion getter pump with titanium sublimation pump and liquid nitrogen cryotrap with an estimated combined pumping speed of approximately 1500 l/s. As ion getter pumps have a limited lifetime of approximately 50,000 hours and this can be drastically reduced if operated at elevated pressures, this pump was not used at pressures above 5×10^{-9} mbar. Until reaching the 10^{-9} mbar regime, the turbo molecular pump was usually operated as the only pump. To achieve these pressures the vacuum chamber needs to be baked for several days using commercial bakeout tapes and timer switches for temperature control.

If both the turbo molecular pump and the ion getter pump are operated simultaneously, a base pressure of just below 1×10^{-9} mbar can be reached. This is mainly limited by back streaming of gas molecules through the turbo molecular pump and is improved if the turbo molecular pump is shut off from the chamber.

With a sealed-off turbo molecular pump the ion getter and Ti sublimation pumps together are capable of pumping the chamber to a base pressure in the 10^{-11} mbar regime (the lowest pressure achieved was 3.8×10^{-11} mbar).
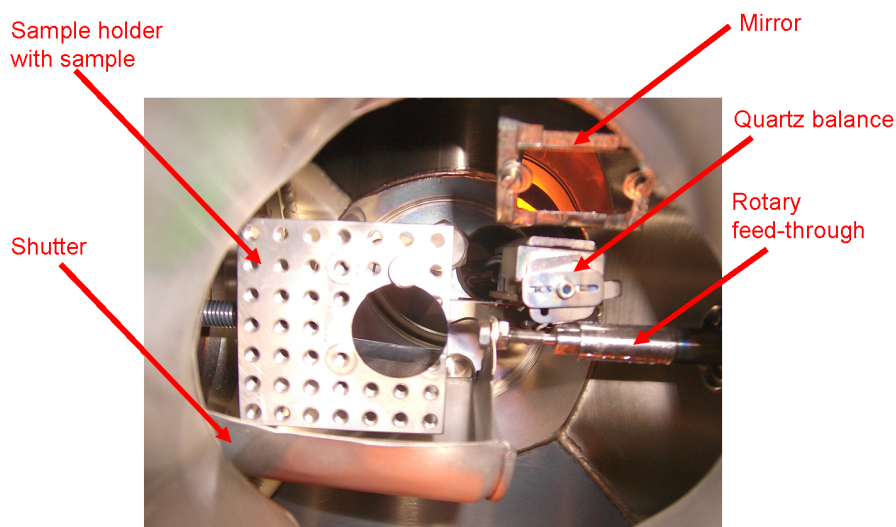
Figure 4.8: *Sample position and sample environment inside the electron beam evaporation vacuum chamber: visible are the sample holder with mounted sample, the shutter mounted on a rotary feed-through, the mirror used to look onto the evaporant hearth and the quartz balance to monitor the deposition rate and the deposited film thickness. The orange glow that illuminates parts of the mirror and the shutter from underneath originates from the evaporant melt in the e-beam evaporator.*
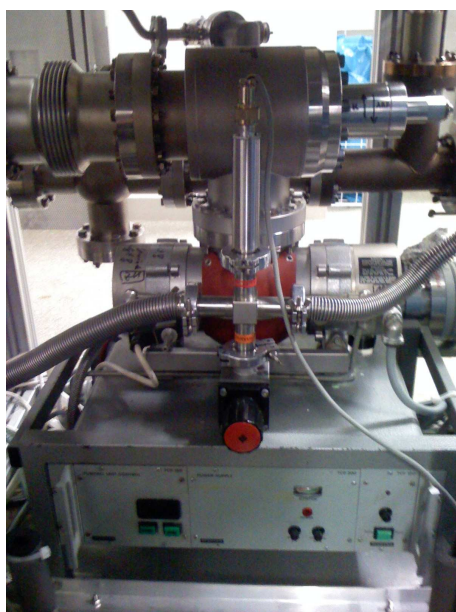

Figure 4.9: *The attached turbo molecular pump of the electron beam evaporation chamber with full metal angle valve.*

4.3.2 Gauges

A Leybold Heraeus© IE-514 extractor gauge was used to measure these very low pressures in the main deposition chamber, controlled by a Leybold Heraeus© IM-540 gauge controller. This gauge type has a Röntgen barrier of 10^{-12} mbar, making it suitable to measure pressures well below the range of a standard Bayard Alpert hot cathode ionisation gauge with a Röntgen barrier of approximately 1×10^{-9} mbar. The initial pumpdown of the electron beam evaporation chamber was performed via the airlock system with open gate valve to the main chamber to pressures of approximately 10^{-5} mbar before turning on the extractor gauge and closing the gate valve to the airlock chamber. The gauge controller also allows the measured pressure to be read by a computer via a serial port (4.3.3).

4.3.3 Computer Control

As it proved impossible to manually control the deposition parameters with sufficient accuracy, a method was developed to monitor the parameters and to control the sample deposition process using a LabVIEW™ computer program. This program also records the main parameters during the deposition process into a file. As additional data acquisition and control hardware, a Meilhaus Electronic LabJack™ U12 AD/DA USB board was connected to a Pentium III™ class computer with installed Windows XP™ and LabVIEW™ 6.1. The USB board has various analog and digital input-/output-ports that allow several analog peripheral components, including the pressure from the vacuum gauge in the argon ion beam milling/airlock chamber and the opening and closing of the shutter for deposition, to be monitored and controlled simultaneously. Other peripheral equipment, like the IC/4 deposition controller and the IM-540 gauge controller were connected to the PC via RS-232 serial ports.

Shutter-Controller

The shutter inside the UHV chamber is moved by a rotary feed through, which in turn is rotated by an attached geared electrical motor. Switching of the shutter position to the open or closed state is done by one of the digital outputs of the AD/DA USB board connected to a custom shutter control circuit described in appendix B.3.2.

Control Software

The control software combines routines for reading various parameters with additional routines to control the deposition process. Figure 4.10 shows the user interface: the display block shows the pressure in the HV and UHV chambers, the current deposition rate and the current film thickness as graphs and numerical values. An additional control section on the right next to the display section of the program allows the displays to be reset either manually or automatically when the deposition is started and selects whether the relevant deposition parameters and conditions should be recorded into a file. If set to "on", the software records the
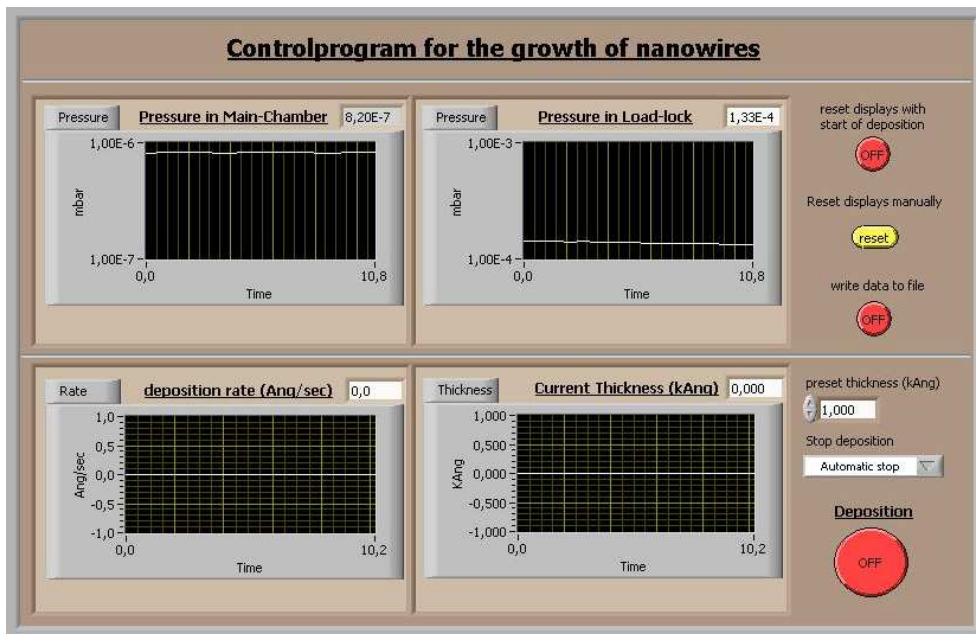
Figure 4.10: *User interface of the LabVIEW*™ *program for controlling the deposition process of the e-beam evaporation chamber.*

time (in seconds since the start of deposition), the vacuum-pressure in both chambers (in mbar), the deposition rate (in Å s^{-1}) and the layer thickness as reported by the crystal monitor (in Å) in tab-delimited columns. The user is prompted at the end of the deposition process to provide a file name under which these values should be saved. The lower right part of the user interface controls the deposition process: the final sample film thickness can be set (in kÅ), but is only used by the program if the "automatic stop" function is selected, which will automatically close the shutter and stop the deposition process when the preset thickness is reached. Alternatively a "manual control" can be chosen where the deposition is user controlled through the "deposition" button. On activation, this button opens the shutter inside the deposition chamber and resets the thickness counter on the crystal monitor to zero. In either operating mode ("automatic stop" or "manual control"), switching the state of the "deposition" button from "ON" to "OFF" closes the shutter and stops the deposition. A more detailed explanation of the program on a source code level is given in appendix B.3.

4.4   Sample Holder

As both vacuum chambers are interconnected, a sophisticated sample holder had to be designed to combine both vacuum systems to one operative unit. It has to fulfill various functions: firstly it must seal the e-beam evaporation chamber against the argon ion beam milling chamber if used inside the UHV part of the setup. Secondly it has to provide a suitable sample handling environment for all sample preparation steps that are performed either by deposition with e-beam evaporation or by deposition or removal of material in the argon ion beam milling chamber.
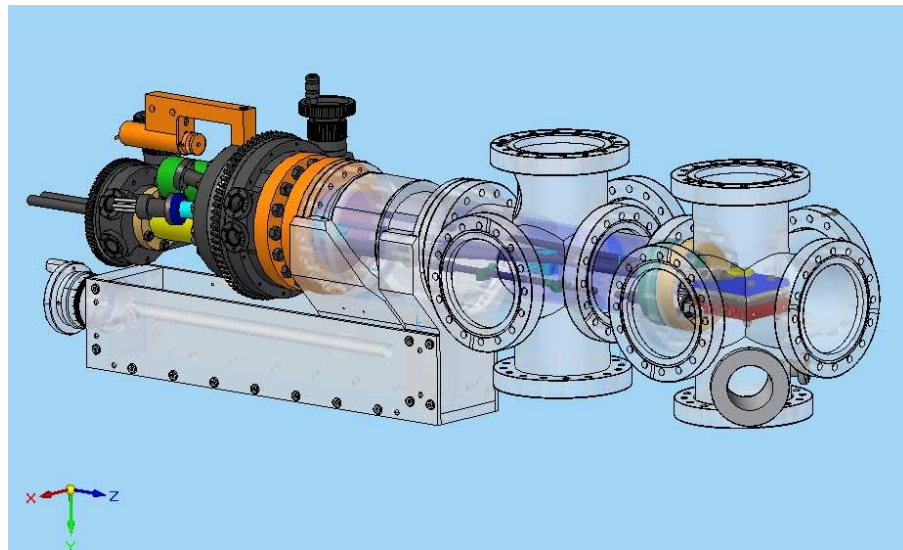
Figure 4.11: *The substrate holder design: the entire substrate holder is mounted on the end of an edge-welded bellow and can be transferred from the argon ion beam milling chamber to the electron beam evaporation chamber. If positioned inside the electron beam evaporation chamber, a nozzle inside the argon ion beam chamber becomes part of the e-beam evaporation chamber and seals it against the high vacuum regime of the argon ion beam milling chamber (design drawing by Thorsten Böttcher, GKSS).*

As the number of implemented features increases, the likelihood of a component failure also increases. With this in mind, the sample holder was designed to be entirely retractable into the argon ion beam milling and airlock chamber when changing the sample. The main advantage of this construction is that in the event of a component failure, the UHV of the e-beam chamber does not have to be broken.

Figure 4.11 demonstrates the operating principle in which part of the airlock chamber temporarily becomes a part of the main deposition chamber, which is sealed against the high vacuum of the airlock chamber. In order to bake this retractable part of the chamber before attaching it to UHV, the substrate holder is entirely bakeable in the airlock chamber using a 1000 W halogen lamp. The inner design of the sample holder head is shown in figure 4.12. Design and construction work for this complex piece of vacuum equipment was first begun in September 2006 and is since being carried out in cooperation with the technical department and the workshop of GKSS. Due to delays in the workshop, it is scheduled to be operational in the first half of 2010. Although the intended sample holder could not be put into operation within the timeframe of this project, its main features are outlined due to its central role and future utility.

4.4.1 Requirements for Argon Ion Beam Milling

Argon ion beam milling is usually performed under an ion incidence angle other than 90° with the workpiece rotating around its normal. Therefore, the sample holder is rotateable inside the vacuum chamber by ±180° around its horizontal axis. This
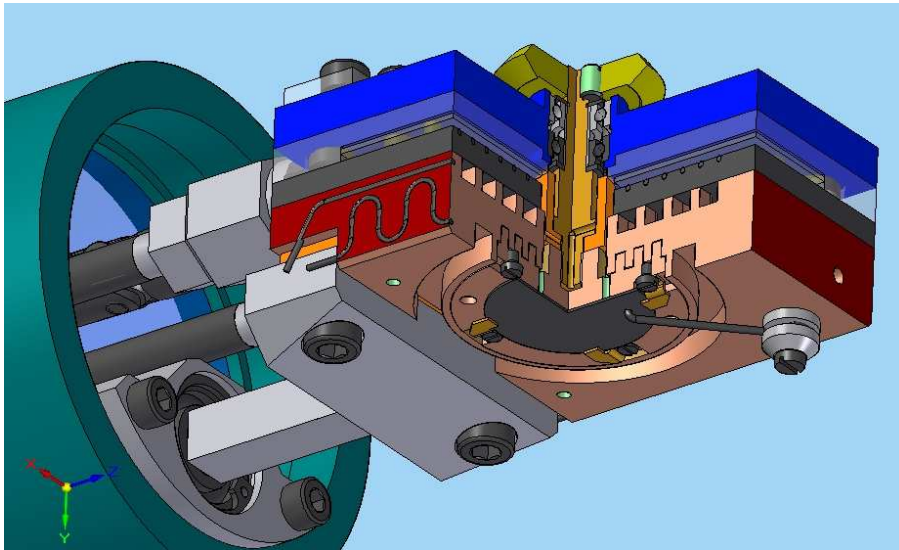
Figure 4.12: *Section through the planned substrate holder along the well that rotates the sample showing cooling channels for water or liquid nitrogen, parts of the heating coils and a contact arm for resistance measurements. Additionally, the complex mounting is visible that allows to incline the sample around its surface (design drawing by Thorsten Böttcher, GKSS).*

allows the sample holder to be rotated such that the sample side faces the argon ion gun. An additional horizontal axis through the sample surface, parallel to the horizontal axis of the sample holder, is also implemented: it allows the sample to be inclined relative to the ion source by $\pm 45°$. Finally, a third axis perpendicular to this inclination axis, allows the sample to be continously rotated around its normal with a controllable frequency of up to 1 Hz. As argon ion beam milling also transfers a significant amount of heat onto the workpiece, additional water or liquid nitrogen cooling is implemented. Due to a demand for a rudimentary endpoint detection for etching of laterally structured samples, the substrate holder also contains a setup for a two probe resistance measurement across the workpiece. For this method, silver electrodes need to be deposited on two sides of the workpiece in a way that the resistance can be measured across the thin film. The plot of Rd^2 versus d, where R denotes the measured resistance and d the film thickness, shows a minimum at the point of last coalescence of the metallic layer as described in [35] and hence can be used to determine the endpoint of the etching process for nanostructured films [36].

4.4.2 Requirements for Deposition by e-Beam Evaporation

In order to facilitate either polycrystalline or epitaxial thin film growth via the surface mobility of newly arriving adatoms, the substrate holder must be heatable to at least 600 °C in a well controlled manner. This was implemented using three vacuum conform soldered resistively heated elements with a maximum element temperature of 900 °C. For the preparation of nanostructured samples by self shading effects, the sample must be rotateable inside the vacuum chamber and precisely inclineable to
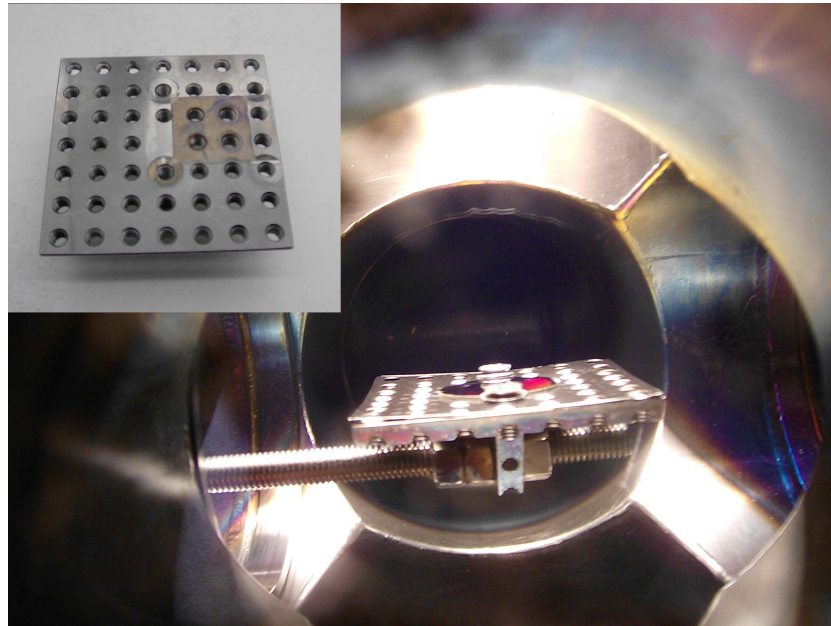
Figure 4.13: *Preliminary substrate holder located using a threaded rod inside the vacuum chamber; the mounted sample faces the argon ion gun during argon ion beam milling. The inset shows the sample holder.*

the evaporation source. This is implemented in such a way that the inclination and rotation axes are identical to those required for the argon ion beam milling.

4.4.3   Preliminary Substrate Holder

The complex sample holder described above was specifically designed for the sample preparation envisioned for this work.

Due to its unavailability, a much simpler substitute substrate holder consisting of a steel plate with multiple threaded holes was used, mounted in the vacuum chamber on a threaded rod as shown in figure 4.13. The possibilities that this provided for sample preparation were quite limited as no temperature control of the sample during argon ion beam milling or deposition was available. However, this construction offered a rudimentary method to incline the sample relative to the electron beam evaporation source by mounting the steel plate slightly rotated on the threaded rod. The angle of inclination was estimated by measuring the distances between two opposite substrate holder edges to the rim of a fixed access port on the vacuum chamber with a ruler. It therefore allowed the deposition of nanowires by self-shading effects to be carried out but did not give a sufficient reproducibility in sample preparation. Despite these restrictions, all the nanowire sample preparation on pre-structured substrates (7.2) and the argon ion beam milling of the samples described in section 7.1 and appendix A could be carried out using this substrate holder and demonstrate the potential of the applied techniques.

Chapter 5

Sample Analysis Techniques

Due to their feature sizes, samples with nanoscale lateral structures require certain advanced analysis techniques. The methods used to characterise the prepared samples are briefly described in this chapter.

5.1 Scanning Electron Microscopy and Microprobe Analysis

5.1.1 Scanning Electron Microscopy Imaging

Scanning electron microscopy (SEM) images the surface of a sample by use of an electron beam which is focused onto the sample by a set of electromagnetic lenses. Since an electron beam can interact with air particles, the instrument and the sample are kept under high vacuum (sample) and ultrahigh vacuum (filament and electron optics) conditions. Upon impact of the electron beam on the sample surface a variety of electrons and photons are emitted, as shown in figure 5.1. For imaging purposes, primary backscattered electrons as well as secondary electrons can be used. Today's highest resolution SEMs have an in-lens detector which detects the secondary electrons emitted near the electron spot on the sample surface in a very narrow angle, giving a resolution that allows structures down to below 1 nm [37, 38] to be displayed.

Since electrons would also eventually charge the sample, only samples made of conductive materials can be imaged without further preparation. Samples which are not conductive have to be coated with a grounded layer of carbon for elemental analysis, or grounded chromium or gold for high resolution imaging.

Electron Probe Microanalysis (EPMA)

Together with various secondary and backscattered electrons, element-specific characteristic and Bremsstrahlung radiation is emitted when the electron beam hits the sample. The energy of this x-ray radiation can be analysed with an Energy Dispersive X-ray (EDX) spectrometer and information on the material can be obtained (with the exception of very light materials with atomic masses of 1 to 4). Most modern SEMs are equipped with an EDX detector, as having the option of probing the
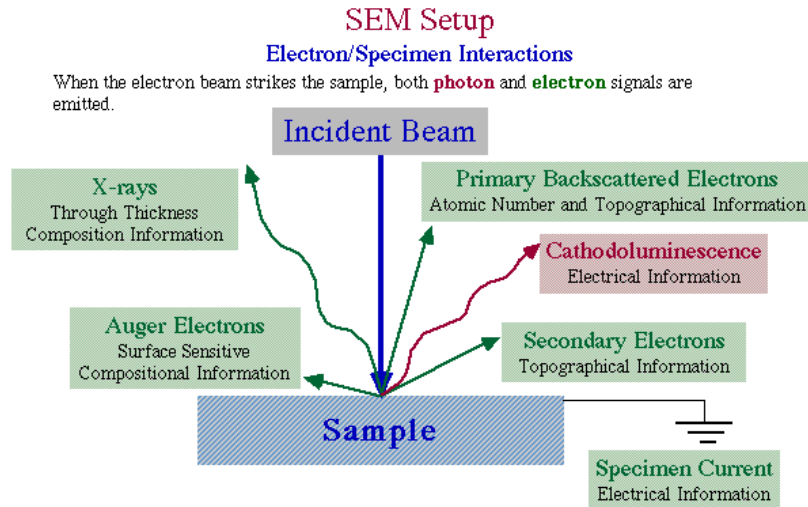
Figure 5.1: *Induced emission of various electrons and photons from the surface of a sample inside the SEM (taken from [33]).*

chemical composition of the sample under study is desirable. Additionally, since the spot size of the electron beam on the sample surface is well below 1 µm, a chemical mapping of regions of the displayed SEM image can be performed with sub-micron resolution.

Certain conditions such as the energy of the primary beam (which predominantly determines the x-ray emitting volume of the sample by its penetration depth), the self absorption and the surface roughness of a sample influence the results obtained from the microprobe analysis. At a primary beam energy of less than 5 kV, self absorption dominates the mathematical correction of the measured EDX spectrum. Today, very powerful computer software exists to automatically correct for essentially all of these effects.

Nevertheless, the experimenter has to choose the primary beam energy such that the minimum energy for the emission of characteristic x-ray radiation for the material of interest is reached whilst also keeping the absorption of the emitted radiation in mind and minimizing it by choosing a primary beam energy no greater than required for the element of interest. Good starting values are a primary beam energy of approximately 15 kV for elements with $Z \leq 20$ and of 20 kV for heavier elements. Higher energies can also be chosen to increase the volume sensitivity, whereas lower electron energies are more suitable for surface sensitive analysis, simply determined by the penetration depth of the electrons into the sample.

5.2 Atomic Force Microscopy and Magnetic Force Microscopy

The principle behind Atomic Force Microscopy (AFM) is to measure attractive or repulsive forces between a very sharp tip (usually less than 10 nm in diameter) of a scanning probe and the surface of a sample. The tip is located on the free end

of a cantilever $100\,\mu m$ to $200\,\mu m$ in length. In "contact mode" the scanning probe permanently (lightly) touches the sample, while in intermittent contact ("tapping") mode it is only periodically tapped onto the surface. In both cases the surface is raster scanned. The vertical deflection of the cantilever (in permanent contact mode) or the change in frequency (tapping mode) gives the local sample height and is usually measured by laser beam deflection. The linked detector consists of position-sensitive photo diodes and, depending on the actual geometry, can achieve atomic-scale resolution. Associated software uses this data to generate a map of the surface topography. In non-contact mode, raster-scanned topographical information is given by measuring the attractive forces between the probe and the sample without the tip touching the sample. This mode extends the lifetime of the tip, since there is less wear associated with not being dragged along or tapped onto a surface. However, non-contact mode is also less sensitive and results in poorer resolution. Contact mode as well as tapping mode AFMs can reach very small theoretical resolutions [39] and can be operated in air or even liquids. In practice, the equipment is very sensitive to vibrations and hence the theoretical resolution cannot always be achieved, despite attempts to minimise vibrations (e. g. by floating the AFM together with a large seismic mass on an air-cushion). Furthermore, features which are small compared to the diameter of the tip can not always be resolved well, as (due to the functional principle of AFMs) a convolution of tip and surface features is imaged. For resolving such small features the AFM can often also be operated in Scanning Tunneling Microscopy (STM) mode. In this mode the tip either scans across the surface at a fixed distance from the sample, measuring a varying tunneling current between the tip and the (conductive) sample, or the tip follows the surface topography at a distance from the sample by keeping the tunneling current constant.

Magnetic Force Microscopy (MFM) in principle operates identically to an AFM but the use of a magnetic tip allows the magnetic stray field properties of a sample to be probed. The image is a convolution of the atomic and the magnetic forces between the tip and the sample. MFM is mainly done in non-contact mode and the resolution is very limited if compared to AFM or STM. This is due to the fact that the magnetisation of the MFM tip influences the magnetisation of the sample and vice versa. It is hence difficult to deduce quantitative values from MFM. A schematic diagram of a typical AFM/MFM is shown in figure 5.2.

5.3   Vibrating Sample Magnetometer (VSM)

A dipole moment is induced in any sample placed into a uniform magnetic field between the poles of an electromagnet. If the sample is vibrated along the z-axis perpendicular to the magnetic field, an electrical signal with the same frequency is induced into appropriately placed pick-up coils. The amplitude of this signal is proportional to the magnetic moment of the sample. It is amplified by lock-in amplifiers and usually processed by a computer. The sensitivity of modern VSMs is in the range of 1×10^{-7} emu and many instruments can rotate the sample relative to the magnetizing field and operate at a range of temperatures down to only a few Kelvin. With such an apparatus the susceptibility and magnetisation of a sample
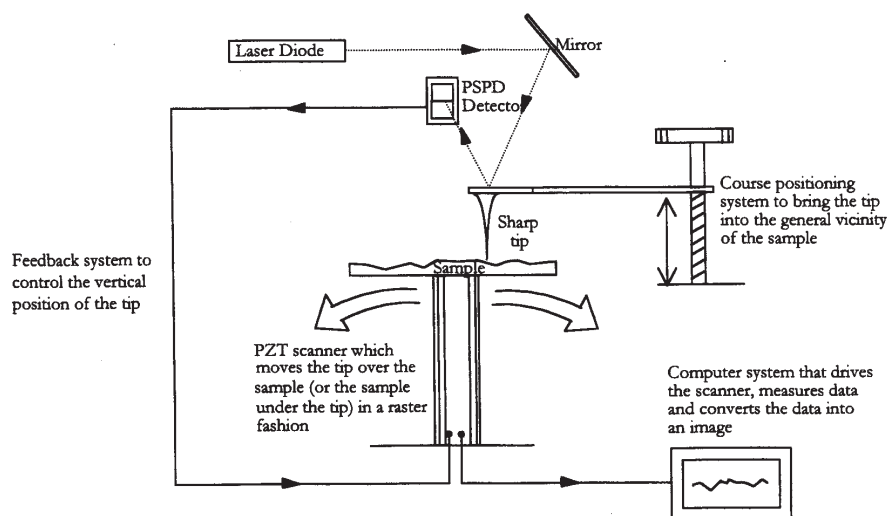
Figure 5.2: *Schematic of an AFM/MFM setup (taken from [33].)*

can be measured as a function of temperature and external field, as well as the rotation angle of the sample relative to the external magnetizing field. This means that hysteresis loops, thermo-magnetic properties and anisotropies can be directly investigated. The schematics of a commercial VSM are shown in [40].

5.4 X-Ray Diffraction (XRD)

Interatomic distances of crystalline materials are comparable to the wavelength of x-ray radiation. Being an electromagnetic wave, x-ray radiation strongly interacts with the charge distribution in the electron shells of atoms. As a result, the crystalline structure of a material acts as a grating for x-rays such that diffraction patterns can be observed which allow the analysis of the lattice parameters if the wavelength of the x-ray radiation is known. The Bragg equation

$$2d \sin \theta = n\lambda \tag{5.1}$$

gives the mathematical relation for this analysis, where λ is the wavelength of the x-rays, d is the interplanar spacing, θ is the angle of incidence relative to the sample surface, and n is the diffraction order.

A typical x-ray diffractometer generates x-rays using a standard x-ray tube with Cu being the most common anode material. These x-rays are monochromated, collimated and directed onto a sample which diffracts the x-rays according to its lattice parameters and the type of atoms present. The most common diffractometers work either in a Bragg-Brentano [41] geometry or with parallel beam optics using Göbel mirrors [42]. The resulting diffraction pattern intensity can be measured by a detector at specific angles (figure 5.3) from which the crystalline structure of the investigated sample can be determined [41, 43, 44].
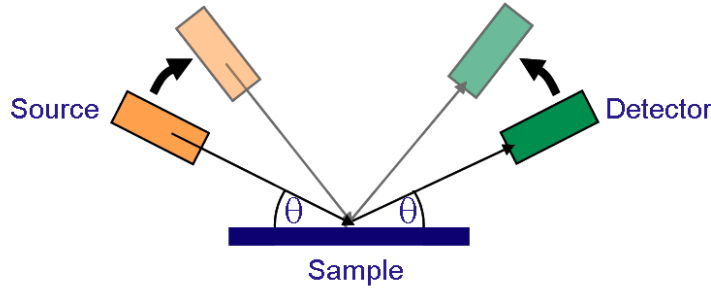
Figure 5.3: *Schematic of a diffraction scan: the 2θ-angle between the x-ray source, the sample and the detector is scanned. By this method high angle specular scattering vectors Q_z can be probed.*

5.5   X-Ray Reflectometry (XRR) and Off-specular Scattering

In contrast to conventional diffraction scans, which are also referred to as high angle scans, x-ray radiation is also a very sensitive probe at small incidence angles. An incident electromagnetic wave penetrates into a medium which is characterised by its index of refraction

$$n = 1 - \delta + \mathrm{i}\beta \tag{5.2}$$

where δ and β denote the dispersion and absorption terms respectively [45]. On each interface the electromagnetic wave with wavevector $\vec{k_i}$ and angle of incidence θ_i splits into a reflected ($\vec{k_f}$, θ_f) and a transmitted wave ($\vec{k_t}$, θ_t) as shown in figure 5.4 with the corresponding Fresnel coefficients for reflection (r) and transmission (t) given by

$$r_s = \frac{k_{i,z} - k_{t,z}}{k_{i,z} + k_{t,z}} \tag{5.3}$$

$$t_s = \frac{2k_{i,z}}{k_{i,z} + k_{t,z}} \tag{5.4}$$

for the s-polarisation[1] component of the incident electromagnetic wave. For the p-polarisation[2] component these Fresnel coefficients are

$$r_p = \frac{n^2 k_{i,z} - k_{t,z}}{n^2 k_{i,z} + k_{t,z}} \tag{5.5}$$

$$t_p = \frac{2k_{i,z}}{n^2 k_{i,z} + k_{t,z}}, \tag{5.6}$$

where $k_{i,z} = k\sin\theta_i$, $k_{t,z} = nk\sin\theta_t = k\sqrt{n^2 - \cos^2\theta_i}$ [45]. The reflectivity at each interface is therefore directly related to a change in the refractive index of the material, and the reflectivity spectrum shows an interference pattern where more

---

[1]linear polarisation with the electric field vector perpendicular to the (x,z)-scattering plane
[2]polarisation of the electric field vector parallel to the (x,z)-scattering plane
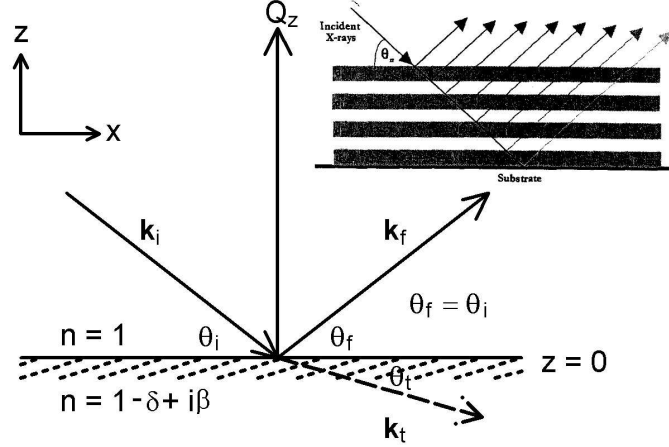
Figure 5.4: *Reflectivity at an air/solid interface: an incident x-ray beam with wavevector $\vec{k}_i$ reaches the interface at an angle of incidence θ_i where it is partially reflected ($\vec{k}_f$) and partially refracted ($\vec{k}_t$) (after [45]). The inset gives a schematic of the interference in a multilayer sample (taken from [49]).*

than just one interface exists [45]. However, for incidence angles which are below a critical angle $\theta_c \approx \sqrt{2\delta}$, total external reflection occurs with small losses due to the absorption term β. The corresponding critical scattering vector Q_c is given by

$$Q_c = \frac{4\pi}{\lambda} \sin \theta_c \tag{5.7}$$

As real surfaces and interfaces are also always rough, the refractive indices n_j, n_{j+1} do not change abruptly from one layer (j) to the other (j+1) but exhibit variations from the ideal flat interface which cause diffuse scattering into off-specular[3] directions, damping the specular reflectivity. This allows the density, thickness and roughness of the layers to be examined from their measured specular reflectivity curve. Furthermore, the use of analysis and fitting software like PARRATT [46], REFSIM [47] or XOP with IMD-plugin [48] facilitates the theoretical calculation of specular reflectivity curves and allows models to be fitted to the measured data (e. g. in 6.4.2). However, for artificially laterally structured samples, these standard software packages cannot always reproduce the measured specular reflectivity curves, such that purpose-designed simulation and fitting programs, based on specifically chosen theoretical models for the investigated systems, need to be applied (as demonstrated in 8.4.3).

5.5.1 Specular XRR

Under specular reflectivity conditions, measurements are carried out such that the incident angle θ_i and the angle of the reflected radiation θ_f to the sample surface are equal and hence only sensitive to a momentum transfer $Q_z = k_{f,z} - k_{i,z}$ transversal to

---

[3]under off-specular scattering, the incident angle θ_i is not equal to the angle of the reflected radiation θ_f

the sample surface (figure 5.4). The parallel momentum transfer $Q_\parallel$ in this scattering geometry is not measured and only the vertical structure in the form of averaged electron densities of a sample can be analysed. The Q_z-values are given by

$$Q_{z_{\text{XRR}}} = k_{f,z} - k_{i,z} = \frac{2\pi}{\lambda} \sin \theta_f + \frac{2\pi}{\lambda} \sin \theta_i = \frac{4\pi}{\lambda} \sin \theta_i \tag{5.8}$$

where λ is the wavelength of the x-rays.

For incidence angles θ_i which lie below the illumination angle $\theta_{\text{illum}} = \sin^{-1} w/l$ (where w is the width of the x-ray beam and l is the length of the sample under investigation [50]) the primary x-ray beam illuminates the sample under a very shallow angle of incidence and hence the footprint of the x-ray beam is larger than the sample. To account for this effect, an intensity correction is commonly performed on the measured reflectivity curve. For this the measured data is multiplied by a correction factor C which depends on the angle of incidence and is given by

$$C(\theta_i) = \frac{w}{l \sin \theta_i}. \tag{5.9}$$

For correcting an underlying diffuse background (5.5.2) in the specular XRR measurements, typically a longitudinal diffuse or "offset" scan is used (figure 5.5). In principle, this is a standard XRR scan, but with a slight additional inclination of the sample surface into the direction of the tube or the detector which introduces a slight misalignment $\delta\theta_i$ of the sample and measures the diffuse background in the vicinity of the specular reflectivity condition (figure 5.5). The offset-XRR scan is converted into reciprocal space values through [50]

$$Q_{x_{\text{Offset}}} = -\frac{4\pi}{\lambda} \left(\sin \theta_i \sin \delta\theta_i \right) \tag{5.10}$$

$$Q_{z_{\text{Offset}}} = \frac{2\pi}{\lambda} \left(\sin \theta_i + \sin \theta_f \right) \tag{5.11}$$

and subtracted from the specular XRR scan for background correction (for this only Q_z is of interest). The trajectories in reciprocal space that are scanned by the reflectivity and offset scans are shown in figure 5.5.

5.5.2   Off-specular X-ray Scattering

Inhomogeneous surfaces and interfaces dampen the specular reflectivity by e.g. off-specular scattering. These off-specular intensities, however, hold the information about the lateral structures which caused them. In this way, x-rays not only probe the scattering length density (N_b, SLD) distribution normal to the surface but the full three-dimensional SLD profile

$$\begin{aligned}
N_b &= r_e \rho(\vec{r}) \tag{5.12} \\
&= r_e \rho(z) + \Delta(r_e \rho(x, y)) \\
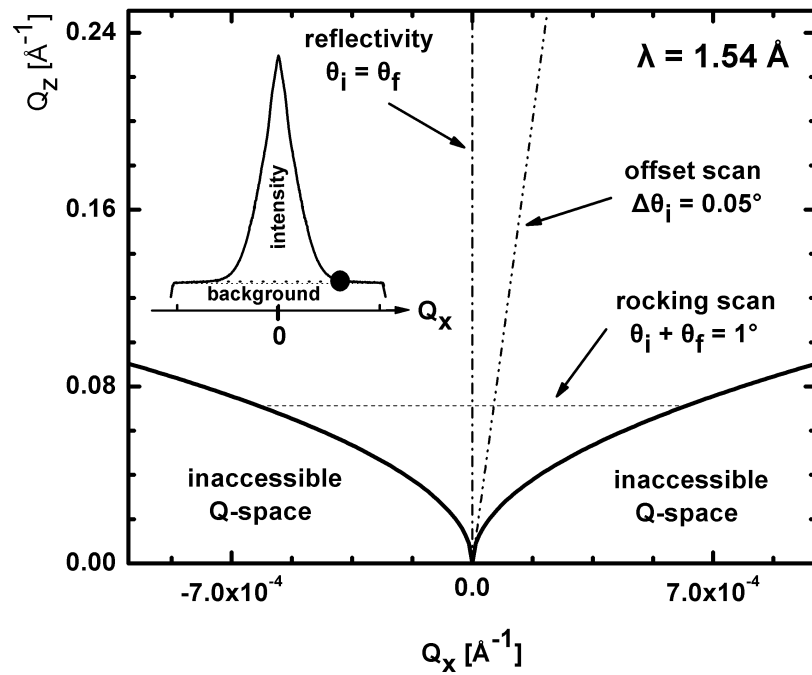&= N_b(z) + \Delta N_b(x, y, z)
\end{aligned}$$

Figure 5.5: *Regions in reciprocal space scanned by the reflectivity, offset and rocking scans. The trajectories through reciprocal space are shown by the three dashed/dotted lines. The solid line marks the transition to inaccessable regions in which either the x-ray source or the detector is below the surface of the sample (for neutrons, parts of these regions are accessible as neutrons are not shaded-off by the sample). The inset shows a schematic rocking scan with a dot marking the intersection point with the offset scan which allows the background in the vicinity of the specular reflectivity path at $Q_x = 0$ to be measured (after [45]).*
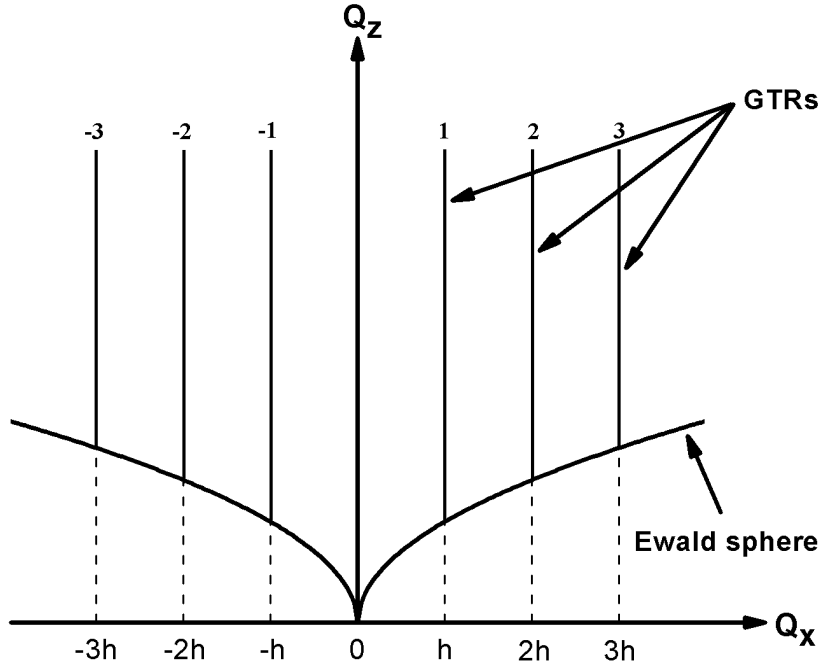
Figure 5.6: *Grating Truncation Rods (GTRs) in reciprocal space located at* $h = (2\pi/d)m$ *where* m *is the grating order. The parts below the Ewald sphere are not accessible by x-ray scattering in coplanar scattering geometry (i. e. rocking scans). In laterally homogeneous samples, the non-zero GTRs vanish (after [51]).*

where $N_b(z)$ is the mean value of the laterally averaged SLD and $\Delta N_b(x, y, z)$ describes the lateral variations caused e. g. by naturally occurring interfacial roughness and/or artificial structures. $r_e = e^2/4\pi\epsilon_0 mc^2$ is the classical electron radius and $\rho(\vec{r})$ is the (electron) density. The corresponding scattering function is essentially a Fourier transform of $\rho(\vec{r})$. Therefore, if $\Delta N_b(x, y, z)$ is periodic then its transform into reciprocal space is also periodic. For the case of a sample with a lateral surface grating periodicity d along the x-direction, the reciprocal grating vectors are then given by $h = (2\pi/d)m$ where m is the grating order [51]. The resulting reciprocal lattice of the grating is a periodic arrangement of Grating Truncation Rods (GTRs), transverse to the normal of the sample surface whose intersection points with the Q_x axis are defined by h (figure 5.6) [51].

To calculate the intensity distributions in detail for a multilayer system (total of N layers), the problem amounts to finding the exact solution to a multiple scattering problem [52]. Generally one can decompose the interaction potential of each layer n into two parts [53]

$$V(\vec{r}) = \sum_{n=1}^{N}(V_n + \Delta V_n(\vec{r})), \tag{5.13}$$

where $\Delta V_n(\vec{r})$ is a deviation of the averaged scattering potential V_n for layer n which only contributes to the reflection and transmission in the specular direction.

Kinematic Approximation

In the kinematical approach only single scattering events are considered in the first order Born Approximation (BA). Refraction and reflection effects are not explicitly taken into account such that BA is only valid for scattering events far from the critical edge, where these effects are negligible. The scattering amplitude is given by [53]

$$
\begin{aligned}
F_{\mathrm{BA}}(\vec{Q}) \quad &\propto \quad \sum_n \int_{z_{n-1}}^{z_n} dz\, e^{iQ_z z} \\
&\times \int dx\, dy\, e^{i(Q_x x + Q_y y)} V_n(\vec{r}) \\
&\propto \quad \int d\vec{r}\, e^{i\vec{Q}\vec{r}} N_b(\vec{r})
\end{aligned}
\tag{5.14}
$$

and the intensity distribution in reciprocal space is of the form [54]

$$
I \propto |F(\vec{Q})|^2 \times \sum_n \delta\left(Q_x - \frac{2\pi}{d}m\right),
\tag{5.15}
$$

where m is the diffraction order.

Although some conclusions can be drawn from the BA, its most noticeable weakness is its non-applicability for low angular regions where the scattering is dominated by optical effects (e.g. manifested by the occurrence of total reflection). Although BA can be used for a qualitative discussion, a quantitative interpretation of specular or off-specular scattering results from laterally structured samples, which are typically collected at low incidence angles, is not possible [53, 54].

Distorted-Wave Born Approximation

An extension of BA to include optical effects, making the description compatible with the case of shallow scattering angles, is the Distorted-Wave Born Approximation (DWBA) which assumes the decomposition of the scattering potential into a laterally averaged mean optical potential and its lateral deviations (figure 5.7). The optical effects at interfaces are precisely taken into account by dynamical treatment and the scattering on lateral inhomogeneities is treated kinematically from the distorted waves in the medium.

The scattering amplitude in DWBA is modified to include the exact refraction and reflection effects from the layer potentials and becomes [53]

$$
\begin{aligned}
F_{\mathrm{DWBA}}(\vec{k_i}, \vec{k_f}) \quad &= \quad \sum_n \int_{z_{n-1}}^{z_n} dz \int d\vec{r}\, e^{i(Q_x x + Q_y y)} \\
&\times \hat{S}_{n;i}(z) \Delta V_n(x, y) \hat{S}_{n;f}(z)
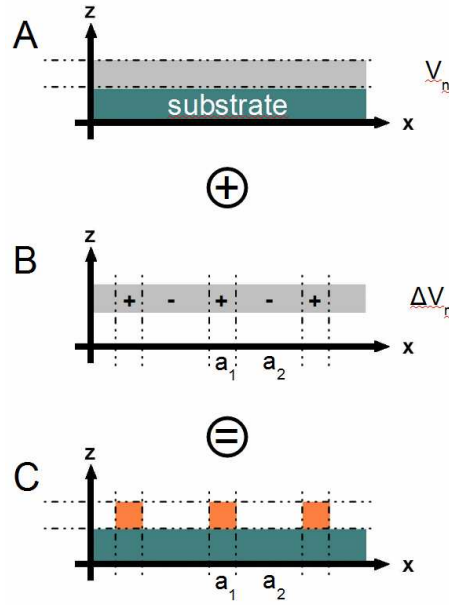\end{aligned}
\tag{5.16}
$$

Figure 5.7: *The scattering potential profile (C) as composed of transverse (A) and lateral (B) components. From the averaged transverse component V_n a scattering length density for the layer structure can be obtained which contributes to the intensities on the specular path ($Q_x = 0$). The lateral deviations ΔV_n lead to periodic off-specular diffraction (after [53]). a_1 and a_2 give the lateral dimensions of the structures.*

where

$$
\begin{aligned}
\hat{S}_{n;i}(z) &= \hat{S}_{n;i}(t_{n;i}, r_{n;i}) \\
&= t_{n;i}e^{ik_{z,n;i}(z-z_{n-1})} + r_{n;i}e^{-ik_{z,n;i}(z-z_{n-1})}
\end{aligned}
\tag{5.17}
$$

and $\hat{S}_{n;f} = \hat{S}_{n;f}(t_{n;f}, r_{n;f})$ respectively describe the x-ray propagation normal to the surface inside the n-th laterally averaged effective layer before (i) and after (f) scattering on $\Delta V_n(\vec{r})$. $k_{z,n;i}$ and $k_{z,n;f}$ are the wave vector transfer components given by [53, 54]

$$
k_{n;i/f} = \sqrt{k_n^2 \sin^2 \theta_{n;i/f} - \left(\frac{Q_{c,n}}{2}\right)^2}.
$$

DWBA generally describes real samples very well and has been widely applied to a variety of systems [55–60], including systems with a periodic arrangement of surface structures [53]. It was also used in this work for obtaining structural parameters of a sample from the corresponding off-specular scattering x-ray pattern (8.4).

Statistical Description of Surfaces and Interfaces

Simulation of a theoretical model using DWBA reverts to a statistical description of surface morphologies with correlation functions $C(\vec{R})$ as the main component. This allows the sample to be described by only a few distinct parameters, viz. the root-mean-square (rms) roughness σ, the correlation length ξ and the Hurst parameter
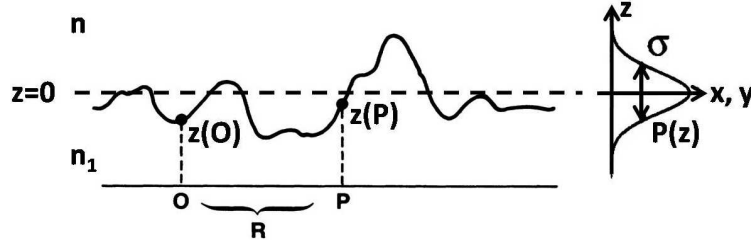
Figure 5.8: *A rough interface separating two media characterized by the refractive indices n and n_1 with a mean coordinate $z = 0$ and fluctuations thereof as described by the contour function $z(x, y)$. For a statistical description, the surface is replaced by an ensemble of smooth surfaces at the coordinates z, weighted by a probability density $P(z)$. σ gives the rms roughness of the interface. A correlation function $C(\vec{R})$ describes the probability of finding a point $P(\vec{R})$ with the same height $z(P)$ above/below the mean interface level as at the origin O. (figure composed of two figures found on pages 15 and 92 of [45]).*

h. Figure 5.8 shows a rough interface between two media characterized by their refractive indices n and n_1 with mean coordinate $z = 0$ and fluctuations in z as characterized by a profile function $z(x, y)$ which contains the exact information on the topography of the interface. Statistically, this interface can be described by an ensemble of smooth interfaces at the height coordinates z, weighted by a probability density $P(z)$. It is apparent that the rms roughness σ (as defined by equation 5.18) can be equal for different microscopic surface topographies and that the lateral averaging over a sufficiently large area A yields exactly the same result as vertical averaging over z with the probability density function $P(z)$ [45]

$$\sigma^2 = \int dz\, z^2 P(z) = \frac{1}{A} \iint_A dx\, dy\, z^2(x, y). \tag{5.18}$$

Therefore, for a complete statistical description, a correlation function $C(\vec{R})$ is also required, describing the probability of finding a point $P(\vec{R})$ at the position $\vec{R} = (X, Y)$ with the same height $z(P)$ above/below the mean interface level as at the origin O. For isotropic solid surfaces the correlation function proposed by Sinha et al. [59] is given by

$$C(\vec{R}) = \sigma^2 e^{-(\vec{R}/\xi)^{2h}}. \tag{5.19}$$

The correlation length ξ describes the lateral length scale on which an interface "begins to look rough" [45]. In the case of $\xi \ll R$, the surface is self-affine[4] rough, whilst in the case of $\xi \gg R$ the surface looks absolutely smooth [61]. Figure 5.9 shows the influence of the correlation length and the Hurst parameter on surfaces with identical rms roughnesses σ and either a fixed correlation length ξ or a fixed Hurst parameter h. The Hurst parameter (with $0 < h \leq 1$) defines the fractal box dimension [61, 62] $D = 3 - h$ of the interface and essentially describes its jaggedness:

---

[4]On transition from one length-scale with the characteristic dimension R to the other length scale aR, self-affine surfaces are only similar. This means that the z direction scales with a factor $f < a$, making the surface appear smoother on a larger scale.
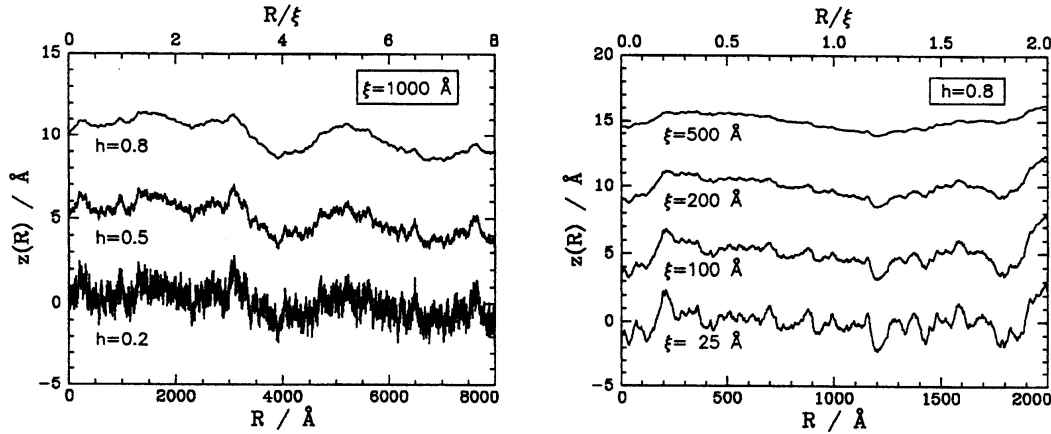
Figure 5.9: *Surface cuts as obtained for different parameters ξ and h. It can be seen (right) that ξ controls the size of typical lateral distances for surfaces with identical rms roughnesses σ and identical Hurst parameters h. For fixed values of ξ and σ (left) the influence of h is such that small values describe strongly jagged surfaces, whilst larger values of h lead to a more regularly undulated appearance (taken from [61]).*

small values of h correspond to extremely jagged surfaces, whilst large values lead to interfaces with a smooth appearance.

Experimental Analysis

For the experimental analysis of lateral sample structures, regions of reciprocal space which lie outside the specular reflection rod must be investigated. In order to access these regions of reciprocal space, the momentum transfer $Q_{\parallel} = \sqrt{Q_x^2 + Q_y^2}$ must be nonzero. Although other methods, such as the previously mentioned offset scan exist for this purpose, the most common method to access off-specular regions of the reciprocal space by probing Q_x is the so called "rocking" scan used in this work. At a constant angle of $2\theta = \theta_i + \theta_f$, the x-ray source and the detector are scanned in unison from $\theta_i = 0$ to $\theta_f = 0$ as shown in figure 5.10 and the Q values are given by [50]

$$Q_{x_{\text{rocking}}} = \frac{2\pi}{\lambda} \left(-\cos\theta_i + \cos\theta_f \right) \tag{5.20}$$

$$Q_{y_{\text{rocking}}} = 0 \tag{5.21}$$

$$Q_{z_{\text{rocking}}} = \frac{2\pi}{\lambda} \left(\sin\theta_i + \sin\theta_f \right) \tag{5.22}$$

In practice, and depending on the geometry of the diffractometer, the sample is often simply inclined around the ω axis instead (the axis that lies within the surface of the sample perpendicular to the scattering plane) within the angular region of $-\theta \leq \omega \leq +\theta$ whilst the source and the detector arms of the diffractometer are at a fixed position. Therefore, "rocking" scans are also referred to as ω-scans.
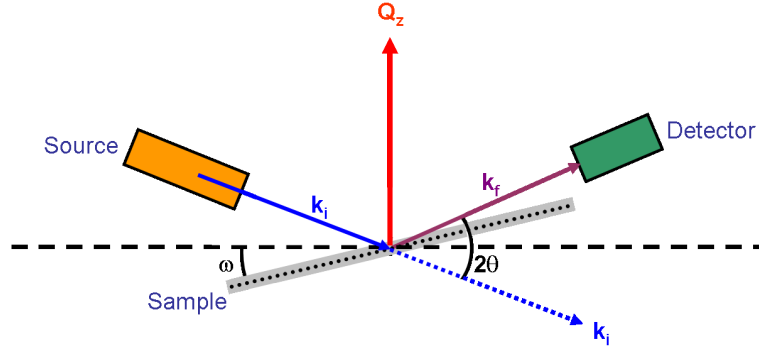
Figure 5.10: *Schematic of an ω- or "rocking" scan: at a fixed 2θ-angle between the x-ray source and the detector the sample is inclined around the ω axis. Off-specular intensities in Q_x can thus be probed.*

Varying the 2θ angle and repeatedly performing ω-scans for each value of 2θ maps certain regions of the reciprocal space. It should be noted that not all off-specular regions can be accessed by this method, as the sample surface shades off the x-ray beam or the scattered intensities, if the angle of incidence or of reflection lies below the surface of the sample. The accessible regions are shown in figure 5.5 and figure 5.12.

Due to the typically short wavelength of laboratory source x-ray radiation, large values of Q_z must be probed to access Q_x regions that are of interest for nanometre scale laterally structured samples. Unfortunately, this causes a dramatic decrease in the diffuse intensities as the Fresnel reflectivity R_f decreases with $R_f \approx (\theta_c/2\theta_i)^4$ [45]. This problem becomes even more prominent with decreasing lateral structure periodicities as due to the relation between real and reciprocal space the Q_x value of the off-specular intensities increases. Hence, this method is often not suitable for samples with very small lateral periodicities. For the analysis of such samples, however, a Grazing Incidence Small Angle Scattering (5.7) geometry can be applied.

5.6 Neutron Reflectometry

The scattering process as for neutrons and x-rays have different physical origins. Whilst x-rays are electromagnetic waves which strongly interact with the electron shell of an atom, neutrons are neutral particles and are mainly undisturbed by the electron shell. Instead, they interact with the Fermi potential of the atomic nuclei [63]. The strength of this interaction is a function of the nuclear scattering length density $N_b/\rho = b_{\text{nuclear}}$, which depends on the atomic number (and therefore also differs for isotopes, which have a different scatterer density ρ). The refractive index of a material for neutron radiation can be written analogous to the x-ray case as

$$n_n = 1 - \delta_n + \mathrm{i}\beta_n.$$

The absorption term β_n is in most cases negligible (with the exception of only a few materials like B, Cd or Gd which are good neutron absorbers), whilst the dispersion

term δ_n is of the same order of magnitude as it is for x-ray radiaton. δ_n is a function of the scattering length and therefore allows the vertical structure of a sample to be determined by neutron reflectometry as a variation in averaged scattering length densities. The analysis is carried out analogously to the x-ray case (5.5). It should be noted that, although neutron sources are usually of very complicated nature (reactors or spallation sources), the primary beam flux of the best monochromatic neutron instruments is usually exceeded by the flux of a standard laboratory x-ray source. Therefore, neutron reflectivity is generally applied as a complementary method to x-ray reflectometry for structural analysis if a sensitivity for hydrogen or a contrast between various isotopes is required, which x-ray scattering cannot provide. Also the unrivaled penetration depth of neutrons allows massive bulk samples to be investigated and parts of the inaccessible regions in x-ray reflectometry (figure 5.5) can be accessed as no shading of neutrons occurs by the sample. In addition, the sensitivity of neutron radiation to the magnetic properties of a sample makes them an irreplaceable tool in materials science, as detailed in the following.

Polarised Neutron Scattering

Although neutrons are electrically neutral, they are spin-$\frac{1}{2}$ particles and therefore carry a magnetic moment. Used as a probe, neutrons not only interact with the nuclear potential of an atom, but are also sensitive to magnetic moments of unpaired electrons in the electron shell of magnetic elements. Polarised neutron reflectivity (PNR) allows magnetic properties of a sample to be measured by the reflectivity profile for the two polarisation states. The scattering amplitude of neutrons depends on their polarisation state relative to the magnetisation of the sample. For magnetic moments that are collinear or anti-parallel to the polarisation vector of the neutrons, the scattering length b_{total} is a sum of the nuclear b_{nuclear} and the magnetic scattering length p:

$$b_{\text{total}} = b_{\text{nuclear}} \pm p \qquad (5.23)$$

and the magnetic scattering length p is given by

$$p = 0.27 \times 10^{-4} n\mu \frac{\lambda^2}{2\pi} \qquad (5.24)$$

where n is the density of the unit cell, λ the applied wavelength and μ the magnetic moment in units of μ_B [63].

5.7 Grazing Incidence Small Angle Scattering

The specular and off-specular measurements described in 5.5 and 5.6 work only within the plane of reflection and hence always probe a zero Q_y value. For measuring scattered intensities outside this plane a geometry known as grazing incidence diffraction is commonly used for both x-rays (GISAXS) and neutrons (GISANS).

The diffuse intensities are usually measured by a position sensitive detector (PSD) that is either of sufficient size or can be moved perpendicular to the re-
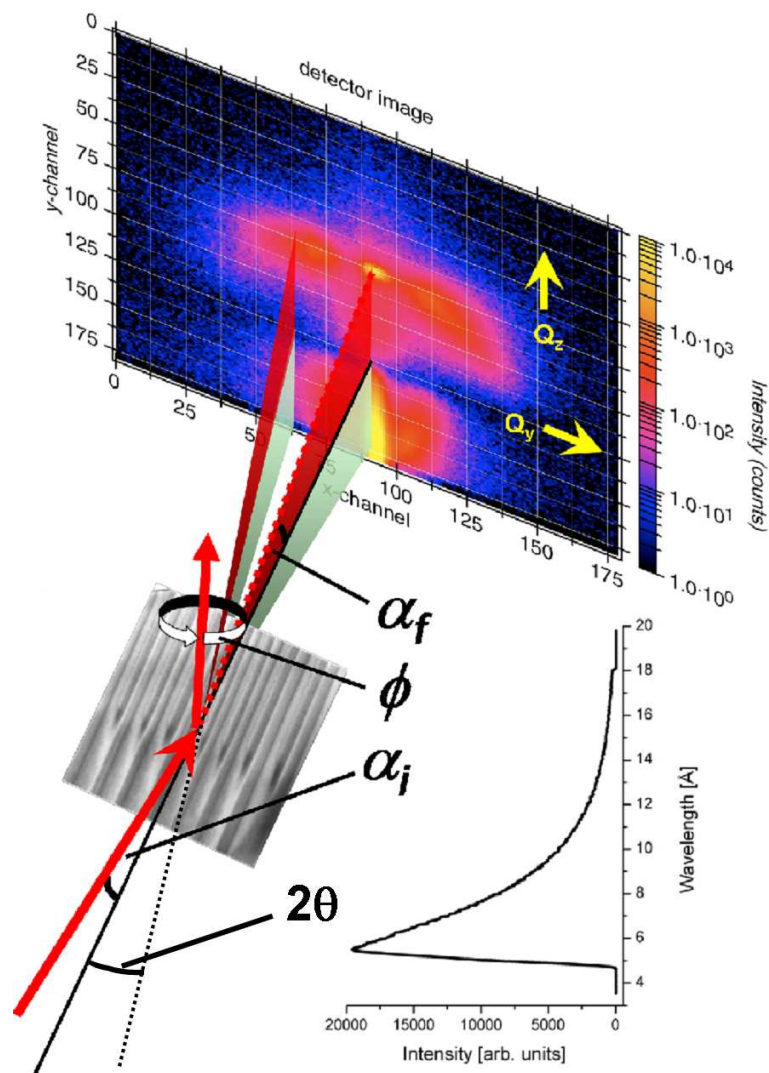
Figure 5.11: *Schematic of the scattering geometry used for Time-Of-Flight GISANS. The geometry is the same as for conventional monochromatic GISAXS or GISANS measurements, but the detector is not only position but also time sensitive. A chopper system in combination with a fixed flight distance allows the wavelength of the detected neutron to be measured. The inset graph shows a typical "cold"-source neutron wavelength distribution.*
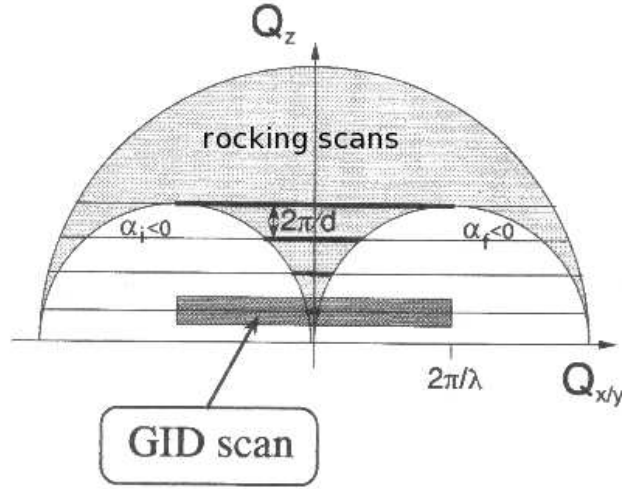
Figure 5.12: *Ewald sphere construction showing the accessible portions of reciprocal space using either rocking scans or grazing incidence (GID) geometry (taken from [50]).*

flection plane. In this geometry the incident angle α_i and the reflected intensity angle α_f can be measured as well as the angle 2θ perpendicular to this plane (figure 5.11). The momentum transfer is then given by [50]

$$Q_{x_{\text{grazing incidence}}} = \frac{2\pi}{\lambda}\left(\cos\alpha_f\cos 2\theta - \cos\alpha_i\right) \tag{5.25}$$

$$Q_{y_{\text{grazing incidence}}} = \frac{2\pi}{\lambda}\left(\sin 2\theta\cos\alpha_i\right) \tag{5.26}$$

$$Q_{z_{\text{grazing incidence}}} = \frac{2\pi}{\lambda}\left(\sin\alpha_i + \sin\alpha_f\right) \tag{5.27}$$

This scattering geometry has various advantages: firstly, due to the very shallow angle of incidence the penetration depth of the probe radiation can be minimised so that this geometry becomes purely surface sensitive; secondly, it is sensitive to a wide range in Q_y, as for very small α_i the lateral momentum transfer $Q_\parallel = \sqrt{Q_x^2 + Q_y^2}$ is dominated by the value of Q_y and hence for small values of Q_z a wide range in Q_y can be probed whilst the Q_x value is typically negligible.

The accessible regions of the reciprocal space by grazing incidence and rocking scan geometry are compared in figure 5.12.

5.7.1   Time-of-Flight GISANS

A very recent variant of GISANS is to use multiple wavelengths rather than a quasi-monochromatic neutron beam. By applying a continuous wavelength spectrum, the size of the Ewald sphere is varied in reciprocal space. Hence, for laterally structured samples it is not only possible to reconstruct intersection points of the GTRs with the Ewald sphere for one wavelength, but also larger portions of the GTRs by obtaining the integral image over all wavelengths using a single measurement. This is possible

by the use of sophisticated neutron reflectometers that operate with time-of-flight analysis and hence can not only detect the position of a scattered neutron but also its wavelength. For evaluation of this data, however, one has to correct each wavelength slice by the background, weight its intensity by the primary beam intensity, correct for ballistic effects and add the intensities in reciprocal space. The use of TOF-GISANS [LOP-3, LOP-4], carried out at the GKSS's novel combined Reflectometer and Small Angle Neutron Scattering instrument REFSANS [64, 65] at the FRM II neutron source Garching, and its outstanding suitability for the analysis of highly ordered lateral surface structures will be demonstrated further in 8.2.4.

Chapter 6

Epitaxial Growth Studies

This chapter describes studies for the growth of epitaxial Ni on Si. In the context of this project, this is an essential step toward the goal of structuring a single crystalline Ni layer using the top-down-process described in 7.1. In comparison to the sample described in 7.1.1, a well defined crystalline anisotropy of the Ni nanodots or nanowires is expected as an additional sample feature.

Epitaxial thin film growth of magnetic metals on silicon substrates has been widely studied because of its importance in industrial applications such as non-volatile Magnetic Random Access Memory (MRAM) or (future) spin-injection devices [66–73]. Si, however, does not directly match the lattice constant of any of the ferromagnetic metals. Therefore, a Cu seed layer is commonly employed for epitaxial growth, a technique known as Metal-Metal-Epitaxy-on-Silicon (MMES). This has the advantage that epitaxial growth at room temperature without intentional cooling or heating of the substrate can be achieved for a variety of deposition methods [66, 67, 71, 72, 74–76]. Wet-chemical processes, e-beam evaporation and ion-beam assisted deposition techniques have also been used to grow magnetic films of Fe, Co, Ni and their alloys directly epitaxially on Si substrates without the need of a Cu seed layer, but with varying epitaxial quality [77, 78]. A poor epitaxial crystal quality for direct epitaxial growth on Si is particularly apparent for the case of Ni and publications thereof are rare [77, 79].

However, it has been shown that Cu can be deposited epitaxially on hydrogen terminated Si surfaces by sputtering. Using the sputter deposition setup available at GKSS (3.1.2), a plan was followed to first reproduce the epitaxial growth of Cu by DC magnetron sputtering followed by MMES of Ni on Cu/Si. Use of this Ni on Cu/Si layer system proved unsuitable for the preparation of nanostructured samples by a top-down structuring process, as it was found that argon ion beam milling destroys the epitaxy (appendix A).

Consequently a novel deposition process was developed allowing epitaxial growth of unprecedented quality of Ni onto a Si(100) substrate without the need for a Cu buffer layer (6.4). In contrast to the case where a Cu seed layer is applied, the epitaxy of Ni is also not destroyed by argon ion beam milling, which therefore is an important step toward the preparation of a single crystalline Ni nanodot sample.

6.1 Sample Analysis in Epitaxial Growth Studies

6.1.1 Out-of-plane Structure

Out-of-plane structural XRD analysis was carried out using a Bruker AXS-D8 Advance two-circle x-ray diffractometer with parallel beam optics and Cu-K$_\alpha$ source ($\lambda = 1.54\,\text{Å}$). Conventional out-of-plane $\theta - \theta$ diffraction scans were used to determine the crystalline structure and ω or "rocking"-scans to measure the directional alignment of the crystallites. At a given film thickness, the full width at half maximum (FWHM) of the ω-scans, and both the FWHM and the peak intensities of the diffraction scans are a measure of the epitaxial crystal quality. A lower FWHM value of the ω-scans corresponds to a lower mosaic spread and a better epitaxial quality. The size of the crystallites is analogous to the coherence length and can be determined by the Scherrer formula [44]:

$$B(2\theta) = \frac{0.94\lambda}{L\cos\theta} \tag{6.1}$$

where λ is the wavelength of the applied x-ray radiation, $B(2\theta)$ is the FWHM (in rad) of the diffraction peak, θ the angular peak position and L the coherence length. All prepared samples were aligned with respect to the Si(400) out-of-plane substrate reflection for a well defined reference for the determination of any potential miscut of the silicon substrate and crystalline direction of the deposited Cu and Ni films.

6.1.2 In-plane Structure

Out-of-plane analysis is not sufficient for the examination of the epitaxial growth of a thin film as misalignment can also occur in-plane. Thus, both out-of-plane and in-plane scans are needed to verify epitaxial growth (e. g. figures 6.10 and 6.13). A Seifert XRD 300 PTS four-circle x-ray diffractometer also utilising Cu-K$_\alpha$ radiation with $\theta - 2\theta$ diffraction geometry and additional axes for sample inclination (χ) relative to the specular beam direction and axis rotation (ϕ) around the sample normal was used to probe the in-plane crystal information. Alignment of the sample in ϕ and χ was made with reference to the Si(111) reflection. By setting the 2θ angle to the desired in-plane peak positions and rotating the sample around its normal (ϕ) at the corresponding inclination-angle (χ) information on the in-plane crystal symmetry can be obtained together with information on the epitaxial relationship of substrate crystal and deposited films. Instrumental resolution of the x-ray diffractometers is defined by the FWHM of the Si(400) out-of-plane rocking curve and is smaller than 0.08°, which is sufficient to neglect instrumental broadening in the analysis of the Cu and Ni layers [41].

6.1.3 Structural and Magnetic Layering of the Samples

XRR (5.5) was used to measure the thickness of the deposited layers. Additionally, for the Ni thin film sample with the best epitaxial structure, Magneto Optical Kerr Effect (MOKE) and PNR (5.6) were used to probe the magnetisation profile of the

single layer and determine the magnetisation of the thin film. MOKE uses the rotation of polarised laser light caused by the magnetic moments of the sample to probe the overall magnetic behavior, i.e. for measuring the magnetisation of the sample as a function of the applied magnetic field and its history. These measurements were carried out by Dr Holger Stillrich, University of Hamburg. PNR was performed at the NERO neutron reflectometer at the Geesthacht Neutron Facility (GENF) of the GKSS Research Centre using a neutron wavelength of $4.335\,\text{Å}$. Quantitative analysis of the XRR and PNR data was made using the PARRAT32 1.5.2 software package [46].

6.2 Epitaxial Growth of Cu on Si(100) by DC Magnetron Sputtering

6.2.1 Thin Film Preparation

A Si(100) wafer was cut to an appropriate substrate size of $20 \times 60\,\text{mm}^2$ and ultrasonically cleaned using acetone followed by ethanol. Subsequently the native silicon oxide layer was removed using hydrofluoric acid, which also hydrogen-terminates the Si surface [79, 80].

Sputter deposition was carried out in the chamber described in 3.1.2, with base pressures of typically $\leq 1 \times 10^{-8}\,\text{mbar}$. A $99.99\,\%$ pure Cu target was DC sputtered at $50\,\text{W}$ with a working gas of ultra-high-purity argon at a pressure of $4.0 \times 10^{-4}\,\text{mbar}$, resulting in a deposition rate of approximately $0.25\,\text{Å/s}$. Prior to deposition, the substrate temperature was adjusted to the desired value and allowed to stabilise for approximately $2\,\text{h}$.

6.2.2 Sample Analysis Results

The influence of the film thickness and of the substrate temperature during the deposition process on the epitaxial quality were investigated.

Influence of Deposition Parameters onto Epitaxial Quality

Out-of-plane XRD measurements in the range $45°$ to $72°$ in 2θ of two Cu films with a constant film thickness of approximately $65\,\text{nm}$ are shown in figure 6.1 for substrate temperatures of $T = -30\,°\text{C}$ and $T = 200\,°\text{C}$ (these being the minimum and maximum in the investigated temperature range). The observed intensity at $2\theta = 50.6°$ corresponds to the Cu(200) reflection. At only slightly elevated temperatures ($T = 200\,°\text{C}$) this reflection vanishes and a reflection at $2\theta = 64.9°$ can be observed, corresponding to the (003) reflection of η-Cu$_3$Si, indicating that a Cu silicide phase is formed.

The effect of increasing the Si substrate temperature on the FWHM of the out-of-plane rocking scans as a measure for the corresponding epitaxial quality is shown in figure 6.2. In the case of deposition at room temperature, the effect of the Cu thin film thickness is given in figure 6.3. In both figures exponential fits to the experimental data are also given.
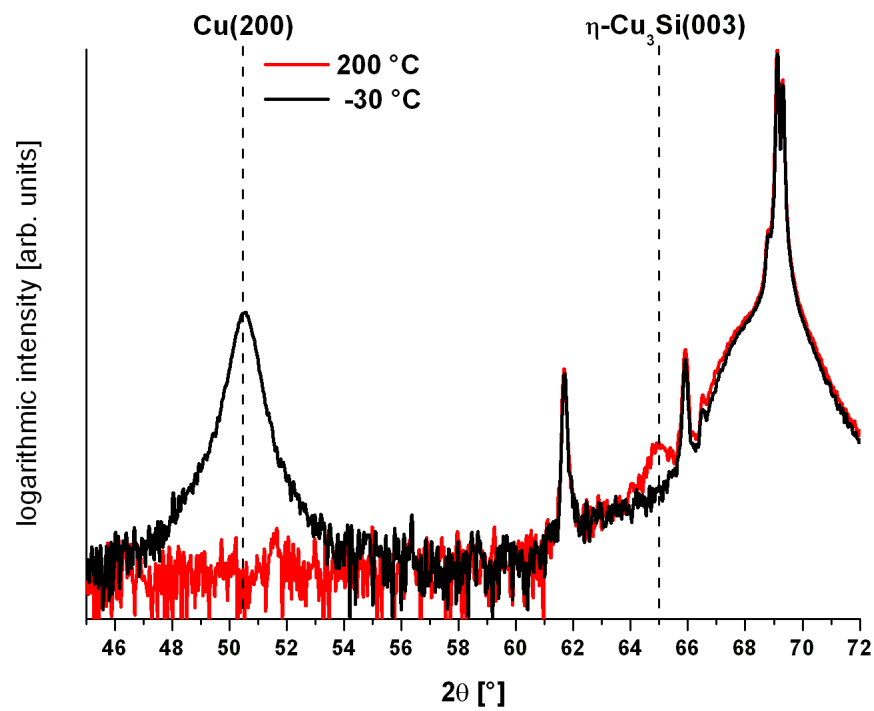
Figure 6.1: *Out-of-plane XRD scans for two substrate temperatures during deposition. For the Cu film deposited at a substrate temperature of $T = -30\,^{\circ}C$ only a Cu(200) out-of-plane reflection is visible. A Cu film made with identical deposition parameters but at a substrate temperature of $T = 200\,^{\circ}C$ shows only a $\eta\text{-}Cu_3Si$ phase.*
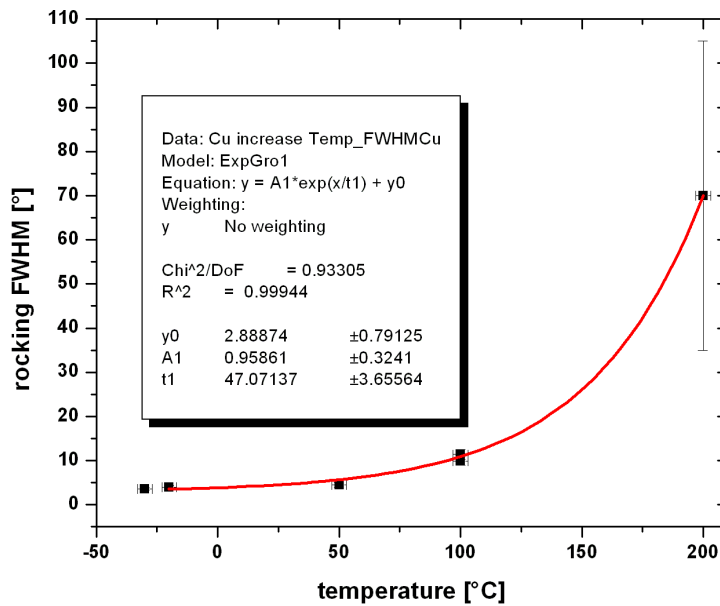
Figure 6.2: *Effect of the substrate temperature during the deposition process on the epitaxial quality of the Cu films plotted together with an exponential relationship. The parameters of the mathematical fit are given in the inset.*
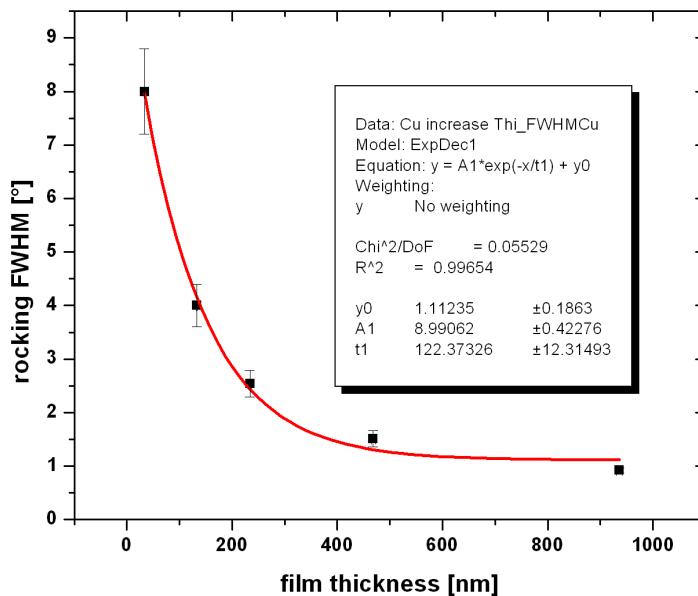
Figure 6.3: *Effect of the film thickness on the epitaxial quality of the Cu thin films which were deposited at room temperature, plotted together with a fitted exponential relationship. The parameters of the mathematical fit are given in the inset.*
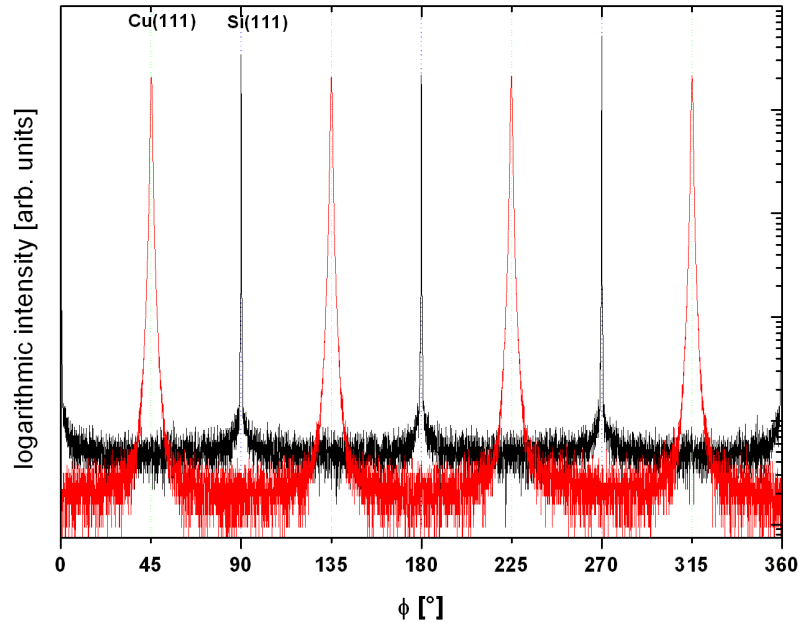
Figure 6.4: *In-plane XRD scans for Si(111) and Cu(111) taken at an inclination of $\chi = 57.54°$ relative to the (100) crystal directions. The rotation of the Cu crystal by $\Delta\phi = 45°$ to the Si single crystal substrate is clearly visible.*

An in-plane ϕ-scan of the Cu thin film sample with best epitaxial Cu(200) out-of-plane quality for Si(111) and Cu(111) reflections is shown in figure 6.4. A clear fourfold symmetry of the Cu(111) in-plane reflection is observed 45° to the Si(111) substrate peaks, showing a clear epitaxial relationship of Cu[100]‖Si[110] and Cu(001)‖Si(001).

6.2.3   Discussion

The epitaxial growth of Cu on Si(100) by DC magnetron sputtering has been discussed in detail in [72]. Also, the formation of a silicide phase at elevated temperatures by interdiffusion is a well known phenomenon [81]. Judging by the results, an elaborate cooling of the substrate is not necessary as the epitaxial quality of the room temperature-deposited Cu film is nearly identical to the quality of films deposited at lower temperatures (figure 6.2). An increasing film thickness (figure 6.3), on the other hand, also improves the epitaxial quality of the Cu layer, indicating that a thicker Cu seed layer contributes to a higher quality epitaxial growth of subsequent metal layers. This can be explained by the relaxation of the crystal structure in thicker films. The balance between the required quality and production effort for MMES was therefore investigated with an additional epitaxially grown Ni layer and is described in the following section.

6.3   Metal-Metal-Epitaxy of Ni on Si(100)

6.3.1   Thin Film Preparation

The Si(100) substrates were prepared identical to those described in 6.2.1. One of the available sputter guns of the sputter deposition chamber described in 3.1.2 was equipped with a 99.99 % pure Ni sputter target at a distance of 25 cm from the substrate. The second sputter gun was fitted with a 99.99 % pure Cu target and located 40 cm from the substrate surface. Substrate temperature was not monitored or intentionally regulated. The available shutter system was used to switch between the materials and to control the film thickness. Cu was DC sputtered at 50 W with 3.75 sccm of working gas of ultra-high-purity argon at a pressure of 4.0×10^{-4} mbar at a deposition rate of 0.25 Å/s. Ni was DC sputtered at 50 W with 10 sccm working gas of ultra-high-purity argon at a pressure of 8.0×10^{-4} mbar and a deposition rate of 0.2 Å/s.

6.3.2   Sample Analysis Results

Influence of Seed Layer Thickness on the Epitaxial Quality

Out-of-plane XRD measurements in the range 42° to 54° in 2θ of the prepared bilayers with variable Cu seed layer thickness and a Ni layer of 75 nm are shown in figure 6.5.

The observed peaks at $2\theta = 44.5°$ and at $2\theta = 51.8°$ correspond to the Ni(111) and Ni(200) reflections, respectively. The peaks at $2\theta = 50.6°$ correspond to the Cu(200) reflection of the seed layer. With increasing seed layer thickness the intensities of the Ni(111) reflections vanish at a seed layer thickness of approximately 4 nm and the intensity of the Ni(200) reflections increases significantly. This demonstrates that MMES of Ni(200) on Si(100) can be achieved by DC magnetron sputtering. With further increasing thickness of the Cu seed a concurrently reduced improvement in the epitaxial quality of Ni is observed, following an exponentially decreasing curve as shown in figure 6.6.

In-plane XRD measurements of the sample with the lowest out-of-plane FWHMs of both Cu and Ni (figure 6.7) confirm the epitaxy and give the epitaxial relationship between the layers with Ni[100]‖Cu[100]‖Si[110] and Ni(001)‖Cu(001)‖Si(001).

6.3.3   Discussion

The epitaxial growth of Ni on Cu/Si and the observed epitaxial relationship are well known [75, 82, 83] and are mainly due to the identical fcc crystal structure and a small lattice mismatch, as the lattice parameters of Cu (3.615 Å) and Ni (3.524 Å) are very similar. The fact that a thicker seed layer thickness benefits the epitaxial quality of Ni can be explained by the fact that less lattice stress from the early stages of Cu growth on Si influences the subsequent Ni layer. The reproducibility of MMES using the sputter deposition chamber available at GKSS allowed for the first attempts at nano-structuring epitaxial Ni layers. The attempted preparation and structuring process is given in appendix A. However, as the argon ion beam milling
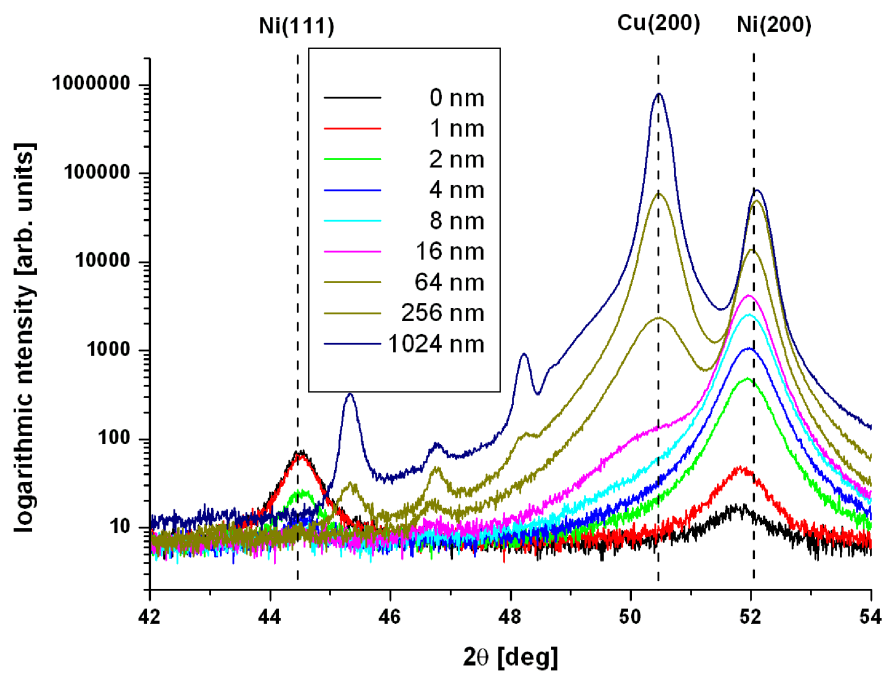
Figure 6.5: *Out-of-plane XRD scans as a function of the epitaxial Cu seed layer thickness as given in the legend. A clear switch from polycrystalline growth of Ni to an epitaxial out-of-plane growth of Ni(200) occurs at a Cu seed layer thickness of 4 nm and an increase in the thickness of the seed layer improves the epitaxial quality.*
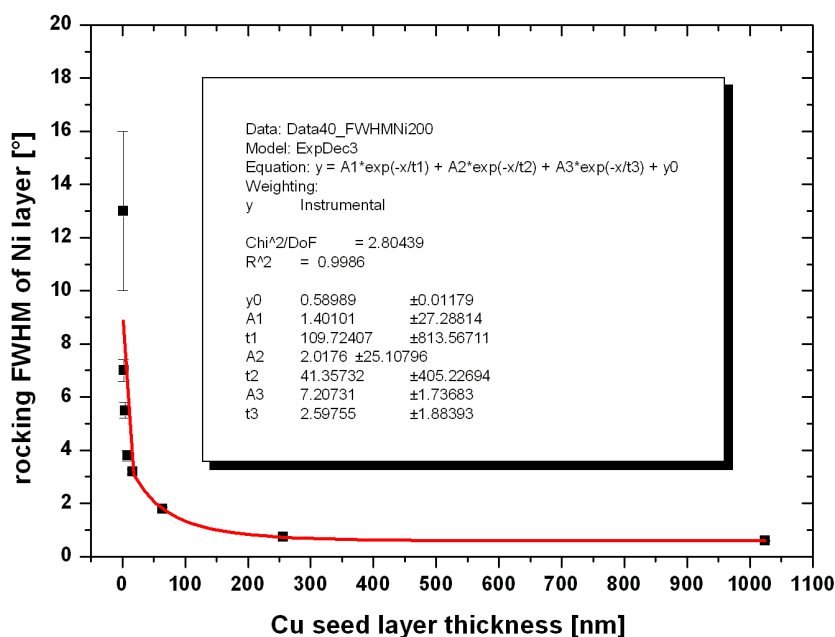
Figure 6.6: *The FWHM of out-of-plane rocking scans taken of the Ni(200) diffraction peak. The mosaic spread decreases exponentially with the Cu seed layer thickness and is fitted using the parameters given in the inset.*
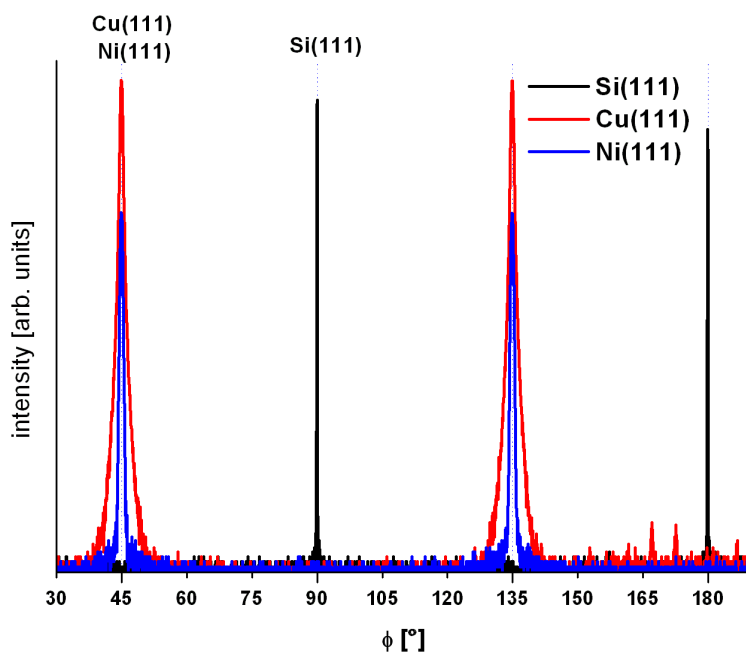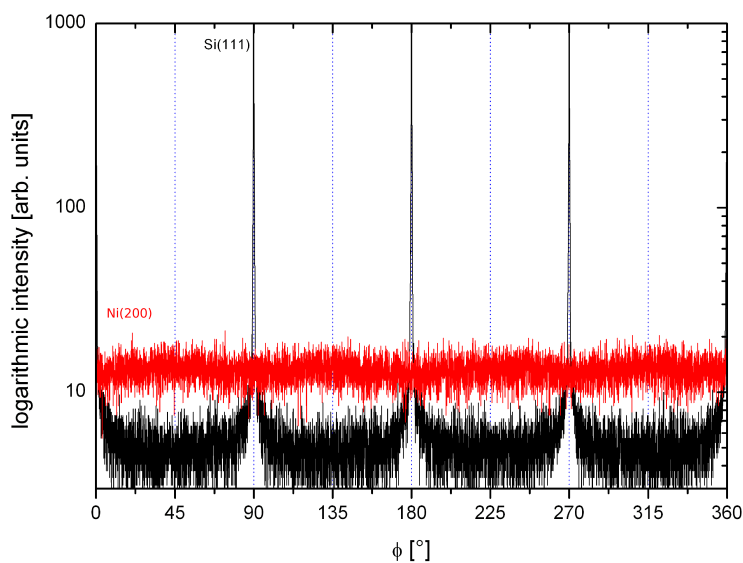

Figure 6.7: *The in-plane XRD scans for Si(111), Cu(111) and Ni(111) taken at 54.74° inclination to the (100) plane of the Si substrate. For reasons of clarity only a limited ϕ-range is shown. The in-plane orientation of Ni follows that of the Cu seed layer with $\Delta\phi = 45°$ relative to the Si(111) direction.*

process in a preparatory step was found to destroy the epitaxy (figure A.1), MMES was rendered useless for the intended application and a new method for the epitaxial deposition of Ni on Si was developed as is described in the following section.

6.4 Epitaxial Growth of Ni on Si(100) by DC Magnetron Sputtering

6.4.1 Thin Film Preparation

A Si(100) wafer was prepared as described in 6.2.1 and deposition was carried out using the GKSS sputter deposition system (3.1.2). A bakeable substrate holder and the indirect cooling method were used.

One of the available sputter guns, located $25\,cm$ from the substrate, was fitted with a $99.99\,\%$ pure Ni sputter target, which was DC sputtered at $50\,W$ with a working gas of ultra-high-purity argon at a pressure of $8.0 \times 10^{-4}\,mbar$, resulting in a deposition rate of $0.2\,\text{Å/s}$.

The prepared specimens can be categorised as either continuously deposited with constant substrate temperature (type 1), or as a two step deposition procedure in which the substrate temperature is varied (type 2).

6.4.2 Sample Analysis Results

Type 1 Samples

Out-of-plane XRD measurements in the range $42°$ to $54°$ in 2θ of type 1 Ni films of thickness $75\,nm$ are shown in figure 6.8 as a function of the substrate temperature. The observed peaks at $2\theta = 44.5°$ and at $2\theta = 51.8°$ correspond to the Ni(111) and Ni(200) reflections. At highly elevated temperatures ($T > 700\,°C$) peaks at $2\theta = 42.4°$ and $2\theta = 53.4°$ can be observed. These correspond to the (310) and (320) reflections of orthorhombic δ-Ni_2Si, indicating that at temperatures above $700\,°C$ a nickel silicide phase is energetically favoured over the growth of a separate Ni phase.

Figure 6.8 clearly shows a maximum in the Ni(111) peak intensity with a corresponding minimum in the FWHM of the respective rocking curve at around $350\,°C$. Increasing substrate temperatures cause the disappearance of the out-of-plane Ni(111) peak and the formation of a Ni(200) peak with maximum intensity and minimum FWHM of the rocking curve at a substrate temperature of $625\,°C$. The intensities (figure 6.8) and calculated (equation 6.1) coherence length of the Ni(200) reflections (figure 6.9) are significantly smaller than those observed for the Ni(111). Even if the expected intensity factor of the Ni(200) peak of only 0.4 compared to that of the Ni(111) peak is taken into account, these observations clearly indicate that the out-of-plane texture of the Ni(200) is less pronounced than that of the Ni(111) directions.

Figure 6.10 shows the in-plane scan for the Si(111) substrate peak and the Ni(200) film peaks for the Ni(111) textured film deposited at $350\,°C$. The four-fold symmetry, typical for a cubic system, of the Si(111) reflections is clearly seen;
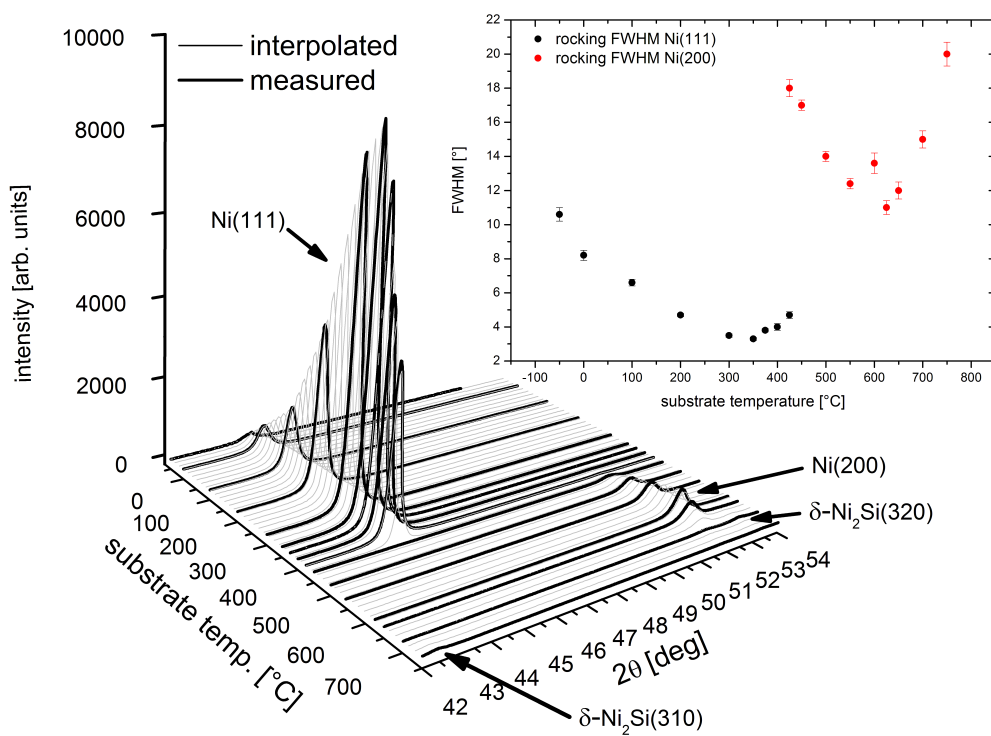
Figure 6.8: *Out-of-plane Ni-film XRD scans as a function of the substrate temperature during deposition. The inset graph gives the FWHM values of the corresponding out of plane rocking scans for the Ni(111) and Ni(200).*
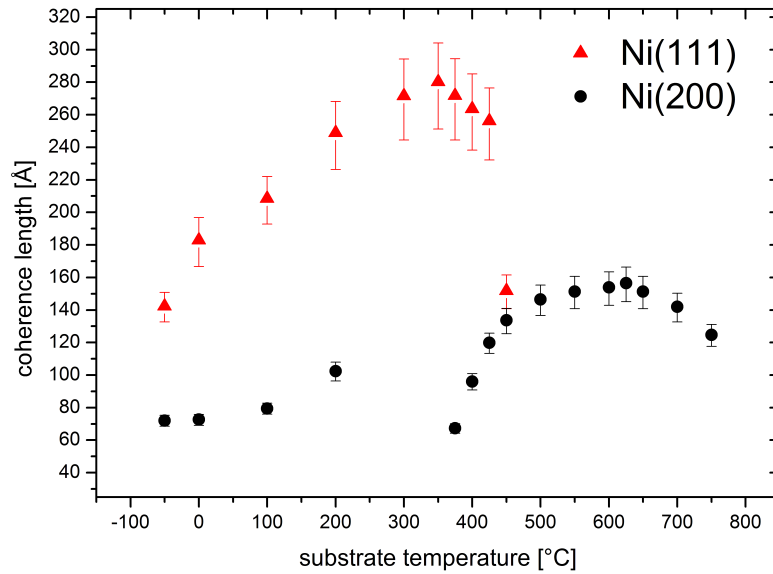
Figure 6.9: *Coherence length values as a function of the substrate temperature during the deposition process as obtained from the out-of-plane XRD scans. The graph gives the coherence length values of both the Ni(111) and Ni(200) components.*

however, no Ni(200) in-plane reflections were observed, showing that the grains are randomly oriented in-plane and thus the epitaxial growth of Ni(111) on Si(100) is not achieved.

In-plane ϕ-scans of the type 1 sample with Ni(200) out-of-plane texture (substrate temperature: 650 °C) for Si(111) and Ni(111) reflections are shown in figure 6.11. In contrast to the Ni(111) textured films, a clear fourfold symmetry of the Ni(111) in-plane reflections is observed with an offset angle of 45° to the Si(111) substrate peaks, demonstrating that Ni grows epitaxially on the Si(100) surface with the relationship Ni[100]‖Si[110] and Ni(001)‖Si(001). However, the observed Ni(111) reflections split into two peaks, indicating the presence of twinning or the possible formation of small angle grain boundaries [84, 85]. The splitting is $\Delta\phi = 2.3°$ to either side of the expected Ni(111) peak positions. The out-of-plane rocking scan for this sample is shown in the inset in figure 6.12, showing a splitting of $\Delta\omega = 4.5°$ from the Ni[001] direction.

Type 2 Samples

A significant improvement in the epitaxial quality of Ni(200) could be achieved by depositing the Ni layers in two steps. The deposition parameters and the corresponding rocking scan FWHM values of the Ni(200) peaks are summarised in table 6.1 together with the coherence lengths. Although the coherence length values of the type 2 Ni(200) samples are mostly above those of the type 1 Ni(200) samples, there is no clear trend observable from which ideal deposition parameters for epi-

Figure 6.10: *In-plane XRD scans for Si(111) and Ni(200) taken at 54.74° inclination to the (100) plane of the Si substrate. For growth parameters which favour a strong Ni(111) out-of-plane texture, no in-plane Ni(200) peak is visible, revealing that this direction does not grow epitaxially on a Si(100) substrate.*
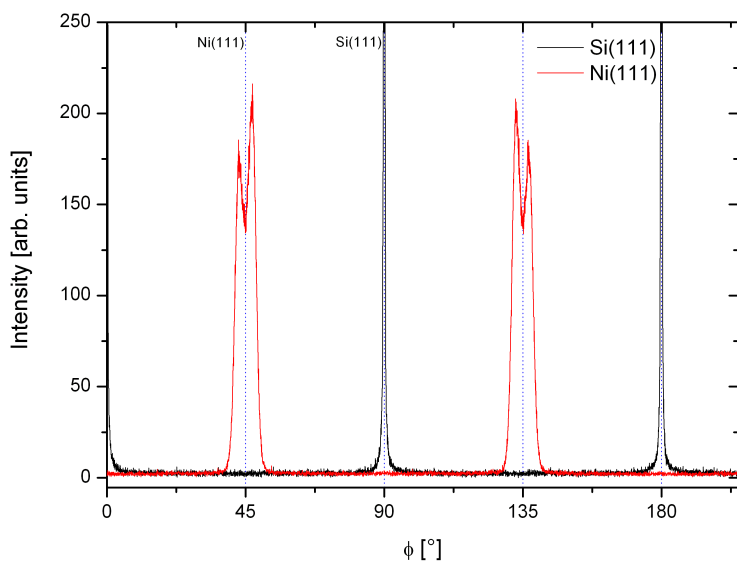
Figure 6.11: *In-plane scans with $\chi = 54.74°$ for Ni(111) and Si(111) for the sample deposited at $650°C$. For reasons of clarity, only a limited ϕ-range is shown.*

Table 6.1: *The out-of-plane FWHM of the Ni(200) rocking scan peaks of 75 nm thick Ni films with a total deposition time of 3600 s. Shown are the temperature (T_1) of the first higher temperature Ni deposition step, the temperature for the low temperature (T_2) phase and the deposition times (t_1, t_2) of the high and low temperature deposition as well as the coherence length (L) as obtained from the diffraction scans. The ideal deposition parameters for the lowest rocking FWHM found are underlined in the table.*

T_1 [°C]	t_1 [s]	T_2[°C]	t_2 [s]	$L_{Ni(200)}$ [Å]	$FWHM_{Ni(200)}$ [°]
550	200	325	3400	135	16.4 $\left(^{+0.6}_{-0.6}\right)$
644	200	325	3400	181	2.24 $\left(^{+0.04}_{-0.03}\right)$
662	200	325	3400	178	2.20 $\left(^{+0.05}_{-0.03}\right)$
700	200	325	3400	188	2.23 $\left(^{+0.04}_{-0.04}\right)$
750	200	325	3400	185	2.24 $\left(^{+0.04}_{-0.05}\right)$
662	200	175	3400	181	2.23 $\left(^{+0.05}_{-0.04}\right)$
662	200	212	3400	174	2.23 $\left(^{+0.04}_{-0.04}\right)$
<u>662</u>	<u>200</u>	<u>250</u>	<u>3400</u>	<u>185</u>	<u>1.98</u> $\left(^{+0.05}_{-0.07}\right)$
662	200	287	3400	185	2.16 $\left(^{+0.04}_{-0.04}\right)$
662	200	400	3400	196	2.24 $\left(^{+0.03}_{-0.05}\right)$
662	100	250	3500	165	2.80 $\left(^{+0.06}_{-0.05}\right)$
662	300	250	3300	178	2.46 $\left(^{+0.05}_{-0.05}\right)$
662	400	250	3200	132	7.3 $\left(^{+0.3}_{-0.2}\right)$

taxial growth could be concluded. However, the rocking FWHM values give a clear indication for the epitaxial quality. The XRD patterns obtained for the highest quality out-of-plane Ni(200) growth and the corresponding rocking scans are shown in figure 6.12 and its inset graph.

In-plane scans (figure 6.13) show a fourfold symmetry with Ni(111) peaks at 45° to the Si(111) substrate peaks. In contrast to the type 1 samples, no splitting of the intensity is observed, indicating higher quality epitaxial growth.

The interface quality was assessed by XRR. The data and a theoretical fit are shown in figure 6.14. The model consists of three layers as indicated in the caption. Attempts were also made to fit a four-layer model that included an additional silicide layer between the Ni and the substrate to account for the two step deposition process of the Ni film; however, the data shows better agreement using the three-layer model, indicating that Ni grows as a single layer on Si.

Corresponding PNR data collected in a magnetic field of 80 mT at room temperature for the as-prepared Ni sample in a reciprocal space range of $Q_z = 0.01$ Å^{-1} to $Q_z = 0.09$ Å^{-1} are shown in figure 6.15. The corresponding MOKE measurement are given in the inset graph. The square-like magnetisation behaviour with sharp flipping fields symmetrically at approximately 20 mT indicates that the remagnetisation of the sample occurs completely at low magnetic fields in a single domain state. In PNR data a clear splitting of the spin-up and spin-down reflectivity curves is observed. By fitting the reflectivity using the standard PARRATT algorithm with $n_{Ni} = 9.14 \times 10^{-2}$ Å^{-3} and $\lambda = 4.335$ Å, the optimised value of the magnetic mo-
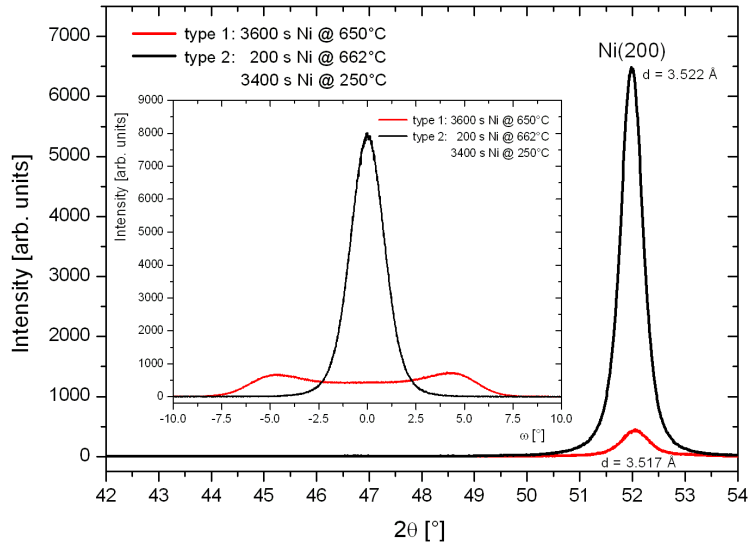
Figure 6.12: *Out-of-plane XRD scan for the Ni(200) peak for the highest quality type 2 sample (with d = 3.522 Å). For comparison, the type 1 XRD scan of the sample which was deposited at a substrate temperature of 650 °C is also shown (d = 3.517 Å). The inset graph gives the corresponding out-of-plane rocking scans.*
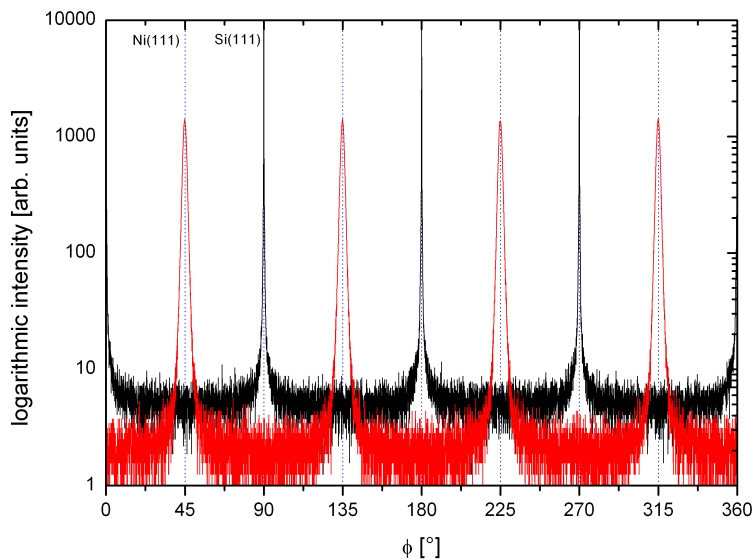

Figure 6.13: *In-plane XRD scans for Si(111) and Ni(111) taken at 54.74° inclination to the (100) plane of the Si substrate.*
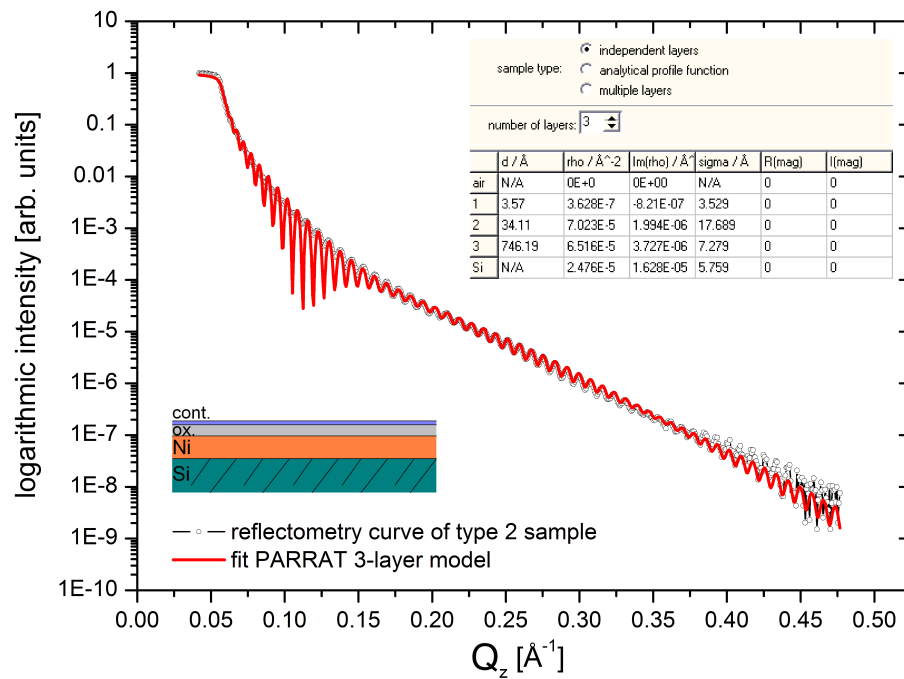
Figure 6.14: *X-ray reflectometry data for the type 2 sample of best epitaxial quality. A three-layer model was simulated. Starting from the surface, the first layer corresponds to an undefined contamination (e. g. condensed moisture from the air). The second layer can be interpreted as an oxidised Ni-to-air interface layer; the third next layer is the unoxidised Ni layer which is in direct contact with the Si substrate. The inset shows the fitting parameters.*
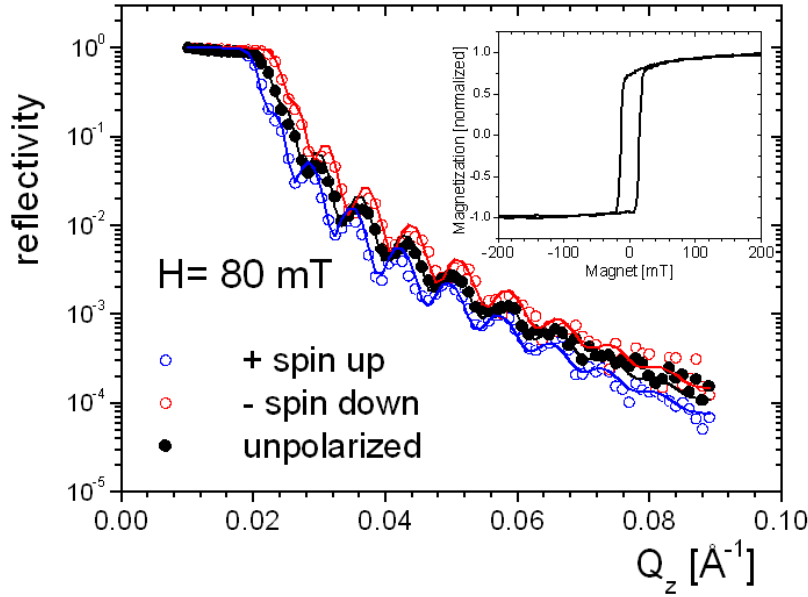
Figure 6.15: *Unpolarised and polarised neutron reflectometry data points and fitted reflectivity curves (line) on sample 2H at a field of $H = 80\,mT$. The inset graph shows the corresponding MOKE measurement.*

ment of the Ni in the thin layer can be determined as $\mu = 0.6\mu_B$ which is identical to the bulk value of ferromagnetic Ni [86]. Moreover, the reflectivity curves can be simulated best by assuming a homogeneous magnetisation profile throughout the Ni layer and emphasise the excellent magnetic property of this epitaxial thin film of Ni on Si. Hence, it is also concluded that the magnetic thickness of the Ni layer is identical to the structural thickness.

6.4.3   Discussion

Due to its novelty, the epitaxial growth of Ni on Si(100) by DC magnetron sputtering is discussed in detail.
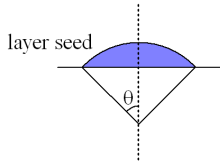
Silicide Formation

Potential formation of a silicide layer at the Si/Ni interface is an important issue and should be addressed. The literature shows for photoemission/Auger and ion scattering techniques [69, 87, 88] that nickel silicide formation takes place at the Ni to Si substrate interface for temperatures above $200\,^{\circ}C$, typically extending over approximately 10 mono-layers (ML). As the temperatures used in this study are well above this, silicide formation is to be expected, at least in the early stages of deposition. However, a silicide layer of only a few nm is too small to give sufficient phase diffraction signal for detection with conventional laboratory XRD methods. There

were no nickel silicide phases detectable below a deposition temperature of $700\,°C$ for type 1 samples and neither XRD nor XRR showed evidence for the presence of a silicide phase in the type 2 samples where an interface layer was assumed in an attempt to fit a four-layer model to the XRR data, giving a poorer fit than the simplier model (figure 6.14). The possible existence of an interface phase can therefore only be clarified by other methods such as systematic cross sectional Transmission Electron Microscopy (TEM), but is beyond the scope of this project. However, as there was no epitaxial growth of Ni at temperatures above $700\,°C$ at which nickel silicide phases were present (figure 6.8), it is concluded that a potential nickel silicide layer negatively influences epitaxy and must therefore be limited to a few atomic layers or would otherwise destroy the epitaxial growth. Although the existence of such a silicide phase could not be clarified with the applied methods and was also not in the focus of this study, there is no evidence that its potential presence influences the epitaxial growth of Ni on Si. For the following dicussion, it can therefore be assumed that a potential silicide phase is negligible.

Type 1 Samples

There are a number of thermodynamic models for the growth of a thin layer on a substrate. Capillary theory [84, 89] describes it by the preference for the Gibbs free enthalpy (G) to reach a minimum state with the free nucleation enthalpy given by

$$\Delta G = \Delta G_v a_1 r^3 + a_2 r^2 \gamma_{vl} + a_3 r^2 \gamma_{ls} + a_3 r^2 \gamma_{sv} \qquad (6.2)$$

where v stands for "vacuum", l for "layer" and s for "substrate". γ is the specific interface energy as derived from geometrical considerations. $a_1 = 2\frac{1}{3}\pi(2 - 3\cos\theta + \cos^3\theta)$, $a_2 = 2\pi(1 - \cos\theta)$, $a_3 = \pi\sin^2\theta$ and θ is the opening angle of the spherical sector of each layer seed. The theory does not include any lattice match but the Si surface is regarded as flat. Therefore, it cannot explain the observed epitaxial growth, but gives a satisfactory explanation for the observed polycrystalline and highly textured Ni(111) out-of-plane growth.

For the epitaxial growth of Ni on Si an epitaxial lattice rule match is employed based on the assumption that epitaxial growth takes place if the substrate and film structures have a similar lattice constant.

Textured Growth of Ni(111):

The tendency to grow in a closest-packed direction is well known for various metals [90–92]. At low substrate temperatures, one can assume that the adsorbates do not have sufficient energy to diffuse large distances on the surface after their arrival at the substrate. In the capillary theory this case corresponds to the situation in which

$$\gamma_{sv} < \gamma_{ls} + \gamma_{vl}\cos\theta \qquad (6.3)$$

which is the case if

$$\theta > 0$$

[93]. Therefore, adatoms form small nuclei whose diffusion on the surface is low. Consequently, in the first stages of film growth various crystal orientations occur and can persist. This sufficiently explains the observed film growth of polycrystalline Ni films at low temperatures.

With increasing deposition temperature the diffusion length of the adatoms also increases until a wetting of the entire surface takes place with the Young equation of the capillary theory being fulfilled

$$\gamma_{sv} = \gamma_{ls} + \gamma_{vl} \cos \theta \tag{6.4}$$

which is the case if

$$\theta = 0.$$

[93]. This means that the previous Volmer-Weber (island) growth which was favoured for lower deposition temperatures also changes to a Frank-van-der-Merve (layer-by-layer) growth [94]. This naive point of view is sufficient to explain the (with the substrate temperature increasing) Ni(111) out-of-plane texture without a long-range epitaxial in-plane correlation. In this context the sample with the most pronounced Ni(111) texture corresponds to the case in which perfect wetting of the Si substrate takes place.

Further increasing the substrate temperature denotes that the Young equation of the capillary theory can no longer be fulfilled, as the situation would become

$$\gamma_{sv} > \gamma_{ls} + \gamma_{vl} \cos \theta. \tag{6.5}$$

[93]. Hence γ_{ls} and γ_{vl} would need to be density dependent or additional energy terms need to be introduced. In this situation Stranski-Krastanov (mixed island and layer by layer) growth [94] is expected to take place and can also be used to explain the steep decrease in the Ni(111) texture after its maximum as was observed in the present case.

Growth of Defect Rich Ni(200) on Si(100):

With sufficient energy present in the system (i. e. sufficiently elevated substrate temperature), one has to take the atomic structure of the substrate into account. In this scope, it would be very interesting to perform ab initio calculations in the style of [95], but would be beyond the scope of this work. However, the phenomenological lattice match rule is sufficient to explain the results.

Si has a diamond structure and Ni an fcc structure. The uppermost unreconstructed atomic layer of the Si(100) surface consequently has a quasi-2D rectangular structure with an expected bulk lattice spacing of $5.431\,\text{\AA}$. Ni has a bulk lattice constant of $3.524\,\text{\AA}$. This results in a lattice mismatch of $54\,\%$ along the {100} axes and hence is much larger than the commonly accepted figure of approximately $10\,\%$ as an upper limit for epitaxial growth. The lattice mismatch decreases to $9\,\%$ if Ni[100] arranges parallel to the Si[110] direction, which results in a 45° rotation around the [001] axis of silicon. This rotation was observed experimentally by the in-plane XRD scans (figure 6.11) and therefore gives a satisfactory explanation for the epitaxial relationship. This relationship was also reported [72] and previously
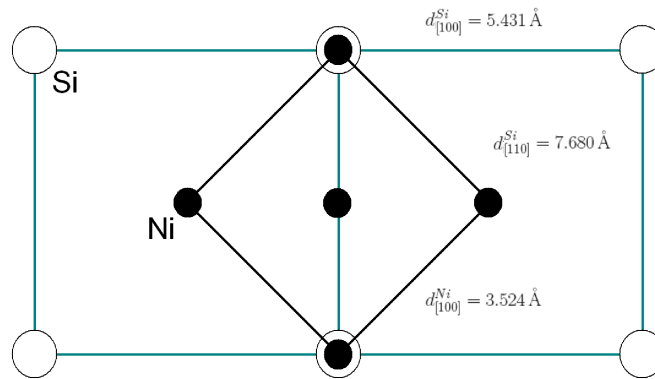
Figure 6.16: *The epitaxial relationship of Ni to the Si(100) substrate. Shown is the last atomic layer of the Si substrate and the first atomic layer of the deposited Ni with their d-spacings of $d_{Ni(100)} = 3.524\,\text{Å}$, $d_{Si(110)} = 7.680\,\text{Å}$ and $d_{Si(100)} = 5.431\,\text{Å}$. This relationship can directly explain the observed $45°$ rotation angle of the Ni layer crystal relative to the Si(100) substrate.*

reproduced (section 6.2) for sputter deposited Cu. The idealised situation on the Ni/Si interface is therefore as sketched in figure 6.16.

The high temperatures of about $650\,°\text{C}$ are apparently necessary and favour the initial stages of the epitaxial growth discussed above of Ni(200) on Si(100) where heteroepitaxy takes place. However, with the first few atomic Ni layers the surface properties significantly change as the newly arriving Ni adatoms start to grow on the already deposited Ni as their new substrate. Consequently, the adjusted deposition parameters for the growth of Ni on Si are no longer optimal for the epitaxial growth of Ni on Ni.

Assuming that with increasing Ni seed layer thickness the mobility of newly arriving adatoms also increases, the occurrence of the observed crystal defects can be explained. Ideally, newly arriving atoms would diffuse on the surface until they reach a minimum energy state. At highly elevated temperatures, present in the case of type-1 Ni(200) samples, an atom might simply fall into a state where its energy is only a local approximation to the global minimum. There it can act as a nucleation centre for increasingly larger islands. It is known that with an increased mobility on the surface, atoms have a tendency to form larger and less numerous nucleation centres than in the case of less surface mobility [96].

Due to the non-minimised energy state, these larger islands form at random locations. Consequently, they do not all have the same lattice alignments and therefore a misfit at the moment of coalescence exists. If the islands were small they would rotate or change their position at the point of coalescence to accomodate for the misfits, but larger islands are already too immobile to do this. Hence, crystal defects like the observed small angle grain boundary related pattern persist if the film growth takes place at too-high temperatures. Such crystal defects then minimise the energy of the over-all system [84, 85]. This can adequately explain the structure of the type-1 samples with Ni(200) out-of-plane texture. The observed splitting in the rocking scan (inset of figure 6.12) of $\Delta\omega = 4.5°$ in either direction from the Ni[001]

out-of-plane direction thus gives the out-of-plane angle between the reflecting planes and corresponds to an average lattice displacement of one additional or missing atom per ten atomic layers.

Type 2 samples

Based on the explanations for the growth of Ni on Si(100) as a function of substrate temperature and the corresponding adatom diffusion mobility, one can also explain the observed increase in epitaxial quality of out-of-plane Ni(200) on Si(100) if deposited in two steps. By stopping the growth process after the first step and by cooling to more favourable temperatures for the epitaxial growth of Ni on Ni, one can remove excess energy from the system and with it the too-high adatom mobility. This avoids the formation of crystal defects and leads to the observed higher quality of epitaxial growth (figure 6.13).

The interrupted deposition of Ni on Si also raises the question of whether contamination takes place at the interface between the Ni seed and the successively deposited Ni. At the deposition parameters used (base pressure: 1×10^{-8} mbar; time between deposition steps: 2 h), this would be expected as the required time for the contamination of an atomically clean surface with one atomic layer of undefined residual gas adsorbates can be roughly estimated (by applying the kinetic gas theory and assuming a sticking coefficient of one) by

$$P \times t \approx 10^{-6} \, \text{mbar} \cdot \text{s} = const \tag{6.6}$$

where P is the Pressure (in mbar) and t the time (in s) [97]. This would mean that in the 2 h for which the deposition was interrupted between the Ni seed and the remaining Ni layer, an approximately 70 ML thick (and hence detectable) contamination layer of unknown composition would be expected; yet, XRD and XRR show no evidence of such a contamination. This may be a result of desorption processes that take place simultaneously. Desorption is strongly temperature dependent and at the elevated temperatures of the substrate can significantly counteract the adsorption processes [97]. The situation on the Ni seed to Ni layer interface is, however, currently only speculated and must be investigated further. It should also be noted that due to restrictions in the experimental setup (no active cooling of the substrate) the cool-down time could not be reduced. However, a shorter cool down phase after the deposition of the initial Ni seed layer would only decrease the likelihood of potential contamination.

Despite its minor limitations, this newly developed deposition process is currently the only known way to deposit Ni epitaxially directly on Si with the achieved quality [LOP-2] and its development marks an important contribution to applied research. In this project it is utilised for the first preparation step of nanostructured single crystalline nanodot samples. The proof of concept for the preparation process is given in appendix A.

Chapter 7

Sample Preparation

For neutron scattering analysis of thin layered films a minimum sample size of $1\,cm^2$ is required. For laterally structured samples, this area must be significantly larger, as the structuring process reduces the amount of material on the sample surface. Depending on the size and separation of the surface structures, surface coverage can be as little as only a few percent. Thus it was the central goal of this project to produce samples providing a homogeneously structured area of several cm^2. The preparation parameters of nanostructured samples, fulfilling these requirements and which are suitable for neutron scattering analysis (chapter 8), are given in this chapter. However, preparing an area of several cm^2 of lateral submicrometer to nanometer structured samples is a challenging task and two approaches were followed for this work: one is a top-down structuring process using a laser interference lithography technique (3.3) and the other is a bottom-up method in which the desired structure is directly grown onto a pre-structured substrate (7.2 and 7.2.4).

7.1 Top-Down Structuring

Figure 7.1 shows schematically the steps carried out to produce nanostructured samples by structuring from the top to the bottom. Starting with a substrate, a continuous layer of the desired (magnetic) material is deposited by sputtering (3.1) and structured by laser interference lithography (3.3). Transfer of the photoresist pattern into the underlying thin film is performed by means of argon ion beam milling (3.4). Without an underlying layer, this method can also be used to structure substrates (7.2.1).

Due to many demanding challenges in each step of the structuring procedure, the process was first optimised for samples of 5 mm diameter before it was systematically scaled to samples of 1 cm diameter and finally to a substrate sample size of 2.54 cm in diameter. Only the parameters for the largest sample are reported.

7.1.1 Ni Dot Array on a Si Substrate

Preparation of this sample was partially performed at GKSS Research Centre and University of Hamburg. The three main preparation steps, thin film deposition,
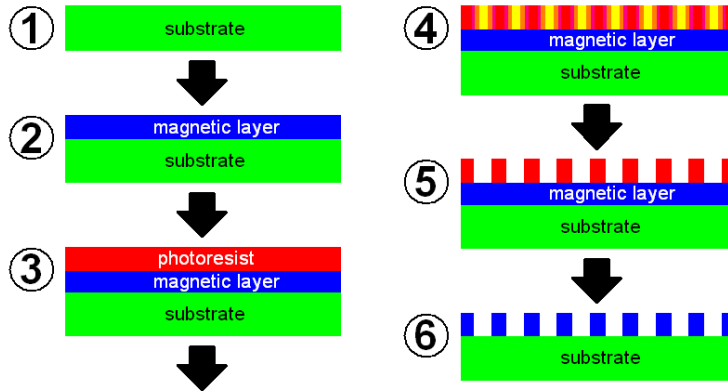
Figure 7.1: *Schematic of the top-down structuring process used for making samples for this work: starting with a substrate (1), a thin magnetic film is deposited (2), which is then spin coated with photoresist (3). This photoresist is exposed to interfering laser beams (4) and developed chemically, so that only a mask of photoresist remains on the thin magnetic layer (5). Then the mask is transferred by an etching process into the underlying film and a structured magnetic pattern remains on the substrate (6).*

preparation of the photoresist mask and the etching of the photoresist pattern into the underlying film are given in detail.

Thin Film Deposition

A circular Si(100) substrate of 2.54 cm in diameter was cleaned using the standard procedure of alternating ultrasonic baths of acetone and ethanol, followed by a rinse with de-ionised water and was blown dry using high purity nitrogen gas.

Deposition of a polycrystalline[1] 35 nm thick Ni film was carried out using the GKSS sputter deposition apparatus (3.1.2) with a base pressure of 1×10^{-7} mbar and an ultra high purity argon working gas pressure of 8×10^{-4} mbar. A 99.99 % pure Ni target was sputtered for 1800 s with 100 W at a substrate-to-target distance of 40 cm. This resulted in a deposition rate of approximately 0.2 Å/s.

Before removing the sample from the vacuum system a 3 nm thick TiN capping layer was deposited inside the airlock system by reactive sputtering of Ti in a mixed argon and nitrogen gas atmosphere. This was accomplished by a gas flow of 0.6 sccm of 99.99 % pure nitrogen with argon additionally admitted into the chamber through a needle valve for a total working pressure of 3.4×10^{-3} mbar. Ti was sputtered at 600 W with a deposition time of 30 sec.

---

[1]Until the completion of the project an epitaxially grown Ni nanodot sample could not be prepared successfully due to a missing endpoint detection scheme (see 4.4.1) in the sample preparation step of argon ion beam milling. However, proof of concept for structuring epitaxial Ni films, grown by utilising the epitaxial growth process described in 6.4, is given in appendix A. For the principal analysis which was carried out analogous to the epitaxial case, the polycrystalline structure of this Ni sample was of no concern.

Preparation of Photoresist Mask

The prepared Ni thin film on Si substrate was transported to the clean room at University of Hamburg where it was again cleaned with acetone and ethanol. As a first preparation step, the sample was spin-coated with 15 µl of Microchemicals TI PRIME primer at a ramp of 10000 rpm/s, a final rotating speed of 6500 rpm and a spinning time of 60 s. This was followed by a 15 min soft bake at 90 °C in a standard laboratory furnace. After 10 min of cool down, 15 µl of Microchemicals AZ MIR 701 I-line photoresist (diluted 1:1 with AZ EBR solvent) were applied with identical spin coating parameters. The coated sample was then given another 15 min soft bake at 90 °C and another cool-down phase of 10 min.

The coating procedure was followed by the exposure of the sample in the laser-interference lithography setup (3.3). The argon-ion-laser was operated at a current of 50 A giving a beam intensity of 0.54 mW measured directly before the beam splitter. Both deflection mirrors were placed approximately 36 cm from the beam splitter at 0° and 90° respectively to the primary beam direction. The distance of the sample holder (which holds the sample by a suction pump) to the beam splitter was set to 127 cm. On interference of the laser beams at the sample position this geometry gives a nominal lateral periodicity of 750 nm.

To avoid any disturbance of the process, the lithography room was exited during a pre-set 30 second delay countdown prior to the automatic shutter control activating a 27 second exposure. The sample was then rotated around its out of plane axis by 90° and a second exposure step was performed with identical parameters.

The sample was chemically developed for one minute in a bath of Microchemicals AZ 726 MIF developer followed by a one minute stop bath in de-ionised water. To dry the sample, it was placed on the spin coater and rotated with a programmed ramp-up of 400 rpm/s to a final rotation speed of 1500 rpm, at which stage it was carefully blown dry by hand using high purity nitrogen, working outwards from the centre. In order to increase the nitrogen flow and to avoid the formation of water stains or streaks during this process the distance of the hand-held nitrogen valve to the surface was decreased as a function of the drying state. This process, however, is an experience based parameter. Quality control for the prepared photoresist mask was performed by means of phase contrast light microscopy (figure 7.2).

Argon Ion Beam Milling

Argon ion beam milling (3.4) was performed at GKSS. The sample was clamped onto the provisional substrate holder (4.4.3) using two washers held by screws and mounted in the purpose-designed argon ion beam milling vacuum setup (4.2) such that the argon ions hit the sample surface at a 90° angle of incidence at a distance of 25 cm from the extraction grids of the ion gun. The process was carried out in two steps.

A first 15 min milling step was performed at a base pressure of 4.8×10^{-7} mbar and a gas flow rate of 0.3 sccm of standard house quality argon gas (99.9 % purity), which resulted in a working pressure of 3.5×10^{-4} mbar. The ion gun discharge current was at 0.38 A with a discharge voltage of 55 V; the beam current was 23 mA with 250 V of ion energy and the accelerator current was minimal at 1 mA and 290 V.
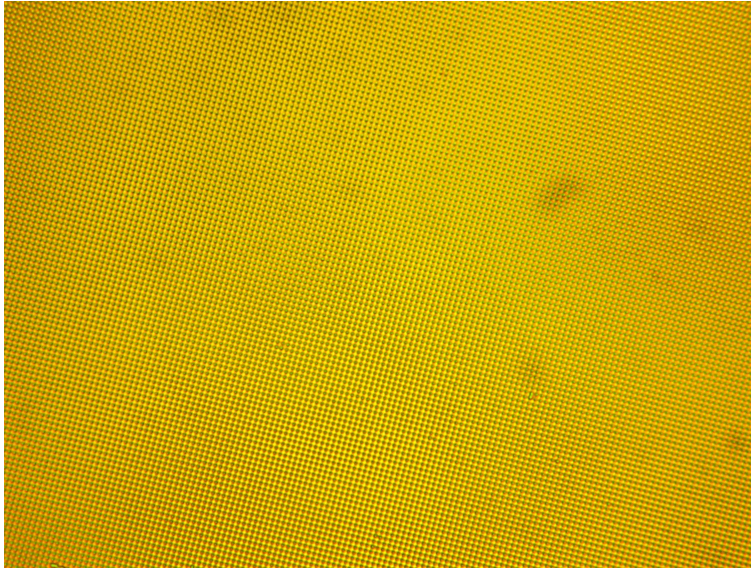
Figure 7.2: *Optical micrograph of the structured photoresist mask after double exposure and chemical development. This sub-micrometre structured dot pattern is transferred into the underlying film by physical etching. The darker regions, mainly visible in the right half of the picture, are due to dust particles on the microscope lenses and are not features of the photoresist mask.*

The ion gun power supply automatically regulated the neutraliser emission current to 28 mA with a corresponding neutraliser filament current of 2.43 A.

After the first step, the sample was allowed to cool down for approximately 12 hours before the chamber was vented and the progress of sample etching was examined. It was found that the sample resembled a continuous Ni layer and no longer showed traces of photoresist. However, the sample also refracted light as previously with the photoresist mask. It was hence concluded that the structure was successfully transferred into the Ni layer but the etching process had not yet progressed to the substrate.

A second etching run was carried out for another 15 min at a base pressure of 6.1×10^{-7} mbar and with an Ar gas flow of 0.48 sccm. This resulted in a working pressure of 3.8×10^{-4} mbar. A discharge current of 0.38 A at a discharge voltage of 55 V, a beam current of 23 mA and 250 V of ion energy, an accelerator current and voltage of 1 mA and 290 V, and an automatically controlled neutraliser emission current of 29 mA and a neutraliser filament current of 2.74 A were read on the power supply unit.

After this preparation step, the sample was again allowed to cool down overnight before it was removed from the vacuum chamber for sample analysis (8.1), which confirmed the intended sample structure. It should be noted that due to slight variations in the thickness of the photo resist mask of different samples, the argon ion beam milling process is not fully time controllable and also identical etching parameters do not precisely produce the same results. Only an endpoint detection mechanism (see 4.4.1) will eventually allow a reproducibility of the etching steps of sample preparation.

7.2 Sample Preparation by Bottom-Up Structuring

The other technique applied in this project for preparation of magnetic nanostructures is to grow nanowires by means of geometrical self shading on pre-structured substrates. For this purpose, the vacuum chamber described in 4.3 was designed and used for the deposition of Ni and Gd under the deposition geometry shown in figure 7.3 where the case for a pre-structured M-plane cut Al_2O_3 substrate is demonstrated. Additionally a lithographically pre-structured Si substrate was used (7.2.4). In this section, the structuring of the substrates and the subsequent nanowire deposition are described.
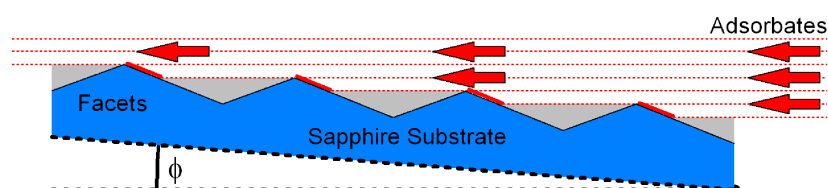
Figure 7.3: *Schematic of the bottom-up structuring process used for preparing samples for this work: starting with a pre-structured substrate, a thin magnetic film is deposited under a very shallow (< 5°) angle, so that certain parts of the substrate are shaded and deposition only occurs on the unshaded edges of the substrate.*

7.2.1 Structuring of Substrates

Prestructuring Process of M-plane Cut Al_2O_3 Substrate by Self Organisation

It is known [98, 99] that $(10\bar{1}0)$-cut (M-plane) Al_2O_3 forms a periodically faceted substrate surface if it is annealed for 24 h at temperatures of approximately 1500 °C to 1600 °C in air with the sides of the facets parallel to the $(1\bar{1}02)$ and the $(\bar{1}101)$ planes of the sapphire crystal.

Prior to annealing, an epipolished, $20 \times 20 \times 0.5\,mm^3$ large M-plane cut α-Al_2O_3 substrate was cleaned using acetone and ethanol. The substrates were then laid into coverable alumina crucibles and placed into a CARBOLITE$^©$ HTF 1700 high temperature furnace. This furnace was only used for this purpose and hence cleanliness of the process could be ensured. The annealing process was controlled by the custom written LabVIEW™ program described in section 4.1 and the temperature curve was logged to a text-file.

The annealing process gave best structuring results if the furnace was ramped to 750 °C, at 5 °C/min, followed by 30 min of dwell time after which the temperature was increased to 1500 °C at 10 °C/min. The temperature of 1500 °C was then held for 24 h before being reduced to 750 °C at 10 °C/min. After another 30 min the temperature was ramped to room temperature at 5 °C/min. A typical temperature curve of the annealing process is given in figure 7.4 showing the programmed and de-facto temperature curves.
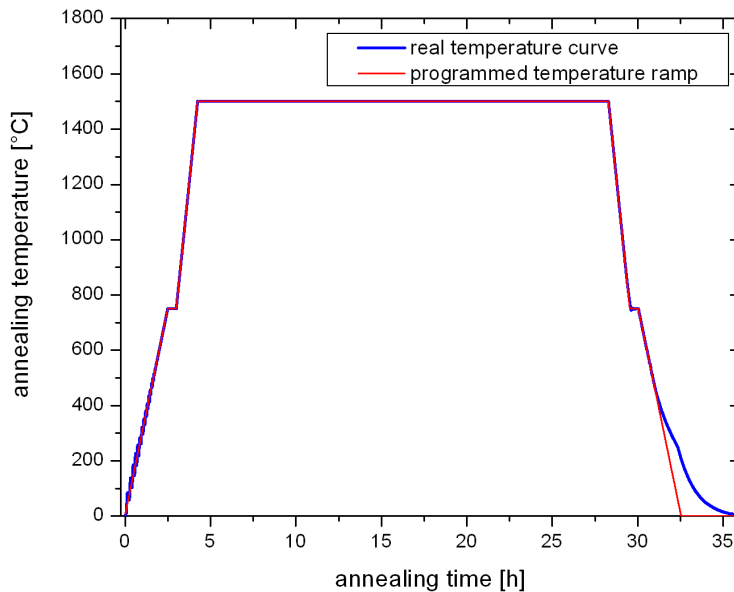
Figure 7.4: *Typical temperature curve for the annealing process of M-plane cut sapphire substrates.*

The faceting of each annealed substrate was verified by SEM imaging (5.1.1) and a typical micrograph is shown in figure 7.5.

Prestructuring Process of Silicon Substrates

The structuring process for a Si substrate was essentially identical to the process used in the preparation of the polycrystalline Ni nanodot array (section 7.1.1). This includes the use of Ti primer, the mixing ratio of photoresist and solvent, spin coating parameters, soft bake, chemical development of the photoresist after exposure and the drying procedure of the sample. As a wire pattern is desired, a minor difference lies in the fact that for the purpose of self shading the substrate is only single-exposed by laser interference lithography before the development process takes place. The exposure time was typically around 40 s at a laser beam intensity of approximately 0.45 mW. Figure 7.6 shows a photograph of a Si substrate with the structured photoresist refracting the light.

The photoresist structure was transferred into the Si substrate by an argon ion beam milling step of 15 min at typical base pressures of 5×10^{-6} mbar and a gas flow rate of 0.275 sccm, which resulted in a working pressure of 3.5×10^{-4} mbar. The ion gun operated with a discharge current of 0.28 A, a beam current of 23 mA, a corresponding neutraliser emission current of 29 mA and the beam voltage set to 250 V. The distance of the work piece from the extractor grids of the ion gun was 20 cm.

An AFM image and a height trace of the resulting surface of the Si substrate are shown in figure 7.7.
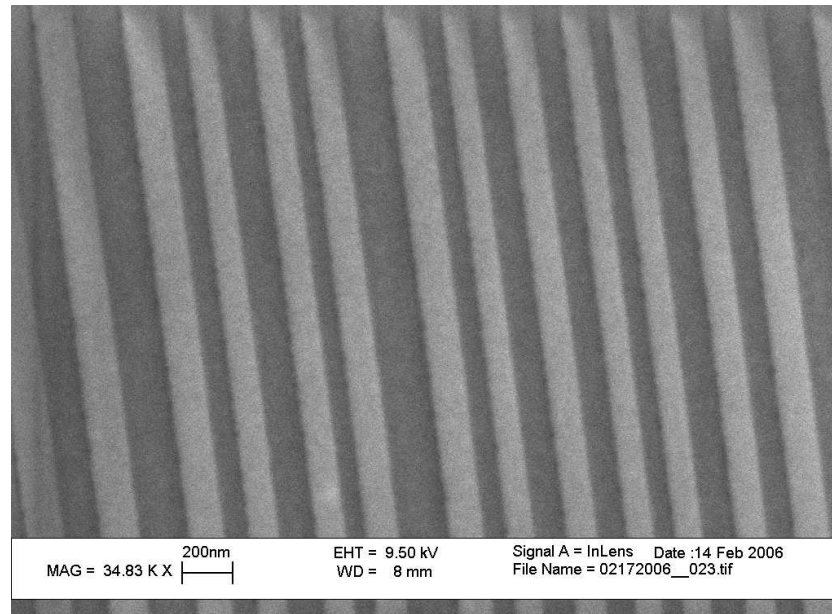
Figure 7.5: *Typical scanning electron microscopy image of faceted α-Al_2O_3 substrate surface after the annealing at 1500° C in air for 24 h.*

7.2.2   Ni Nanowires on Pre-Structured Al_2O_3 Substrates

For the deposition of Ni nanowires a pre-structured sapphire substrate (7.2.1) with a size of $20 \times 20 \times 0.5 \, mm^3$ was fixed to the preliminary substrate holder (4.4.3) and mounted in the argon ion beam milling/airlock chamber of the newly designed vacuum setup such that it could be transferred into the main deposition chamber with the facets oriented to the evaporation source under an angle of approximately 3° to 4° as shown in figure 7.3.

The airlock chamber was pumped down to a base pressure of 4.4×10^{-7} mbar, before the gate valve to the electron beam evaporation vacuum chamber was opened and the sample stage with the sample was moved into the e-beam chamber. Without the sample and the sample stage present the base pressure of the e-beam evaporation chamber was at 9×10^{-10} mbar. With the sample and the sample stage this pressure increased to 2×10^{-9} mbar, which can therefore be seen as the base pressure for the deposition process. The evaporation of Ni was then started and the deposition controller was allowed approximately 15 min to stabilise the evaporation rate at 1.0 ± 0.2 Å/s as read by the quartz balance next to the sample position. During the pre-deposition time the working pressure (counting for the gas pressure of the evaporated material) increased to 4×10^{-8} mbar where it stabilised and remained for the duration of the deposition process. A nominal Ni film thickness of 300 Å was preset and the deposition process was computer controlled by the LabVIEW™ program described in 4.3.3.

After the end of the deposition process, the evaporation of Ni was stopped and the sample was retracted into the air lock chamber and removed from the vacuum.
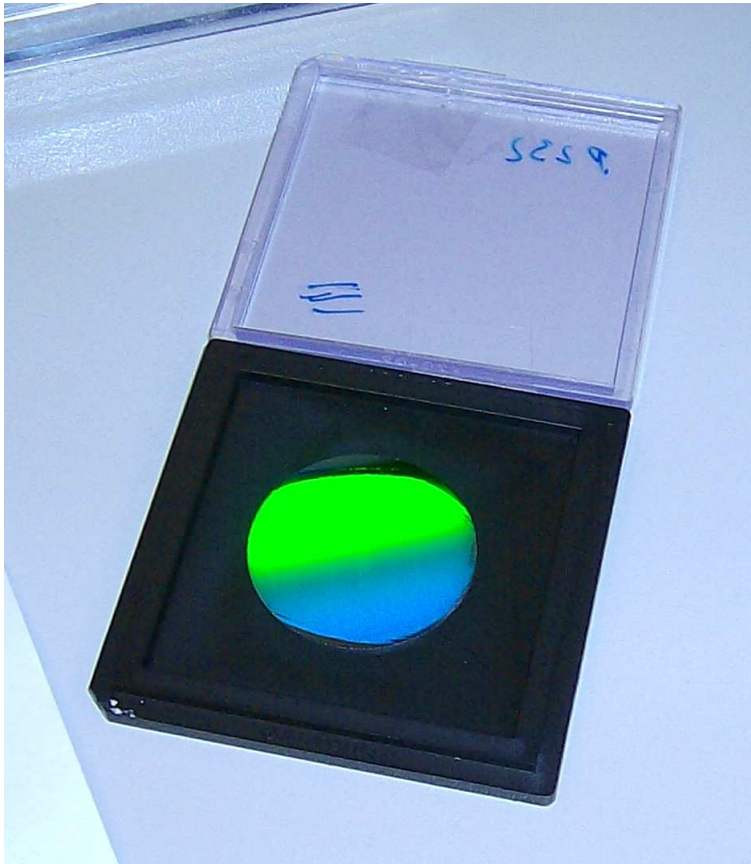
Figure 7.6: *Photograph of a Si substrate with a structured photoresist pattern before argon ion beam milling. The refraction of light by the surface structures is clearly visible and also demonstrates the homogeneity of this sample with a diameter of 1 inch.*
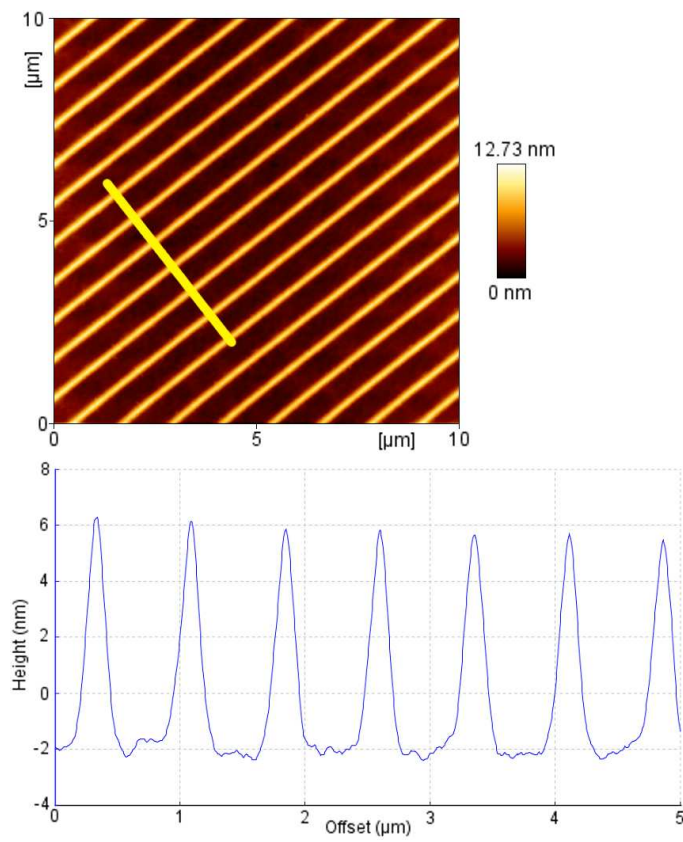
Figure 7.7: *Typical AFM image and height trace of the pre-structured Si substrate after ion beam milling (data by Dr. Andreas Frömsdorf, University of Hamburg).*

An initial quality control was carried out by means of SEM imaging; the sample's structure is shown in figure 8.22 (page 103), showing good agreement with the anticipated sample topology.

7.2.3   Gd Nanowires on Pre-Structured Al$_2$O$_3$ Substrates

For deposition of Gd nanowires, a pre-structured sapphire substrate with a size of $20 \times 20 \times 0.5 \, \text{mm}^3$ and a smaller pre-structured sapphire substrate with a size of $10 \times 6 \times 0.5 \, \text{mm}^3$ (7.2.1) were mounted on the preliminary substrate holder (4.4.3) and transferred into the e-beam evaporation chamber of the vacuum setup as described in section 7.2.2. The smaller sample was mounted such that the resulting Gd nanowires were identical to those on the larger substrate; this is required for VSM (5.3), where a limitation in sample size must be obeyed due to the technical design of the apparatus.

Deposition of 50 nm Gd was performed under computer control (4.3.3) at an angle of approximately 3° to 4° to the evaporation source at a base pressure of 8×10^{-10} mbar and 3×10^{-8} mbar working pressure with a deposition rate of 1 Å/s. A pre-deposition time of approximately 10 min was allowed for the parameters to stabilise. The self-shading effect of neighbouring facets allows deposition of Gd only on the upper edges of each facet, resulting in the growth of nanowires with a periodic spacing of approximately 200 nm and a cross-section of approximately 50 nm × 50 nm. Before removing the sample from the vacuum, a 25 nm thick Al capping layer was additionally sputter deposited at a rate of 2.5 Å/s as an oxidation barrier. Deposition of Al was carried out in the airlock chamber with 100 W of sputtering power at an argon gas flow rate of 2.5 sccm that corresponded to a working pressure of 5×10^{-3} mbar. A Scanning Electron Microscopy (SEM) image of a typical sample surface is shown in figure 8.9, with a lateral lattice spacing of the Gd nanowires of approximately 225 nm. The successful preparation of this Gd nanowire sample demonstrates the capabilities of the deposition technique for use with rare earth materials.

7.2.4   Ni Nanowires on Pre-Structured Si Substrate

A sample was also prepared by geometrical self shading on a lithographically pre-structured Si substrate (7.2.1) with approximately 10 nm high Si lines at a distance of approximately $700 - 750$ nm. It was mounted on the substrate holder and transferred into the e-beam evaporation chamber of the vacuum setup as described in 7.2.2 and 7.2.3 for the case of pre-structured sapphire substrates but mounted under a 0.75° angle to the Ni evaporation source. This resulted in approximately 750 nm wide shades of the Si lines on the substrate, which allowed only the deposition of Ni on one side of neighbouring Si lines. After 15 min of pre-deposition, 10 nm of Ni were deposited with a deposition rate of 1 Å/s. Due to a long previous shutdown phase of the vacuum chamber the base pressure for the preparation of this sample was only at 4×10^{-7} mbar and the working pressure during the deposition of Ni was at 1×10^{-5} mbar. The sample was capped with an approximately 10 nm thick Al layer deposited in the airlock chamber with sputtering parameters that were similar to

those given in 7.2.3. After removing the sample from the vacuum system a quality check by means of SEM imaging was carried out (figure 8.24 on page 106).

Chapter 8

Sample Characterisation

Prior to probing with x-ray and neutron scattering techniques, also a detailed characterisation of the samples was carried out to assess and tune the homogeneity of the nanoscale pattern over macroscopic distances. The analysis results for the prepared samples (chapter 7) are given in this chapter. Moreover, a novel approach to using the multi-wavelength capabilities of the TOF reflectometer REFSANS is presented (8.2.4).

8.1 Ni Dot Array on a Si Substrate

SEM, EDX, AFM/MFM and x-ray and neutron scattering methods were used to characterise this sample.

8.1.1 Scanning Electron Microscopy

To investigate the structure of the prepared polycrystalline Ni-dot array on Si, SEM images were taken, using a LEO™ 1530 Scanning electron microscope at GKSS Research Centre, department WPM, with a theoretical resolution of $1\,\mathrm{nm}$ at $15\,\mathrm{kV}$.

The as-prepared sample was mounted on the substrate holder stage of the electron microscope with no further treatment. Also, the sample was not electrically grounded using conductive silver or carbon paint to preserve the sample in its as-prepared state for analysis by other methods. This, however, resulted in a stronger charging of the sample and reduced the achievable resolution. Typical working pressures of the SEM sample chamber are in the range of $10^{-6}\,\mathrm{mbar}$, with a gun vacuum in the $10^{-10}\,\mathrm{mbar}$ regime. Images at various apertures, electron beam voltages, working distances and magnifications were taken using the in-lens detector of the microscope.

Figure 8.1 shows one of the collected SEM images, from which an approximate Ni nanodot diameter of $200\,\mathrm{nm}$ and a spacing of approximately $700 - 750$ nm between the centres of the dots on a square lattice is observed. It was also found that in regions close to the edges of the sample an increasing number of defects in the Ni dot array structure occur (figure 8.2). These can be due to the varying photoresist thickness in these regions from the structuring process transferred into the Ni layer by ion beam milling.
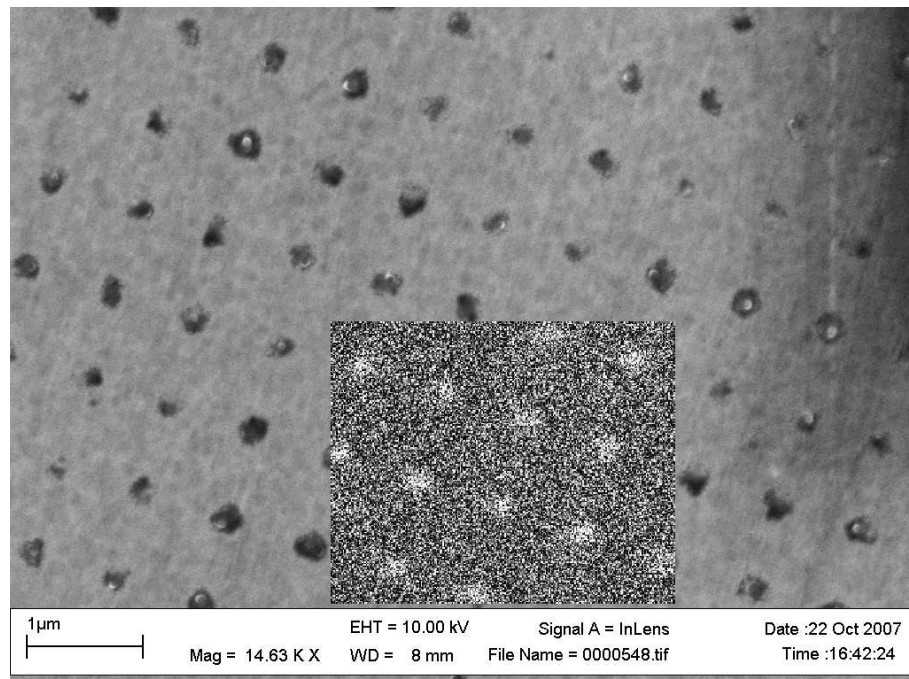
Figure 8.1: *SEM micrograph and overlaid EDX map of the Ni dot array. High Ni-L line intensities correspond to the positions of the Ni dots in the array and confirm their chemical nature.*
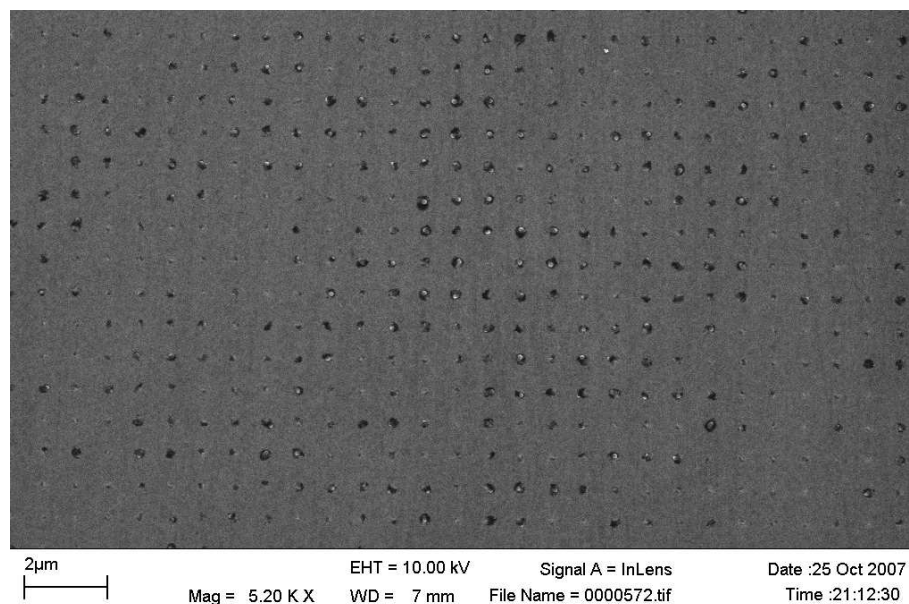
Figure 8.2: *SEM micrograph of a region with a large number of defects in the Ni dot array pattern. These defects occur in regions close to the edges of the sample and are concluded to be due to thickness variations of the photoresist before the ion beam etching process.*

8.1.2 Energy Dispersive X-ray Mapping

To confirm the chemical nature of the observed structures, an energy dispersive x-ray map was acquired using the EDAX™ Phoenix HX EDX apparatus with Genesis™ Spectrum v5.2 software package of the SEM apparatus. Data acquisition proved very complicated for this sample due to the small feature sizes and resulting low signal intensity. The strong charging and drifting of the sample in the SEM added to the difficulties.

Suitable parameters for this sample are a primary electron energy of $10\,kV$ at a working distance of $8\,mm$ and a magnification of $14630\times$. The electron energy of only $10\,kV$ also makes the process very surface sensitive. Despite the use of an automatic drift correction, the drifting of the sample was too strong to be corrected for more than a few minutes. Consequently, the data acquisition had to be performed quickly whilst maintaining adequate statistics to obtain a useful signal. As a compromise, a resolution of 256×200 pixels for the mapped area as shown in figure 8.1 was chosen. This gives a resolution of approximately $12\,nm$ per pixel and is hence just sufficient to resolve EDX intensities for each separate Ni nanodot in the array. Because of the low primary electron beam energy, only the Ni-L line with a corresponding energy of $0.743\,keV$ could be analysed.

The EDX data acquisition time was $109\,s$, accounting for the time between starting the process and when the automatic drift correction could no longer compensate for the sample drift. The collected data is shown in the overlaid inset in figure 8.1. It can be clearly seen that high Ni-L line intensities correspond to the position of the Ni nanodots, confirming their chemical nature.

8.1.3 AFM and MFM Measurements

Supplementary height information and the magnetic nature of the Ni nanodots were investigated by AFM and MFM imaging carried out at the IFW Dresden, Institute for Metallic Materials, Department Magnetic Microstructures using a VEECO™ Digital Instruments 3100 Atomic Force Microscope [100] with an extended MFM box for phase shift measurements. A magnetic VEECO™ MESP probe with $40\,nm$ Co/Cr alloy tip was used at a scan speed of $0.5\,Hz$. The magnetic information was collected by a two-pass technique, separately measuring the topography in tapping mode and the magnetic force by an interleave scan using the topographical information to track the probe tip at a constant height above the sample surface on the second pass. The tip deflection then directly gives the magnetic information.

Figure 8.3 shows an AFM image over a range of $15\,\mu m \times 15\,\mu m$ with a resolution of 512×512 pixels demonstrating the good homogeneity of the prepared sample with a Ni nanodot valley-to-rim height of approximately $15\,nm$.

For MFM, the scan area was reduced to $3.95\,\mu m \times 3.95\,\mu m$ and an area with a distinct sample defect (one missing dot) was chosen. The latter was necessary as changing the direction of the magnetic field requires the MFM head to be removed and remounted. Here, the sample defect allows the same position on the sample to be found and information to be obtained on the identical Ni nanodots for the applied in-plane magnetic field directions. Figure 8.4 shows the height information on the left with the corresponding magnetic force image on the right taken with a

```
Digital Instruments NanoScope
Scan size            15.00 µm
Scan rate           0.5008 Hz
Number of samples        512
Image Data            Height
Data scale          25.00 nm
```

```
                                        µm

                            10

                    5

                        × 5.000 µm/div
                        z 25.000 nm/div
```
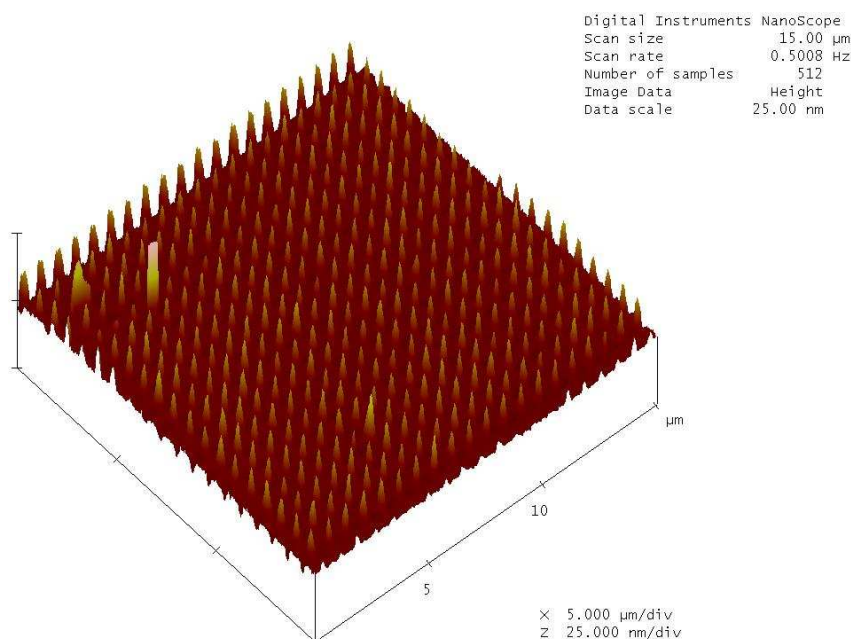
Figure 8.3: *AFM micrograph of the prepared Ni nanodots sample as obtained from the first pass of the MFM measurements. The extreme homogeneity over a range of $15\,\mu m \times 15\,\mu m$ with only very few noteworthy variations from the average height of approximately $15\,nm$ of the prepared Ni nanodots array is visible.*

$40\,nm$ lift at $80\,mT$, at zero magnetic field and at a reversed $80\,mT$ field. This field does not saturate the Ni nanodots but is sufficient to align them with the external field. The visible bright/dark contrast which follows the direction of the magnetic field is due to the probed stray fields. At zero field the Ni nanodots orient randomly but appear to favour a vortex state.

The switching behaviour in the vicinity of zero magnetic field could not be investigated in detail, as no precisely controllable magnet was available. However, the measurements directly confirm the magnetic behaviour of the sample which was the main goal of this investigation.

8.1.4 Off-Specular X-ray Scattering

As described in 5.5.2, off-specular x-ray scattering by means of rocking scans can be used to determine the lateral structure of a sample surface.

The reciprocal space map shown in figure 8.5 was collected using the Bruker™ AXS D8 Advance two-circle x-ray diffractometer described in 6.1.

Due to the restrictions in the diffractometer geometry a precise sample alignment could not be performed for the zero position of the ω-axis for this type of measurement. However, the misalignment only introduces a fixed offset and can be corrected during the data analysis process.

Reciprocal space was mapped for 2θ values from $0.100°$ to $1.650°$ with a step width of $\Delta 2\theta = \Delta 2\omega = 0.005°$. At a wavelength of $\lambda = 1.54\,\text{Å}$ this accounted for
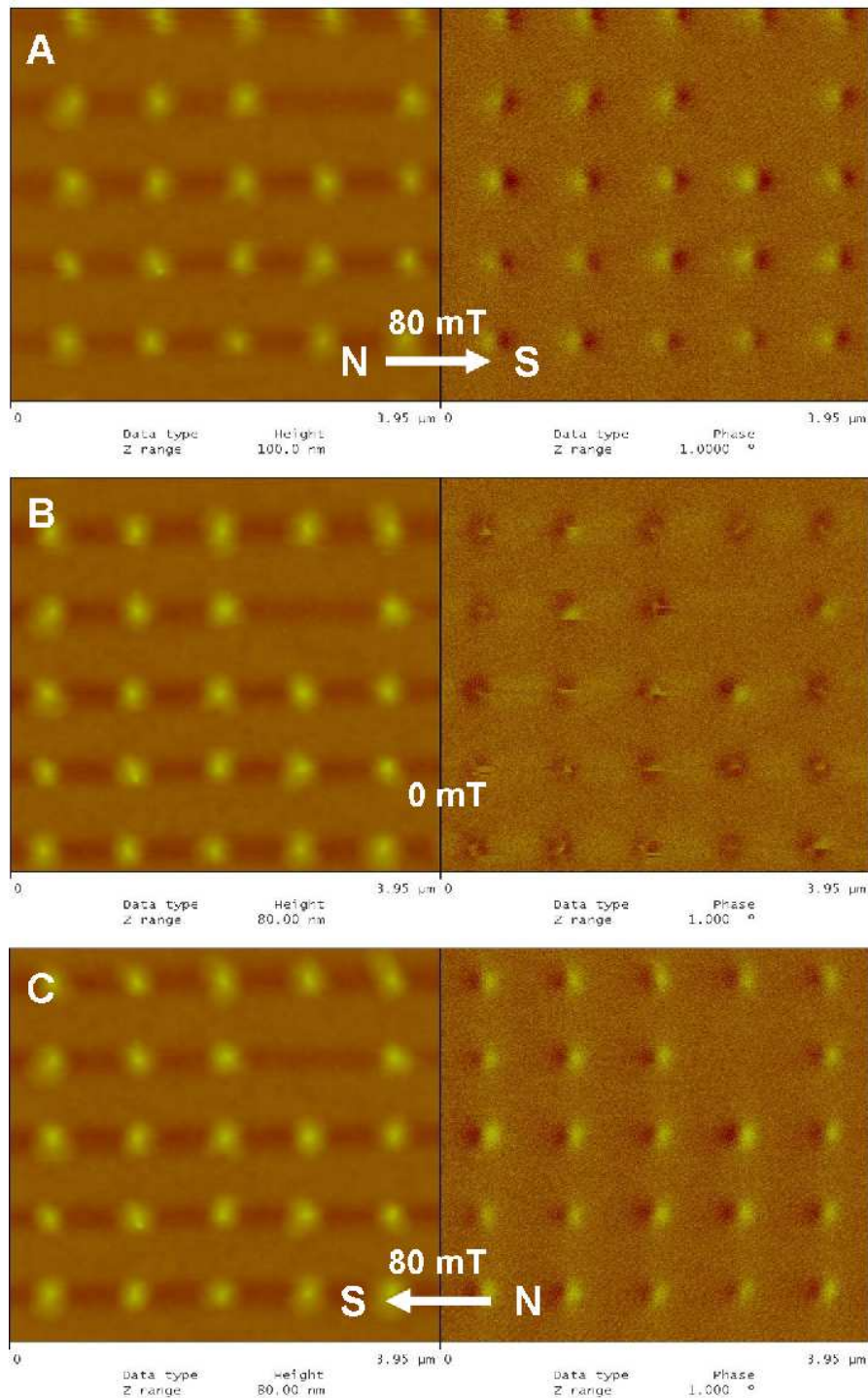
Figure 8.4: *AFM (left) and MFM (right) micrographs of the Ni nanodot sample in an in-plane oriented magnetic field of 80 mT to right (A), 0 mT (B) and 80 mT to left (C). The bright/dark contrast of the MFM image (A) indicates the magnetisation of the Ni nanodots and reverses with the reversed magnetic field (C). At zero-field (B) the magnetic orientation of the Ni dots is partially random in an in-plane direction but most of the nanodots show a vortex-like magnetisation state. The magnetisation of the MFM tip also influences the Ni dots in zero-field, visible as horizontal streaks along the scan direction.*
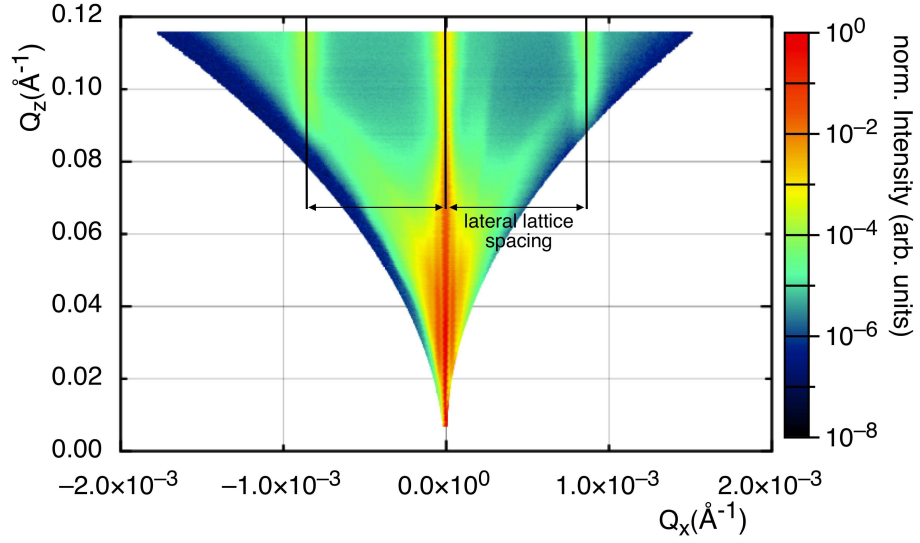
Figure 8.5: *Reciprocal space map of the Ni dot array on Si substrate collected by rocking scans. The Q_x-values of the diffuse intensities in the higher Q_z regions give the lattice spacing through their separation ΔQ_x.*

reciprocal space regions of $0.01 \,\text{Å}^{-1} \leq Q_z \leq 0.12 \,\text{Å}^{-1}$ giving access to off-specularly scattered intensities with $-1.75 \times 10^{-3} \,\text{Å}^{-1} \leq Q_x \leq 1.75 \times 10^{-3} \,\text{Å}^{-1}$.

Corresponding real space nanostructure distances d were obtained using the relationship [101]

$$d = \frac{2\pi}{\Delta Q_\parallel} = \frac{2\pi}{\Delta Q_x},$$

where ΔQ_x is the reciprocal lattice vector spacing along the x-direction[1].

From this rocking map the lattice spacing is obtained, given by

$$d = \frac{2\pi}{(8.63 \pm 0.12) \times 10^{-4} \text{Å}^{-1}} = 728 \pm 10 \,\text{nm}.$$

This is in good agreement with the value determined from the SEM image (figure 8.1).

A well controllable alignment in ϕ (rotation angle around the out of plane axis) was not possible on the Bruker™ diffractometer. To investigate and to correct the influence of the rotation on the diffusely scattered intensity pattern, rocking scans of the sample were collected at a fixed 2θ value of $2\theta = 1.80°$ in steps of $\Delta\phi = 1.00°$ from $\phi = 0°$ to $\phi = 90°$ using the SEIFERT™ XRD 300 PTS 4-circle x-ray diffractometer described in 6.1.2. The influence of the sample rotation on the diffusely scattered intensities is shown in figure 8.6.

---

[1]The corresponding reciprocal lattice vector Q_y along the y-direction is equal to zero for this scattering geometry
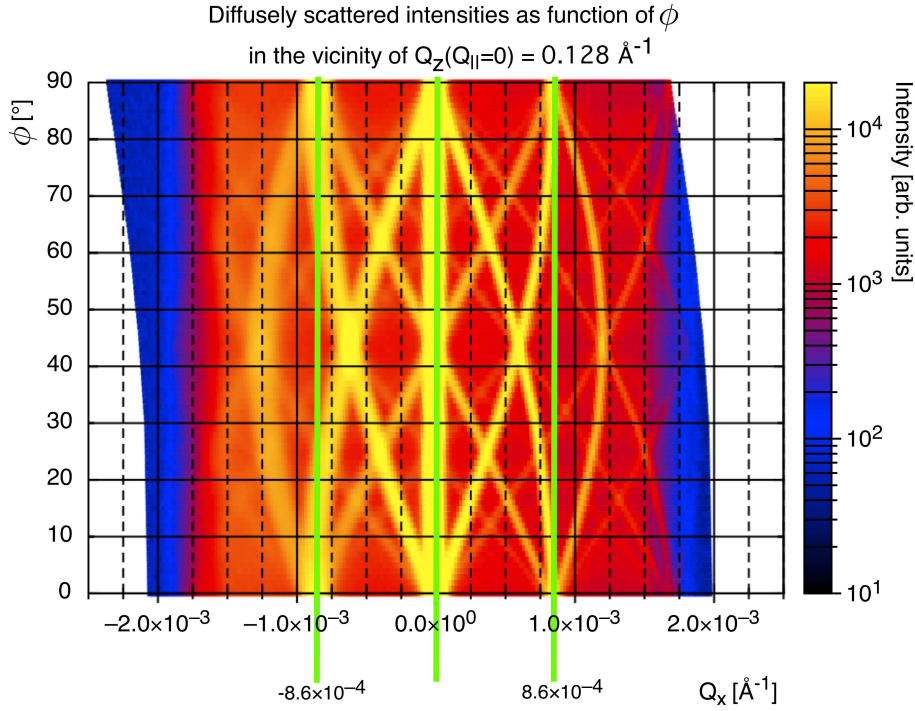
Figure 8.6: *Diffusely scattered intensities, showing the reciprocal lattice distances as a function of the sample rotation ϕ.*

This method allows the correct lateral lattice spacing to be determined, as a misalignment in the sample rotation can be eliminated as shown in figure 8.6. A lattice spacing of

$$d = \frac{2\pi}{(8.6 \pm 0.1) \times 10^{-4} \mathring{A}^{-1}} = 731 \, \binom{-9}{+8} \text{ nm}$$

is obtained.

From this scan it is also found that the nanodot spacings are identical for the 0° and 90° directions which proves the structural homogeneity of the sample.

By comparing the intensity distribution at certain ϕ-values, it is also possible to conclude that the reciprocal space map in figure 8.5 was collected with a misalignment in ϕ of less than $\pm 5°$. A more precise value cannot be given due to the width of the truncation rods, which is a convolution of instrumental resolution and sample imperfections[2].

8.1.5   Off-specular Neutron Scattering

Reciprocal space maps were collected by means of rocking scans using NERO at the GENF facility in Geesthacht. NERO is a neutron reflectometer in a $\theta - 2\theta$ geometry

---

[2]As the sample was rotated around ϕ and a reduced resolution was only present in the case of a shallow x-ray incidence angle (i. e. left half of figure 8.6) but not for a shallow detector angle (right half), the resolution is dominated by the optics on the source side of the x-ray setup.
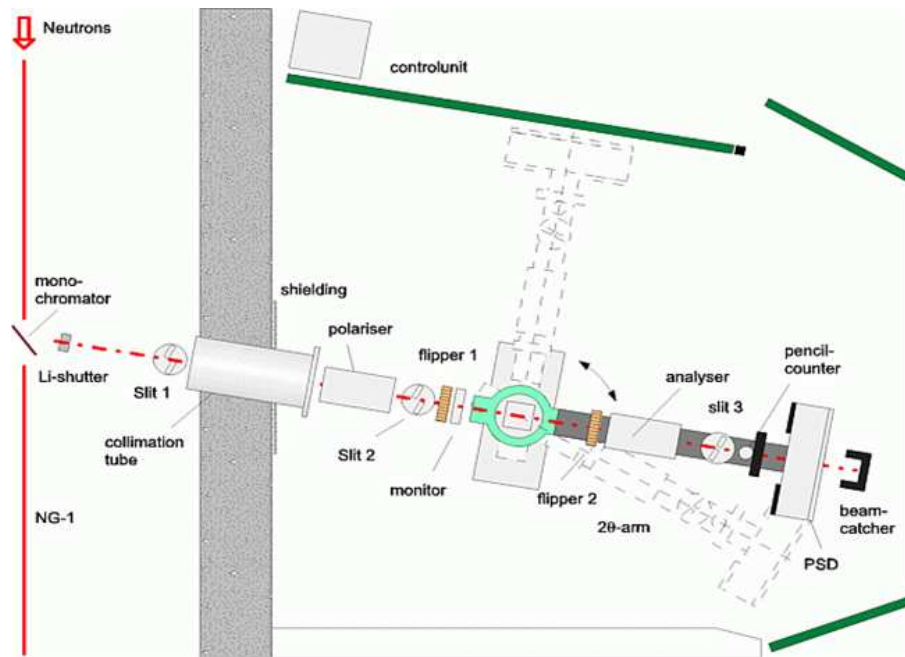
Figure 8.7: *Schematic of the NERO reflectometer at the Geesthacht Neutron Facility (taken from [102]).*

with optional polarisation capabilities. A schematic of its setup is shown in figure 8.7.

Unpolarised neutron reflectivity measurements were carried out at room temperature for the as-prepared Ni sample without an external magnetic field at a neutron wavelength of about 4.34 Å. The intensities were mapped by means of rocking scans in the range of $0.00° \leq 2\theta \leq 3.80°$, which corresponds to reciprocal space values of 0.00 Å$^{-1} \leq Q_z \leq 0.09$ Å^{-1} and -3.9×10^{-3} Å$^{-1} \leq Q_x \leq 1.6 \times 10^{-3}$ Å^{-1}, respectively. The absolute ϕ rotation state of the sample on the NERO goniometer was determined by comparing the reciprocal space map after the measurements to the ϕ-dependent x-ray data (figure 8.6).

Figure 8.8 shows the off-specular x-ray and complementary neutron data for a sample rotation of $\phi = -2°$. The figure clearly shows that scattered neutrons penetrate the sample and access Q_x-values which are below the sample horizon and inaccessible by x-ray rocking scans. However, the signal intensity is significantly lower for neutrons such that no intensities above the neutron background are obtainable for Q_z-values which are accessed by the x-ray rocking map. The arbitrary cuts along $Q_z = 0.030$ Å^{-1} for neutrons and along $Q_z = 0.111$ Å^{-1} for x-rays show excellent agreement and the off-specular neutron scattering confirmed the lateral structure spacing of approximately 730 nm.

8.2 Gd Nanowires on faceted Al$_2$O$_3$ Substrates

The sample was characterised by SEM, AFM/MFM, VSM and TOF-GISANS. The analysis of this sample initiated the development of a TOF-GISANS evaluation soft-
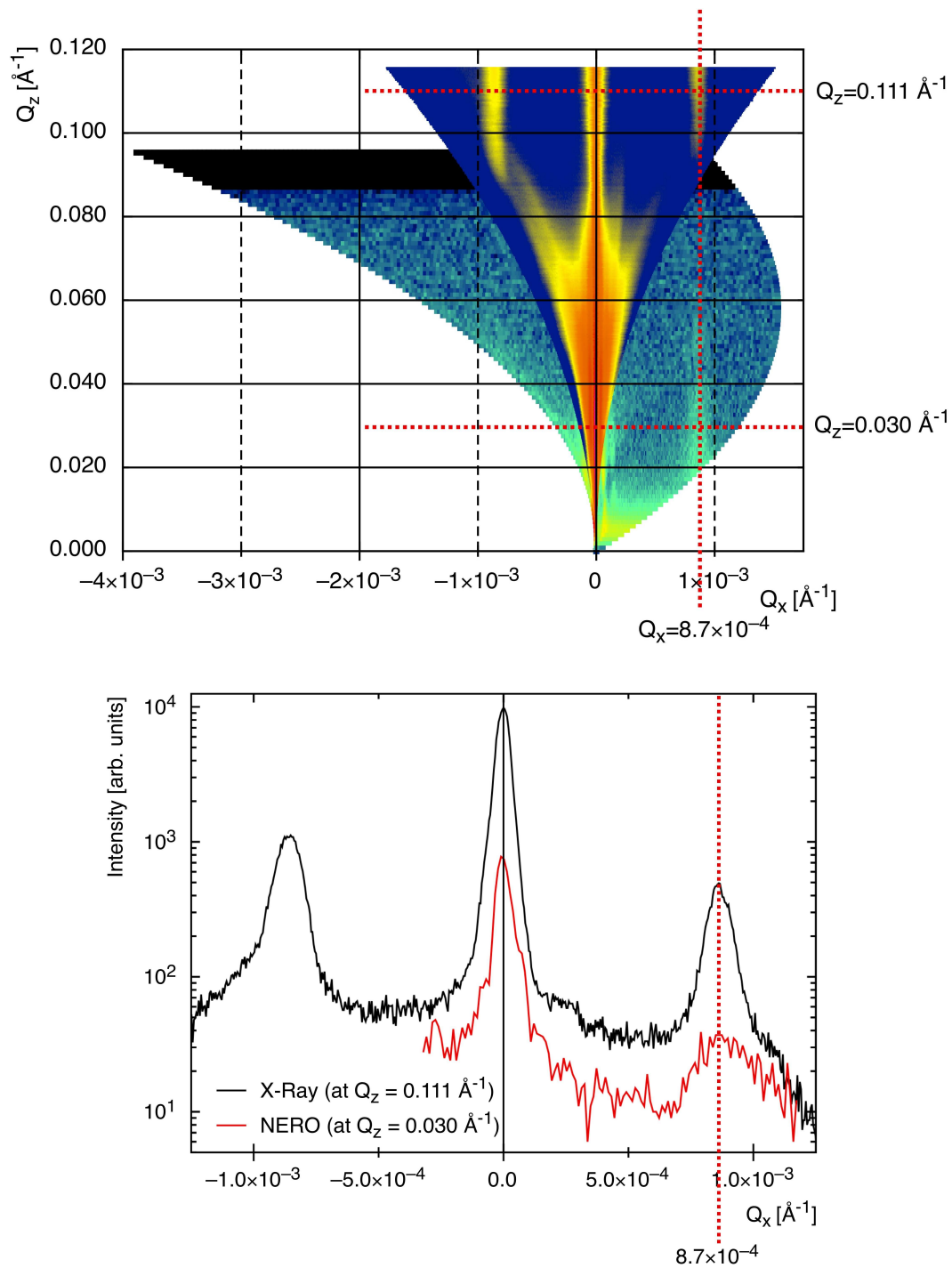
Figure 8.8: *Reciprocal space maps for the Ni nanodots sample with a sample rotation state of $\phi = -2°$, as collected by x-ray and neutron measurements. The lower graph shows a cut along $Q_z = 0.030 \, Å^{-1}$ for the neutron data and a comparative cut along $Q_z = 0.111 \, Å^{-1}$ from the x-ray data. An identical lateral lattice spacing of $730 \, nm$ is obtained by both methods.*
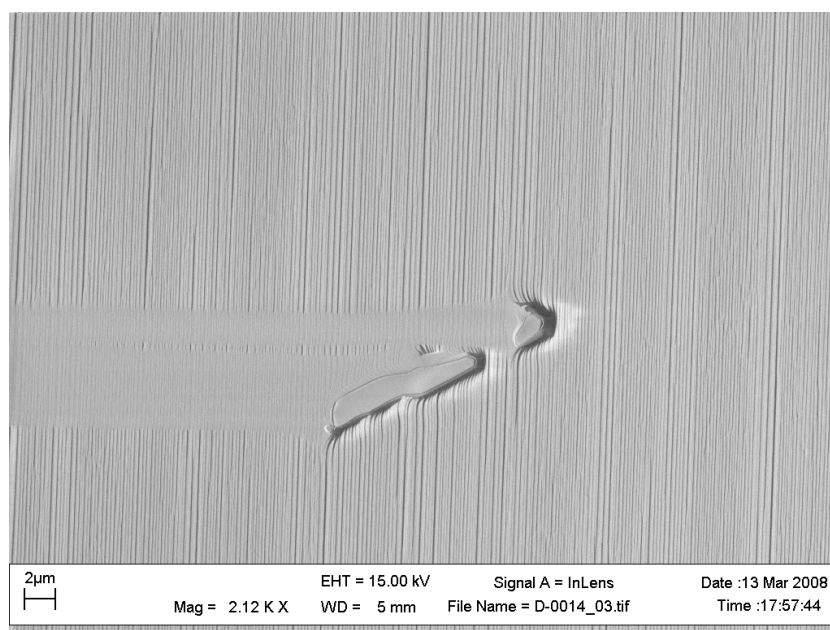
Figure 8.9: *SEM image of the Gd nanowire sample grown by geometrical self shading. The dark Gd wires are visible through the aluminium capping layer. The specifically imaged, but uncharacteristic sample defect allows the difference between regions with and without Gd nanowires to be seen.*

ware, which resumes the data analysis process where the REFSANS data evaluation program "DART" reaches its limits; the first TOF-GISANS results by this novel analysis method are presented [LOP-4, LOP-3].

8.2.1 Scanning Electron Microscopy

The structure of the prepared Gd-nanowire sample was investigated by SEM using the apparatus described in 8.1.1, with similar working conditions.

Due to the electrically insulating substrate, a strong charging of the as-prepared sample by the SEM electron beam significantly reduced the obtainable resolution and only focusing onto (rare) sample defects which showed a sufficient contrast to the surrounding sample area was possible. Consequently, the image given in figure 8.9 shows also only a low magnification; it gives a nanowire periodicity of approximately 225 nm. Additionally, the sample features are below the resolution of the attached EDX setup. Hence, no elemental analysis map could be collected for this sample.

8.2.2 AFM and MFM Measurements

To obtain conclusive topographic results and information on the magnetic properties of the sample, AFM and MFM micrographs were collected with AFM supplementing the SEM information.

All height and magnetic information images shown hereafter were collected at the IFW Dresden using the instrument and magnetic tip described in 8.1.3 at a scan speed of 0.5 Hz.
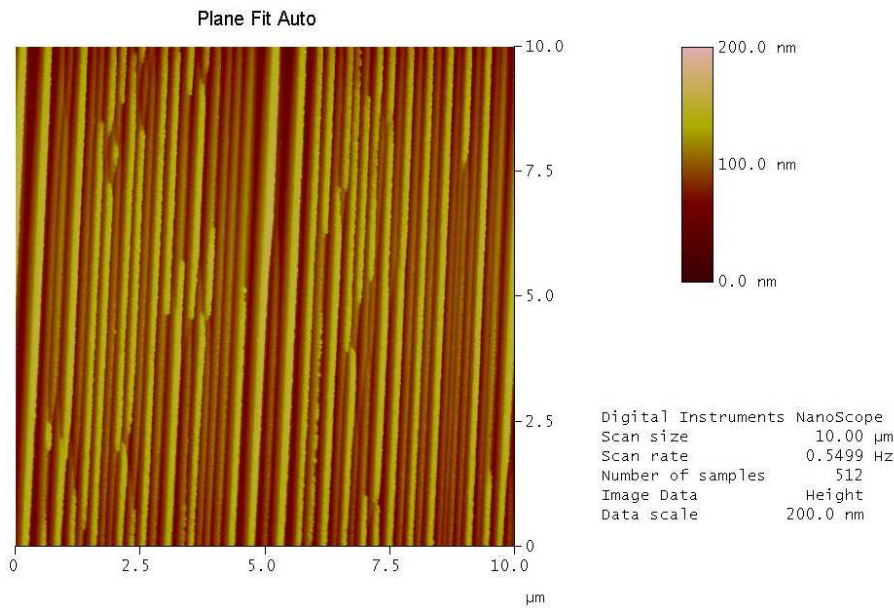
Figure 8.10: *AFM micrograph of the prepared Gd nanowire sample with a scan area of 10 μm × 10 μm. The height information is clearly dominated by the roughness of the underlying surface and hence only the location of the nanowires could be obtained reliably, not their size.*

An AFM image with a scan area of 10 μm × 10 μm and a resolution of 512 × 512 pixels is shown in figure 8.10. The roughness of the substrate dominates the height information, which can therefore not be interpreted in terms of Gd nanowire dimensions. However, the Gd nanowires are still clearly visible on the upper edges of the substrate facets.

Although the sample was at room temperature and no magnetisation of Gd was expected, the sample was measured for magnetic information to investigate the influence of the very rough surface topography on the two-pass MFM technique (8.1.3).

Figure 8.11 shows the AFM and MFM image over an area of 4 μm × 4 μm with a resolution of 512 × 512 pixels. No magnetic signal was expected but the influence of the topography onto the magnetic signal dominates the scan and the MFM image displays artefact magnetic information. As the magnetic information on the Gd nanowires has to be collected at low temperatures, a different microscopy setup with a low temperature stage must be used. This setup does not operate with the interleave scan available on the VEECO™ instrument and therefore has a lower magnetic sensitivity. Consequently, it would not be possible to resolve the magnetic from the topographic information and no information on the magnetic behaviour of the Gd nanowires by means of MFM could be collected.

8.2.3   VSM Measurements

The sample with a dimension of $10 \times 6 \times 0.5 \, \text{mm}^3$ was measured using VSM, carried out at the IFW Dresden using a Quantum Designs™ Physical Properties Measure-
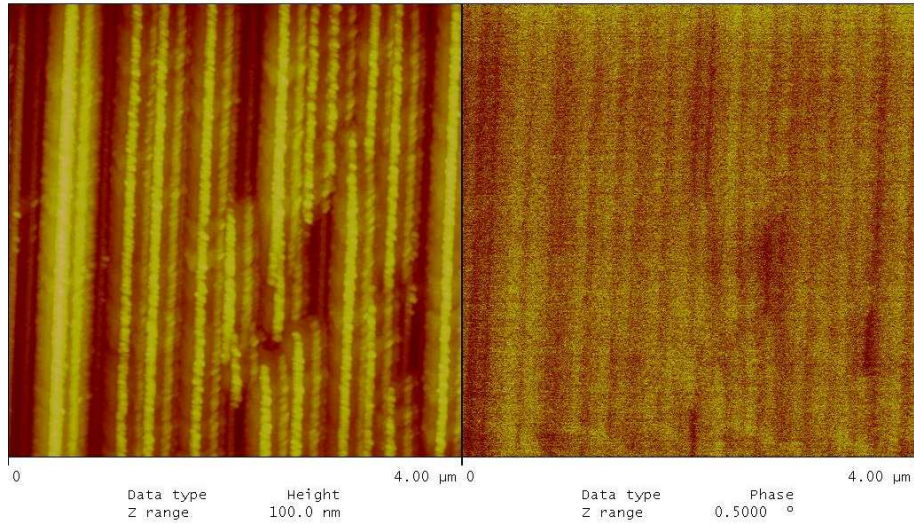
Figure 8.11: *AFM and MFM micrographs of the prepared Gd nanowire sample with a scan area of 4 µm × 4 µm. The height information overlaps the MFM information making it impossible to extract a reliable MFM signal. The MFM image gives the appearance of probed magnetic stray fields, which is however caused by the topography of the sample.*

ment System (PPMS) with VSM option. The hysteresis of the sample was measured at a rate of 100 Oe/s in the range of −90 kOe to +90 kOe at a temperature of 100 K. Measurements were performed with the magnetic field oriented in-plane along and perpendicular to the Gd nanowires as shown in figure 8.12. A clear shape anisotropy of the Gd nanowires is observable with a strong diamagnetic background from the sapphire substrate. The overlapping linear slope of the signal can be corrected in first order by subtracting a previously measured diamagnetic signal of a glass substrate (figure 8.13). A saturation magnetisation along the Gd nanowires of approximately 3 T and a saturation magnetisation of approximately 6 T to 7 T perpendicular to the nanowire direction can be obtained, which is slightly below that of bulk Gd [103].

The magnetisation curve of the sample was measured as a function of the temperature at a fixed magnetic field value of $H = 0.5$ T parallel to the Gd nanowires using a temperature ramp of 4 K/min in the range from 100 K to 350 K (figure 8.14). It shows a very broad transition regime with the Curie temperature just below room temperature near the expected value of approximately 290 K [104, 105]. The offset of 0.07 memu in the magnetic moment is due to the diamagnetic background from the substrate.

8.2.4 Time-of-Flight Grazing Incidence Small Angle Neutron Scattering

TOF-GISANS was performed at the combined Reflectometer and Small Angle Neutron Scattering instrument REFSANS [64, 65] at the FRM II neutron source in Garching with a point-collimated primary neutron beam of 4 mm in diameter. The sample-to-detector distance was 11710 mm with the approximately 500 mm × 500 mm
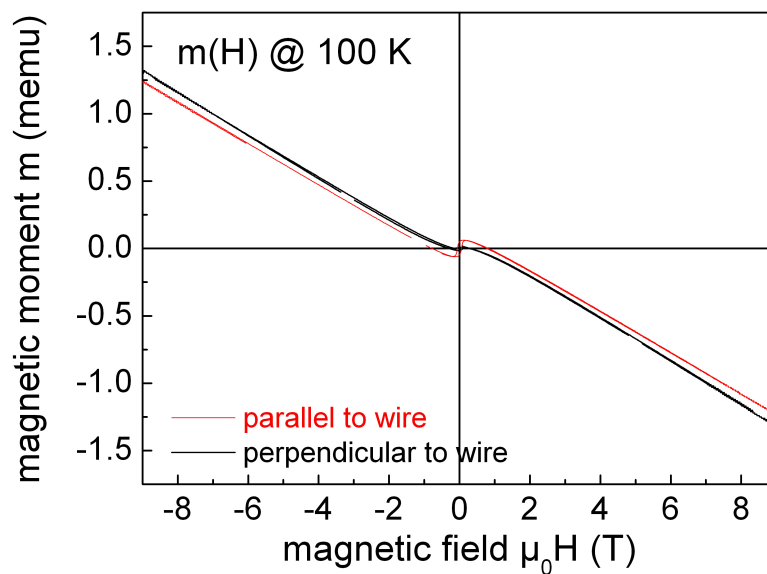
Figure 8.12: *Hysteresis loops for Gd nanowires on pre-structured sapphire substrates in the range of of* −90 *kOe to* +90 *kOe measured at a temperature of 100 K. A strong diamagnetic background from the sample substrate is visible together with a shape anisotropy.*
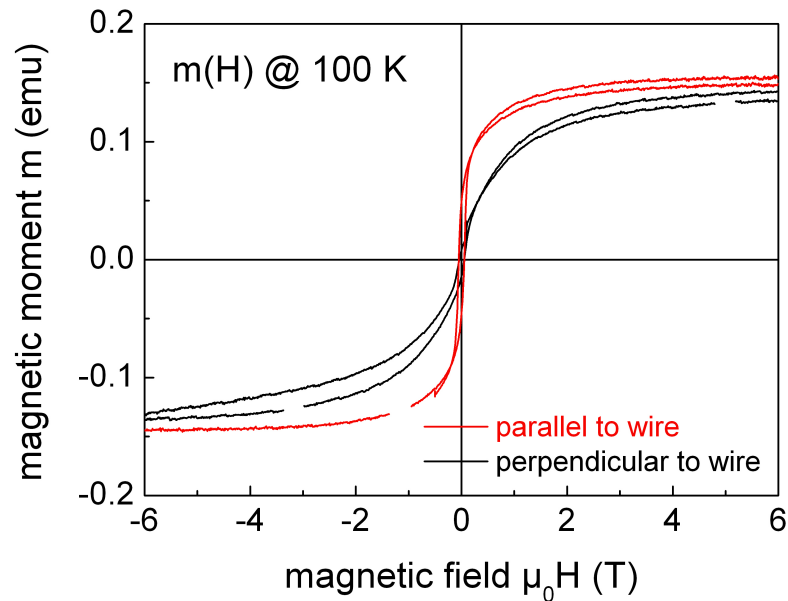
Figure 8.13: *First-order background-corrected hysteresis loops for Gd nanowires on pre-structured sapphire substrate. The shape anisotropy for magnetisation directions along and perpendicular to the Gd nanowires is visible with a saturation field of slightly above 6 T.*
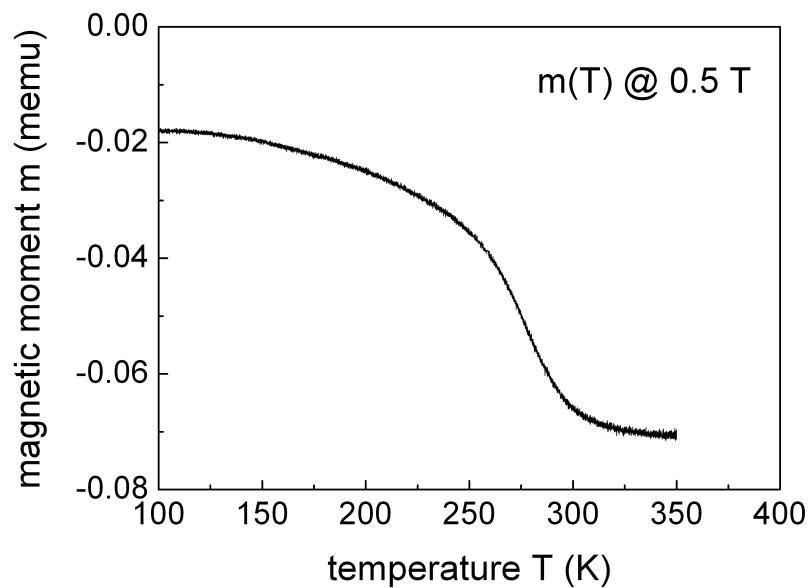
Figure 8.14: *Magnetisation of Gd nanowires as a function of temperature. As expected for Gd, a Curie temperature of approximately room temperature is obtained.*

large area detector positioned at such a height that the primary neutron beam was just below the lower edge of the detector. The resolution is defined by the detector channel size of $2.7\,\text{mm} \times 2.7\,\text{mm}$. The incident white neutron beam was pulsed by the REFSANS chopper at a repetition rate of $10\,\text{Hz}$ and the bandwidth was limited to $4.5\,\text{Å} - 18\,\text{Å}$. The time-of-flight detection scheme allows the reconstruction of the different 2D intensity maps as a function of the wavelength λ by the software package DART (Data Acquisition and Reconstruction Tool, version 0.6.5.259). The scattering geometry and the definition of the relevant goniometer head angles are given in figure 5.11 (page 47). The measurements were performed for various orientations in ϕ around the sample normal at a fixed (goniometer) angle of incidence $\alpha_i = 0.67°$. The continuous wavelength spectrum applied in this experiment varies the size of the Ewald sphere in reciprocal space. Hence, for each wavelength the Ewald sphere intersects the Grating Truncation Rods (GTR) at a different Q_z value. It is therefore not only possible to reconstruct intersection points but also larger portions of the GTRs by obtaining the integral image over all wavelengths.

Development of Additional Evaluation Software

As neutrons carry a mass they follow a ballistic path in the earths gravitational field. Due to the usually long distances between sample and detector in GISANS geometry, this leads to a significant (neutron wavelength dependent) deviation in Q_z. Typically, ballistic effects are corrected mathematically in the data evaluation software as they are of particular concern when multiple wavelengths are analysed or whenever the results of experiments which were carried out using different neutron wavelengths are compared.

At present, DART does not include a ballistic correction scheme, nor does it allow intensities to be weighted by the primary beam intensities. Therefore, an additional data evaluation software was developed as part of this work as a LabVIEW™ implementation. The user interface of this software is shown in figure 8.15. The software allows the ballistically uncorrected detector images with the corresponding wavelengths, the primary beam spectrum and a background measurement file to be read from the relevant DART-output files. For the program to correctly treat ballistic effects, variable instrument parameters are required as input. This includes the sample-to-detector distance, free neutron path before the sample and the position of the scattering tube. As multiple wavelengths are used, the angle of incidence varies with the wavelength of the neutrons due to the ballistics before the sample. DART does not take this effect into account and consequently the angle of incidence must be obtained manually for each wavelength slice from the specular beam position. In contrast to this, the newly developed program only requires input for a single incidence angle for one wavelength slice from which the angles of incidence for all other applied wavelengths are calculated. The software outputs a tabulator-delimited text file containing columns of the detector channel in horizontal direction, the corresponding 2θ value, calculated Q_y, ballistically corrected detector channels in perpendicular direction, the corrected take-off angle α_f, corresponding Q_z-values, weighted intensities, the wavelength λ, and Q_x and $Q_\parallel$ for each detected neutron. A description of the program on a source-code level is given in appendix B.4.
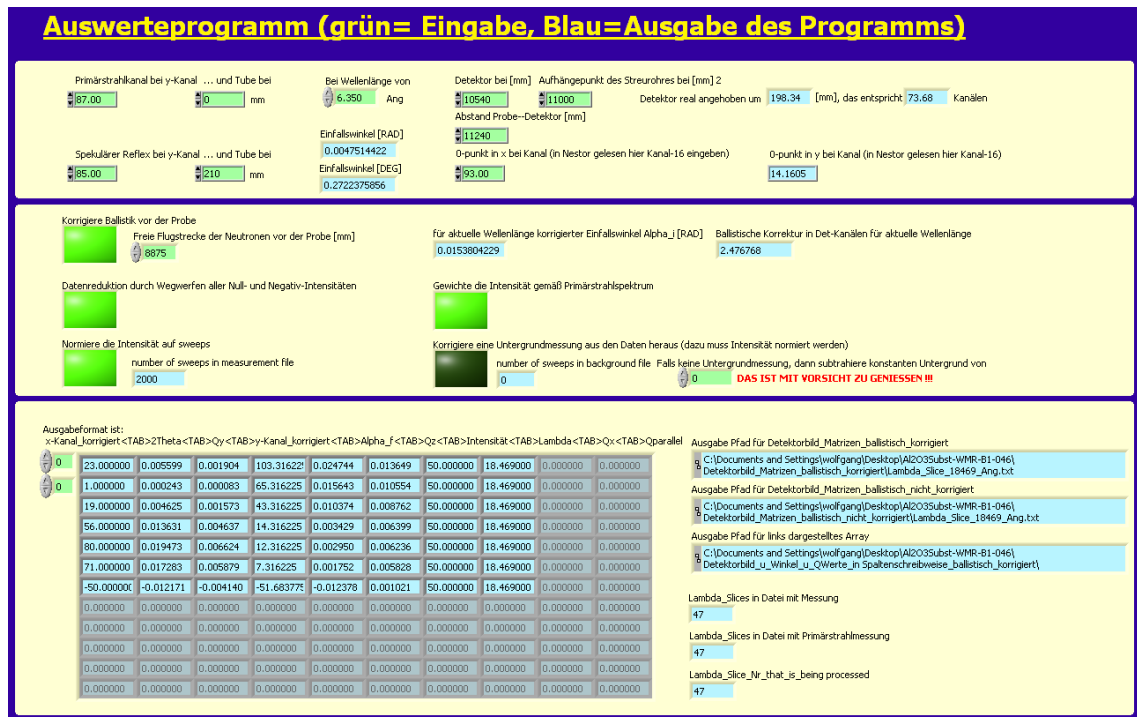
Figure 8.15: *The user interface of the software developed for the evaluation of Time-Of-Flight-GISANS data collected on REFSANS.*

This output file allows the full advantages of the multi-wavelength capabilities of REFSANS to be used to find the critical wavelength at a given incidence angle and to reconstruct various reciprocal space planes without changing the inclination of the sample, which is in contrast to fixed wavelength instruments.

Aligned Sample

The critical wavelength at which the chosen angle of incidence corresponds to the critical angle [63] is 9.2 Å as can be seen in figure 8.16 for a nominal sample orientation of $\phi = 0°$. The corresponding detector images at wavelengths of 6.9 Å, 9.2 Å and 10.7 Å are given in figure 8.17 showing intensities at the intersection of the GTRs with the corresponding Ewald sphere. From the location of these intersection points or from the location of the reconstructed (by integration over all applied wavelengths) portions of the GTRs of a well-aligned sample (figure 8.18) one can directly obtain the periodicity ($d = \frac{2\pi}{\Delta Q_y}$) of the lateral structure of approximately 220 ± 20 nm. This is in good agreement with the periodicity of 225 nm obtained from the SEM and AFM images (figures 8.9 and 8.10).

Rotated Sample

GISANS on lateral gratings is also very sensitive to a rotation of the sample around its surface normal. The strong influence of the rotation on the scattered detector image is shown in figure 8.19 for a single wavelength slice, showing the asymmetri-
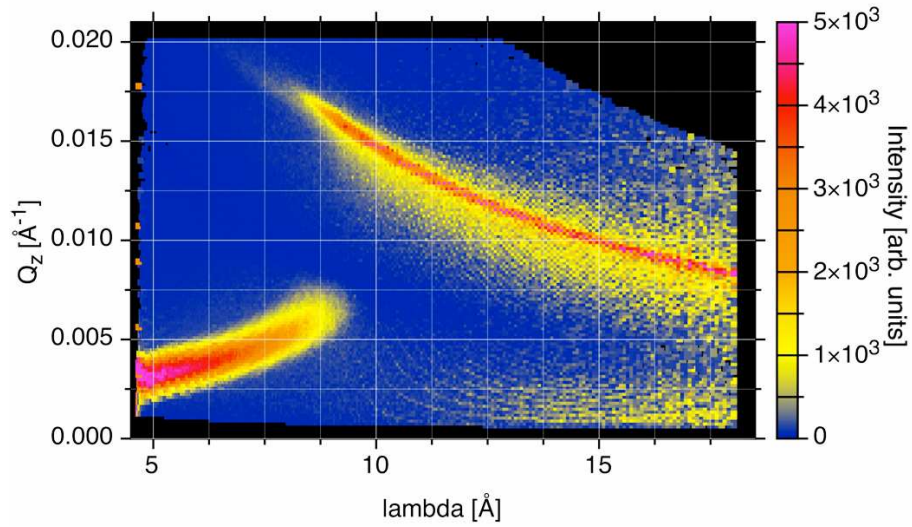
Figure 8.16: *Q_z versus the wavelength λ. With increasing wavelength the transition from refracted intensities to reflected intensities occurs with the transition at the critical wavelength of $\lambda \approx 9.2\,\mathring{A}$.*
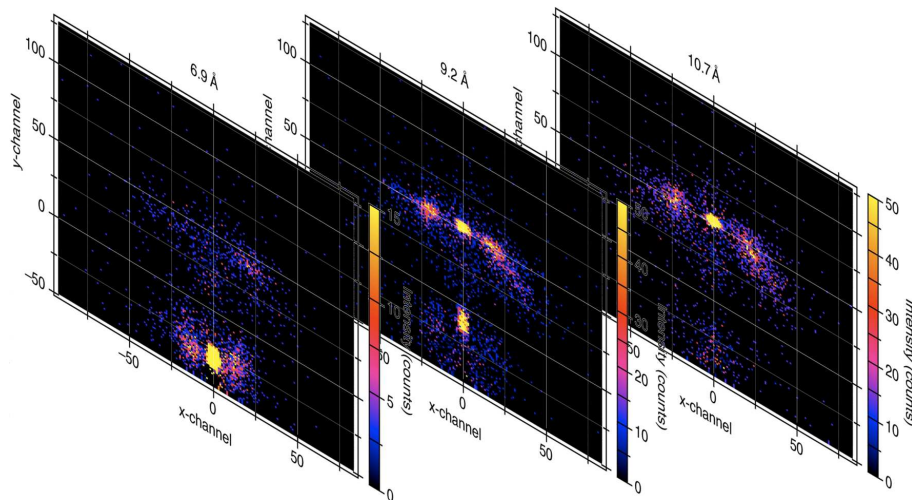
Figure 8.17: *Detector images for a single wavelength slice which are extractable from the Time-Of-Flight information collected for each neutron. Shown are the detector images for wavelengths of $\lambda = 6.9\,\mathring{A}$ (below the critical wavelength), $9.2\,\mathring{A}$ (at the critical wavelength) and $10.7\,\mathring{A}$ (above the critical wavelength).*
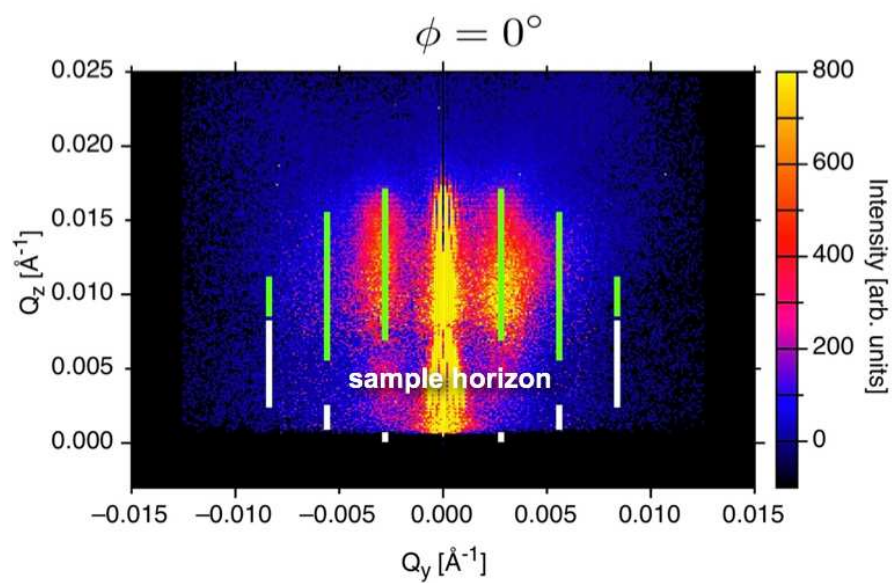
Figure 8.18: *Reconstructed integral reciprocal space image for a nominal sample orientation of $\phi = 0°$ with the intensities obtained for all applied wavelengths plotted together with theoretically expected locations of the intensities for reflected (green) and transmitted (white) neutrons. A large portion of the grating truncation rods can be reconstructed allowing for a fast assessment of the lateral structure. In reciprocal space the sample horizon is not at a well defined Q_z value but shifts due to the ballistics before and after the sample.*
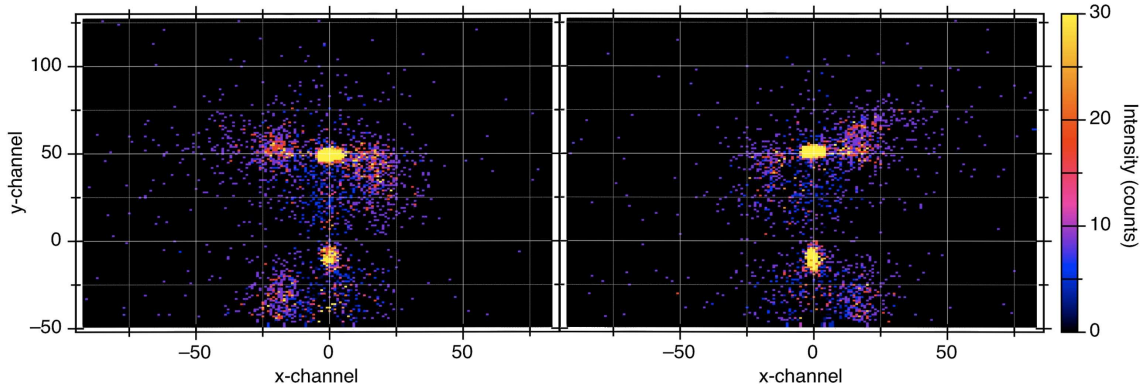
Figure 8.19: *Detector images at the critical wavelength of $\lambda = 9.2\,\mathring{A}$ obtained for orientations around the sample normal of $\phi = +0.50°$ (left) and $\phi = -0.75°$ (right) showing the drastic influence of only a slight sample rotation onto the location of the intersection of the GTR with the Ewald sphere.*

cally scattered intensity distribution at the critical wavelength for transmitted and reflected intensities. The orientations are $\phi = +0.5°$ and $\phi = -0.75°$. The corresponding integral reciprocal space images of the rotated samples are shown in figure 8.20 and figure 8.21 and are discussed together with the theoretical expectations.

Discussion

Yan and Gibaud [106] recently published theoretical and experimental results on the intersection of GTRs in reciprocal space with the Ewald sphere using GISAXS. Following their theoretical approach but by also taking the neglected solutions for transmission into account, intensities in reciprocal space are to be expected at

$$Q_y = \frac{2\pi\,n\,\cos\phi}{d} - \frac{2\pi\,sin^2(\alpha_i)\,\cos\phi\,\sin\mp\phi}{\lambda} \times A \qquad (8.1)$$

$$Q_z = \frac{2\pi\,\sin\alpha_i\,\cos\alpha_i\,\cos\phi}{\lambda} \times A \qquad (8.2)$$

where $A = 1 \pm \sqrt{1 - \frac{\lambda^2\,n^2}{d^2\,\sin^2\alpha_i\cos^2\phi}\left(1 - \frac{2d\,\sin\mp\phi}{n\,\lambda}\right)}$, λ denotes the neutron wavelength, α_i is the angle of incidence, ϕ is the angle of the sample orientation around its normal with $\phi = 0°$ being the case in which the nanowires on the sample are aligned parallel to the scattering plane, d is the periodicity of the nanowire grating and n is the order of the scattered intensities. In both formulae, the positive sign before the square root accounts for reflected intensities and the negative sign accounts for the transmitted intensities with the opposite relationship for the sign in $\sin\mp\phi$. As neutrons also penetrate the sample after scattering by the nanowires, both solutions should be considered.

In order to compare the positions of the experimentally collected portions of the GTRs to the theory, calculations were performed using equations 8.1 and 8.2. The
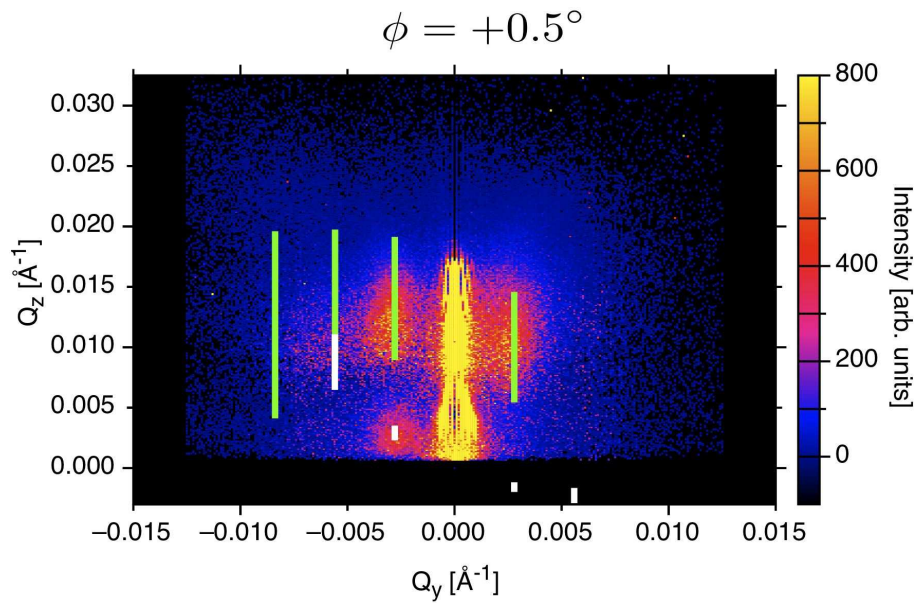
Figure 8.20: *Reconstructed integral reciprocal space image for a nominal sample orientation of $\phi = +0.50°$ plotted together with the theoretically expected locations of the intensities for reflected (green) and also transmitted (white) neutrons.*
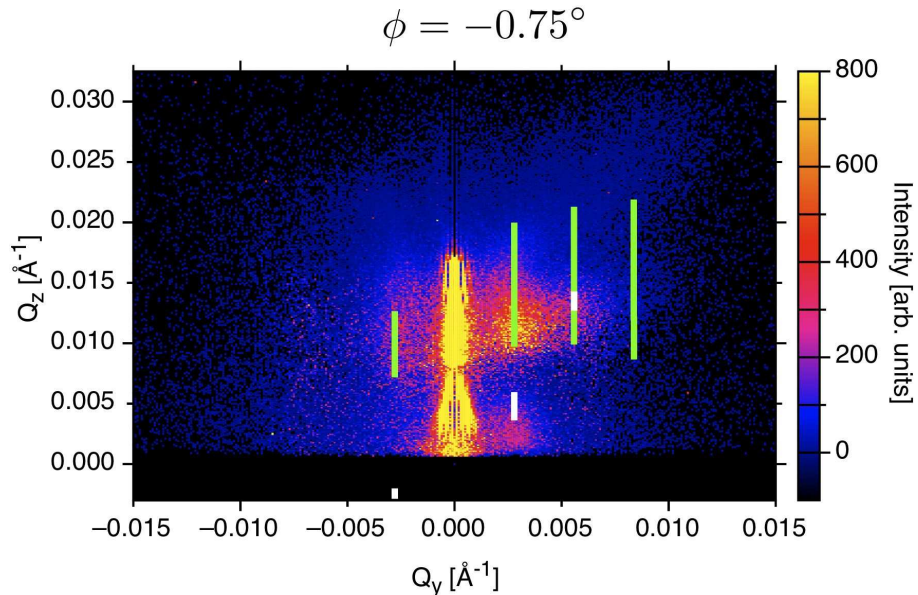
Figure 8.21: *Reconstructed integral reciprocal space image for a nominal sample rotation state of $\phi = -0.75°$ plotted together with the theoretically expected locations of the intensities for reflected (green) and transmitted (white) neutrons.*

applied wavelength spectrum above and below the critical wavelength, as obtained from the plot in figure 8.16, are taken into account and a real space grating periodicity of 225 nm is assumed. These calculated intensity positions up to the third order GTRs for reflected and transmitted neutrons are plotted into the corresponding figure 8.18 for direct comparison with experimental data. The length and the positions of the GTRs can be well described for reflected neutrons. However, the calculated positions of transmitted intensities are not obtainable with the experimentally applied measurement parameters as they lie below the lower edge of the detector for this sample orientation (first order) or are too low in intensity (higher orders). It is apparent that the above formulae do not describe the transmission areas in reciprocal space in the vicinity of the sample horizon where intensities that extend the GTRs of reflected neutrons into the regime below the sample horizon are visible. For an explanation of this intensity distribution, refraction corrections and more sophisticated theoretical methods must be used. Close to the sample horizon, Yoneda peaks [107] are expected (and visible) and the transmission function is also expected to be complicated for the transmitted intensities; therefore, a Distorted Wave Born Approximation (DWBA) approach as used in [101, 108] is necessary to describe the observations and is planned for the near future after the first DWBA based calculations currently carried out on the simpler system of Ni nanowires on pre-structured Si substrate (8.4) are completed.

Due to the term $\frac{2\,d\,\sin\mp\phi}{n\,\lambda}$ in the square root of equations 8.1 and 8.2, the GISANS pattern is very sensitive to a rotation of the grating around the plane of incidence. As a consequence, the accessible portions of the GTRs also change very asymmetrically around the scattering plane for a given wavelength distribution. The theoretically expected GTRs calculated analogous to the case of the non-rotated sample are shown together with the experimental results in figure 8.20 and figure 8.21. If compared to the case of the non-rotated sample, the theoretically expected intensities of the rotated sample agree less precisely with the measurement for the intensity distributions above the sample horizon, but the first order of transmitted intensities is accessible and their location in reciprocal space is in good agreement with the theoretical predictions.

8.3 Ni Nanowires on faceted Al_2O_3 Substrates

SEM and grazing incidence small angle neutron scattering have been carried out on this sample.

8.3.1 Scanning Electron Microscopy

To investigate the structure of the prepared polycrystalline Ni-nanowire sample, SEM images were taken using the SEM described in 8.1.1.

Figure 8.22 shows the image with the highest magnification. The Ni nanowires on the upper edge of each facet can be identified, as well as the underlying substrate with steep and shallow sides. The observable sample defect is due to a dust particle which shaded parts of the substrate during sample preparation, such that no deposition of
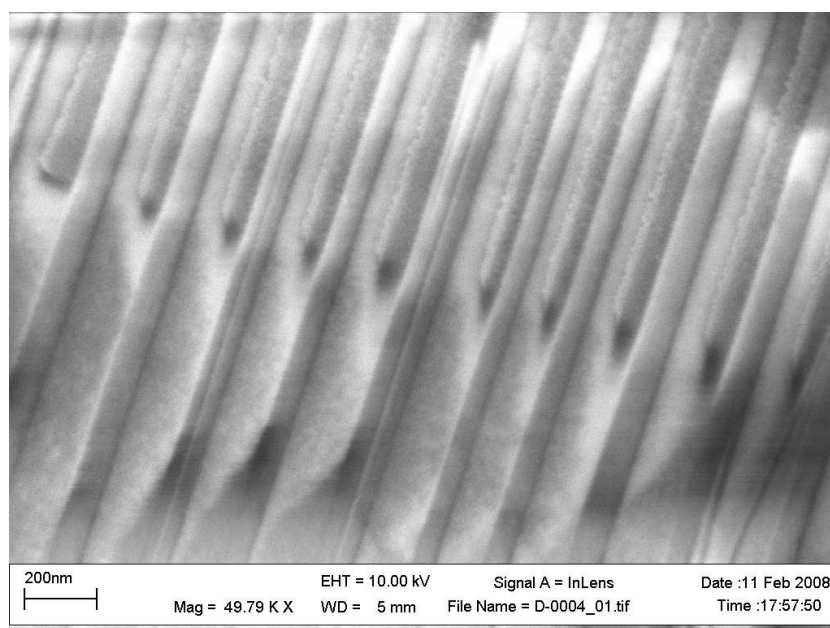
Figure 8.22: *SEM image of nickel nanowires grown by geometrical self shading of a pre-structured sapphire substrate. A sample position is shown where a dust particle shaded parts of the substrate during the deposition process so that no deposition onto the faceted substrate occurred in its shadow. This (rare) sample defect allows the difference between the substrate without nanowires and the area where nanowires were grown to be seen.*

Ni occurred in its shadow. A nanowire periodicity of approximately 225 nm and a corresponding width of approximately 50 nm can be determined.

As with the Gd nanowires (8.2.1), the sample features are below the resolution of the attached EDX and therefore no EDX map could be collected.

8.3.2 Time-of-Flight Grazing Incidence Small Angle Neutron Scattering

TOF-GISANS measurements on the Ni nanowire sample were carried out using REF-SANS with instrument parameters identical to those in 8.2.4. The measurements were performed for various orientations in ϕ around the sample normal. One set of measurements was carried out in the vicinity of $\phi = 0°$ at a fixed goniometer angle of incidence $\alpha_i = 0.621°$ and another set in the vicinity of $\phi = 180°$ at $\alpha_i = 0.618°$.

Data evaluation was performed as described in 8.2.4 and the reconstructed integral reciprocal space images are given in figure 8.23 for various orientations in ϕ, together with the corresponding measurements for the $\phi + 180°$ rotated sample.

Discussion

As expected, the images taken near $\phi = 180°$ are mirrored measurements of those taken in the vicinity of $\phi = 0°$. They display a highly complex situation due to multiple overlapping effects.
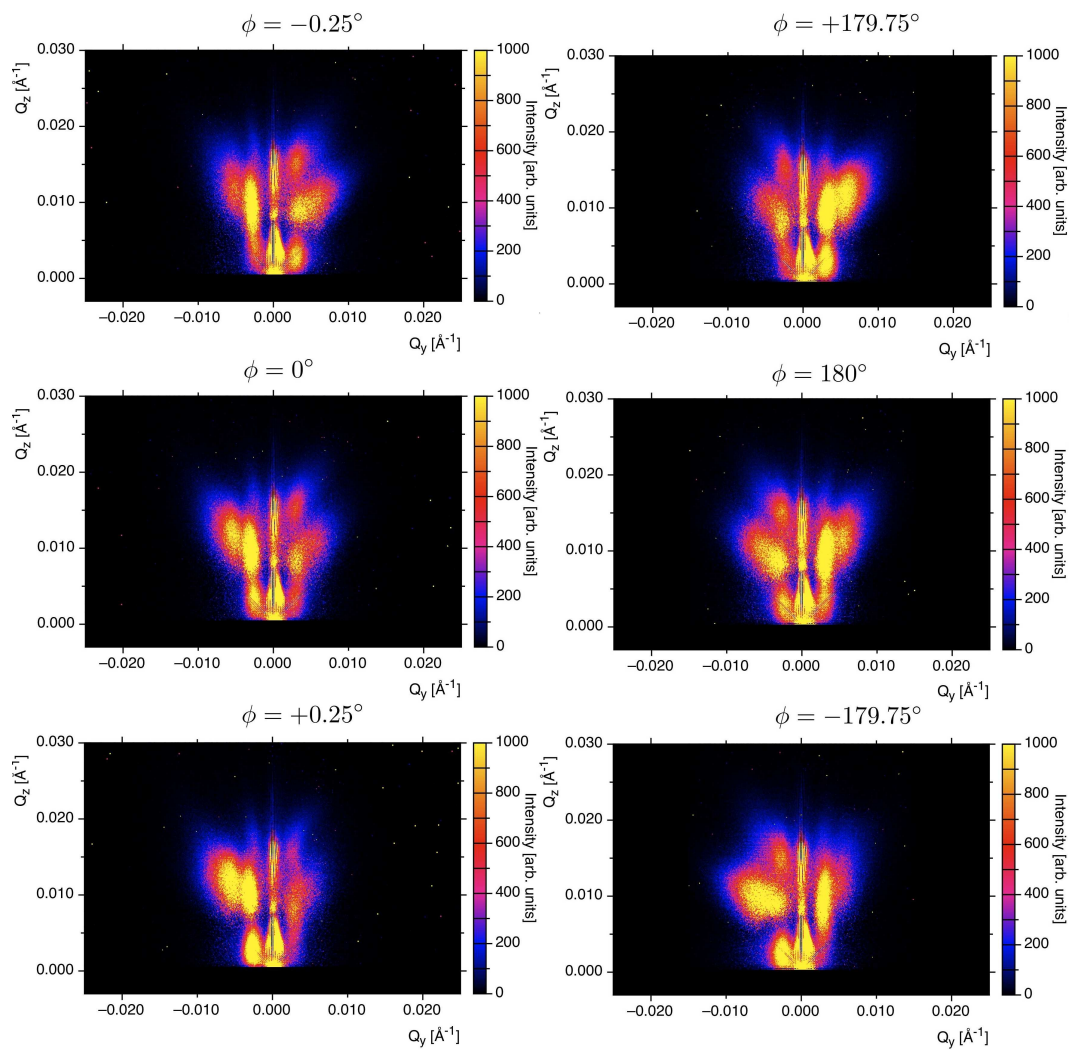
Figure 8.23: *Integral images over all wavelengths showing the complete reciprocal space image for all the applied multiple wavelength slices for corresponding rotation angles of $\phi = -0.25°$ and $\phi = 179.75°$, $\phi = 0°$ and $\phi = 180°$ as well as $\phi = 0.25°$ and $\phi = -179.75°$.*

The intensities at $Q_y = \pm 3.1 \times 10^{-3}\,\text{Å}^{-1}$ on both sides of the specular beam direction can be associated with reconstructed portions of the GTRs which result from a lateral nickel nanowire periodicity of 224 nm. This value is identical to the periodicity obtained from the SEM image (figure 8.22).

In addition to these in Q_y static GTRs, intensities are visible which change their Q_y-location as a function of the corresponding Q_z-values. A rational explanation is to conclude that these in Q-space non-localised intensities originate from diffuse scattering on the flanks of the sapphire facets on the substrate. The observable pronounced asymmetric intensity distribution also strengthens this conclusion as the facets of the pre-structured surface have sides with different slopes and consequently offer asymmetric scattering conditions. Diffuse scattering from the substrate also explains an observable cross-correlation in the intensity distribution of the measurements which were taken from slightly rotated samples: the reciprocal space image of $\phi = 180.25°$ which is expected to show a mirrored intensity distribution of the case where the sample is orientated at $\phi = +0.25°$ actually more closely resembles the mirrored reciprocal space image of the sample with an orientation state of $\phi = -0.25°$. This can also be observed for the situations of $\phi = 179.75°$ and $\phi = +0.25°$. This cross-correlation can only be due to the sample substrate which is rotated by $\phi = 180°$ and hence mirrored to the case of $\phi = 0°$ whilst the scattering from the nanowires should be identical for both cases, $\phi = 180°$ and $\phi = 0°$.

In order to conclusively clarify the nature of these in Q_y non-localised intensities and to quantitatively isolate them from the scattered intensities which are solely due to scattering on the nanowires, additional measurements on a blank faceted substrate and subsequent DWBA analysis are planned.

If comparing these TOF-GISANS results to the results obtained from TOF-GISANS on Al-capped Gd nanowires (8.2.4) on identical substrates, a significantly less symmetric intensity distribution is obtained. Except for the type of material (Ni instead of Gd) the only structural difference lies in the presence of an Al capping layer in the case of Gd. A suitable explanation for the observed difference in the intensity distribution is that the capping layer smoothens the sample surface and hence reduces the scattering from the substrate. This assumption is reasonable as a similar effect has been observed for roughness propagation in thin polysterene films [45]. The influence of the capping layer on the TOF-GISANS signal hence also requires a systematic future study on variously prepared samples, with and without capping layers.

8.4   Ni Nanowires on Pre-structured Si Substrate

This sample was prepared immediately prior to the completion of the project and represents the state-of-the-art in sample preparation capabilities. Here, a characterisation by SEM, AFM/MFM and off-specular x-ray and polarised neutron scattering is presented. Also first DWBA based analysis is carried out on off-specular x-ray data.
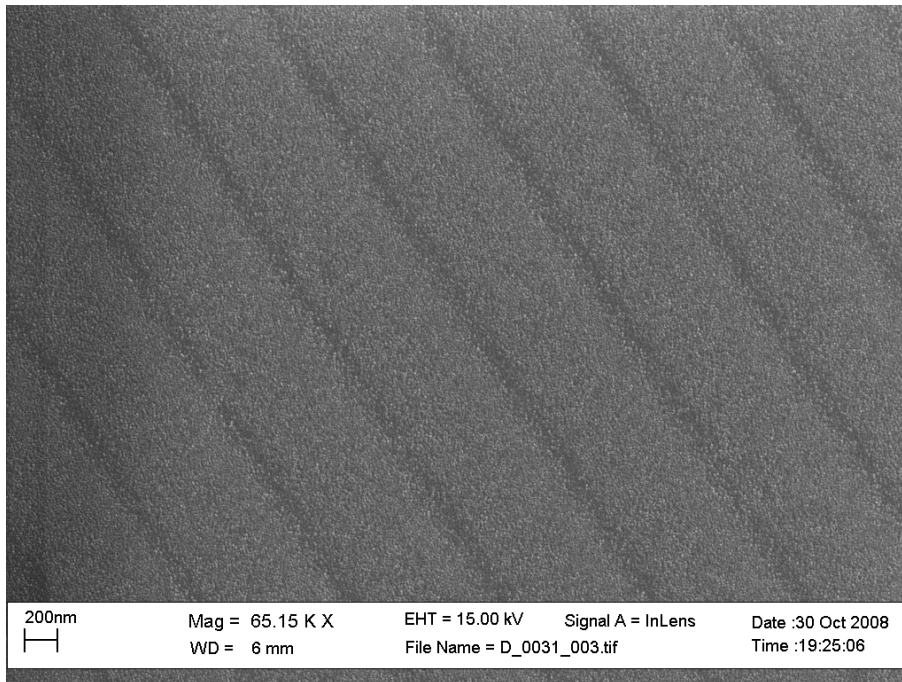
Figure 8.24: *SEM micrograph of 10 nm wide Ni nanowires grown on pre-structured Si substrates with a spacing of 750 nm. The wires are visible through the Al capping layer as dark regions.*

8.4.1   Scanning Electron Microscopy

Initial structural analyses of the prepared Ni-nanowires on pre-structured silicon substrates were performed by SEM imaging, using the SEM described in 8.1.1 and similar working and imaging parameters.

Figure 8.24 shows the sample surface with approximately 10 nm wide Ni nanowires at a spacing of approximately 750 nm as dark regions below the Al capping layer whose nanocrystalline structure is also visible.

8.4.2   AFM and MFM Measurements

In order to confirm the SEM results and to collect information on the magnetic character of the Ni nanowire sample, AFM and MFM micrographs were taken. As in 8.1.3, all the height and magnetic information images shown hereafter were collected at the IFW Dresden using the VEECO™ Digital Instruments 3100 Atomic Force Microscope with identical primary operation parameters.
Figure 8.25 shows an AFM image over a range of $4 \, \mu m \times 4 \, \mu m$ with a resolution of 512×512 pixels giving a Ni nanowire valley-to-rim height of approximately 10 nm.

The MFM images were obtained with a 30 nm lift height at zero magnetic field and with a magnetic field of 80 mT applied in-plane perpendicular to the direction of the nanowires. This direction was chosen because only magnetic stray fields can be probed by MFM and these are not visible if the magnetisation lies within the
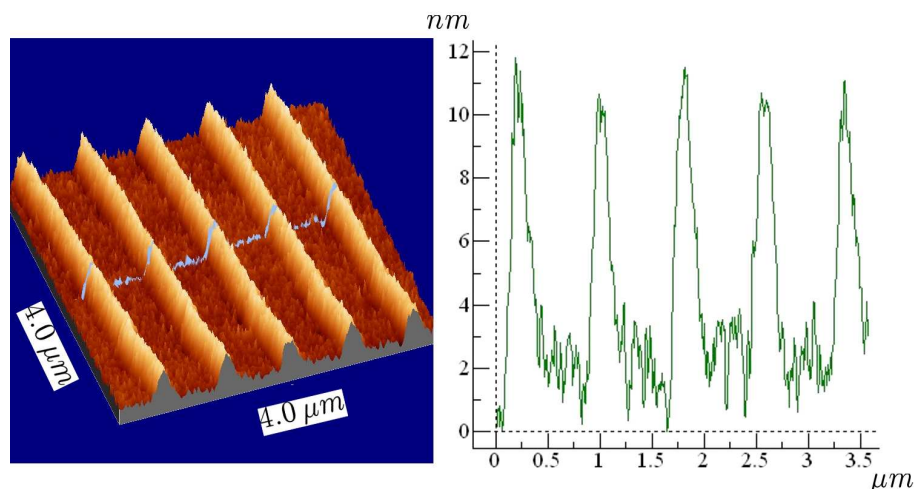
Figure 8.25: *3D representation of the AFM micrograph showing the prepared Ni nanowire sample as obtained from the first pass of the MFM measurements. The scan range is 4 µm × 4 µm and a corresponding height trace along the drawn line is shown on the right of the 3D representation.*

magnetically saturated nanowires[3]. Figure 8.26 shows the height information on the left with the corresponding magnetic force image on the right at zero magnetic field and in a field of 80 mT. The visible bright/dark contrast in the case of an applied magnetic field confirms the magnetic nature of the sample.

8.4.3   Off-Specular X-ray Scattering

The lateral periodicity over a macroscopic distance was probed for this sample by off-specular x-ray scattering. The reciprocal space map shown in figure 8.27 was collected using the Bruker™ AXS D8 Advance two-circle x-ray diffractometer in the configuration described in 8.1.4. A slight misalignment, accounting for a fixed offset in ω, was corrected in the data analysis process.

For this Ni nanowire sample, reciprocal space was mapped for 2θ values of $0.100° \leq 2\theta \leq 6.000°$ with a variable step width of $\Delta 2\theta = 0.010°$ to $\Delta 2\theta = 0.025°$. Data acquisition time was adapted to the scattered intensities from 0.1 s/point for low 2θ values to 14.2 s/point for the highest 2θ angles probed, resulting in a total data collection time of approximately 68 h.

The reciprocal space map covers regions in reciprocal space from $Q_z \approx 0.01 \, \text{Å}^{-1}$ to $Q_z \approx 0.43 \, \text{Å}^{-1}$ and gives access to diffusely scattered intensities in the region of $Q_x \approx -2.3 \times 10^{-2} \, \text{Å}^{-1}$ to $Q_x \approx 2.3 \times 10^{-2} \, \text{Å}^{-1}$.

The corresponding real space nanowire centre-to-centre distance d was calculated as

$$d = \frac{2\pi}{(8.3 \pm 0.1) \times 10^{-4} \text{Å}^{-1}} = 757 \pm 9 \, \text{nm}$$

---

[3]The magnetisation along the nanowires can only be probed if domain boundaries or other termination points exist which allow magnetic stray fields to leave the nanowire.
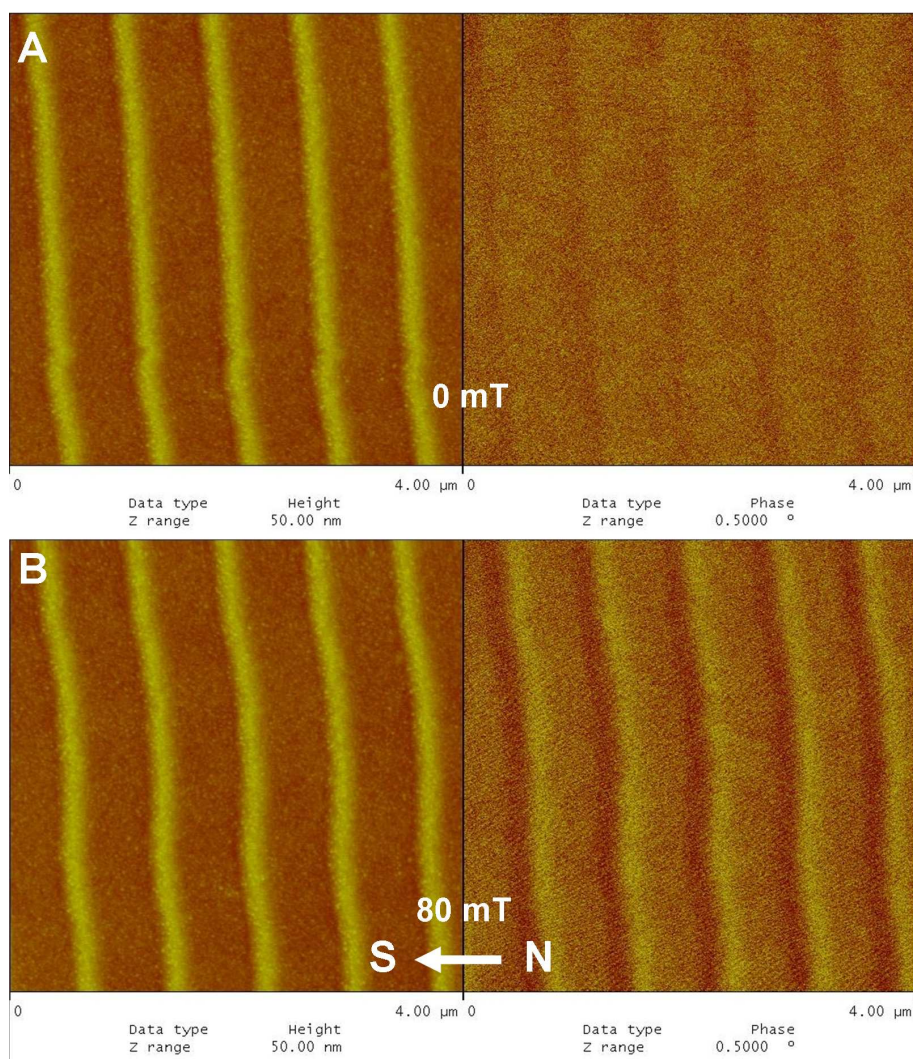
Figure 8.26: *AFM (left) and MFM (right) micrographs of the Ni nanowires in an in-plane oriented magnetic field of 0 mT (A) and 80 mT (B). The bright/dark contrast of the MFM image (B) indicates the magnetic nature of the Ni nanowires. At zero-field (A) the magnetic contrast is not visible.*
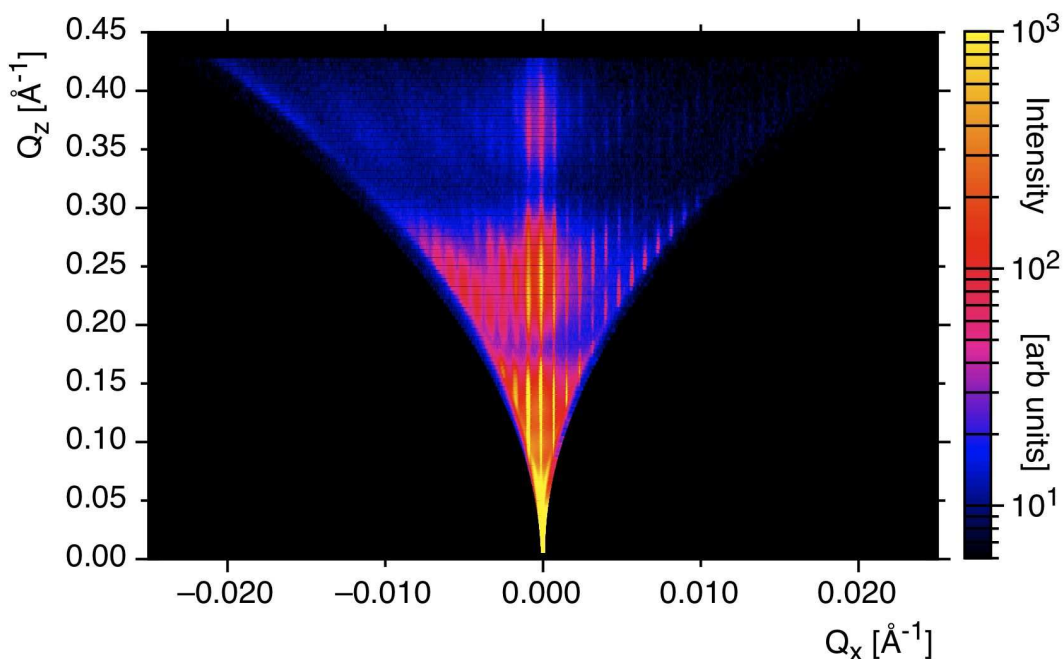
Figure 8.27: *Reciprocal space map of the Ni nanowire sample, prepared on a pre-structured Si substrate and collected using rocking scans. The Q_x-values of the off-specular intensities give the lattice spacing through the distance ΔQ_x to $Q_x = 0$.*

which is in good agreement with the value obtained from the SEM image of this sample (figure 8.24).

DWBA based analysis

The outstanding off-specular x-ray scattering results shown in figure 8.27 with 21 visible side maxima in the investigated reciprocal space range indicate a superb lateral structure periodicity of this sample. It was therefore an archetypal candidate for the first DWBA analysis carried out within the framework of this project. In close cooperation with Prof. Dr Boris Toperverg (Ruhr-Universität Bochum), who programmed the DWBA based fitting and simulations program, suitable for the investigated system, the DWBA approach described in 5.5.2 was followed. First the specular reflectivity was extracted from the measurement and a corresponding theoretical model was found by computer aided fitting of the specular reflectivity curve. The obtained transverse layer structure with corresponding averaged scattering length densities was then modified by lateral variations in the SLD and used to simulate the off-specular scattering behaviour.

Fitting of the specular reflectivity curve

From sample preparation and previous analysis it was concluded that the specular reflectivity curve could best be simulated using a four-layer model as shown in the inset of figure 8.28. The lateral variations from which the averaged SLDs for each of these layers can be derived are shown in figure 8.29. From AFM results (8.4.2),
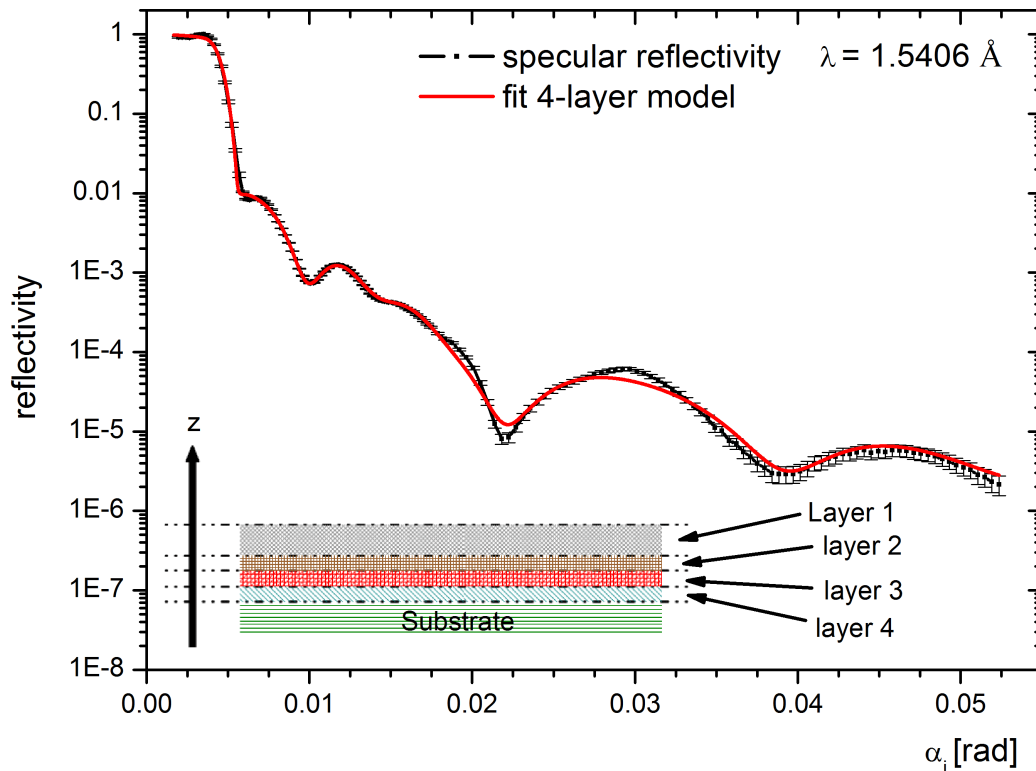
Figure 8.28: *X-ray reflectometry data extracted from the off-specular rocking map of the Ni nanowire sample on Si substrate plotted together with the simulated reflectivity curve of the four-layer model as shown in the inset. Starting from the surface, "layer 1" corresponds to the air/Al capping-layer. The second layer can be interpreted as a layer with a scattering length density (SLD) which is the weighted average of the SLDs of air, Si-Oxide, Ni and Al; the third layer is an Al, Si and Ni layer. Between "layer 3" and the Si substrate an additional layer consisting of Si and naturally present Si-Oxide is assumed ("layer 4").*

it is known that the Al capping layer reproduces the topography of the underlying Si and Ni grating. The uppermost model layer was therefore assumed to have an averaged SLD which may be composed of the SLDs of Al and air. From sample preparation and previous analysis it is further known that the SLD of the second layer from the top must be a weighted averaged of the SLDs of air, Si-Oxide, Ni and Al. The third layer can be assumed to be made of Al, Si and Ni. Between the Si substrate and the just described layer structure an additional layer of Si-Oxide and Si was introduced (layer four) to account for a natural oxide layer, which formed prior deposition of Ni and the Al capping layer. Figure 8.28 shows the good agreement between the extracted and the simulated reflectivity curves as obtained for the four-layer model. The fitted layer structure with the layer thicknesses and averaged SLDs is summarized in table 8.1.

Table 8.1: *Layer parameters as obtained from fitting the specular reflectivity curve. Shown are the layers, the corresponding thicknesses, the real (Re) and imaginary (Im) parts of the averaged scattering length density, together with the roughness factor for each layer, which accounts for damping of the specular reflectivity. A background of order 1×10^{-6} and a slight offset in α_i is included to account for diffuse air scattering and minimal misalignment of the sample below the experimental alignment accuracy ($\approx 2 \times 10^{-4\,\circ}$). The given scaling factor accounts for minimal errors in normalisation of the measured data.*

	thickness [Å]	Re [Å^{-2}]	Im [Å^{-2}]	roughness factor
layer 1	104.701	11.2994×10^{-6}	0.40000×10^{-6}	17.1119
layer 2	38.7849	12.5436×10^{-6}	0.10000×10^{-6}	4.00932
layer 3	39.1774	22.0193×10^{-6}	0.40000×10^{-6}	0.00000
layer 4	12.6843	10.6589×10^{-6}	0.24450×10^{-6}	1.46960
substrate		19.6401×10^{-6}	0.45880×10^{-6}	0.00000
total scaling factor	1.00397			
offset in α_i [rad]	3.49×10^{-6}			
background	2.15413×10^{-6}			

Simulation of off-specular scattering

From the thicknesses and mean SLDs which were obtained by fitting the specular reflectivity curve and by taking into account the information which is available from the sample preparation, a model for the lateral structure could be derived consisting of five lateral variations in the SLD profile with an over-all periodicity of 750 nm. The lateral dimensions (represented by the back coordinates a, b, c, d) as shown in figure 8.29 can be found by simulating the off-specular intensity distribution. By assuming that the Al capping layer has the same SLD as the bulk material ($22.42\,\text{Å}^{-2}$), a starting value of $d \approx 378$ nm could be derived from the averaged SLD of the uppermost layer. As additional starting values, the underlying Si, Si-Oxide and Ni structures were assigned with a width of 94.5 nm each and assigned their bulk SLD values. Due to lateral surface structures, the analysed sample is not isotropic. Therefore, the correlation function 5.19 (page 43) could not be applied. Instead, a suitable K-class correlation function [45] was used to simulate the off-specular scattering. Its Fourier transform can be written as

$$\tilde{C}(\vec{q}_{\parallel}) \propto \frac{\sigma^2 \xi^2}{(1 + q_{\parallel}^2 \xi^2)^{\eta}} \tag{8.3}$$

where $\eta = 1 + h$ is the fractional (fractal) exponent controlling the correlations over distances greater than the correlation length ξ. In detail, for this particular sample ξ accounts for the distance over which irregularities such as stripe roughness and deviations from perfect periodicity in the lateral structures are correlated with each other. Both ξ and η determine the exact line shape of the off-specularly scattered intensities and were adjusted systematically. By further systematic variation of the
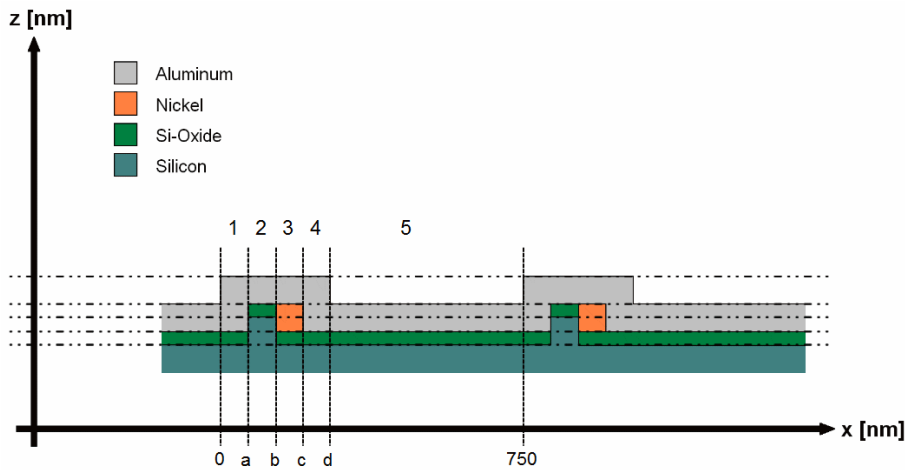
Figure 8.29: *Model of the transverse and lateral structure of the nanowire sample. The thicknesses of the layers and their mean SLDs are known from the specular reflectivity curve. For obtaining the lateral SLD profile with an over-all periodicity of 750 nm, the back coordinates a,b,c,d of the lateral structures (1 to 5) can be determined by simulating the off-specular intensity distribution.*

lateral dimensions and the corresponding SLDs and by additional adjustment of optical parameters such as the divergence or line shape, the measured off-specular intensity distribution could be simulated with excellent agreement (figure 8.30). The simulation parameters are given in table 8.2 and are all of very reasonable physical value such that the nature of the buried sample structures which are not accessible by surface sensitive methods such as SEM or AFM could be clarified. In particular, a slightly reduced density of the Al capping layer $(20.3764\,\text{Å}^{-2})$ as compared with its bulk value $(22.42\,\text{Å}^{-2})$ was identified. Such a variation in the density of thin films is well known [109] and its identification from within the simulation strongly supports the reliability of the simulated model.

8.4.4   Off-specular Neutron Scattering

Motivated by the outstanding off-specular x-ray scattering results, polarised off-specular neutron scattering on this sample was also carried out to probe the magnetic nature of the sample. Reciprocal space maps were collected using the NERO reflectometer at the GENF facility in Geesthacht as described in 8.1.5. Two identical measurements at room temperature in an external magnetic field of 70 mT parallel to the nanowires with opposite polarisation states (spin-down or spin-up) of the incident neutrons were performed. In both cases, the reciprocal space was mapped by means of rocking scans from $\omega = 0°$ to $\omega = 1.8°$ in 90 steps at a measurement time of 200 s/step. For higher angular regions of $\omega = 1.8°$ to $\omega = 3.0°$ the accumulation time was increased to 300 s/step. The reconstructed reciprocal space maps and a difference plot are shown in figure 8.31.

Table 8.2: *Parameters used for simulating the off-specular intensity distribution. Shown are the back coordinates (a,b,c,d) of the lateral structures, the corresponding real (Re) and imaginary (Im) parts of the SLDs, and the parameters which account for the exact line shape of off-specular (η, ξ) and specular (η_0, ξ_0) intensities. The damping of off-specular intensities is realised by a lateral roughness factor. A background of 10 counts and a total scaling factor of 3.13×10^7 were applied for best agreement with the experimental data. The dispersion $\Delta\alpha_i$ and $\Delta\alpha_f$ can be calculated from the slit geometry of the x-ray apparatus. For the lateral structures in all layers, a deviation of the mean periodicity of 10% was allowed. The software used calculates the real (Re) and imaginary (Im) parts of the SLDs for the first lateral structure from the mean SLD of the layer and the SLDs of the remaining lateral structures, such that no values are given in the table.*

	layer 1	layer 2	layer 3	layer 4	substrate
lateral structure 1					
lateral coordinate a [Å]	1042				
lateral structure 2					
lateral coordinate b [Å]	2605				
Re [$\times 10^{-6}$Å^{-2}]	20.3764	20.1500	20.1200	19.6401	19.6401
Im [$\times 10^{-6}$Å^{-2}]	0.41000	0.45750	0.45750	0.24450	0.45880
lateral structure 3					
lateral coordinate c [Å]	3126				
Re [$\times 10^{-6}$Å^{-2}]	20.3764	64.35	64.35	10.3985	19.6401
Im [$\times 10^{-6}$Å^{-2}]	0.41000	1.349	1.349	0.24450	0.45880
lateral structure 4					
lateral coordinate d [Å]	4168				
Re [$\times 10^{-6}$Å^{-2}]	20.3764	20.3764	20.3764	10.3985	19.6401
Im [$\times 10^{-6}$Å^{-2}]	0.41000	0.41000	0.41000	0.24450	0.45880
lateral structure 5					
periodicity [Å]	7500				
Re [$\times 10^{-6}$Å^{-2}]	0.00000	0.00000	20.3764	10.3985	19.6401
Im [$\times 10^{-6}$Å^{-2}]	0.00000	0.00000	0.39000	0.24450	0.45880
optical parameters					
wavelenght [Å]	1.5406				
$\Delta\alpha_i$ [mrad]	0.475				
$\Delta\alpha_f$ [mrad]	0.475				
η	0.27				
η_0	0.12				
ξ [Å^{-1}]	5×10^4				
ξ_0 [Å^{-1}]	1×10^5				
lat. roughness fact.	1.7×10^3				
dev. in lat. mean per.	0.9				
total scaling factor	3.13×10^7				
background [cts]	10				
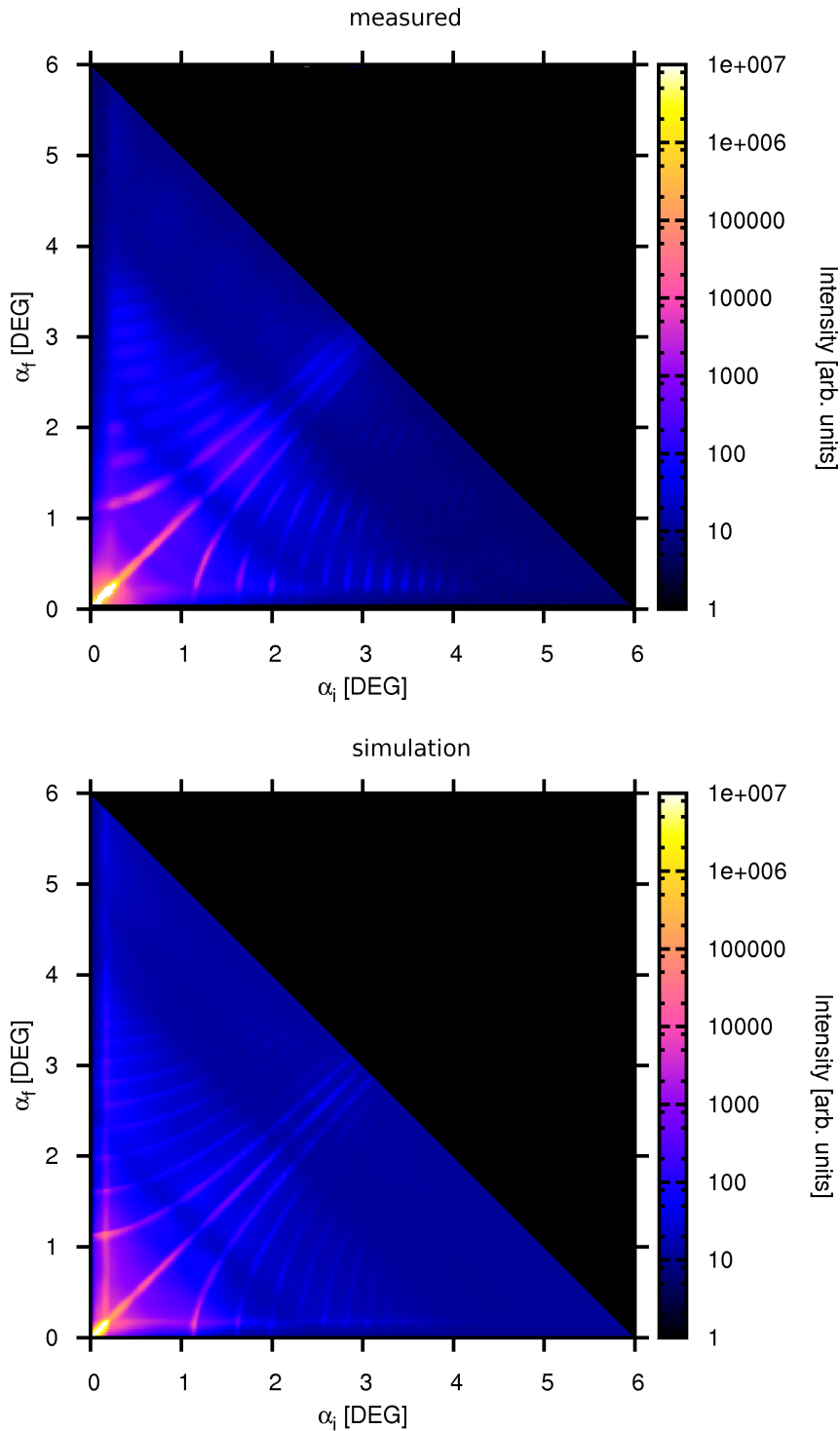
Figure 8.30: *Off-specular scattering maps for Ni nanowires on prestructured Si substrate. The top image shows the intensities as measured by x-ray rocking scans. The bottom image gives the intensity distribution as obtained from the DWBA fit and simulations. Apart from a slight discrepancy in the diffuse background, the theoretical model is in excellent agreement with the measurements. In this representation the fitted specular path is on the diagonal through the origin.*
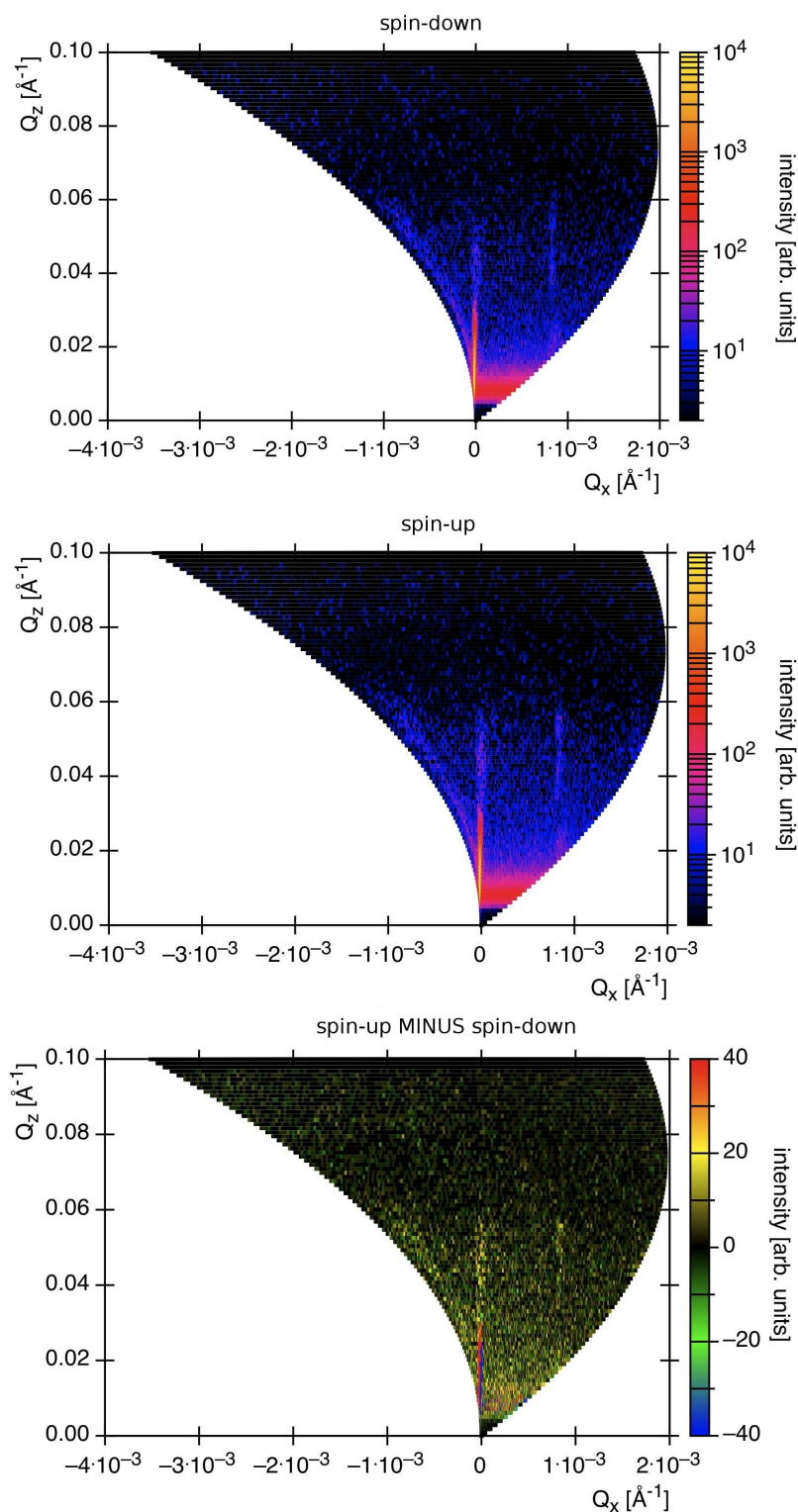
Figure 8.31: *Reciprocal space maps as obtained by "rocking" scans using spin-down (top) and spin-up (centre) polarised neutrons, shown together with the difference in the intensity distribution (bottom). The off-specular intensities at $Q_x = 8.4 \times 10^{-4} \, \AA^{-1}$ give the first order of lateral lattice spacing of the Ni nanowires in reciprocal space.*

In all cases, off-specular intensities at $Q_x = 8.4 \times 10^{-4}\,\text{Å}^{-1}$ are visible, which corresponds to a lattice spacing of

$$d = \frac{2\pi}{(8.4 \pm 0.1) \times 10^{-4}\text{Å}^{-1}} = 748 \pm 9\,\text{nm}.$$

This is again in excellent agreement with the x-ray and SEM data. Additionally, a small shift in Q_z for specular and off-specular intensities is observed if the polarisation state of the neutrons is changed. Qualitatively, this can be explained by the modification of the scattering length due to the magnetic component p which also varies the scattered intensities (equation 5.23 on page 46). Also, the very fact that a magnetic signal can be obtained from polarised neutron scattering in the off-specular regions from a sample with a weak magnetic behaviour (Ni) and with less than 2 % of surface coverage[4] clearly marks a significant milestone in the achievement of sample preparation and analysis in this project.

The methodology for a quantitative analysis of the polarised neutron scattering data has been established by the successful simulation of the off-specular x-ray intensity distribution (8.4.3). However, as the observed magnetic effect is currently not sufficiently resolved for a quantitative analysis of the NERO data, the measurements will be repeated on the GKSS high flux neutron reflectometer REFSANS [64, 65] at the FRM II neutron source which offers a better signal-to-noise ratio. The required polarisation capabilities are planned to be installed on REFSANS in the first half of 2010. Until then, the DWBA based fitting and simulation software will also be modified to not only allow the regions above the sample horizon (as was sufficient for the x-ray case), but also the regions below the sample horizon to be simulated where the highest off-specular intensities, caused by neutrons which penetrate the sample after the scattering event, are observable. Complementary to the structural information obtained by off-specular x-ray scattering, these measurements with polarised neutrons and the corresponding DWBA analysis allow the full magnetic profile of the Ni nanowire sample to be analysed, including the magnetisation within the wires and their magnetic interfaces.

---

[4]The total quantity of Ni on this sample correspons to that of an only 1.3 Å thick Ni layer

Chapter 9

Conclusion and further research

Significant progress has been achieved in developing the experimental capabilities for preparing highly ordered nanometre to submicron structured magnetic samples with a homogeneous sample area of several cm^2 for proposed future inelastic neutron scattering experiments.

As the first experimental step of this project, existing equipment was used for sample growth and preparation studies. In parallel, these sample preparation capabilities were extended by setting up new equipment and techniques. Additionally, the experimental research carried out within the framework of this project also motivated a new theoretical approach to the spin wave dynamics in systems of two- and three-dimensional superlattices of magnetic particles [LOP-1], which was therefore briefly reviewed and put into the context of other theoretical approaches in chapter 2.

Magnetron sputtering onto silicon substrates is the standard method at GKSS Research Centre for the deposition of thin films of various materials. This method, combined with laser interference lithography, carried out in the clean room facilities at University of Hamburg, was used initially for the successful preparation of a Ni nanodot sample (chapter 7). As the use of sputter deposition for film growth and laser interference lithography for lateral structuring requires a means of transferring a photo resist pattern into an underlying layer, Argon ion beam milling equipment was designed, set up and put into successful operation for this purpose as a component of a custom designed UHV e-beam evaporation chamber (chapter 4). However, the combined use of these techniques does not allow the preparation of samples with lateral structures below approximately 200 nm. Therefore, another sample preparation process was simultaneously followed for depositing smaller structures, in the form of geometrical self-shading of a pre-structured substrate (chapter 7).

Preparation of finer nanostructured samples by this technique requires a directed evaporant beam which is not achievable by sputtering due to its high working gas pressures. Electron-beam evaporation was therefore specifically chosen as the deposition technique and a new vacuum chamber with corresponding peripheral equipment was constructed, designed especially for preparation of nanostructured samples by the outlined self-shading technique (chapter 4). The setup proved very suitable for the purpose of nanowire growth by self-shading of pre-structured substrates. It al-

lowed several samples with nanoscale Ni structures, as well as the first reported Gd nanowire sample, to be prepared (chapter 7).

In the framework of sample preparation, epitaxial growth studies for Ni on Si were also carried out (chapter 6) to allow the preparation of laterally structured samples with a well defined crystalline order. In particular, a new deposition method for direct epitaxial growth of Ni on Si with the epitaxial relationship Ni[100]‖Si[110] and Ni(001)‖Si(001) was developed and an unprecedented crystalline quality was achieved by thermal tuning during the deposition process [LOP-2]. This technique can now also be used to prepare epitaxial Ni nanodot and nanowire arrays.

Sample characterisation of the prepared Ni nanodot, and Ni and Gd nanowire samples (chapter 8) was carried out by several techniques (described in chapter 5), with emphasis on using x-ray and neutron scattering with laboratory (x-ray) and reactor (neutron) sources. The investigated samples showed a superb lateral homogeneity and the expected magnetic behaviour. In the framework of sample analysis, a novel application of time-of-flight grazing incidence small angle neutron scattering technique was followed [LOP-3]. It also required the development of additional analysis software which allows for a combined evaluation of all applied wavelengths and extends the standard REFSANS [64, 65] data analysis by allowing an integral reconstruction of large portions of reciprocal space (8.2.4). These data analysis capabilities are an essential basis for inelastic neutron scattering on REFSANS.

The current state of the art in sample preparation was demonstrated immediately prior to the completion of the project with the preparation of a Ni nanowire sample of superb lateral homogeneity. Its outstanding off-specular scattering behaviour also allowed a Distorted-Wave Born Approximation based analysis of the collected off-specular x-ray data which was carried out in cooperation with Prof. Dr Boris Toperverg (Ruhr-Universität Bochum). This also cleared the way to a future quantitative analysis of the magnetic structure using polarised off-specular neutron scattering experiments (8.4.3), which are planned to be carried out in 2010, as soon as polarised neutrons become available on REFSANS.

In 2010, REFSANS will also be upgraded to a novel chopper system with faster rotating chopper discs. These will offer specifically designed inelastic mode neutron windows for forming the required intense and short neutron pulses, thereby making REFSANS the world's first neutron reflectometer capable of inelastic neutron scattering experiments. Inelastic mode measurements were previously not possible on REFSANS due to the large losses in neutron intensity caused by the slow rotation speed of the current chopper system. After a short commissioning phase conducting inelastic test measurements on bulk-like samples such as a thick Dy layer for which reference data sets collected on a triple-axis neutron spectrometer are available, the first inelastic scattering experiments on laterally nanostructured samples are expected to be attempted late in the year.

In parallel, further improvements in the nanostructured samples can be made by the already successfully demonstrated use of rare earth materials with high magnetic moments. These can increase the magnetic (and inelastic) neutron scattering signal by more than one order of magnitude. As a longer term perspective, the spacing between the nanostructures can be reduced by using x-ray lithography [16, 110] to realise artificially and therefore highly regularly pre-structured substrates with

periodicities significantly below 100 nm. In this project, priority was given to first mastering the technique of applying the self-shading effect to the growth of nanowires on large pre-structured surfaces, with the goal of producing highly homogeneous interacting nanowires in the low nanometre range as the next development step.

In summary, this project marks significant progress towards inelastic neutron scattering of lateral magnetic nanostructures and raises the possibility of such investigations in the near future. This is essential in, for instance, verifying the theoretical model motivated by this project (chapter 2) and opens the way to a more detailed understanding of the spin wave dispersion in interacting magnetic nanostructures.

Bibliography

[1] R. Skomski. Nanomagnetics. *Journal of Physics: Condensed Matter*, 15(20): R841 – R896, 2003.

[2] C. A. Ross. PATTERNED MAGNETIC RECORDING MEDIA. *Annual Review of Materials Research*, 31(1):203 – 235, 2001.

[3] B. D. Terris and T. Thomson. Nanofabricated and self-assembled magnetic structures as data storage media. *Journal of Physics D: Applied Physics*, 38 (12):R199 – R222, 2005.

[4] G. N. Kakazei, P. E. Wigen, K. Yu. Guslienko, V. Novosad, A. N. Slavin, V. O. Golub, N. A. Lesnik, and Y. Otani. Spin-wave spectra of perpendicularly magnetized circular submicron dot arrays. *Applied Physics Letters*, 85(3):443 – 445, Jul 2004.

[5] Jeffrey B. Kortright, Olav Hellwig, Karine Chesnel, Shouheng Sun, and Eric E. Fullerton. Interparticle magnetic correlations in dense Co nanoparticle assemblies. *Physical Review B*, 71(1):012402, 2005.

[6] B. Hillebrands and K. Ounadjela (Eds.). *Spin Dynamics in Confined Magnetic Structures I*. Springer-Verlag Berlin Heidelberg New York, 2002. ISBN 978-3-540-41191-8.

[7] J. A. C. Bland and B. Heinrich (Eds.). *Ultrathin Magnetic Structures I*. Springer-Verlag Berlin Heidelberg New York, 1st edition, 1994. ISBN 3-540-57407-7.

[8] B. Heinrich and J. A. C. Bland (Eds.). *Ultrathin Magnetic Structures II*. Springer-Verlag Berlin Heidelberg New York, 1st edition, 1994. ISBN 3-540-57687-8.

[9] R. Arias and D. L. Mills. Magnetostatic modes in ferromagnetic nanowires. *Physical Review B*, 70(9):094414, Sep 2004. doi: 10.1103/PhysRevB.70. 094414.

[10] M. P. Kostylev, G. Gubbiotti, J.-G. Hu, G. Carlotti, T. Ono, and R. L. Stamps. Dipole-exchange propagating spin-wave modes in metallic ferromagnetic stripes. *Physical Review B*, 76(5):054422, 2007.

[11] S. Sun, C. B. Murray, D. Weller, L. Folks, and A. Moser. Monodisperse FePt Nanoparticles and Ferromagnetic FePt Nanocrystal Superlattices. *Science*, 287(5460):1989 – 1992, Mar 2000.

[12] E. V. Shevchenko, D. V. Talapin, A. L. Rogach, A. Kornowski, M. Haase, and H. Weller. Colloidal Synthesis and Self-Assembly of $CoPt_3$ Nanocrystals. *Journal of the American Chemical Society*, 124(38):11480 – 11485, 2002.

[13] G. Gubbiotti, G. Carlotti, R. Zivieri, F. Nizzoli, T. Okuno, and T. Shinjo. Spin wave modes in submicron cylindrical dots. *Journal of Applied Physics*, 93(10):7607 – 7609, 2003.

[14] C. Bayer, J. Jorzick, B. Hillebrands, S. O. Demokritov, R. Kouba, R. Bozi-noski, A. N. Slavin, K. Y. Guslienko, D. V. Berkov, N. L. Gorn, and M. P. Kostylev. Spin-wave excitations in finite rectangular elements of $Ni_{80}Fe_{20}$. *Physical Review B*, 72(6):064427, Aug 2005.

[15] Gary M. McClelland, Mark W. Hart, Charles T. Rettner, Margaret E. Best, Kenneth R. Carter, and Bruce D. Terris. Nanoscale patterning of magnetic islands by imprint lithography using a flexible mold. *Applied Physics Letters*, 81(8):1483 – 1485, 2002.

[16] N. Bardou, B. Bartenlian, F. Rousseaux, D. Decanini, F. Carcenac, E. Cam-bril, M. F. Ravet, C. Chappert, P. Veillet, P. Beauvillain, R. Mégy, W. Geerts, and J. Ferré. Elaboration and magneto-optical study of submicron magnetic structures in Au/Co/Au ultrathin films. *Journal of Magnetism and Magnetic Materials*, 156(1-3):139 – 140, 1996. Proceedings of the Second International Symposium on Metallic Multilayers.

[17] Z. R. Dai, Shouheng Sun, and Z. L. Wang. Phase Transformation, Coalescence, and Twinning of Monodisperse FePt Nanocrystals. *Nano Letters*, 1(8):443 – 447, 2001.

[18] R. M. Nicklow. Spin-Wave Dispersion Relation in Rare-Earth Metals. *Journal of Applied Physics*, 42(4):1672 – 1679, 1971.

[19] Helena Tartakovskaya. private communication, 2009. Institute for Magnetism, National Ukrainian Academy of Science, Vernadsky ave 36b, Kiev 03142, Ukraine.

[20] A. Schreyer, T. Schmitte, R. Siebrecht, P. Bodeker, H. Zabel, S. H. Lee, R. W. Erwin, C. F. Majkrzak, J. Kwo, and M. Hong. Neutron scattering on magnetic thin films: Pushing the limits (invited). *Journal of Applied Physics*, 87(9):5443 – 5448, 2000.

[21] J. Nogami, B. Z. Liu, M. V. Katkov, C. Ohbuchi, and Norman O. Birge. Self-assembled rare-earth silicide nanowires on Si(001). *Physical Review B*, 63(23): 233305, May 2001.

[22] Xun Wang and Yadong Li. Rare-Earth-Compound Nanowires, Nanotubes, and Fullerene-Like Nanoparticles: Synthesis, Characterization, and Properties. *Chemistry - A European Journal*, 9(22):5627 – 5635, May 2003.

[23] B. A. Kalinikos and A. N. Slavin. Theory of dipole-exchange spin wave spectrum for ferromagnetic films with mixed exchange boundary conditions. *Journal of Physics C: Solid State Physics*, 19(35):7013 – 7033, Dec 1986.

[24] K. Yu. Guslienko, S. O. Demokritov, B. Hillebrands, and A. N. Slavin. Effective dipolar boundary conditions for dynamic magnetization in thin magnetic stripes. *Physical Review B*, 66(13):132402, Oct 2002.

[25] A. Yu. Galkin, B. A. Ivanov, and C. E. Zaspel. Collective modes for an array of magnetic dots in the vortex state. *Physical Review B*, 74(14):144419, 2006.

[26] M. A. Załuska Kotur. Interacting small-particle systems: Modified local-mean-field model. *Physical Review B*, 54(2):1064 – 1071, Jul 1996.

[27] D. Kechrakos and K. N. Trohidou. Magnetic properties of dipolar interacting single-domain particles. *Physical Review B*, 58(18):12169 – 12177, Nov 1998.

[28] A. Cehovin, C. M. Canali, and A. H. MacDonald. Elementary excitations of ferromagnetic metal nanoparticles. *Physical Review B*, 68(1):014423, Jul 2003.

[29] R. Arias and D. L. Mills. Theory of collective spin-wave modes of interacting ferromagnetic spheres. *Physical Review B*, 70(10):104425, Sep 2004. doi: 10.1103/PhysRevB.70.104425. URL `http://link.aps.org/doi/10.1103/PhysRevB.70.104425`.

[30] Ping Chu, D. L. Mills, and Rodrigo Arias. Exchange/dipole collective spin-wave modes of ferromagnetic nanosphere arrays. *Physical Review B*, 73(9): 094405, 2006.

[31] M. Kafesaki and E. N. Economou. Interpretation of the band-structure results for elastic and acoustic waves by analogy with the LCAO approach. *Physical Review B*, 52(18):13317 – 13331, Nov 1995.

[32] J. Jorzick, S. O. Demokritov, B. Hillebrands, M. Bailleul, C. Fermon, K. Y. Guslienko, A. N. Slavin, D. V. Berkov, and N. L. Gorn. Spin Wave Wells in Nonellipsoidal Micrometer Size Magnetic Elements. *Physical Review Letters*, 88(4):047204, Jan 2002.

[33] Danica Mira Solina. *A Study of Thin Film Interfaces and Multilayers for Hard X-ray Mirrors*. PhD thesis, Department of Applied Physics, University of Technology Sydney, Australia, 2002.

[34] Jae Sung ITS. IonBeamMiller.gif. Online: Last accessed on October 13 2008. `http://www.jsits.com/images/IonBeamMiller.gif`.

[35] A. I. Maaroof and B. L. Evans. Onset of electrical conduction in Pt and Ni films. *Journal of Applied Physics*, 76(2):1047 – 1054, 1994.

[36] A. Matthes, F. Schmidl, K.-U. Barholz, F. Elschner, H. Schneidewind, and P. Seidel. Electrical end-point detection during ion beam etching of thin films and multilayers. *Superconductor Science and Technology*, 8(8):676 – 679, Aug 1995.

[37] Carl Zeiss SMT - Nano Technology Systems Division. SUPRA™ Series with GEMINI® Column, 2005. Prospectus.

[38] FEI COMPANY™ TOOLS FOR NANTECH. Magellan™ XHR SEM, 2008. Prospectus.

[39] F. J. Giessibl. AFM's path to atomic resolution. *Materials Today*, 8(5):32 – 41, May 2005.

[40] www.nanomagnetics.org. Magnetometers vibrating sample magnetometer – magnetometers –. Online: Last accessed on October 13 2008. URL `http://www.nanomagnetics.org/instrumentation_and_characterization/VibratingSampleMagnetometers_vsm.php`. `http://www.nanomagnetics.org/instrumentation_and_characterization/VibratingSampleMagnetometers_vsm.php`.

[41] B. D. Cullity and S. R. Stock. *Elements of X-Ray Diffraction*. Prentice Hall, Pearson Education International, 3rd edition, 2001. ISBN 0-13-178818-3.

[42] M. R. Schuster, H. Goebel, L. Bruegemann, D. Bahr, F. Burgaezy, C. Michaelsen, M. Stoermer, P. Ricardo, R. Dietsch, Th. Holz, and H. Mai. Laterally graded multilayer optics for x-ray analysis. volume 3767, pages 183–198. SPIE, 1999. doi: 10.1117/12.371116. URL `http://link.aip.org/link/?PSI/3767/183/1`.

[43] A. Guinier. *X-Ray Diffraction In Crystals, Imperfect Crystals, and Amorphous Bodies*. Dover Publications Inc., New York, 1994. ISBN 0-486-68011-8.

[44] B. E. Warren. *X-Ray Diffraction*. Dover Publications Inc., New York, 1990. ISBN 0-486-66317-5.

[45] M. Tolan. *X-Ray Scattering from Soft-Matter Thin Films*. Springer-Verlag, Berlin Heidelberg, 1999. ISBN 3-540-65182-9.

[46] BENSC HMI. Parratt32 or the reflectivity tool. Online: Last accessed on October 12 2008. `http://www.hmi.de/bensc/instrumentation/instrumente/v6/refl/parratt_en.htm`.

[47] Grassl and Fuchs. Reflectivity Software WIN-REFSIM, Version 1.1d. Copyright SIEMENS AG (1992–1995).

[48] European Synchrotron Radiation Facility. XOP/IMD. Online: Last accessed on October 12 2008. `http://ftp.esrf.fr/pub/scisoft/xop2.1/`.

[49] D. Lott, D. Solina, M. Störmer, and A. Schreyer. X-Ray and Neutron Scattering Methods: Applied to Thin Films, Oct. 2002. Handout to Internship.

[50] Dieter Lott. *Diffuse Röntgenstreuung an W/Si - Vielschichtsystemen.* Diplomarbeit, Lehrstuhl Prof. Dr. J. Peisl, Ludwig-Maximilians-Universität München, 1995.

[51] P. Mikulík and T. Baumbach. X-ray reflection by rough multilayer gratings: Dynamical and kinematical scattering. *Physical Review B*, 59(11):7632, 1999.

[52] G. Ljungdahl and St. W. Lovesey. Surface Scattering near Grazing Angles: The Distorted Wave Born Approximation for Rough Surfaces. *Physica Scripta*, 53:734 – 748, 1996.

[53] H. Zabel, K. Theis-Bröhl, and B. P. Toperverg. *Handbook of Magnetism and Advanced Magnetic Materials*, volume 33: Novel Techniques for Characterizing and Preparing Samples. John Wiley & Sons, Ltd., 2007. ISBN 978-0-470-02217-7.

[54] Boris P. Toperverg. private communication, 2009. Experimentalphysik IV/Condensed Matter Physics Fakultät für Physik und Astronomie Ruhr-Universität Bochum, 44780 Bochum, Germany.

[55] G. H. Vineyard. Grazing-incidence diffraction and the distorted-wave approximation for the study of surfaces. *Physical Review B*, 26(8):4146, Oct 1982.

[56] S. Dietrich and H. Wagner. Critical Surface Scattering of X Rays and Neutrons at Grazing Angles. *Physical Review Letters*, 51(16):1469, Oct 1983.

[57] S. Dietrich and H. Wagner. Critical magnetic surface scattering of neutrons at grazing angles. *Zeitschrift für Physik B Condensed Matter*, 59:35 – 42, 1985.

[58] S. Dietrich and H. Wagner. Critical Surface Scattering of X-Rays at Grazing Angles. *Zeitschrift für Physik B Condensed Matter*, 56:207 – 215, 1984.

[59] S. Sinha, E. B. Sirota, S. Garoff, and H. B. Stanley. X-ray and neutron scattering from rough surfaces. *Physical Review B*, 38(4):2297, Aug 1988. doi: 10.1103/PhysRevB.38.2297. URL http://prb.aps.org/pdf/PRB/v38/i4/p2297_1.

[60] R. Pynn. Neutron scattering by rough surfaces at grazing incidence. *Physical Review B*, 45(2):602, Jan 1992.

[61] Jens-Peter Schlomka. *Untersuchung der strukturellen und magnetischen Eigenschaften von dünnen NiMnSb-Schichtsystemen.* VWF Verlag für Wissenschaft und Forschung GmbH, Berlin, 1999. ISBN 3-89700-087-3.

[62] Fractal dimension. Online: Last accessed on April 4 2010. http://www.math.sunysb.edu/~scott/Book331/Fractal_Dimension.html.

[63] A.-J. Dianoux and G. Lander (editors). *Neutron Data Booklet.* Institut Laue-Langevin, 38042 Grenoble Cedex 9, FRANCE, 2nd edition, 2003.

[64] R. Kampmann, V. Deriglazov, M. Haese-Seiller, M. Marmotti, M. Tristl, and E. Sackmann. REFSANS: a novel reflectometer for analyses of liquid and soft surfaces at the new research reactor FRM-II in Munich/Germany. *Physica B: Condensed Matter*, 276-278:212 – 213, 2000.

[65] R. Kampmann, M. Haese-Seiller, M. Marmotti, J. Burmester, V. Deriglazov, V. Syromiatnikov, A. Okorokov, F. Frisius, M. Tristl, and E. Sackmann. The novel reflectometer REFSANS for analyses of liquid and soft surfaces at the new research reactor FRM-II in Munich, Germany. *Applied Physics A*, 74 [Suppl.]:S249 – S251, 2002.

[66] Yang-Tse Cheng, Yen-Lung Chen, M. M. Karmarkar, and Wen-Jin Meng. Epitaxial growth of α-Fe films on Si(111) substrates. *Applied Physics Letters*, 59(8):953 – 955, 1991.

[67] Chin-An Chang. Magnetocrystalline Anisotropy of (100) Face-Centered Cubic Co Structures Deposited on Cu/Si(100). *Applied Physics Letters*, 58(16):1745 – 1747, 1991.

[68] Chin-An Chang, Joyce C. Liu, and Joseph Angileilo. Epitaxy of (100) Cu on (100) Si by evaporation near room temperatures: In-plane epitaxial relation and channeling analysis. *Applied Physics Letters*, 57(21):2239 – 2240, 1990.

[69] T. Nishimura, J. Takeda, Y. Asami, Y. Hoshino, and Y. Kido. Initial growth processes of ultra-thin Ni-layers on Si(1 1 1) and electronic structure of epitaxially grown $NiSi_2$. *Surface Science*, 588(1-3):71 – 82, 2005.

[70] T. Ohmi, T. Saito, T. Shibata, and T. Nitta. Room-temperature copper metallization for ultralarge-scale integrated circuits by a low kinetic-energy particle process. *Applied Physics Letters*, 52(26):2236 – 2238, 1988.

[71] G. Gubbiotti, G. Carlotti, C. Minarini, S. Loreti, R. Gunnella, and M. De Crescenzi. Metal-metal epitaxy on silicon: Cu/Ni/Cu ultrathin films on 7x7-Si(111). *Surface Science*, 449(1-3):218 – 226, 2000.

[72] H. Jiang, T. J. Klemmer, J. A. Barnard, and E. A. Payzant. Epitaxial growth of Cu on Si by magnetron sputtering. *Journal of Vacuum Science & Technology A: Vacuum, Surfaces, and Films*, 16(6):3376 – 3383, 1998.

[73] J.M. Daughton. Magnetoresistive memory technology. *Thin Solid Films*, 216 (1):162 – 168, 1992. Papers presented at the International Workshop on Science and Technology of Thin Films for the 21st Century, Evanston,IL, USA, July 28-August 2, 1991.

[74] P. Castrucci, R. Gunnella, R. Bernardini, A. Montecchiari, R. Carboni, and M. De Crescenzi. Epitaxy of Fe/Cu/Si(1 1 1) ultrathin films: an Auger electron diffraction study. *Surface Science*, 482-485(Part 2):916 – 921, 2001.

[75] Chin-An Chang. Reversed magnetic anisotropy in deformed (100) Cu/Ni/Cu structures. *Journal of Applied Physics*, 68(9):4873 – 4875, 1990.

[76] Chin-An Chang. Magnetization of ultrathin (100) Co films deposited on Cu/Si(100). *Journal of Magnetism and Magnetic Materials*, 109(2-3):243 – 248, 1992.

[77] L. Wray and M. Prutton. The structure of nickel and cobalt films on the (111) surface of n-type silicon. *Thin Solid Films*, 15(2):173 – 180, 1973.

[78] D. Berling, P. Bertoncini, A. Mehdaoui, P. Wetzel, G. Gewinner, and B. Loegel. Magnetization reversal mechanisms in epitaxial Fe/Si(0 0 1) layers with twofold and fourfold magnetic anisotropies. *Journal of Magnetism and Magnetic Materials*, 237(2):181 – 190, 2001.

[79] K. S. Grabowski, R. A. Kant, and S. B. Qadri. Epitaxial Growth of Ni on Si by Ion Beam Assisted Deposition. In *Processing and Characterization of Materials Using Ion Beams*, volume 128, pages 279 – 284. Materials Research Society, Pittsburgh, 1989. MRS Symposia Proceedings.

[80] V. A. Burrows, Y. J. Chabal, G. S. Higashi, K. Raghavachari, and S. B. Christman. Infrared spectroscopy of Si(111) surfaces after HF treatment: Hydrogen termination and surface morphology. *Applied Physics Letters*, 53(11):998 – 1000, 1988.

[81] A.M. Ektessabi. Temperature dependence of atomic mixing at the copper-silicon interface. *Thin Solid Films*, 236(1-2):135 – 139, 1993.

[82] Chin-An Chang. Reversal in magnetic anisotropy of (100)Cu-Ni superlattices. *Journal of Magnetism and Magnetic Materials*, 97(1-3):102 – 106, 1990.

[83] P. Rosenbusch, Jaeyong Lee, G. Lauhoff, and J. A. C. Bland. Magnetisation reversal in thin Cu/Ni/Cu/Si(0 0 1) films. *Journal of Magnetism and Magnetic Materials*, 172(1-2):19 – 25, 1997.

[84] K. L. Chopra. *Thin Film Phenomena*. McGRAW-Hill INC, Krieger Publishing Comp., New York, reprint edition edition, 1979. ISBN 0-88275-746-6.

[85] P. H. Leo and M. H. Schwartz. The energy of semicoherent interfaces. *Journal of the Mechanics and Physics of Solids*, 48(12):2539 – 2557, 2000.

[86] J. G. Louderback, A. J. Cox, L. J. Lising, D. C. Douglass, and L. A. Bloomfield. Magnetic properties of nickel clusters. *Zeitschrift für Physik D Atoms, Molecules and Clusters*, 26(1):301 – 303, 1993.

[87] I. Abbati, L. Braicovich, B. De Michelis, U. del Pennino, and S. Valeri. Valence photoemission study of temperature dependent reaction products in Ni-Si interfaces and thin films. *Solid State Communications*, 43(3):199 – 202, 1982.

[88] G.L.P. Berning and L.L. Levenson. Diffusion of nickel in silicon below 475 °C. *Thin Solid Films*, 55(3):473 – 482, 1978.

[89] T. Young. An Essay on the Cohesion of Fluids. *Philosophical Transactions of the Royal Society of London*, 95:65 – 87, 1805. URL `http://upload.wikimedia.org/wikipedia/commons/8/85/Thomas_Young-An_Essay_on_the_Cohesion_of_Fluids.pdf`.

[90] Midori Kawamura, Yoshio Abe, and Katsutaka Sasaki. Orientation of metal films deposited by sputtering using Ar/N2 gas mixtures. *Thin Solid Films*, 469-470:491 – 494, 2004.

[91] J. A. Thornton. High Rate Thick Film Growth. *Annual Review of Materials Science*, 7(1):239 – 260, 1977.

[92] C. V. Thompson. Grain Growth in Thin Films. *Annual Review of Materials Science*, 20(1):245 – 268, 1990.

[93] G. Bayreuther. Vakuum, Oberflächen, dünne Schichten, WS 2001 - 2002. Lecture held at Universität Regensburg, Naturwissenschaftliche Fakultät II - Physik, Universitätsstraße 31, 93053 Regensburg, Germany.

[94] J. A. Venables, G. D. T. Spiller, and M. Hanbucken. Nucleation and growth of thin films. *Reports on Progress in Physics*, 47(4):399–459, 1984. URL `http://stacks.iop.org/0034-4885/47/399`.

[95] C. Ratsch, P. Ruggerone, and M. Scheffler. Study of Strain and Temperature Dependence of Metal Epitaxy. *arXiv:cond-mat/9709293v1 [cond-mat.mtrl-sci]*, 2008.

[96] K. L. Chopra and M. R. Randlett. EFFECT OF ULTRASONIC VIBRATIONS OF THE SUBSTRATE ON THE GROWTH OF THIN METAL FILMS. *Applied Physics Letters*, 11(6):202 – 203, 1967.

[97] M. Henzler and W. Göpel. *Oberflächenphysik des Festkörpers*. Teubner, Stuttgart, 2nd edition, 1994. ISBN 3-519-13047-5.

[98] M. Huth, K. A. Ritley, J. Oster, H. Dosch, and H. Adrian. Highly Ordered Fe and Nb Stripe Arrays on Facetted α-Al$_2$O$_3$(10$\bar{1}$0). *Advanced Functional Materials*, 12(5):333 – 338, May 2002.

[99] A. Westphalen, H. Zabel, and K. Theis-Bröhl. Magnetic nanowires on faceted sapphire surfaces. *Thin Solid Films*, 449(1-2):207 – 214, 2004.

[100] Veeco Instruments. Veeco - Digital Instruments Dimension 3100 Scanning Probe Microscope, Scanning Probe Microscopy - V. Online: Last accessed on November 10 2008. `http://www.veeco.com/Products/metrology_and_instrumentation/AFM_SPM/Dimension_3100/index.aspx?prodGroup=0`.

[101] P. Busch, D. Posselt, D.-M. Smilgies, M. Rauscher, and C. M. Papadakis. Inner Structure of Thin Films of Lamellar Poly(styrene-b-butadiene) Diblock Copolymers As Revealed by Grazing-Incidence Small-Angle Scattering. *Macromolecules*, 40(3):630 – 640, 2007.

[102] GKSS Forschungszentrum Geesthacht GmbH. NERO. Online: Last accessed on October 12 2008. `http://www.gkss.de/central_departments/genf/instruments/003142/index_0003142.html.de`.

[103] H. E. Nigh, S. Legvold, and F. H. Spedding. Magnetization and Electrical Resistivity of Gadolinium Single Crystals. *Physical Review*, 132(3):1092 –1097, Nov 1963.

[104] R. W. Erwin, J. J. Rhyne, M. B. Salamon, J. Borchers, Shantanu Sinha, R. Du, J. E. Cunningham, and C. P. Flynn. Magnetic structure of Dy-Y superlattices. *Physical Review B*, 35(13):6808 – 6825, May 1987.

[105] S. Yu. Dan'kov, A. M. Tishin, V. K. Pecharsky, and K. A. Gschneidner. Magnetic phase transitions and the magnetothermal properties of gadolinium. *Physical Review B*, 57(6):3478 – 3490, Feb 1998.

[106] M. Yan and A. Gibaud. On the Intersection of Grating Truncation Rods with the Ewald Sphere Studied by Grazing-Incidence Small-Angle X-ray Scattering. *Journal of Applied Chrystallography*, 40(6):1050 – 1055, Dec 2007.

[107] Y. Yoneda. Anomalous Surface Reflection of X Rays. *Physical Review*, 131 (5):2010 – 2013, Sep 1963.

[108] Petr Mikulík and Tilo Baumbach. X-ray reflection by multilayer surface gratings. *Physica B: Condensed Matter*, 248(1-4):381 – 386, 1998.

[109] S. Lovell and E. Rollinson. Density of Thin Films of Vacuum Evaporated Metals. *Nature*, 218:1179 – 1180, Jun. 1968.

[110] N. Bardou, B. Bartenlian, F. Rousseaux, D. Decanini, F. Carcenac, C. Chappert, P. Veillet, P. Beauvillain, R. Mégy, Y. Suzuki, and J. Ferré. Light diffraction effects in the magneto-optical properties of 2D arrays of magnetic dots of Au/Co/Au(111) films with perpendicular magnetic anisotropy. *Journal of Magnetism and Magnetic Materials*, 148(1-2):293 – 294, 1995.

[111] National Instruments Corporation. LabVIEW™ 6.1. 11500 N. Mopac Expressway, Austin, Texas, USA.

List of Publications

[LOP-1] E. Tartakovskaya, W. Kreuzpaintner, and A. Schreyer. Spin wave dynamics in two- and three-dimensional superlattices of nanosized ferromagnetic spheres. *Journal of Applied Physics*, 103:023913, 2008.

[LOP-2] W. Kreuzpaintner, M. Störmer, D. Lott, D. Solina, and A. Schreyer. Epitaxial growth of nickel on Si(100) by dc magnetron sputtering. *Journal of Applied Physics*, 104:114302, 2008.

[LOP-3] W. Kreuzpaintner, J. F. Moulin, D. Lott, R. Kampmann, M. Haese-Seiller, M. Störmer, and A. Schreyer. Time-of-Flight Grazing Incidence Small Angle Neutron Scattering on Gd Nanowires. *The European Physical Journal Special Topics*, 167:73 – 79, 2009.

[LOP-4] R. Kampmann, J.-F. Moulin, M. Haese-Seiller, M. Pomm, W. Kreuzpaintner, V. M. Haramus, D. Lott, R. Willumeit, S. Stanglmaier, B. Nickel, M. Müller, J. Rädler, and A. Schreyer. Performance and Use of the Horizontal Reflectometer REFSANS at FRM II Germany. *Journal of Physics: Conference Series*, submitted.

Appendix A

Structuring of Epitaxial Ni Films

This appendix gives the parameters and describes the process for the attempted structuring of epitaxially grown Ni layers. It also demonstrates the state reached in sample preparation at the completion of this project.

A.1 Epitaxial Ni Film Grown by MMES

A Si(100) wafer with a diameter of 2.54 cm was prepared as described in 6.2.1 and deposition was carried out using the MMES technique described in 6.3. The base pressure of the sputter deposition chamber was 7×10^{-8} mbar.

First a 1 µm thick epitaxial Cu seed layer was deposited at 100 W with a gas flow rate of 3.75 sccm of ultra high purity Ar which corresponded to a working gas pressure of 3.3×10^{-4} mbar.

After the Cu seed, 100 nm of Ni were deposited epitaxially at 50 W with Ar working gas flow rate of 10 sccm and working pressure of 8.2×10^{-4} mbar respectively. An additional 100 nm thick epitaxial Cu layer was sputter deposited on top of the Ni layer with the same deposition parameters as used for the Cu seed layer.

After the epitaxial layer growth, the sample was retracted into the airlock chamber of the setup and capped with 3 nm of TiN as described in 7.1.1.

The structuring process of a photo resist layer by laser interference lithography was carried out with parameters identical to those used for the polycrystalline sample described in 7.1.1. However, the exposure time slightly differed, being 35 s.

After the sample preparation steps in the cleanroom, the sample was transported to GKSS for argon ion beam milling (3.4). The sample was mounted on the provisional substrate holder (4.4.3) and positioned in the airlock chamber at a 90° angle of incidence to the argon ion beam.

The initial milling step was performed for 15 min of process time using a base pressure of 2.6×10^{-7} mbar and a gas flow rate of 0.4 sccm of standard quality argon. This resulted in a working pressure of 4.0×10^{-4} mbar. The ion gun discharge current was 0.39 A at a discharge voltage of 55 V. The beam current was at 23 mA and 250 V of ion energy and the accelerator current was at 2 mA and 290 V. The neutraliser emission current was automatically controlled by the ion gun power supply to be 29 mA at a neutraliser filament current of 2.52 A. After approximately 12 hours of
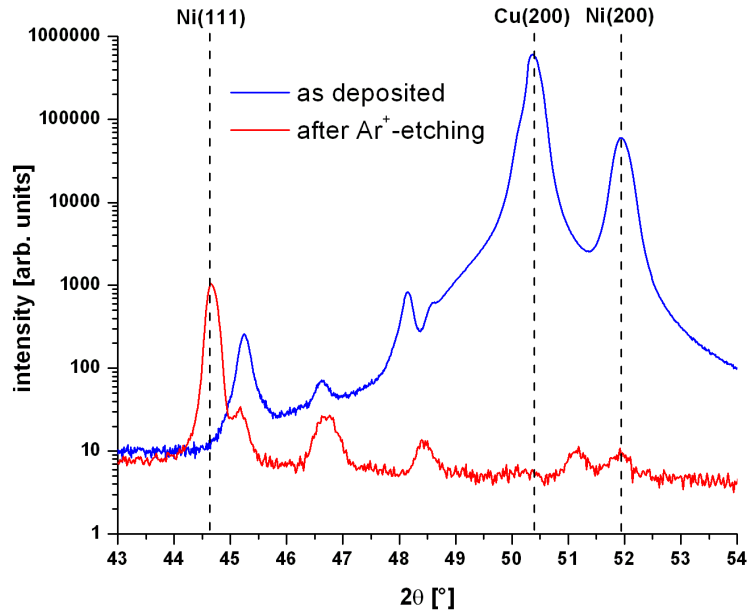
Figure A.1: *X-ray diffractograms of an MMES epitaxially grown Ni layer taken before and after 15 min argon ion beam milling. The argon ion bombardment destroys the epitaxy, as seen from the vanishing Cu(200) out-of-plane intensities and the change of Ni(200) to polycrystalline Ni.*

cool-down the vacuum chamber was vented to investigate the progress of the milling step.

In contrast to the non-epitaxial Ni nanodot sample (7.1.1), which refracted incident light, this sample merely had a grayish brown colour. Hence, an x-ray diffractogram was taken and compared to one collected before the argon ion beam milling (figure A.1). The separate Cu and Ni out-of-plane crystal directions visible in the x-ray diffraction pattern taken before the ion bombardment were no longer present. Instead, primarily an amorphisation of Cu and polycrystalline Ni were observed. It was therefore concluded that argon ion beam milling destroys the epitaxial layer structure of Ni on Cu. This destruction of epitaxial Ni and Cu is reproducible and consequently this path was no longer followed for the preparation of an epitaxial Ni nanodot array.

A.2   Epitaxial Ni Film on Si(100) Substrate

As MMES proved an unsuitable method for preparing epitaxial Ni nanostructures, a novel deposition method for epitaxial Ni on Si was first developed (6.4) and applied for the following experiment.

A Si(100) wafer with a diameter of 2.54 cm was cleaned using the standard procedure of alternate ultrasonic baths of acetone and ethanol followed by a 1 min dip in HF acid and immediately inserted into the sputter deposition chamber.

The base pressure was 2×10^{-8} mbar, and the working pressure was 8.3×10^{-4} mbar at an Ar gas flow rate of 10 sccm. For an initial Ni layer seed the temperature of the Si substrate was increased to 687 °C and given approximately 30 min to stabilise. Approximately 4 nm of Ni were deposited at 50 W after which the sample was given approximately 2 h to cool to 275 °C whereupon the second deposition step of epitaxial Ni(200) was performed to a final Ni layer thickness of 160 nm. After a 6 h cool-down the sample was transfered into the loadlock of the vacuum chamber and capped with 3 nm of TiN using the parameters given in 7.1.1.

Structuring by laser interference lithography was carried out with the same parameters as in 7.1.1 but with an exposure time of only 17 s.

For the argon ion beam milling process (3.4) the sample was clamped to the preliminary substrate holder (4.4.3) and mounted in the Ar ion beam milling vacuum chamber. As this epitaxial Ni(200) layer was thicker than the previously structured samples, more milling steps were necessary with checks on the milling progress on multiple interruptions. In total eleven milling steps were performed. The most important variable parameters are given in table A.1.

Table A.1: *Variable parameters in the argon ion beam milling steps. The beam current was 23 mA with a beam voltage of 250 V. The discharge voltage was set to 55 V, with the constant accelerator voltage being 290 V and the neutraliser emission current 29 mA in all cases. p_{base} and $p_{work.}$ denote the base and working pressures; $I_{Cath.}$, $I_{Dis.}$, $I_{Accel.}$ and $I_{Neutr.}$ are the cathode, discharge, accelerator and neutraliser emission currents; ξ is the argon ion angle of incidence relative to the surface of the sample and t is the process time.*

Run #	p_{base} [mbar]	$p_{\text{work.}}$ [mbar]	$I_{\text{Cath.}}$ [A]	$I_{\text{Dis.}}$ [A]	$I_{\text{Accel.}}$ [mA]	$I_{\text{Neutr.}}$ [A]	ξ [°]	t [mm:ss]
1	6.1×10^{-7}	4.1×10^{-4}	3.05	0.39	2	2.51	135	7:30
2	4.4×10^{-7}	4.1×10^{-4}	3.04	0.39	2	2.51	45	7:30
3	4.3×10^{-7}	4.1×10^{-4}	3.05	0.39	2	2.51	135	7:30
4	2.4×10^{-7}	4.0×10^{-4}	3.01	0.39	2	2.46	45	7:30
5	2.6×10^{-7}	4.0×10^{-4}	3.00	0.39	2	2.54	135	7:30
6	2.6×10^{-7}	4.0×10^{-4}	2.99	0.39	2	2.46	45	7:30
7	3.6×10^{-7}	4.0×10^{-4}	2.97	0.39	2	2.49	135	7:30
8	3.6×10^{-7}	3.9×10^{-4}	2.97	0.39	2	2.46	45	3:15
9	3.6×10^{-7}	3.4×10^{-4}	2.98	0.38	1	2.45	45	3:15
10	6.8×10^{-6}	3.5×10^{-4}	3.12	0.28	2	2.56	90	1:30
11	5.7×10^{-6}	3.5×10^{-4}	3.12	0.28	1	2.56	135	1:30

An x-ray diffractogram taken after the ninth milling step (figure A.2) showed that Ni(200) is the only detectable Ni crystal direction and no other (in particular Ni(111) directions can be observed. It can therefore be concluded that argon ion beam milling does not destroy the epitaxial crystal structure of Ni(200) on Si(100), if Ni is directly grown epitaxially on Si(100). However, due to the lack of an end-point detection, additional milling runs were (falsely) concluded to be necessary and
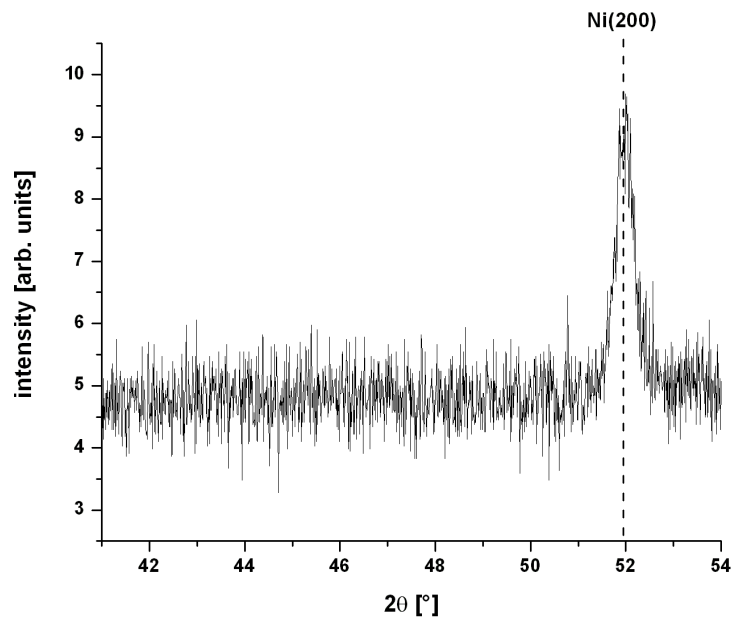
Figure A.2: *X-ray diffractogram taken after the ninth argon ion beam milling step of a thin epitaxial Ni(200) out-of-plane film: the epitaxy is not destroyed and no other crystal directions are detectable.*

after the eleventh run it was found that the Ni was fully removed from the sample, corresponding to a failure of the structuring process due to overshooting with the milling process.

The structuring of epitaxial Ni was attempted again with another sample, but the milling steps were again carried out too many times. More promising structuring processes can be attempted when the final substrate holder (4.4) is available, as it will include an in-situ endpoint detection by resistance measurement.

Appendix B

Program Source Codes and Electronic Circuits

The developed computer programs (on a source code level) and the improvised electronic circuits for interaction of control PCs and peripheral components are described here. The majority of the programs were written using LabVIEW™ [111]. This is a graphical programming environment, based on a Virtual Instruments (VI) concept with each VI containing certain routines for simple initialisation of hardware or a more complex task. A VI can also be a fully independently operable program of its own, and suitably integrated into another more complicated program. However, certain LabVIEW™ block diagrams are quite complex such that only the function of the essential program parts can be addressed.

B.1 Control-Program for the CARBOLITE™ HTF 1700 Furnace

Communication between the control PC and the Eurotherm™ 3216 controller implemented in the furnace is via an RS-232 port using the MODBUS protocol[1]. The program (figure B.1) consists of two "while" loops and their control variables are set to execute the program until it is stopped manually. The first "while" loop (labelled "A" in figure B.1) initialises the Eurotherm™ 3216 temperature controller of the CARBOLITE™ HTF 1700 furnace by reading previously stored serial port communication parameters from a file and retrieves the current state of the furnace from the temperature controller. These parameters are passed to the routines in the second "while" loop, containing the central components of the program.

B.1.1 Initialisation Section "A"

This section (figure B.2) contains the routines for reading the previously saved communication parameters from a file. The tabulator-separated text file contains the serial port number, the MODBUS slave address, the update rate and the BAUD rate in plain numbers. The routine uses these values to read the ramp rate units,

---

[1]The pin assignment of the ports/cable is given in the HTF 1700 handbook
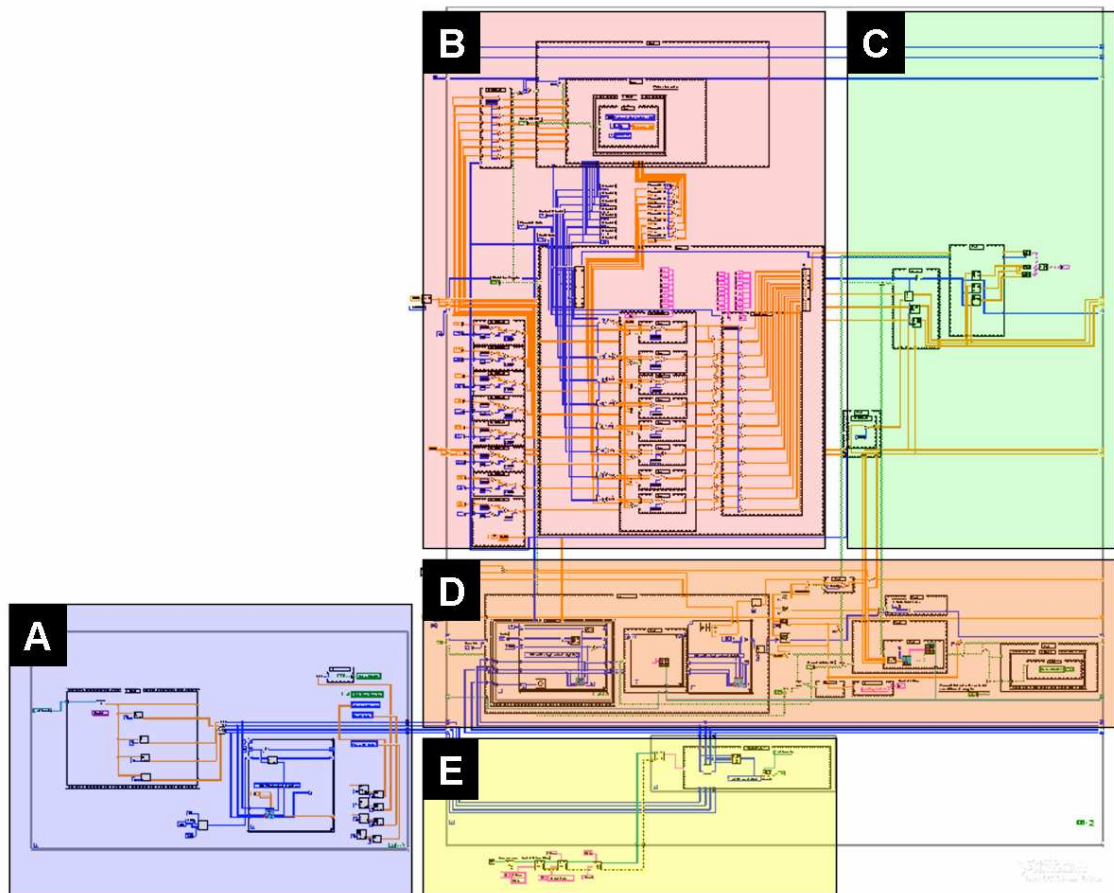
Figure B.1: *Overview of the LabVIEW™ control program for the CARBOLITE™ HTF 1700 high temperature furnace: section "A" initialises the hardware for communication and acquires the current state of the furnace. "B" contains the routines to create and display the temperature ramp, "C" displays the graph on the user interface, section "D" transfers the programmed temperature ramp to the Eurotherm™ controller and records and displays the current status. "E" replaces the file-bar of the LabVIEW™ window and displays the options for program info and serial port setup.*
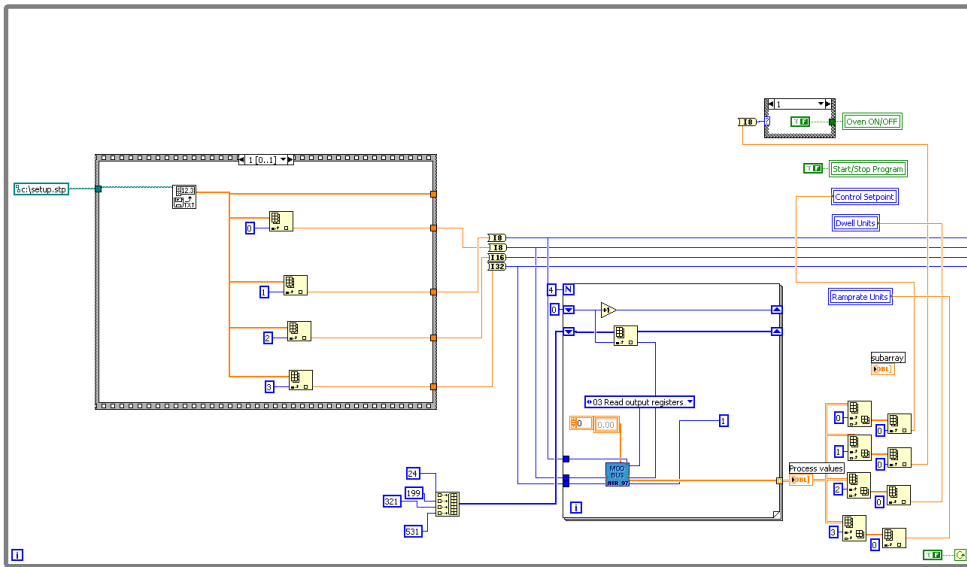
Figure B.2: *Initialisation part of the program which sets the serial port of the PC and determines the current state of the furnace as read from the temperature controller.*

dwell units, control set-point and current controller status (ON or OFF) from the temperature controller.

B.1.2   Temperature Profile Section "B"

This section builds the temperature profile that is transferred to the temperature controller by the routines in section "D". Despite its complex appearance (figure B.3) it is essentially only an input section which adds all the inputs and converts them by basic mathematical relations into values that can be interpreted by the temperature controller of the furnace. For example, the dwell times are required to be transferred in units of milliseconds although the input units can either be in the format of hours and minutes or in minutes and seconds.

B.1.3   Graph-Generation Section "C"

Section "C" of the program (figure B.4) generates the x-y graphs displayed by the user interface. It combines a time array with the corresponding temperature array. If the furnace is not processing a programmed temperature profile, it displays the profile that is currently being programmed and updates it when a value is changed. If a program is processed by the temperature controller of the furnace, the current setpoint and actual temperature values are displayed. The case-structure on the left scales the horizontal time axis, depending on the chosen dwell time units.

B.1.4   Program Section "D"

This section (figure B.5) controls the communication with the temperature controller. Depending on the applicable case, the case-structure on the left programs
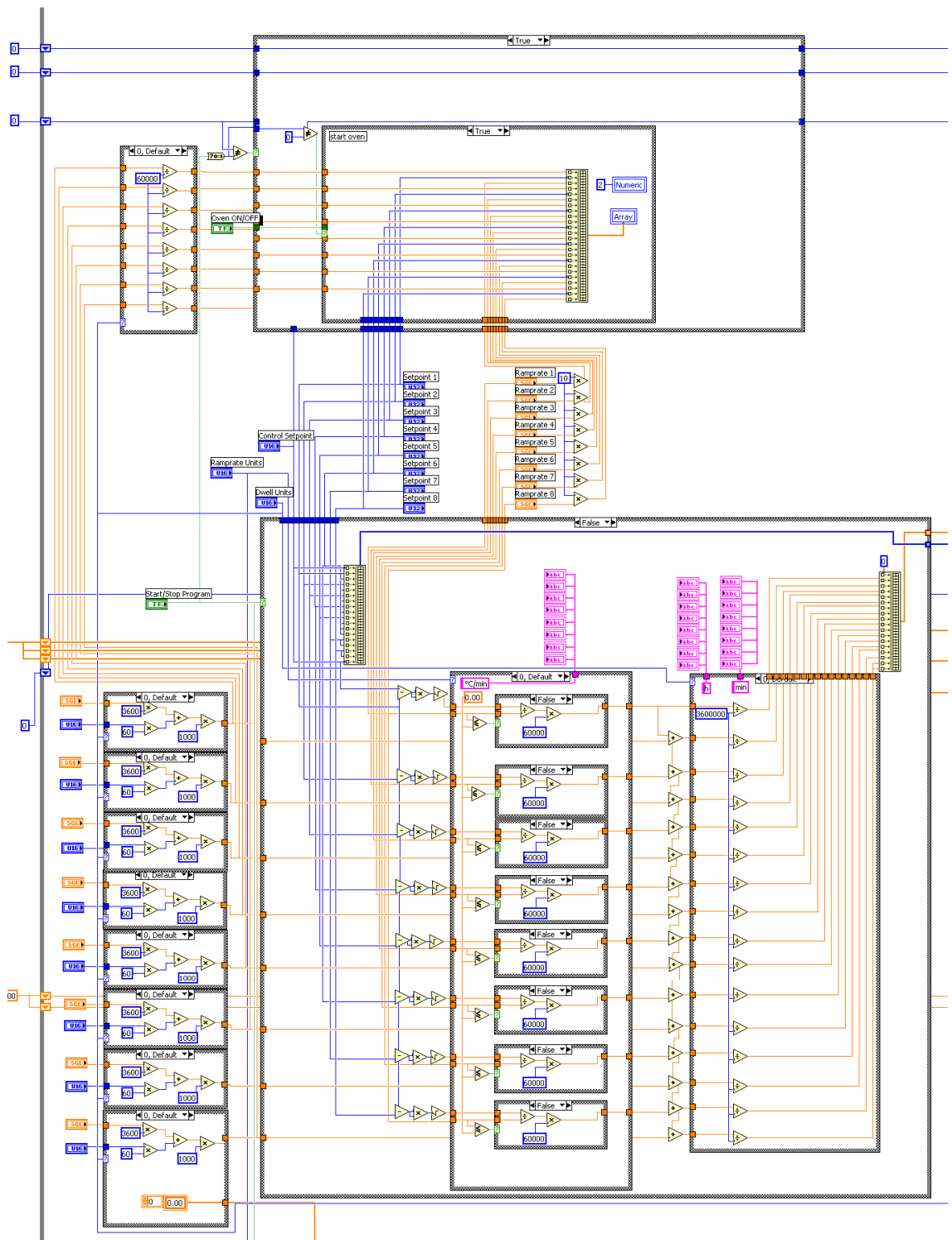
Figure B.3: *Program section "B" which collects the user inputs for temperature profiles and converts them to values interpretable by the temperature controller.*
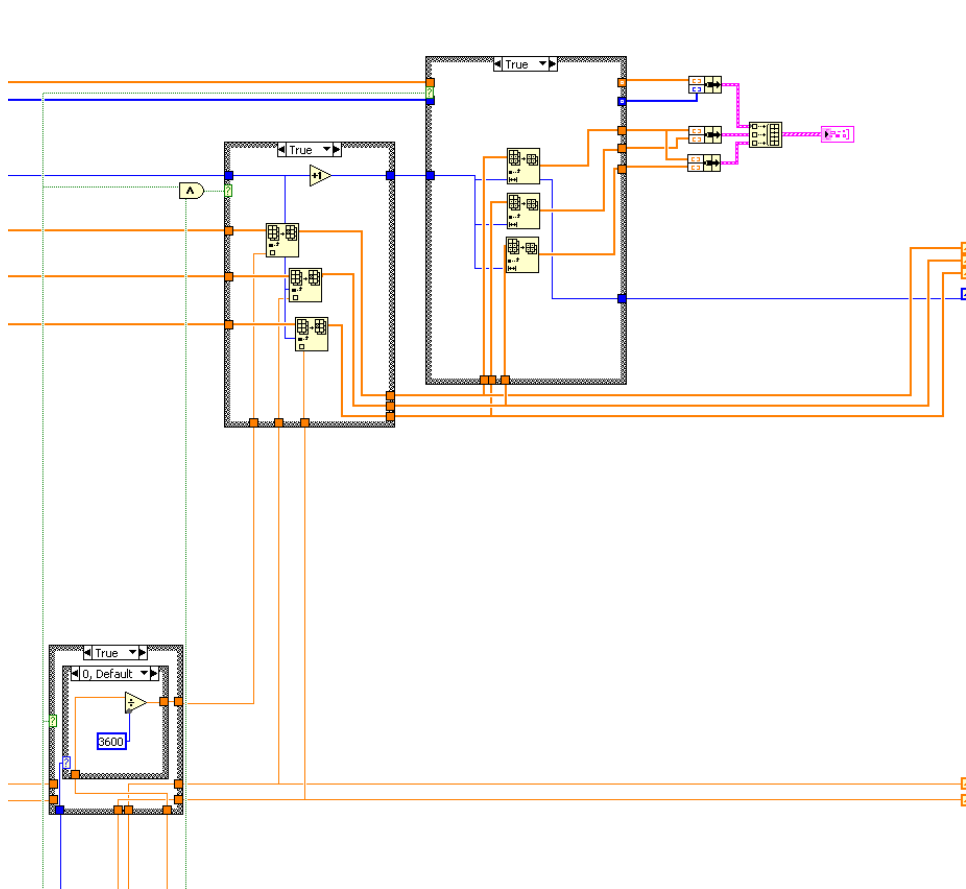
Figure B.4: *Program section "C" of the furnace control program which creates the x-y plot on the user interface.*
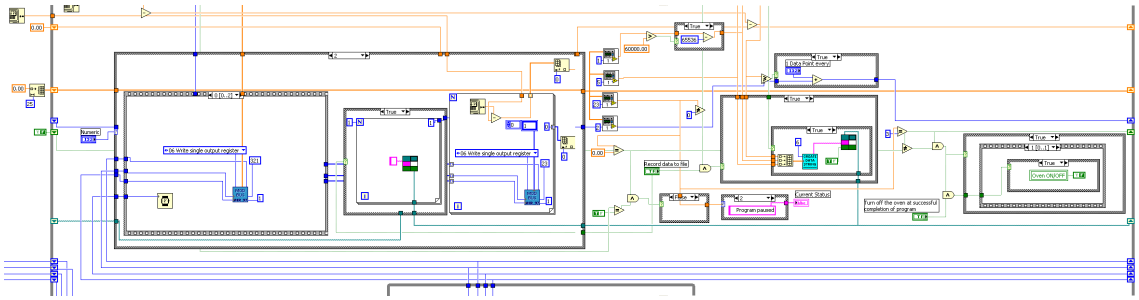
Figure B.5: *Program section "D" which is responsible for the communication with the temperature controller of the furnace and controls the program flow.*
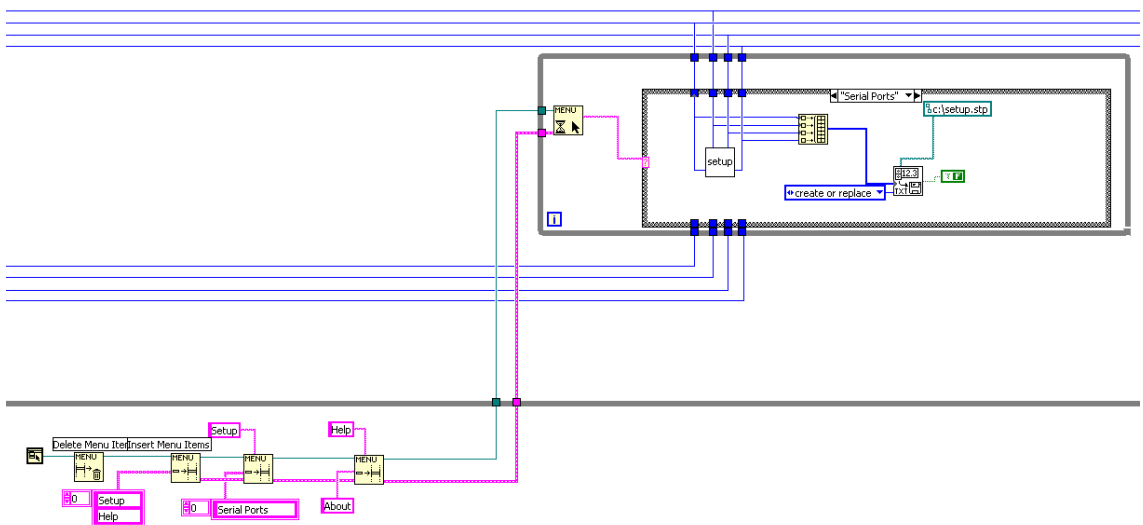
Figure B.6: *Program section "E", which allows the parameters for communication between the computer and the temperature controller of the furnace to be changed.*

the temperature ramp created in section "B" and starts execution of the program or turns the furnace ON or OFF. The default case reads the current temperature from the furnace. The various case-structures on the right of this section regulate the program flow by switching variables that control other case-structures, program parameters and user interface or file outputs.

B.1.5   Setup Section "E"

The program flow is such that the information read in section "A" is first passed to section "E" (figure B.6), where it can be modified and transferred to program section "B" and "D". In section "E" the file-bar replacement of the LabVIEW™ program window is also built, from which the communication parameters read from the input file "setup.stp" used in section "A" of the program can be changed and saved.

B.2   Time Control for Ion Beam Milling

B.2.1   Hardware

An improvised circuit was implemented into the connector bodies on both ends of a cable that connects the serial port of a computer with the corresponding port on the ion gun power supply unit. The RS-232 Port of the PSU can be used to turn on the emission and the ion beam if pin 18 and pin 25 are set to ground potential. The port also offers a +12 V line that is used to supply the improvised circuit with +5 V via a step-down voltage converter. A 74H14 inverter is used as a buffer to protect the serial port chip (MAX220CPE) from over-current and switches the relay, which sets pin 18 and pin 25 on the PSU side to ground potential. The step-down voltage converter, the 74HC14 and the relay are integrated in the 25-pin connector body on one end of the cable. On the 9-pin serial port end of the cable the serial port chip is integrated and inverts the ±11 Volts from the RTS line of the computer to a 0 V or +5 V state. This circuit allows to switch the ion gun on the PSU on or off with a LabVIEW™ program, which only changes the state of the RTS line of the serial port on a PC and ensures that this cable is only operational with the equipment for which it was designed[2]. Attaching it to the wrong equipment will result in an inoperable circuit due to the missing power supply from the 25pin port which protects any other accidentally attached devices from damage.

B.2.2   Software

The corresponding LabVIEW™ program consists of a sequence structure of four steps, labelled 0 – 3. The first three steps initialise the serial port and put it in a standard state with the RTS line at a logical 1. However, it is irrelevant which communication parameters the serial port is set to, as no data is transferred; the settings are 9600 BAUD with 8 data and one stop bit with parity disabled. The program is then executed in the final step of the sequence structure (figure B.8) in which a "while" loop is continuously executed until the program is stopped manually. Various boolean cases, visible in the centre of the program, switch the numeric cases of the right case-structure which contains the routines to change the logical state of the RTS line. The left case-structure performs a timer reset on start of the milling process. The input and display section in the lower part of the "while" loop counts down the process time and displays the remaining time on the user interface.

---

[2]The program is installed on a 166 MHz Pentium© class PC with 32MB of RAM running LabVIEW™ 6.1 under MS Windows 98™. As a minor disadvantage, this program does not run under Windows NT™ and its derivatives (Windows 2000™/XP™/Vista™ etc...) as it requires direct hardware access to the serial port which is blocked under the NT product line of Windows™.
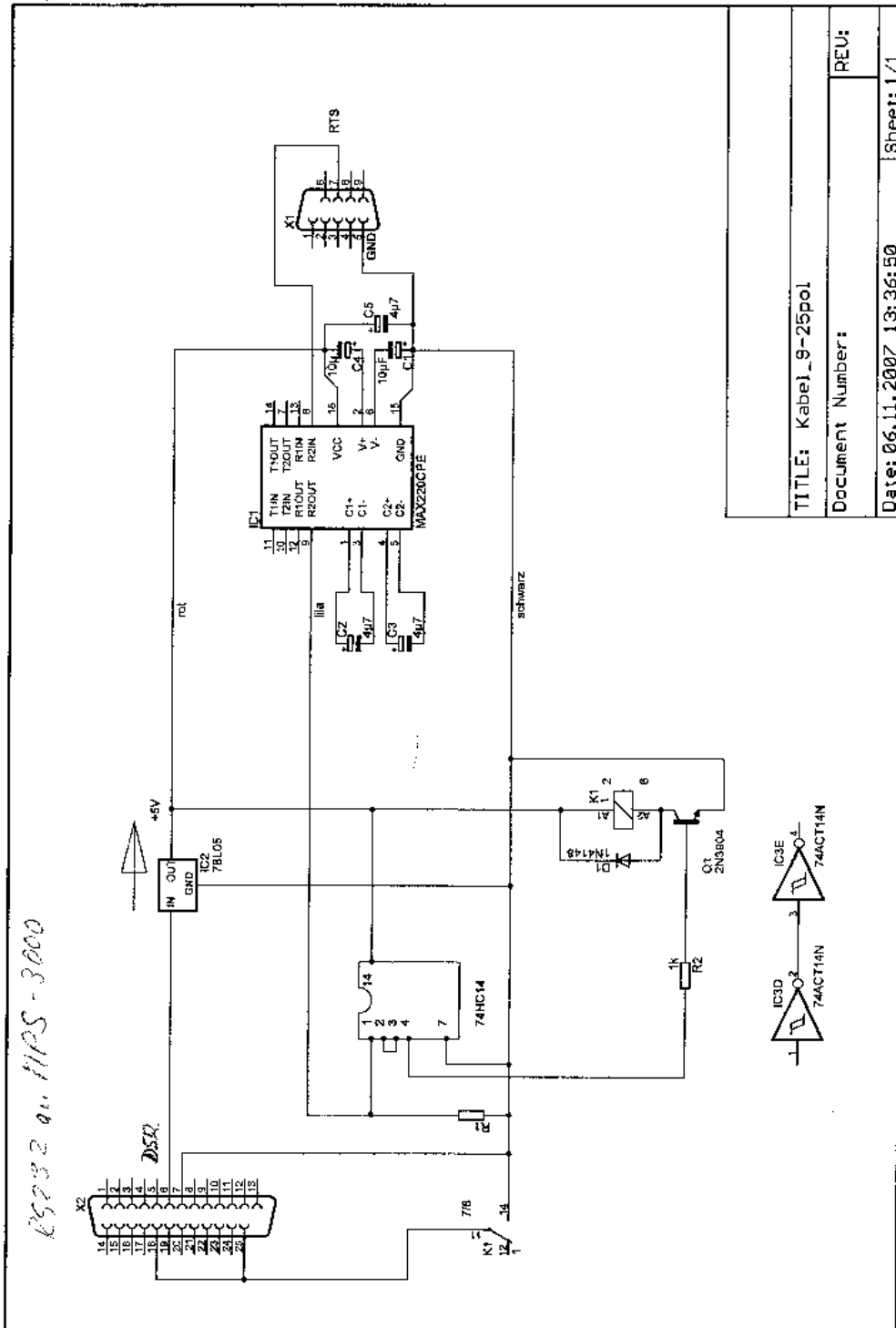
Figure B.7: *Circuit of the improvised cable for connecting the Ion Gun PSU to the serial port of the control PC.*
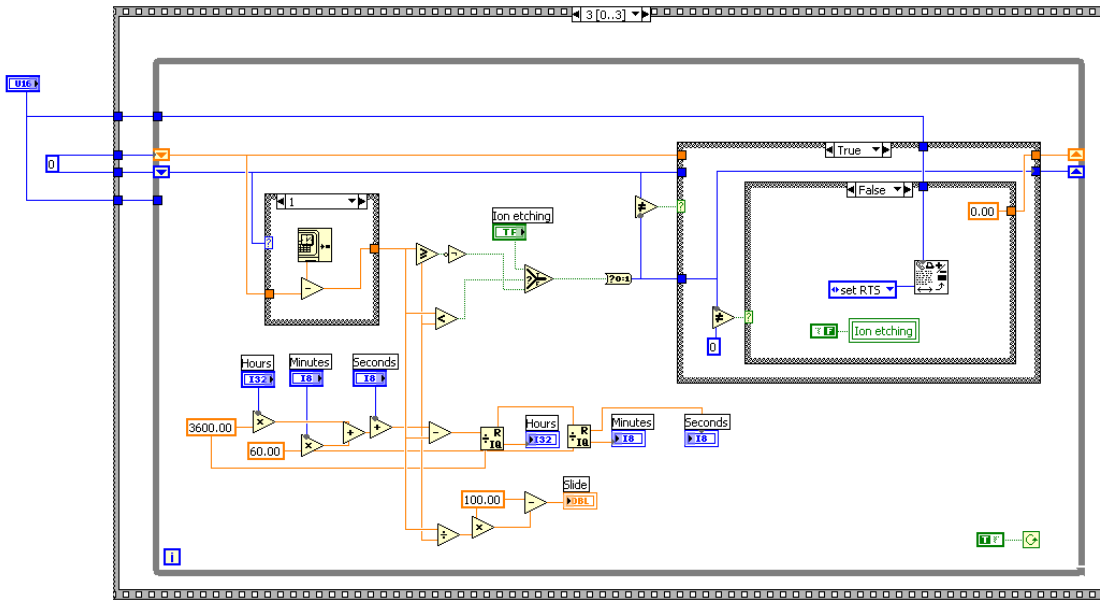
Figure B.8: *LabVIEW™ block diagram of the timer program used to control the duration of the argon ion beam milling.*

B.3 Deposition Control Software

B.3.1 Program Code

The block diagram of the LabVIEW™ deposition control program for the e-beam evaporation vacuum chamber (4.3) is shown in figure B.9. Currently, it only consists of fundamental components for deposition control used in the preparation of the samples described in 7.2. The program runs in a permanent "while" loop and consists of the three functional sections described below.

Graph-Generation Section "A"

In this section of the program (figure B.10) the graphs for the user interface are generated. Furthermore, the "true/false" case-structure on the right side of this block enables the user to reset the displays on the user interface manually or with the start of a deposition process. The lower case-structure generates the array which contains the relevant deposition parameters as outlined in 4.3.3 and is stored into a file after the deposition process.

Deposition Control Section "B"

The routines found in this section of the program (figure B.11) control the start and stop of the deposition process. The case-structure on the left allows the user to choose if the deposition is stopped automatically at a preset layer thickness, or if the deposition has to be stopped manually. The implemented sub-VI (labelled "4") contains all necessary routines to correctly interact with the user interface outputs
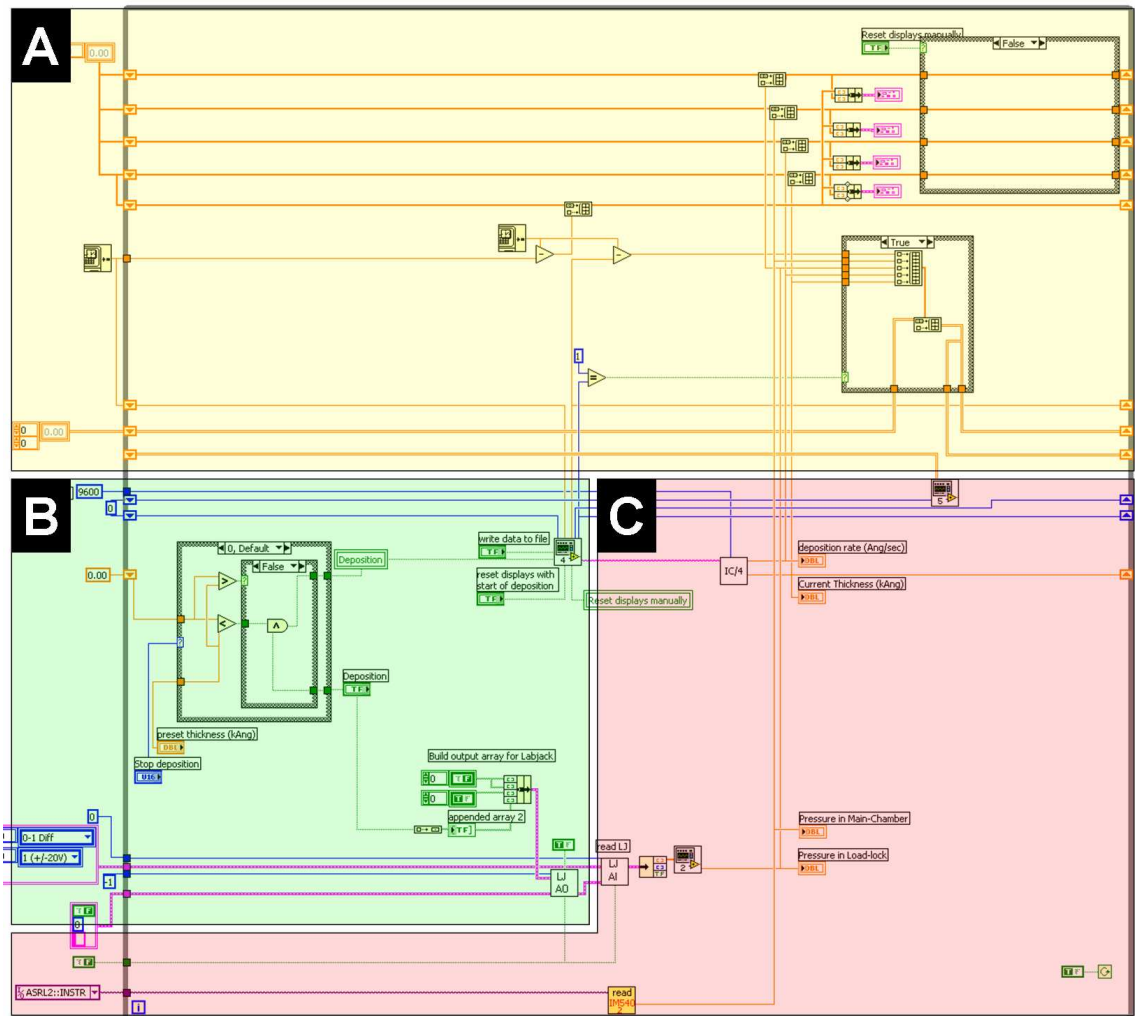
Figure B.9: LabVIEW™ block diagram of the program used to control the deposition process of Ni and Gd nanowires. It contains three functional units: a graph-generation section "A", a deposition control section "B" and a read-data section "C".
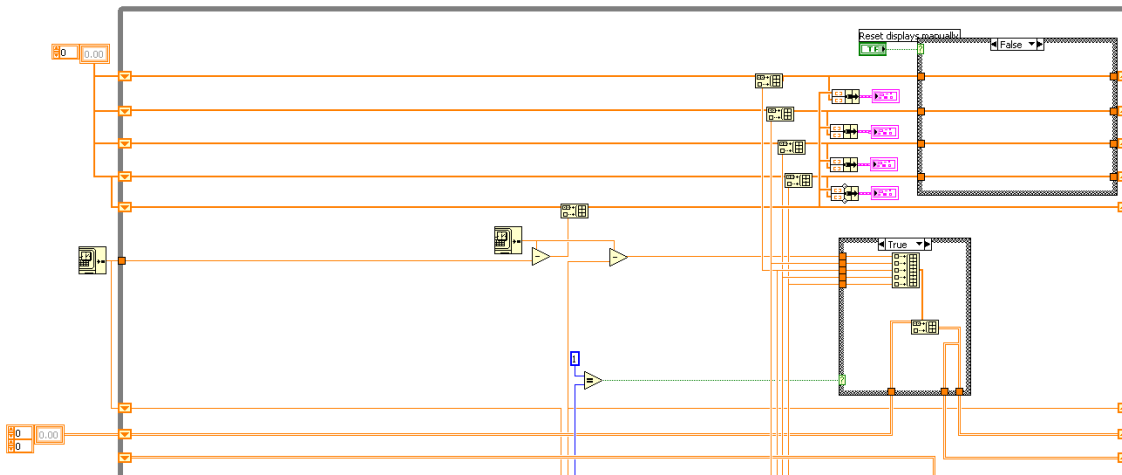
Figure B.10: *LabVIEW™ block diagram of the deposition control program graph-generation section "A".*

and to reset the thickness counter on the deposition controller. When the deposition is stopped, this sub-VI sends an integer signal to the write-file sub-VI of section "C".

Section "B" also contains the sub-VI for setting the digital output of the LabJack™ USB AD/DA board. Depending on the output (0 V or +5 V), it opens or closes the shutter via the shutter controller described in B.3.2.

Read-Data Section "C"

This section (figure B.12) contains most of the routines for reading data from the connected peripheral equipment and meters, including the routines for reading and processing the vacuum pressure in the argon ion beam milling/airlock vacuum chamber via an analog input on the Labjack™ USB board. In the lower half, the subroutine for reading from the Leybold Heraeus© IM-540 gauge controller via the serial port can be found. Subroutine "IC/4" reads the deposited thickness and the deposition rate from the deposition controller and sends a command for resetting the thickness counter on start of deposition. Subroutine "5" writes the recorded parameters to a text file.
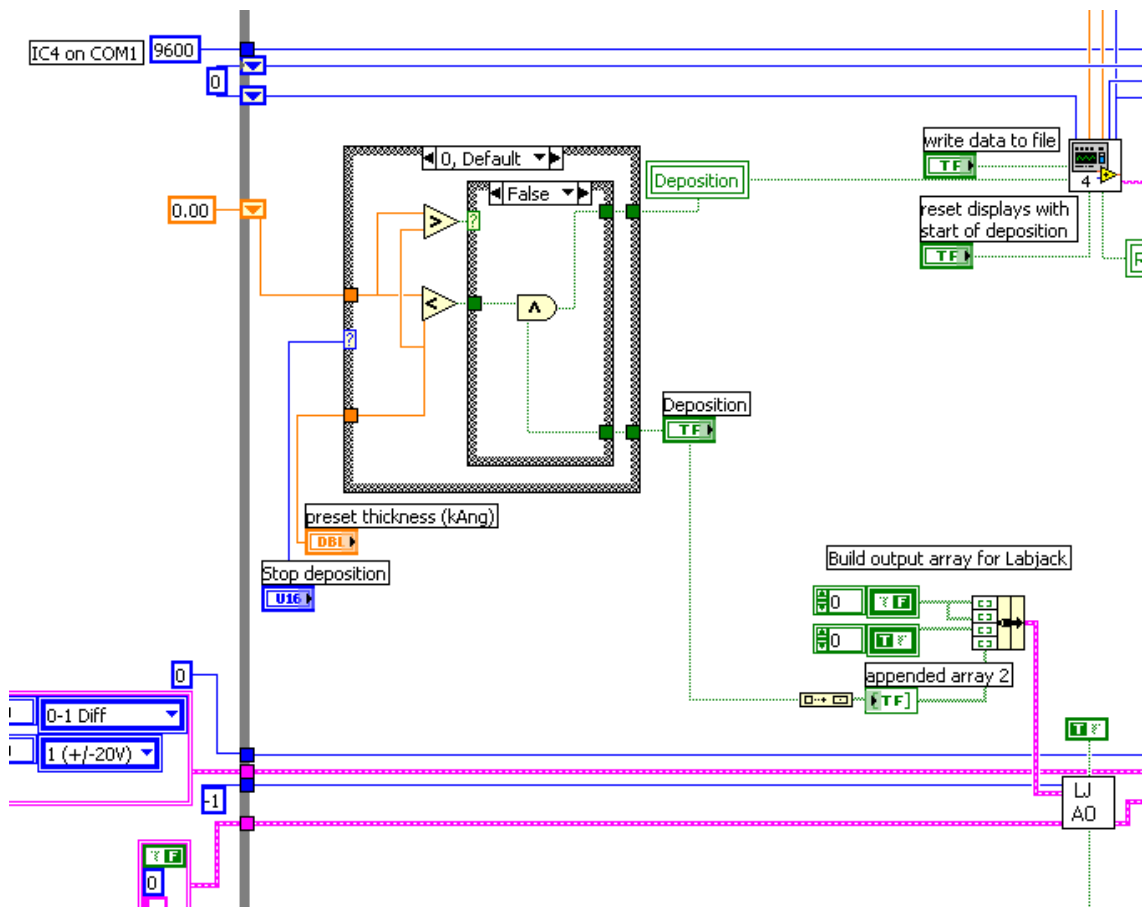
Figure B.11: *LabVIEW™ block diagram of the deposition control section "B".*

Figure B.12: *LabVIEW*™ *block diagram of the read-data section "C".*

B.3.2   Shutter Controller

The shutter control unit (designed, built and programmed by H.-D. Braune, GKSS) is a small processor based circuit board, that controls a geared electric DC motor (commonly used in remote controlled model cars) with the necessary torque attached to the vacuum rotary feed-through. The rotation angle is approximately 120° and allows to fully open the shutter within less than 1 s. The applied signal processor is a 16 bit PIC16F684. Control of the shutter position is via a digital 0 V or +5 V signal from the Labjack™ AD/DA USB board attached to the deposition control computer and controlled by the program described in B.3. Switching of the state causes an "interrupt on pinchange" on "port A2" of the circuit shown in figure B.13. On a logical 1 (+5 V) or a logical 0 (0 V), the motor is rotated in either of two directions. An additional switch allows to reverse the direction of rotation and adjustable magnetic end-switches define the exact rotation angle.

The source-code of the control program stored on the PIC16F684 chip is given in the following listing.

```
1  /*******************************************************************************
2  PIC16F684
3  *******************************************************************************/
4  #include "D:\$\mu$C-C_Projekte\C_unter_MPLAB\CCS-allein\Stepper_Control\DC-Motor_v2
       \dc_motor_v2.h"
5
6  //Pindefinitionen
7  #define  start    PIN_A2        //Startsignal von externer Quelle
8  #define  e2       PIN_A4        //Endschalter 2
9  #define  e1       PIN_A5        //Endschalter 1
10 #define  reverse  PIN_C4        //Drehrichtungsumkehr
11 #define  led_run  PIN_C5        //Programm run
12
13 //*******************************************************************************
14 #int_RA
15 //Interrupt-Subroutine, die eigentliche Fahrroutine
16 void RA_isr()
17 {
18 delay_us(200);                        //Entprellzeit
19 disable_interrupts(INT_RA2);          //Interrupt sperren
20
21 if (input (reverse))                  //"reverse" = "1"
22  {
23    if (!input (start))     {         //Hi_to_Lo Transition drehe cw
24       while (!input (e2))            //bis Endschalter E2 erreicht
25          output_C (0x0A);            //drehe cw bei Blick auf den Dreht.
26       output_C (0x03);       }       //Motor Stop
27
28    else                    {         //Lo_to_Hi Transition drehe ccw
29       while (!input (e1))            //bis Endschalter E2 erreicht
30          output_C (0x05);            //drehe ccw bei Blick auf den Dreht.
31       output_C (0x03);       }       //Motor Stop
32  }
33 else                                  //Input "reverse" = 0
34  {
35    if (!input (start))     {         //Hi_to_Lo Transition drehe ccw
36       while (!input (e1))            //bis Endschalter E1 erreicht
37          output_C (0x05);            //drehe ccw bei Blick auf den Dreht.
38       output_C (0x03);       }       //Motor Stop
39
40    else                    {         //Lo_to_Hi Transition drehe cw
41       while (!input (e2))            //bis Endschalter E2 erreicht
42          output_C (0x0A);            //drehe cw bei Blick auf den Dreht.
43       output_C (0x03);       }       //Motor Stop
44  }
45 enable_interrupts(INT_RA2);           //Interrupt freigeben
```
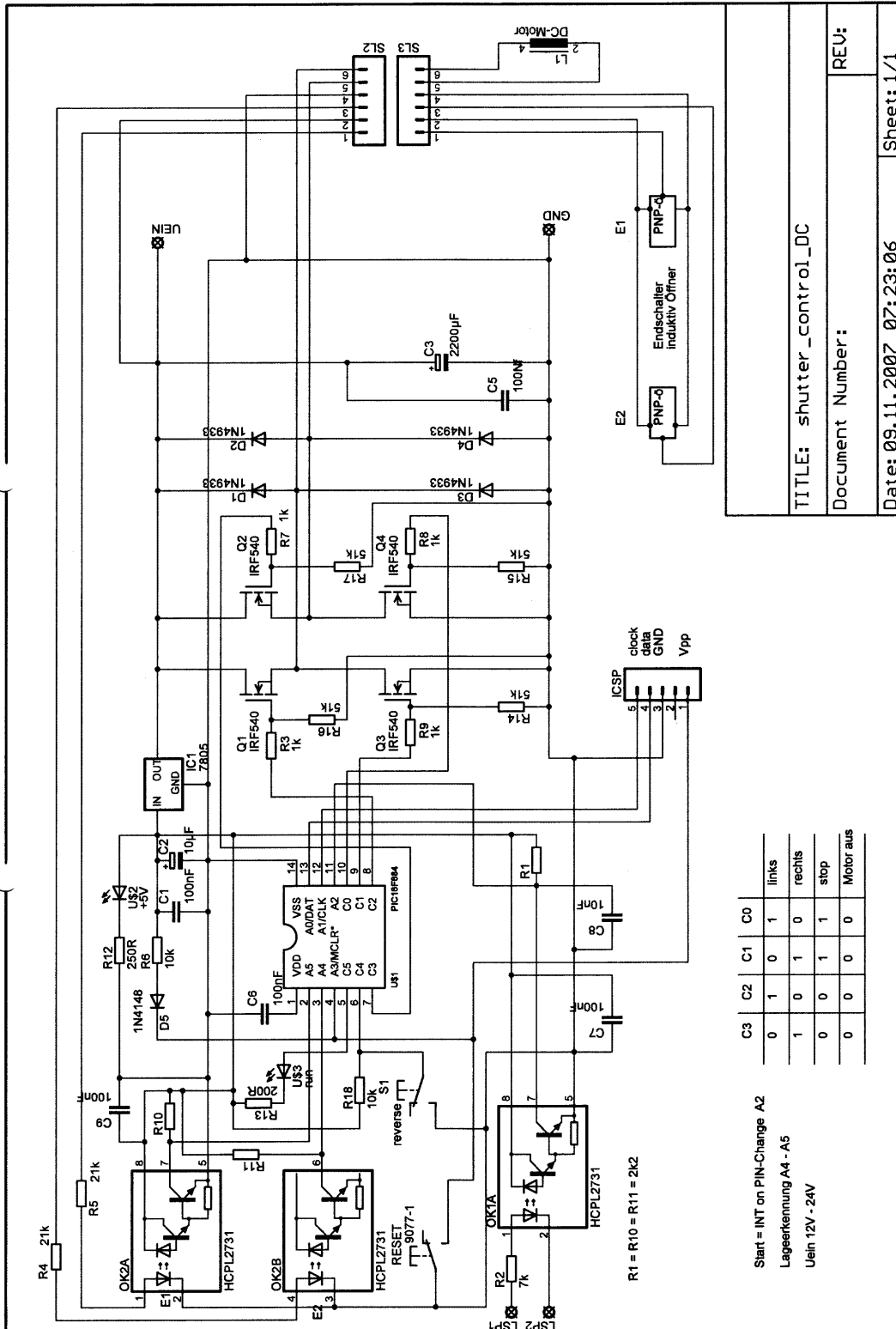
Figure B.13: *Circuit of the shutter control unit.*

```
46  }
47  //*****************************************************************************
48  //*********************"turn-left on high"*******************************
49  void sr_tuloh (void)
50  {
51  //initialisiere IO-Ports
52     #use  fast_io(A)
53     #use  fast_io(C)
54     SET_TRIS_A(0x3F);               //Port A alle Eingang
55     SET_TRIS_C(0xC0);               //Port C alle Ausgang
56
57  //Motor initialisieren
58     output_C (0x00);                //Motor aus
59     output_C (0x03);                //Motor stop
60
61  //fahre auf Position entsprechend des Signals am externen Eingang
62  //Eingang = "0" >> E1(links), Eingang = "1" >> E2 (rechts)
63     if (input (start))              //Eingang start = "1"(am PIC) >> E1
64       {
65         while (!input (e1))         //Motor nicht auf Startposition
66         {
67            output_C (0x05);         //drehe ccw bei Blick auf den Dreht.
68         }
69         output_C (0x03);           //Motor Stop
70       }
71       else                         //Eingang start = "0"(am PIC) >> E2
72         while (!input (e2))        //Position korrigieren (E2 ist Startpos.)
73         {
74            output_C (0x0A);         //drehe cw
75         }
76         output_C (0x03);           //Motor Stop
77  }
78  //*****************************************************************************
79  //*********************"turn-right-on-high"*******************************
80  void sr_turioh (void)
81  {
82  //initialisiere IO-Ports
83     #use  fast_io(A)
84     #use  fast_io(C)
85     SET_TRIS_A(0x3F);               //Port A alle Eingang
86     SET_TRIS_C(0xC0);               //Port C alle Ausgang
87
88  //Motor initialisieren
89     output_C (0x00);                //Motor aus
90     output_C (0x03);                //Motor stop
91
92  //fahre auf Position entsprechend des Signals am externen Eingang
93  //Eingang = "0" >> E2(links), Eingang = "1" >> E1 (rechts)
94     if (input (start))              //Eingang start = "1"(am PIC) >> E2
95       {
96         while (!input (e2))         //Motor nicht auf Startposition
97         {
98            output_C (0x0A);         //drehe cw bei Blick auf den Dreht.
99         }
100        output_C (0x03);           //Motor Stop
101      }
102      else                         //Eingang start = "0"(am PIC >> E1
103        while (!input (e1))        //Position korrigieren (E1 ist Startpos.)
104        {
105           output_C (0x05);         //drehe ccw
106        }
107        output_C (0x03);           //Motor Stop
108 }
109 //*****************************************************************************
110 void main()
111 {
112
113    setup_adc_ports(NO_ANALOGS|VSS_VDD);
114    setup_adc(ADC_OFF);
115    setup_timer_0(RTCC_INTERNAL|RTCC_DIV_1);
```

```
116    setup_timer_1(T1_DISABLED);
117    setup_timer_2(T2_DISABLED,0,1);
118    setup_comparator(NC_NC_NC_NC);
119    setup_vref(FALSE);
120    disable_interrupts(INT_RA2);
121    enable_interrupts(GLOBAL);
122    setup_oscillator(OSC_8MHZ);
123
124 //Schalterabfrage für Drehrichtung  (Startposition)
125 if (input (reverse))
126    sr_tuloh();
127 else
128    sr_turioh();
129
130 enable_interrupts(INT_RA2);
131
132 //Warte auf Interrupt
133    while (TRUE)
134    {
135        output_high (led_run);
136        delay_ms(100);
137        output_low (led_run);
138        delay_ms(100);
139    }
140
141 }
```

B.4 TOF-GISANS Evaluation Program

The block diagram of the LabVIEW™ program used to convert the DART output files into ballistically corrected real and reciprocal space data is shown in figure B.14. The complexity of this program is mainly due to it originating from a simple program used to convert matrices stored in the DART csv-output files into tabulator-separated text files, containing columns with the detector channels and corresponding intensities. It evolved such that it now allows the corrections described in 8.2.4 to be performed and essentially consists of 7 parts, labelled A – G in figure B.14.

B.4.1 Read-Data Section "A"

This part of the program (figure B.15) contains the routines to open three files for data evaluation and extracts the required information for data processing. The first case-structure (top) reads the primary beam intensity distribution as a function of the wavelength and passes it to the routines in section "C". The second case-structure allows a background file to be subtracted from the measurement file and hands the required information to section "C" of the program. These two case-structures can also be set to "false", ignoring this information in the data evaluation process. The while loops at the bottom of section "A" read the measurement file and pass the matrix elements and the corresponding wavelengths to the subsequent data evaluation on the right of section "A".

B.4.2 Ballistic Correction Section "B"

In section "B" (figure B.16) the ballistic correction of the neutron data is calculated from geometrical instrumental REFSANS parameters, including sample position, detector distance, tube position, neutron optical parameters and specular beam position for a single wavelength from which all the remaining wavelength-dependent incidence angles are calculated.

B.4.3 Background-Correction and Weighting Section "C"

Section "C" (figure B.17) of the program corrects the neutron intensities by subtracting the background, which is read from the background measurement file or manually entered as a wavelength-independent constant value. The intensities are also weighted and normalised by the primary beam intensities as read from the primary beam measurement file in section "A".

B.4.4 Data-Conversion Section "D"

This part of the program (figure B.18) converts the ballistically corrected neutron data into reciprocal space values. The influence of the varying incidence angle as a
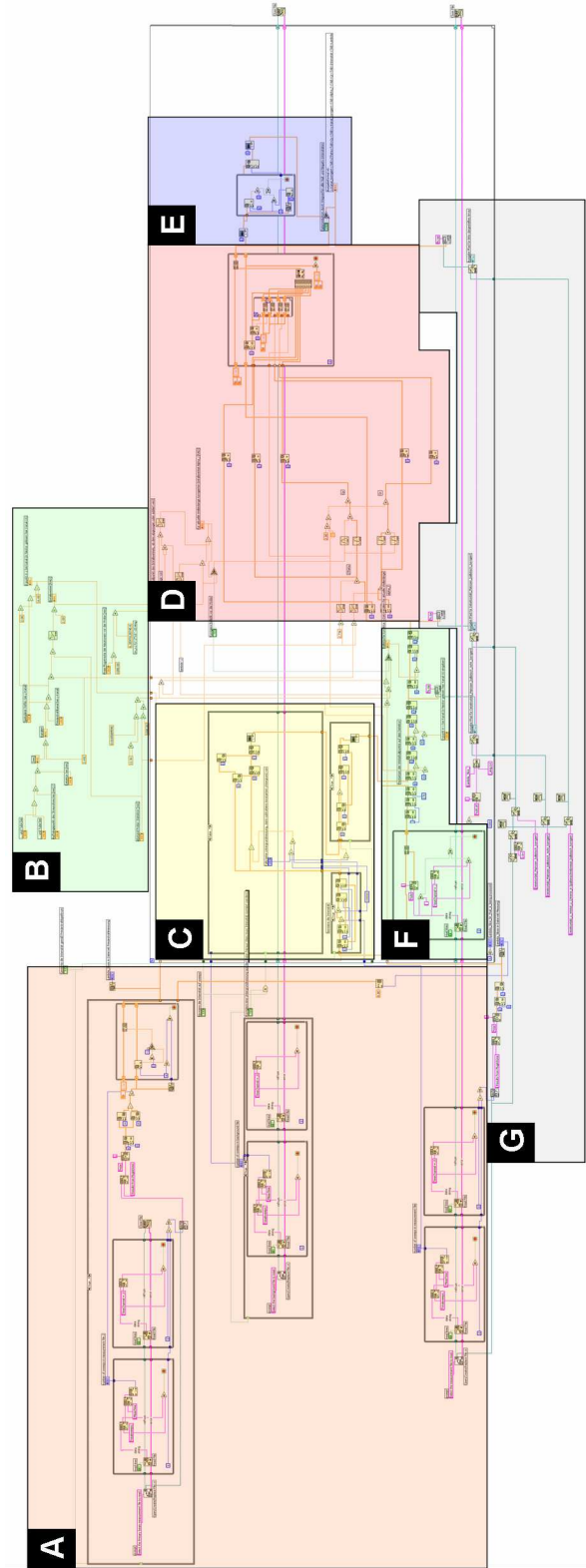
Figure B.14: *Overview of the LabVIEW™ TOF-GISANS evaluation program: "A" reads the required information from the DART output files; "B" contains the routines to calculate the ballistic correction from geometric instrument parameters; "C" performs the background correction and weights the intensities by the primary beam intensity distribution; section "D" converts the ballistically corrected data into reciprocal space values; "E" performs a data reduction by deleting negative and zero intensities from the array; "F" builds the ballistically corrected raw data array processed by section "D". In "G" the file paths and file names are created and the processed data is stored to text files.*
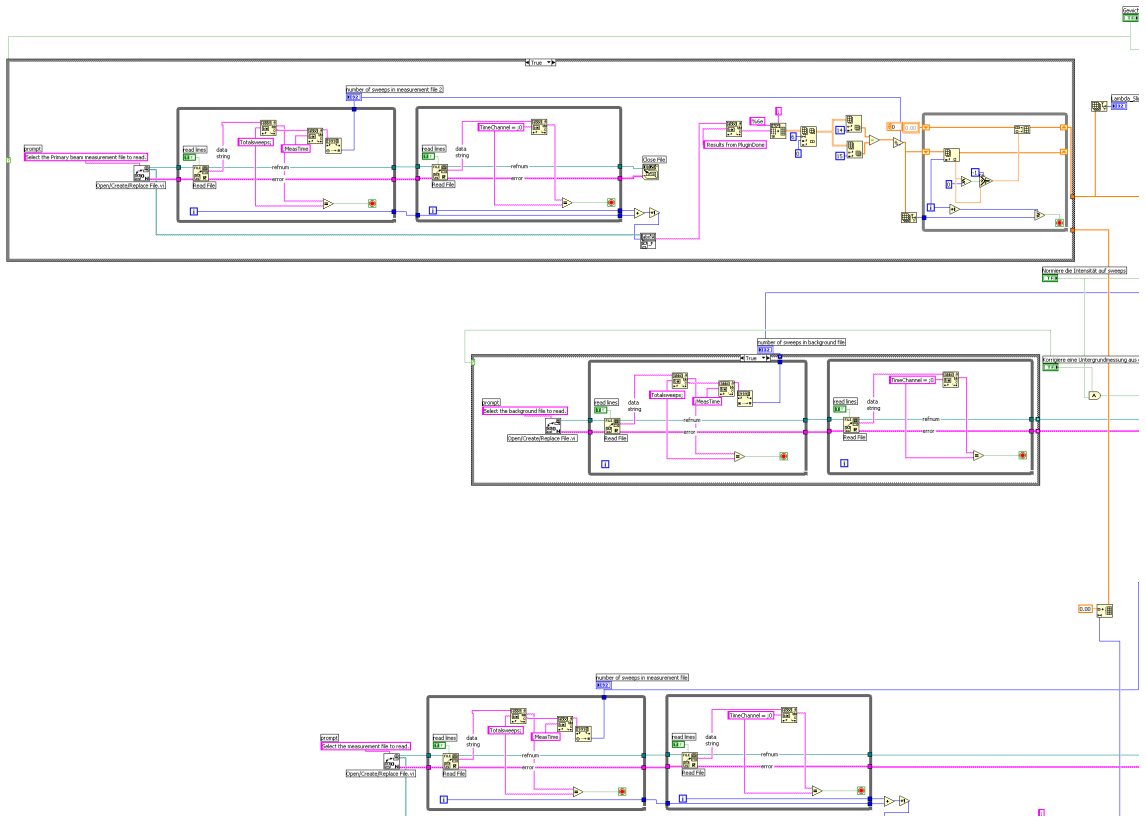
Figure B.15: *LabVIEW™ block diagram of the TOF-GISANS evaluation program read-data section "A".*
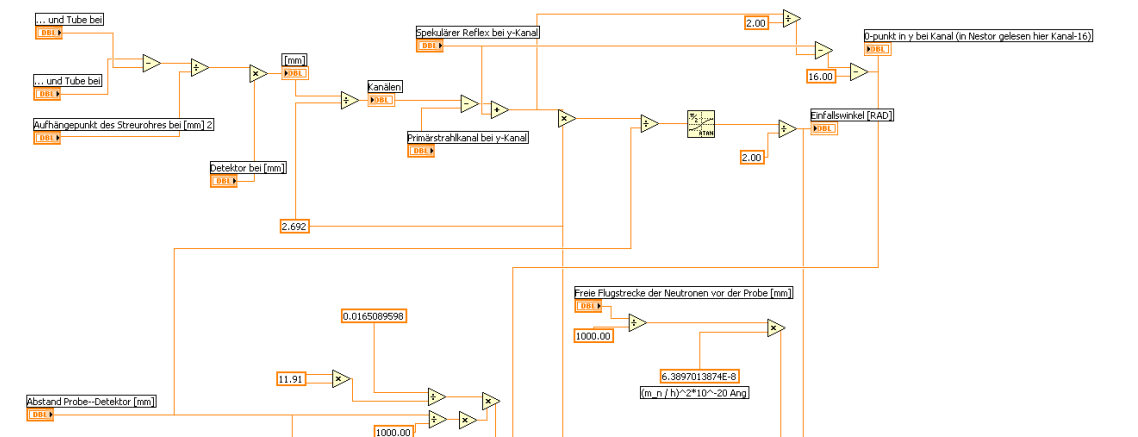
Figure B.16: *LabVIEW™ block diagram of the TOF-GISANS evaluation program section "B" which calculates the ballistic correction for each wavelength slice.*
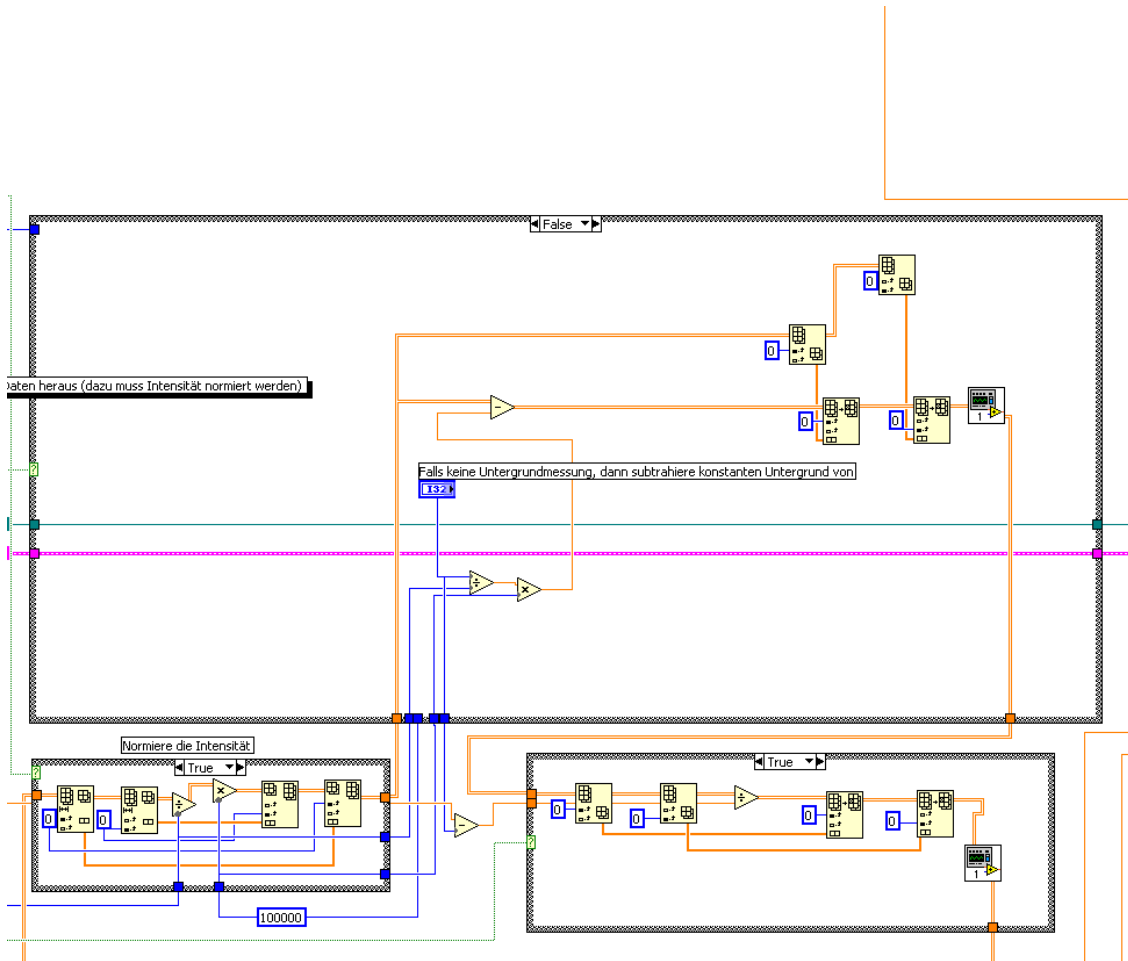
Figure B.17: *LabVIEW*™ *block diagram of the TOF-GISANS evaluation program section "C" for background correction and intensity weighting.*
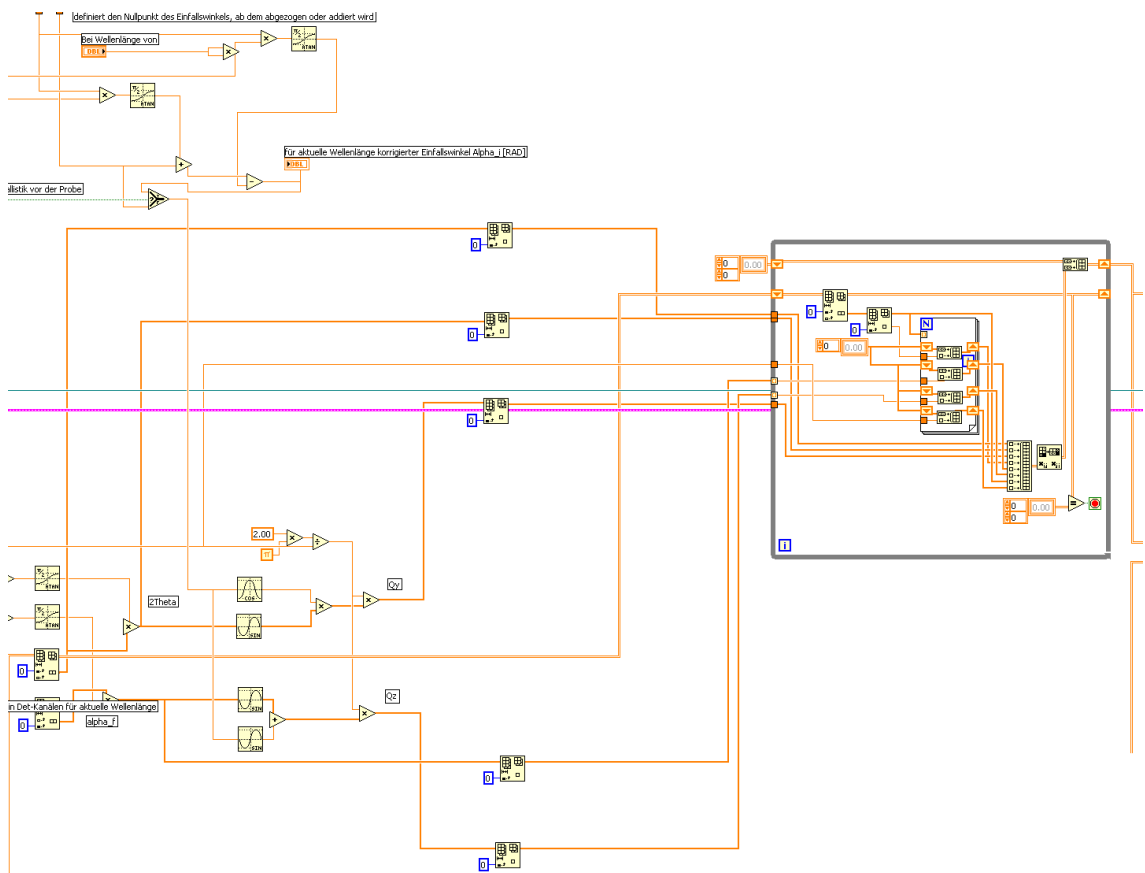
Figure B.18: *LabVIEW™ block diagram of the TOF-GISANS evaluation program data-conversion section "D", which calculates the reciprocal space values.*

function of the wavelength is also corrected and the output array is created containing the information described in 8.2.4 for each wavelength slice.

B.4.5 Data-Reduction Section "E"

A data reduction process on the array built in section "D" is performed in this section (figure B.19) by deleting all zero and negative intensity values from the array before handing the data to section "G" where it is saved to a file. Alternatively, the data reduction routine can also be by-passed by the boolean switch in the lower half of this section.

B.4.6 Data-Processing Section "F"

The while-loop in the left half of this section (figure B.20) converts the matrices from the input file (after pre-processing by section "C") to arrays containing the x-y detector channels and the corresponding intensity information. Each wavelength slice is corrected by the ballistic information obtained from section "B" as a function
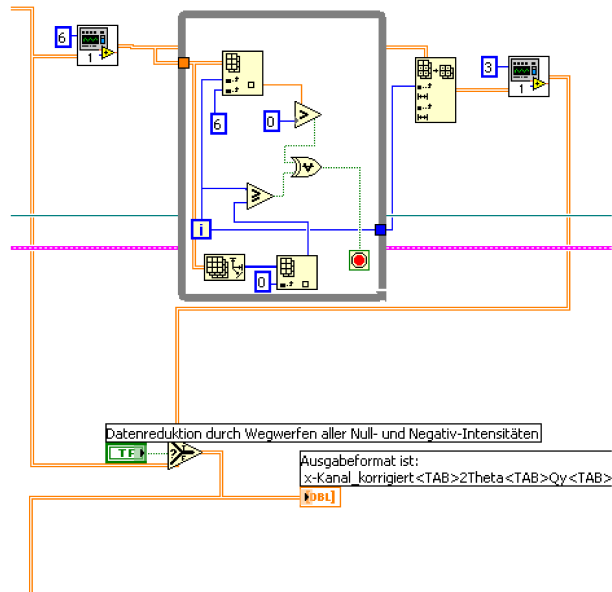
Figure B.19: *LabVIEW™ block diagram of the TOF-GISANS evaluation program data-reduction section "E".*

of the wavelength and then passed to section "D" of the program for conversion into reciprocal space.

B.4.7 Storage Section "G"

The program code in this part (figure B.21) creates the path and file name of the processed file and stores the ballistically corrected and uncorrected wavelength slices into separate files with the file name containing the corresponding wavelength. The fully processed output files, additionally containing the corresponding scattering angles and reciprocal space values, are stored in a separate directory.
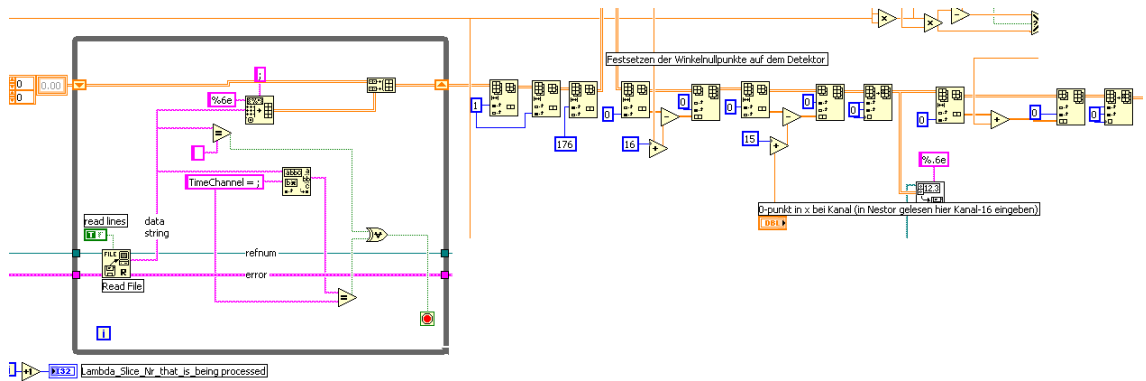
Figure B.20: *LabVIEW™ block diagram of the TOF-GISANS evaluation program section "F", which converts the matrices read from the DART input file into arrays of x-y detector channel with corresponding intensities and performs the ballistic correction.*
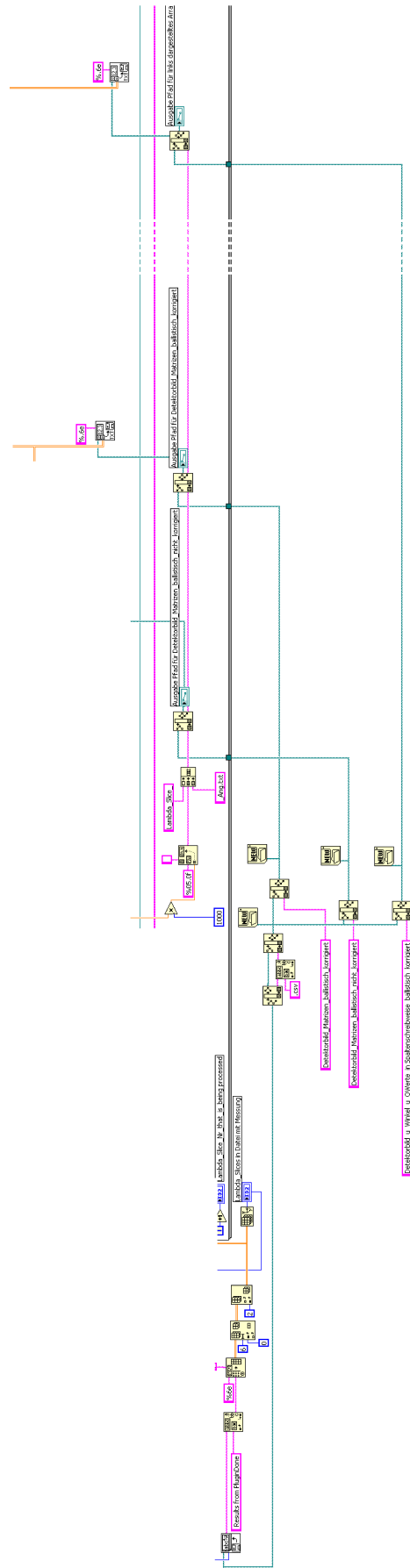
Figure B.21: *LabVIEW™ block diagram of the TOF-GISANS evaluation program storage section "G".*

Conference Contributions

Talks

- W. Kreuzpaintner, M. Störmer, D. Lott, D. Solina, A. Schreyer. Epitaxial growth of Ni on Si(100) by DC Magnetron Sputtering. *Materials Science and Engineering, Nuremberg, 2008*

- W. Kreuzpaintner, M. Störmer, D. Lott, D. Solina, A. Schreyer. Epitaxial Growth of Ni on Si(100) Substrate by DC Magnetron Sputtering. *DPG Frühjahrstagung, Dresden, 2009*

- W. Kreuzpaintner, J.-F. Moulin, D. Lott, R. Kampmann, M. Haese-Seiller, M. Störmer, A. Schreyer. Time-of-flight Grazing Incidence Small Angle neutron Scattering on Gd Nanowires. *JCNS Workshop OffSpec 2009 - Modelling and Data Analysis for Grazing Incidence and Off-Specular Scattering, Feldafing, 2009*

- D. Lott, W. Kreuzpaintner, V.G. Syromyatnikov, A. Schreyer. Magnetic off-specular neutron scattering at the reflectometer NeRo at GKSS. *JCNS Workshop OffSpec 2009 - Modelling and Data Analysis for Grazing Incidence and Off-Specular Scattering, Feldafing, 2009*

- W. Kreuzpaintner, J.-F. Moulin, D. Lott, R. Kampmann, M. Haese-Seiller, M. Störmer, A. Schreyer. Time-of-flight Grazing Incidence Small Angle neutron Scattering on Gd Nanowires. *Deutsche Tagung für Forschung mit Synchrotronstrahlung, Neutronen und Ionenstrahlen an Großgeräten, Berlin, 2010*

- W. Kreuzpaintner, D. Lott, S. Taheri, S. Bohse, A. Kobs, S. Heße, St. Förster, W. Hansen, H. P. Oepen, A. Schreyer. Structural and interface properties of Co/Pt multilayers, Ni_2MnIn/MgO nanostructures, and iron oxide nanoparticles. *1st LEXI - Workshop "NANOSPINTRONICS", Hamburg, 2010*

- W. Kreuzpaintner, M. Störmer, D. Lott, D. Solina, A. Schreyer. Epitaxial Growth of Ni on Si Substrate by DC Magnetron Sputtering. *DPG Frühjahrstagung, Regensburg, 2010*

- W. Kreuzpaintner, Boris P. Toperverg, D. Lott, M. Störmer, V. Neu, Ch. Bran, M. Ernst, A. Schreyer. Preparation and Analysis of Ni Nanowires on Si Gratings. *4th Seeheim Conference on Magnetism, Frankfurt/Germany, 2010*

Poster Contributions

- W. Kreuzpaintner, H. Tartakovskaya, A. Schreyer. Approach to the Neutron Scattering Analysis of Magnetic Nanostructures. *Deutsche Tagung für Forschung mit Synchrotronstrahlung, Neutronen und Ionenstrahlen an Großgeräten, Hamburg, 2006*

- W. Kreuzpaintner, D. Lott, M. Störmer, A. Schreyer. X-ray and Neutron Scattering on a Magnetic Sub-micrometer Ni dot array. *6th International Conference on Fine Particle Magnetism, Rome, 2007*

- W. Kreuzpaintner, D. Lott, M. Störmer, A. Schreyer. X-ray and Neutron Scattering on a Ni dot array. *DPG Frühjahrstagung, Berlin, 2008*

- W. Kreuzpaintner, R. Kampmann, J.-F. Moulin, M. Haese-Seiller, D. Lott, A. Schreyer. GISANS-Measurements on Magnetic Gd-Nanowires. *10th International Conference on Surface X-ray and Neutron Scattering, Paris, 2008*

- W. Kreuzpaintner, R. Kampmann, J.-F. Moulin, M. Haese-Seiller, D. Lott, A. Schreyer. GISAXS- and GISANS-Measurements on Ni- and Gd-Nanowires. *Deutsche Neutronenstreutagung, Garching, 2008*

- W. Kreuzpaintner, V. Neu, R. Kampmann, J.-F. Moulin, M. Haese-Seiller, D. Lott, A. Schreyer. Preparation of Gd Nanowires on faceted sapphire substrates and their properties. *Materials Science and Engineering, Nuremberg, 2008*

- W. Kreuzpaintner, D. Lott, M. Störmer, V. Neu, C. Bran, A. Schreyer. Preparation of Ni nanowires on Si gratings and their properties. *DPG Frühjahrstagung, Dresden, 2009*

- W. Kreuzpaintner, J.-F. Moulin, D. Lott, R. Kampmann, M. Haese-Seiller, M. Störmer, A. Schreyer. Time-of-flight grazing incidence small angle neutron scattering on Gd nanowires. *2. FRM II USER MEETING, Garching, 2009*

- W. Kreuzpaintner, D. Lott, M. Störmer, V. Neu, Ch. Bran, M. Ernst, A. Schreyer. Preparation and Analysis of Ni Nanowires on Si Gratings. *International Conference on Magnetism, Karlsruhe, 2009*

- E. Tartakovskaya, W. Kreuzpaintner, A. Schreyer. Spin wave dynamics in two- and three-dimensional superlattices of nanosized ferromagnetic spheres. *International Conference on Magnetism, Karlsruhe, 2009*

- S. Mehdizadeh Taheri, W. Kreuzpaintner, A. Kornowski, A. Meyer, St. Förster, A. Schreyer. Preparation and Characterisation of Ironoxide Nanoparticles. *4th Seeheim Conference on Magnetism, Frankfurt/Germany, 2010*

List of Figures

Acknowledgements